

May 2017

Dc Line-Interactive Uninterruptible Power Supply (UPS) with Load Leveling for Constant Power and Pulse Loads

Seyed Ahmad Hamidi
University of Wisconsin-Milwaukee

Follow this and additional works at: <https://dc.uwm.edu/etd>

 Part of the [Biomedical Engineering and Bioengineering Commons](#), and the [Electrical and Electronics Commons](#)

Recommended Citation

Hamidi, Seyed Ahmad, "Dc Line-Interactive Uninterruptible Power Supply (UPS) with Load Leveling for Constant Power and Pulse Loads" (2017). *Theses and Dissertations*. 1481.
<https://dc.uwm.edu/etd/1481>

DC LINE-INTERACTIVE UNINTERRUPTIBLE POWER SUPPLY (UPS) WITH
LOAD LEVELING FOR CONSTANT POWER AND PULSE LOADS

by

Seyed Ahmad Hamidi

A Dissertation Submitted in
Partial Fulfillment of the
Requirements for the Degree of
Doctor of Philosophy
in Engineering

at

The University of Wisconsin-Milwaukee

May 2017

ABSTRACT

DC LINE-INTERACTIVE UNINTERRUPTIBLE POWER SUPPLY (UPS) WITH LOAD LEVELING FOR CONSTANT POWER AND PULSE LOADS

by

Seyed Ahmad Hamidi

The University of Wisconsin-Milwaukee, 2017
Under the Supervision of Professor Dr. Adel Nasiri

Uninterruptable Power Supply (UPS) systems are usually considered as a backup power for electrical systems, providing emergency power when the main power source fails. UPS systems ensure an uninterrupted, reliable and high quality electrical power for systems with critical loads in which a continuous and reliable power supply is a vital requirement.

A novel UPS system topology, DC line-interactive UPS, has been introduced. The new proposed UPS system is based on the DC concept where the power flow in the system has DC characteristic. The new DC UPS system has several advantageous with respect to the on-line 3-phase UPS which is extensively used in industry, such as lower size, cost and weight due to replacing the three-phase dual converter in the on-line UPS system with a single stage single phase DC/DC converter and thus higher efficiency is expected.

The proposed system will also provide load leveling feature for the main AC/DC rectifier which has not been offered by conventional AC UPS systems. It applies load power smoothing to reduce the rating of the incoming AC line and consequently reduce the installation cost and time. Moreover, the new UPS technology improves the medical

imaging system up-time, reliability, efficiency, and cost, and is applicable to several imaging modalities such as CT, MR and X-ray as well.

A comprehensive investigation on different energy storage systems was conducted and couple of most promising Li-ion cell chemistries, LFP and NCA types, were chosen for further aggressive tests. A battery pack based on the LFP cells with monitoring system was developed to be used with the DC UPS testbed.

The performance of the DC UPS has also been investigated. The mathematical models of the system are extracted while loaded with constant power load (CPL) and constant voltage load (CVL) during all four modes of operation. Transfer functions of required outputs versus inputs were extracted and their related stability region based on the Routh-Hurwitz stability criteria were found.

The AC/DC rectifier was controlled independently due to the system configuration. Two different control techniques were proposed to control the DC/DC converter. A linear dual-loop control (DLC) scheme and a nonlinear robust control, a constant frequency sliding mode control (CFSMC) were investigated.

The DLC performance was convincing, however the controller has a limited stability region due to the linearization process and negative incremental impedance characteristics of the CPL which challenges the stability of the system.

A constant switching frequency SMC was also developed based on the DC UPS system and the performance of the system were presented during different operational modes. Transients during mode transfers were simulated and results were depicted. The controller

performances met the control goals of the system. The voltage drop during mode transitions, was less than 2% of the rated output voltage.

Finally, the experimental results were presented. The high current discharge tests on each selected Li-ion cell were performed and results presented. A testbed was developed to verify the DC UPS system concept. The test results were presented and verified the proposed concept.

© Copyright by Seyed Ahmad Hamidi, 2017
All Rights Reserved

TABLE OF CONTENTS

Chapter	Page
ABSTRACT.....	ii
TABLE OF CONTENTS.....	vi
LIST OF FIGURES	viii
LIST OF TABLES.....	xvii
ACKNOWLEDGMENTS	xviii
CHAPTER I: Introduction	1
1.1 Background	1
1.2 UPS Classifications.....	1
1.3 Novel UPS Configuration	8
1.4 Thesis Objectives	11
1.5 Thesis Organization	11
CHAPTER II: Description of the System Architecture.....	12
2.1 DC Line-Interactive UPS with Load Leveling	12
2.2 AC/DC Rectifier	15
2.3 DC/DC Bidirectional Converter	16
2.4 Modes of Operation	17
2.4.1 Mode I: Load Leveling Mode	17
2.4.2 Mode II: Standby Mode	19
2.4.3 Mode III: Online Mode	20
2.4.4 Mode IV: Islanded Mode	21
2.5 The Load Profile	22
2.6 Battery Energy Storage System (BESS).....	23
CHAPTER III: Energy Storage Systems and Battery Chemistry Selection	25
3.1 Introduction.....	25
3.2 Battery Energy Storage System (BESS): Types, Characteristics and Modeling	30
3.2.1 Lead Acid.....	30
3.2.2 Lithium-Ion	31
3.2.3 Sodium Sulfur (NaS).....	32
3.2.4 Other Types of Batteries and Energy Storage Systems	32
3.2.5 Battery Energy Storage Modeling and Test Setups	34
3.3 Ultracapacitors Energy Storage: Types, Characteristics and Modeling	44
3.3.1 Ultracapacitor Types and Characteristics	44
3.3.2 Ultracapacitor Modeling	46
3.4 Energy Storage Management Systems (ESMSs).....	48
3.4.1 Main Concepts	48

3.4.2 State of Charge.....	50
3.4.3 State of Health (SOH).....	52
3.4.4 State of Life (SOL)	53
3.4.5 Cell Balancing Systems	53
3.5 Battery Chemistry Selection	54
 CHAPTER IV: System Modeling.....	58
4.1 Introduction.....	58
4.2 AC/DC Converter Modeling.....	58
4.3 DC/DC Bidirectional Converter Modeling.....	63
4.4 Battery Energy Storage System Modeling.....	66
4.5 CPL Modeling.....	66
4.6 DC UPS System Modeling	69
4.6.1 Mode I: Load Leveling Mode	72
4.6.2 Mode II: Standby Mode	73
4.6.3 Mode III: Online Mode	74
4.6.4 Mode IV: Islanded/UPS Mode.....	76
 Chapter V: System Analysis and Control	78
5.1 Introduction.....	78
5.2 Stability Analysis of the System During Mode I.....	79
5.3 Stability Analysis of the System During Mode II.....	90
5.4 Stability Analysis of the System During Mode III	99
5.5 Stability Analysis of the System During Mode IV	101
5.6 Control Strategy	103
5.6.1 AC/DC Rectifier Control Scheme	104
5.6.2 DC/DC Power Converter Controller.....	108
5.6.3 Constant Frequency Sliding Mode Control (CFSMC)	130
 CHAPTER VI: Experimental Results.....	151
6.1 Introduction.....	151
6.2 Battery Energy Storage System (BESS).....	151
6.2.1 Cell Performance Tests	153
6.2.2 Li-ion Battery Pack	165
6.2.3 Battery Management System (BMS)	168
6.3 The Power Interface	173
6.3.1 The Battery Energy Storage System Power Interface.....	174
6.3.2 AC/DC Grid Tied Rectifier.....	176
6.3.3 The DC/AC Grid Tied Inverter: The Constant Power Load.....	177
6.4 Results for Different Modes of Operation	178
 Chapter VII: Conclusion	187
 REFERENCES	191
 CURRICULUM VITAE	200

LIST OF FIGURES

Figure	Page
Figure 1.1: Block diagram of the off-line UPS system.....	2
Figure 1.2: Block diagram of the on-line UPS system.	3
Figure 1.3: Block diagram of the line-interactive UPS topology	4
Figure 1.4: Block diagram of the series-parallel line-interactive UPS topology.....	5
Figure 1.5: Block diagram of a typical rotary UPS system topology.	6
Figure 1.6: Block diagram of a typical hybrid UPS system.	7
Figure 1.7: Block diagram of the proposed DC line-interactive UPS system.	10
Figure 2.1: Schematic of the conventional CT scan system with on-line UPS. The load represents the CT machine.....	12
Figure 2.2: Configuration of the DC UPS system proposed for the CT machine.	13
Figure 2.3: The Load Profile consists of a CPL (140 kW for 2 s and 0 kW for 200 s) and a CVL (10 kW). The BESS provides peak pulsed power for 2 s and then charges with 10 kW from grid.....	14
Figure 2.4: Block diagrams of the proposed DC UPS system.....	15
Figure 2.5: The power flow of the proposed DC UPS during load leveling mode.....	18
Figure 2.6: The power flow of the proposed DC UPS during standby mode.....	19
Figure 2.7: Block diagram of the DC UPS system during mode III, the BESS is fully charged and does not have any power exchange with the DC link.	21
Figure 2.8: Block diagram of the DC UPS system during islanded mode; the DC/DC converter provides entire load power from the BESS.	22

Figure 2.9: The load and the BESS power profiles during different modes of the DC UPS.	23
.....	
Figure 3.1: Different types of energy storage systems.	27
Figure 3.2: Ragone plot for energy and power density for ultracapacitors (UCap), flywheel energy storage (FES), and batteries of the: nickel-metal hydride (NiMH), zinc- bromine (Zn-Br); lead-acid (LAB), lithium-ion (Li-ion); sodium sulfur (NaS) types.	29
Figure 3.3: Zinc-Bromide (ZnBr) flow battery used in the University of Wisconsin- Milwaukee (UWM) Lab for experimentally demonstrating the mitigation of power variability from renewable energy sources. The battery is rated at 50 kW, 675 Ah and when fully charged.....	33
Figure 3.4: Combined detailed equivalent circuit models for batteries,	36
(a) battery lifetime model and (b) V-I characteristics model [21].....	36
Figure 3.5: Open-circuit voltage (Voc) versus state of charge (SOC) for	37
an example Lithium-ion battery of 2.6 Ah.....	38
Figure 3.6: Test bed system of the battery (left) and LabVIEW interface model (right) .	38
Figure 3.7: Pulse discharging voltage and current with 1 A (sampling frequency is 100 Hz).....	39
Figure 3.8: Open-circuit voltage (Voc) as a function of state of charge (SOC)	40
Figure 3.9: Series resistance as a function of soc for various discharging rate (for 0.52, 1, 2, 2.6 A discharging current).	40
Figure 3.10: Transient resistances as functions of SOC	41
Figure 3.11: Transient capacitances as functions of SOC	41
Figure 3.12: Block diagram of the battery model	42

Figure 3.13: Terminal voltage of the battery Simulink model and experimental data	43
Figure 3.14: Classification of ultracapacitors based on the electrode design	45
Figure 3.15: Examples of Li-ion ultracapacitors of 2200F, 2300F and 3300F.....	45
Figure 3.16: Ultracapacitor bank in the UWM Lab. The approximate overall dimensions are 1.03x0.93x1.17 m. Rated at 720V and 0.5Ah.....	46
Figure 3.17: Electric equivalent circuit model for an ultracapacitor [29].....	46
Figure 3.18: Experimental data and simulation results for the Li-ion Ultracapacitor, 10 A pulsed charging DC test at 25°C [29].	48
Figure 3.19: A modular battery management system (BMS) topology: several slave boards collect cells data and send it to the master board.	49
Figure 3.20: A distributed Battery Management System (BMS): each cell sends the data to the main controller.....	50
Figure 3.21: Block diagram of a typical BMS [39].	50
Figure 3.22: Open Circuit Voltage (OCV) versus Depth Of Discharge (DOD) for NCA and LFP types of Li-ion batteries.	52
Figure 3.23: The required load profile. The candidate battery should be capable of providing a peak power rating as high as 400 A discharging for 2 second periods.	55
Figure 4.1: Block diagram of the DC UPS system, including AC/DC and DC/DC converters.....	58
Figure 4.2: Schematic diagram of the DC UPS system.	59
Figure 4.3: Representation of space vector of rectifier voltage in stationary $\alpha\beta$ frame and dq rotating frame.....	61

Figure 4.4: A two-phase interleaved bidirectional DC/DC converter is used to connect the BESS to the DC link	64
Figure 4.5 Simplified model of the DC/DC converter, i_{dc} represents the power from the grid.....	65
Figure 4.6 V-I characteristic of a CPL and the negative incremental impedance characteristic of the CPL.....	67
Figure 4.7 Illustration of a power converter feeding a constant power load, CPL, and a constant voltage load, CVL.....	68
Figure 4.8: Schematic of the DC UPS.....	70
Figure 4.9: The simplified model of the DC UPS system in mode I. i_d represents the grid and rectifier.....	73
Figure 4.10: Electrical equivalent circuit of the DC UPS system in mode II.....	74
Figure 4.11: Schematic of the DC UPS during mode III, the Online mode.....	75
Figure 4.12: Schematic of the DC UPS model during islanded mode.....	76
Figure 5.1: The DC link voltage affected by battery voltage, duty ratio of the DC/DC converter and grid current.....	83
Figure 5.2: Stability region of the open loop system while DC link voltage (v_{dc}) varies.	87
Figure 5.3: Stability region of the open loop system while constant voltage load (CVL) varies.....	88
Figure 5.4: Stability region of the open loop system while equivalent resistant (req) varies.....	89
Figure 5.5: Stability region of the open loop system while duty ratio of the DC/DC converter (D) varies.....	90

Figure 5.6: Block diagram of the grid tied AC/DC rectifier and controller scheme. Direct Power Control method is used to control the rectifier.	106
Figure 5.7: DC UPS system used to illustrate the Direct Power Control (DPC) scheme performance while load varies.	107
Figure 5.8: The of the DC UPS simulation. The AC/DC rectifier is controlled by direct power control (DPC) method to deliver constant power while the load varies.	108
Figure 5.9: Block diagram of the DC UPS system.	109
Figure 5.10: Bode diagram of the current open loop gain	112
Figure 5.11: Bode diagrams of the PI controller, G_{ci} and the current open loop gain, H_i	114
Figure 5.12: The gray area illustrates the current inner loop, T_i	114
Figure 5.13: Bode diagrams of the voltage open loop plant, G_{vd}	116
Figure 5.14: Bode diagrams of the voltage compensator, G_{cv} , and the open loop gain, H_v	117
Figure 5.15: The bode diagrams of the closed loop system.....	118
Figure 5.16: The root locus diagram of the closed loop system	119
Figure 5.17: By increasing the k_p and k_i , the proportional and integral gains, the complex poles move toward right hand side and the pole close to origin move away from origin toward left hand side.	120
Figure 5.18: $k_p = 1$, and increasing k_i up to 17000, further than its stability zone.	121
Figure 5.19 Step response of the closed loop system	122
Figure 5.20: By increasing k_p from 1 to 13, and k_i from 1 to 6000, the step response becomes faster with more oscillation.....	123

Figure 5.21: By increasing the DC link capacitance, the poles move toward imaginary axis.....	124
Figure 5.22: Simulation model of the DC UPS and the Dual-Loop Controller (DLC) ..	125
Figure 5.23: Performance of the system while working on the rated value, battery current and DC link voltage.....	126
Figure 5.24: Performance of the DLC against the CPL variation. The CPL step changes are 0, 10, 50, 100 and 140 kW	127
Figure 5.25: Performance of the proposed DLC controller during different operating modes.....	129
Figure 5.26: Schematic of the DC UPS system used for performing Sliding Mode Control (SMC)	134
Figure 5.27: Block diagram of the proposed constant frequency sliding mode controller	140
Figure 5.28: DC UPS system modeled in MATLAB/Simulink. The proposed constant frequency sliding mode controller (CFSMC) is managed the system.....	145
Figure 5.29: DC UPS system output results. Battery energy storage discharging current and the DC link voltage.....	146
Figure 5.30: Performance of the DC UPS system with CFSMC while CPL load varies.....	148
Figure 5.31: Performance of the proposed CFSMC controller during different operating modes.....	150
Figure 6.1: Characteristic comparison between several types of batteries.....	152

Figure 6.2: Three candidate Li-ion cells, LFP (40 Ah, CALB), NCA (42 Ah, JCI) and LFP (30 Ah, SAFT)	153
Figure 6.3: The terminal voltage (top) and current (bottom) of a 40 Ah LFP type battery from CALB at 1C discharging at room temperature.	155
Figure 6.4: Open circuit voltage versus depth of discharge (DOD) curve extracted from 40 Ah CALB cell	156
Figure 6.5: Voltages and current curves for high rate pulsed dischargetest at 200 A (left side) and 240 A (right side) for the 40 Ah CALB cell.....	157
Figure 6.6: The terminal voltage (top) and current (bottom) of a 42 Ah NCA type battery from JCI at 1C discharging at room temperature.....	158
Figure 6.7: The open circuit voltage vs depth of discharge for 42 Ah NCA type Li-ion cell.....	159
Figure 6.8: Terminal voltage and current curves for high rate test performed at 200 A and 240 A discharging.....	160
Figure 6.9: The terminal voltage (top) and current (bottom) of a 30 Ah LFP type battery from SAFT at 1C discharging (30 A) at room temperature.....	161
Figure 6.10: Open circuit voltage versus depth of discharge (DOD) curve extracted from 30 Ah LFP type SAFT cell.	161
Figure 6.11: Terminal voltage and current of a LFP type SAFT cell, high rate pulsed discharging at 200 A and 240 A.	162
Figure 6.12: Schematic of the Li-ion battery pack.	166
Figure 6.13: Li-ion battery pack contains 54 LFP type Li-ion cells.	167

Figure 6.14: Block diagram of the battery management system (BMS) utilized for the Li-ion battery pack. The BMS can monitor up to 12 Li-ion cells.	168
Figure 6.15: Block diagram of the 5 BMS boards monitor 54 cells in the battery pack. SPI communication is used to transfer information between the boards and laptop.....	170
Figure 6.16: 5 BMS boards monitor the Li-ion battery pack voltage and temperature..	171
Figure 6.17: Screenshot of the BMS graphical user interface (GUI)used to read the date collected by the BMS boards.	172
Figure 6.18: The battery energy storage system consists of Li-ion battery pack, BMS boards and the GUI.	173
Figure 6.19: Block diagram of the DC UPS testbed.....	174
Figure 6.20: Implementation of dual-loop controller with DSP Builder Blocksets.	175
Figure 6.21: Results of the DC/DC controller implemented with DSP Builder Blocksets.	
.....	176
Figure 6.22: Implementation of the Inverter (CPL) controller with DSP Builder Blocksets.	177
Figure 6.23: Results of the inverter model implemented with DSP Builder Blocksets..	178
Figure 6.24: The DC UPS testbed, Li-ion battery pack and the BMS	179
Figure 6.25: Block diagram of the DC UPS testbed in mode I.....	180
Figure 6.26: Power exchange between the battery, grid and load in the DC UPS during mode I.	180
Figure 6.27: Waveforms of the DC UPS testbed operating between modes I and II.	181
Figure 6.28: Block diagram of the DC UPS system during grid disconnection.	182

Figure 6.29: Power exchange between the DC UPS system during the grid disturbance. The battery state changes from being charge with low rate to discharge low rate to compensate the disturbance from grid.	182
Figure 6.30: Performance of the DC UPS testbed during mode II, when grid is disconnected and connected again (grid disturbance). The battery current changes from negative value (charging) to positive value (discharging) in order to respond to the disturbance.	183
Figure 6.31: Block diagram of the DC UPS testbed and power flow during the mode IV, the UPS mode.	184
Figure 6.32: Power exchange between the battery and load in the DC UPS during mode IV, UPS mode; battery provides whole power	185
Figure 6.33: Waveforms of the DC UPS testbed operating on mode IV, the UPS mode, when the gird is out.....	186

LIST OF TABLES

Table	Page
Table 3.1: Worldwide installed electrical energy storage capacity [1].....	28
Table 3.2: Characteristics of common energy storage systems.	29
Table 3.3: Characteristic comparison between batteries of Li-ion family chemistry, lead-acid and ultracapacitor. The highest figure of merit, which is associated with best performance, is equal to 6.....	32
Table 3.4: Correction rate factors for various temperatures	42
Table 3.5: Correction rate factors for various discharging currents	42
Table 3.6: Correction rate factors for various charging currents	42
Table 5.1: DC UPS specifications for the model implemented in the Simulink.	107
Table 5.2: DC UPS specifications for the model implemented in the Simulink.	146
Table 6.1: The performance test result for the CALB battery cell.	157
Table 6.2: The performance test result for the JCI battery cell.	160
Table 6.3: The performance test result for the SAFT battery cell.	163
Table 6.4: Internal resistance of the three Li-ion battery cells AT HIGH RATES	163
Table 6.5: Comparison of measured values for the three Li-ion batteries cells/packs (108 series-connected cells)	164

ACKNOWLEDGMENTS

I would like to express my deepest appreciation to my advisor professor **Adel Nasiri**, director of the Center for Sustainable Electrical Energy System (SEES), for his continuous support, patience and guidance throughout my PhD program. I want to thank him for all of the opportunities I was given to conduct my research and thesis. I'm also grateful for the members of my committee for their valuable comments. I want to thank Mr. Jason Katcha for his excellent collaboration and guidance to build the testbed and generously sharing his valuable experiences with me. I thank Mr. Ezana Mekonnen for his help.

I would also like to offer my sincere gratitude to my beloved parents for their endless love and support. I would like to thank to my lovely wife, Mehrnaz, for her patience, love and support.

Finally, I would like to express my gratitude to all the staff of UWM for providing such a friendly environment for students.

CHAPTER I: Introduction

1.1 Background

Uninterruptable Power Supply (UPS) systems are usually considered as a backup power for electrical systems, providing emergency power when the main power source fails. UPS systems ensure an uninterrupted, reliable and high quality electrical power for systems with critical loads in which a continuous and reliable power supply is a vital requirement. Examples of such systems include healthcare systems, medical facilities and data centers. Technically, UPS systems protect these critical systems against any electrical power disturbances coming from the main source.

UPS systems ideally should be able to provide uninterrupted power immediately when it requires. Due to advancements in power electronics and energy storage industries, different types of UPS with different configuration have been offered and UPS systems can participate in the main system by serving as power factor correction, decreasing total harmonic distortions (THD), boosting immunity against electromagnetic interference (EMI) and providing isolation between inputs and outputs of the system. Also, some topologies offering cost reductions by decreasing number/value of active (switches like IGBT) or passive (such as inductor and capacitor) elements used in the system [1-4].

1.2 UPS Classifications

UPS systems can be sorted in three main categories: static, rotary and hybrid which is combination of static and rotary UPS [1]. The static types are the conventional and most known type which are used for low and medium power applications. The static UPS systems involve off-line, online, line-interactive and series-parallel line-interactive

configurations. High efficiency and high reliability with low THD are the main advantages of the static UPS systems while their poor performances with nonlinear loads besides the expensive cost for achieving the advantages are the drawbacks of the static UPS systems [1-4].

Block diagram of a typical off-line UPS is presented in figure 1.1. The off-line UPS is also known as standby topology, includes three main blocks: an AC/DC rectifier, a battery pack and a DC/AC inverter. There is a static switch which control the direct line between the load and main AC line. The battery pack is charged through the rectifier and discharged the saved energy through the inverter to provide required power to the load in case of any emergency events such as main power line disconnection due to some disturbance. Adding a filter to the output of the UPS or at the output of the inverter can improve the output power quality in this configuration.

The standby topology has the advantages of simple design, low cost, small size and passive line conditioning [1,5]. However, long switching time and poor performance with nonlinear loads and no output voltage regulation are the disadvantages of this type of UPS [1].

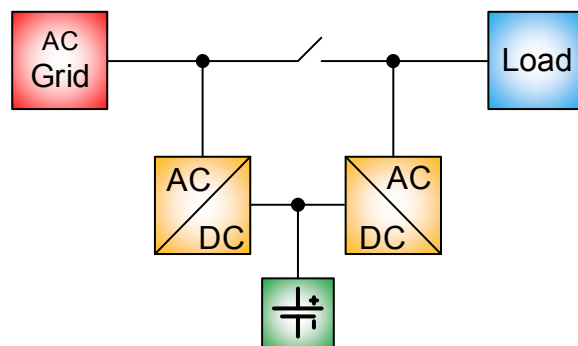


Figure 1.1: Block diagram of a typical off-line UPS system.

The online UPS configuration is the most used and known due to the capability of this topology to offer power quality and load protection [1]. The block diagram of the on-line UPS is illustrated in the figure 1.2. The UPS involves the same blocks as the off-line topology, an AC/DC rectifier, a battery pack and a DC/AC inverter but in on-line topology. The on-line UPS converters, the rectifier and the inverter, are required to be design at the full load rate and the back to back conversion is operating all the time, during normal operation and when the main AC line is not available, which leads to a lower efficiency due to double conversion system. The battery pack is charged during normal operation and discharged when the main AC line is out. The rectifier usually regulates the DC link voltage and the inverter oversees the output power quality and load protection. The main advantage of the online UPS system is the fact that there is no transition time between the normal mode and backup mode of operation This topology provides superiority in performance, power conditioning and load protection while suffers from lower efficiency due to its double stages power conversion [6-12]. To provide isolation for the load protection, an isolating transformer may be used between the inverter and load.

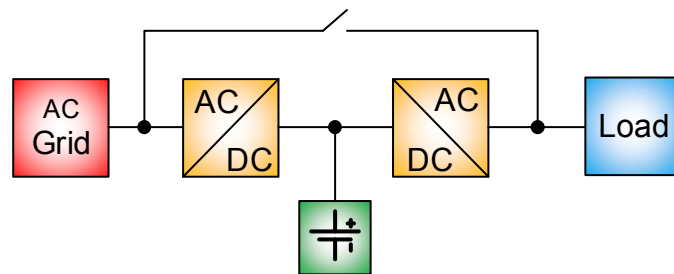


Figure 1.2: Block diagram of a typical on-line UPS system.

The next topology is the line-interactive UPS topology. The block diagram of the line-interactive UPS configuration is shown in the figure 1.3. This UPS type consists of a series inductor, a bidirectional AC/DC converter and a battery pack. Technically, line-interactive

UPS is a combination of off-line and on-line UPS, where the UPS is not in-line with the main AC line as series topology and provides output power compensation as on-line configuration, thus the system can operate on either modes, series or online configuration, however in the series mode of operation the series inductor is not necessary. The bidirectional AC/DC converter provide charging power for the battery and can also improve the power factor of the load and regulate the output voltage for the load. The bidirectional converter can provide reactive power to keep the load power factor close to unity or regulate the output voltage [13-15].

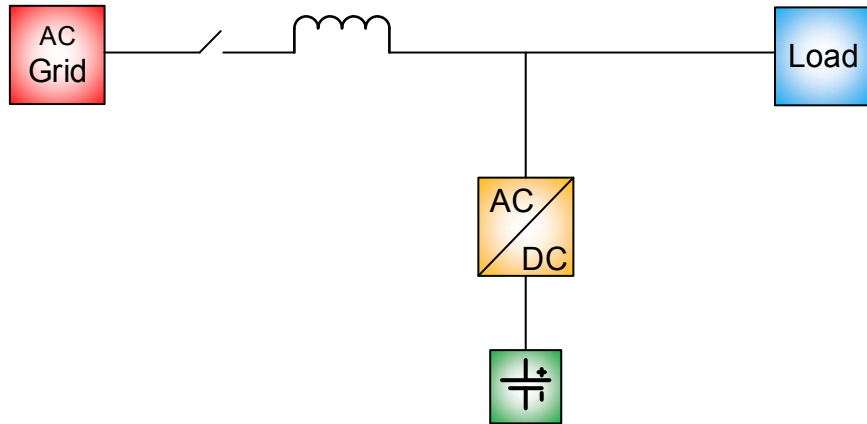


Figure 1.3: Block diagram of a typical line-interactive UPS topology

The main advantage of this topology is its low cost, simple design and highly reliable performance when compared with on-line UPS. The fact that there is single stage power conversion, explains that the higher efficiency compared to on-line UPS topology with double power conversion.

The line-interactive UPS has some disadvantages as well. The main disadvantage is the lack of effective isolation between the load and main AC power. Adding an isolation transformer can provide the isolation but in cost of adding to the price, size, and weight of

the UPS system. In addition, there is no output voltage conditioning during normal mode because the inverter is not connected in series with the load. Furthermore, there is no possibility for regulation of the output frequency during normal mode of operation [1,13].

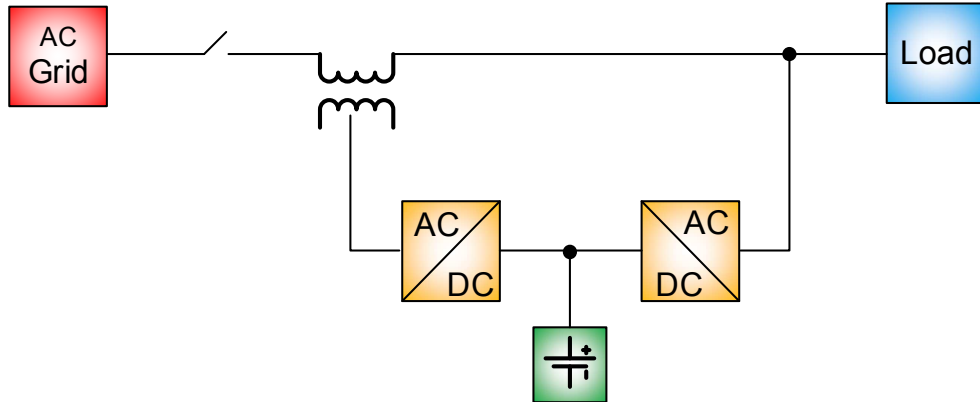


Figure 1.4: Block diagram of a typical series-parallel line-interactive UPS topology

Figure 1.4 depicts block diagrams of the series-parallel line-interactive UPS system topology which is also called universal or delta-conversion UPS. The configuration of the delta-conversion includes two bidirectional converters connected to a battery pack, a static switch and a series transformer. The AC main line is connected to the battery via the series transformer and the series bidirectional converter. The series bidirectional converter is rated for 20% of the rated output power of the UPS. The second converter is a bidirectional converter as the one used in the line-interactive UPS configurations. The parallel bidirectional converter is parallel with the load and rated at full output power of the UPS. The parallel converter regulates the output voltage while the series converter compensates for any mismatches between input and output voltages. The series converter also improves the input power factor to be close to unity and monitors the charging of the battery pack [1, 16-18].

During normal operation, most of the output power demand is provided by the main AC line. A small portion of the total power, usually up to 15%, is passed through the series and parallel converters to compensate for difference between input and output voltages and also to maintain unity power factor at input. Since the most of the required power is directly provided from input AC source to the load without any power conversion, the efficiency is expected to be high. The series-parallel line-interactive UPS can simultaneously achieve both unity power factor and precise regulation of the output voltage, which is not possible with a conventional line-interactive UPS. Basically, the advantages of online and line-interactive characteristics are combined in the series-parallel line-interactive UPS topology. This topology, presents regulated output voltage, high efficiency with line conditioning characteristics [1].

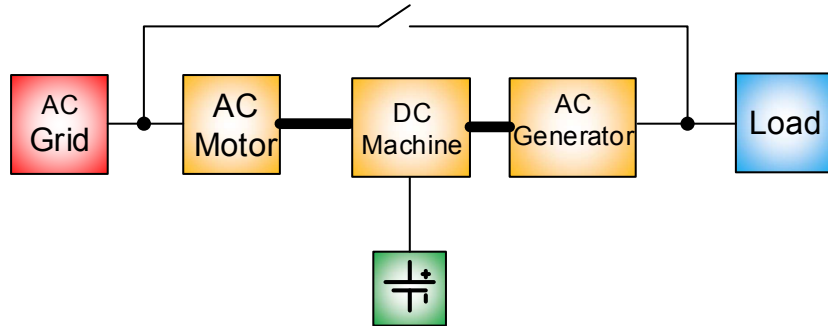


Figure 1.5: Block diagram of a typical rotary UPS system topology.

The static UPS systems are only included static parts such as active and passive components and power converters. However, the rotary UPS configuration consists of several rotary parts such as motor and generator. Block diagram of a rotary UPS topology is illustrated in the figure 1.5. The system consists of an AC motor, a DC machine, an AC generator, which all are mechanically coupled in a common shaft, and a battery pack. During the normal operation, the main AC power source supplies the AC motor which

rotates the coupled shaft and that drives the DC machine. The DC machine then drives the AC generator and the generator supplies the load. During the backup power mode, the battery pack drives the DC machine which drives the AC generator and supplies the load [19-20].

This type of UPS topologies are designed for supporting high power applications. The system typically has a large size and weight with high installation and capital cost. Furthermore, more maintenance is required compared to the static UPS topology. However, they provide a more reliable output performance. Also, the transient overload capability of the rotary UPS systems is much higher than static UPS systems. Furthermore, the rotary UPS systems have a low input current THD with a low EMI [1, 19-20].

Combination of the static configuration and rotary systems results in the hybrid category of UPS system topology. Figure 1.6 shows block diagram of a typical hybrid UPS system. The hybrid UPS topology consists of rotary and static parts. A mechanically coupled AC motor and AC generator are the rotary part and a static switch and a bidirectional AC/DC converter with a battery pack are the static parts.

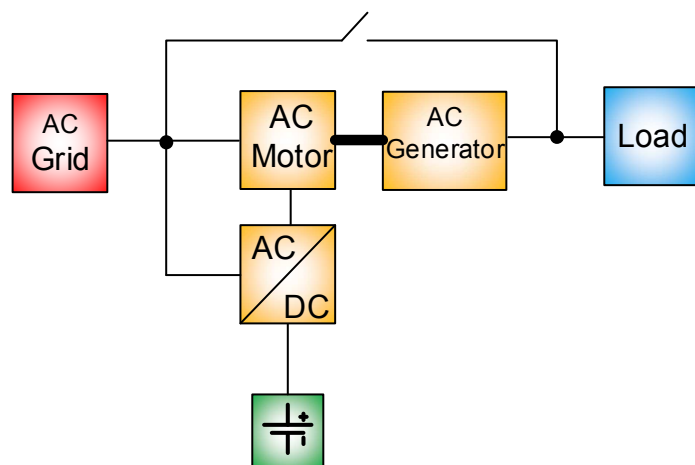


Figure 1.6: Block diagram of a typical hybrid UPS system.

During the normal mode of operation, the main AC line powers the AC motor which turns the AC generator main shaft and the AC power generated at the output terminals of the AC generator supplies the load. The bidirectional power converter rectifies the main AC source and charges the battery pack. During backup mode of operation, the bidirectional converter inverts the battery power to an appropriate AC power and drives the AC motor to rotate the AC generator main shaft. The AC generator, then supplies the load. The static switch provides direct connection from the main AC source to the load in case that the UPS system does not operate properly [1, 19, 20].

Because of the large inertia of the AC generator, the transfer from the AC line to the inverter takes place very smooth and without transfer time due to the fact that the inverter is on all the time. Furthermore, the hybrid UPS systems gathers main features of the static and rotary UPS configurations. They have low output impedance, high reliability, excellent frequency stability, and low maintenance cost [19, 20]. Like rotary UPS systems, this type of UPS is also designed for high power applications.

1.3 Novel UPS Configuration

All the UPS configurations systems, including static, rotary and hybrid UPS systems, are AC based UPS systems as the most UPS systems currently are available in the industry. In these systems, the AC main source directly or through several power conversions are connected to the load and the power exchanged between different parts of the system has an AC format, except for the battery. Working with the AC system means that the UPS system should be able to provide a low THD, a good filter for EMI immunity and close to unity power factor for the input current. Several power conversions also lead to a lower

efficiency as the on-line UPS opposes the lower efficiency among other static UPS due to the dual power conversion.

The novel UPS configuration system is proposed a cost effective and compact DC line-interactive UPS system. The novel UPS configuration is proposed to replace with a three-phase on-line UPS system which is utilized for medical imaging machines. The proposed system is a DC based system where the power exchange between different parts have DC format. The new designed system, shared a DC link bus and all other components in the system connect to this bus. The DC link is also integrated with a battery pack through a DC/DC bidirectional power converter.

Figure 1.7 illustrates the concept of the new UPS system. The figure shows block diagram of the DC UPS system. The DC UPS consists of an AC/DC rectifier, a DC/DC bidirectional converter and the battery pack. The DC/Dc converter regulates the DC link voltage and control the charging and discharging of the battery. The AC/DC rectifier operates in such a way to provide unity power factor. The rectifier is designed to provide 20 % of the total rated power and provides required power to charge the battery pack. The DC/DC converter is designed for full power. The proposed system has a higher efficiency compared with the on-line UPS configuration in which a dual conversion reduces the efficiency. Furthermore, the new designed system compared to the old three-phase on-line UPS system has several advantages including lower cost, size and weight since the three-phase back to back conversion replaced with a single stage single phase power converter, and consequently the efficiency is also higher.

The proposed system will also provide load leveling feature for the main AC/DC rectifier which has not been offered by conventional AC UPS systems. It applies load power smoothing to reduce the rating of the incoming AC line and consequently reduce the installation cost and time. Moreover, the new UPS technology improves the medical imaging system up-time, reliability, efficiency, and cost, and is applicable to several imaging modalities such as CT, MR and X-ray as well.

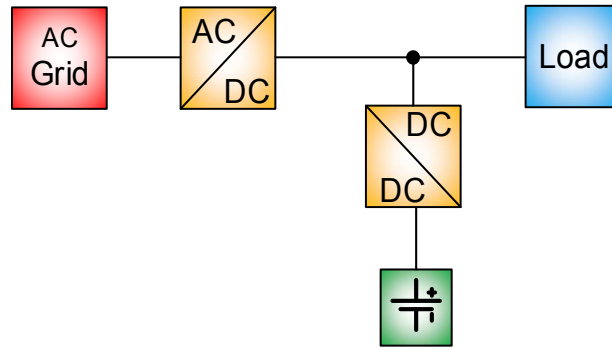


Figure 1.7: Block diagram of the proposed DC line-interactive UPS system.

The proposed DC UPS, as shown in figure 1.7, is integrated with safe and high power density battery, which links to the DC link through a bidirectional DC/DC converter. In case of utility power disruptions, the proposed system provides power from the battery to directly energize the DC section and ensure continue and reliable operation.

The proposed system operates in four different modes which are defined based on the load profile, battery pack status and connection of the main AC source. These modes include high rate discharging mode, so called load leveling mode, the standby mode, online mode and UPS or islanded mode. The fist mode is the high rate discharging mode in which the load requires a pulsed peak power provided by the battery though DC/DC converter, following by a rest time in which battery is charged from the grid power. The third mode begins when the battery is fully charged during second mode. Finally, the fourth mode is

when the AC main source is not available and the entire power provided by the battery pack.

1.4 Thesis Objectives

The main goal for this thesis is to present the novel UPS configuration, the DC UPS, and supports the concept of the novel design with theoretical, simulation and practical analysis. To that regard, the proposed system performances during all four modes has been analyzed and simulation model of the system has been developed to investigate different aspects of the system. Furthermore, since the new system needs to change the modes of operation while operating, high voltage/current transients are expected to happen if the transitions between the modes do not control and manage properly and smoothly. Thus, developing an appropriate control scheme which can ensure a reliable, continuous and constant output in the face of disturbances is a vital requirement and objective for the new system.

1.5 Thesis Organization

This thesis is arranged in the following chapters. Description of the proposed system architecture is explained in the next chapter. The energy storage systems and battery chemistry selection are discussed in chapter three. Chapter four explains the DC UPS system modeling and chapter five investigates the stability analysis of the system and explains the proposed control schemes. Chapter six presents the setup prepared for verifying the new concept and discusses the experimental results of the DC UPS testbed. Finally, chapter six provides the conclusion of the thesis.

CHAPTER II: Description of the System Architecture

2.1 DC Line-Interactive UPS with Load Leveling

Conventional medical imaging systems typically use a full-scale UPS for the machine to continue operation in case of electric power disturbances or outage. This UPS is generally large and expensive since it is designed for the peak power rating of the machine. In addition, this UPS is typically online type with double power conversion from AC to DC and back to line to the machine and UPS is rated at the peak power rating of the machine, which is much larger than the average power rating. For instance, the peak power of the CT system is nearly 150 kW while the average power is less than 10 kW. Design at peak rating means higher total cost and required space for the bulky power supply section of the machine.

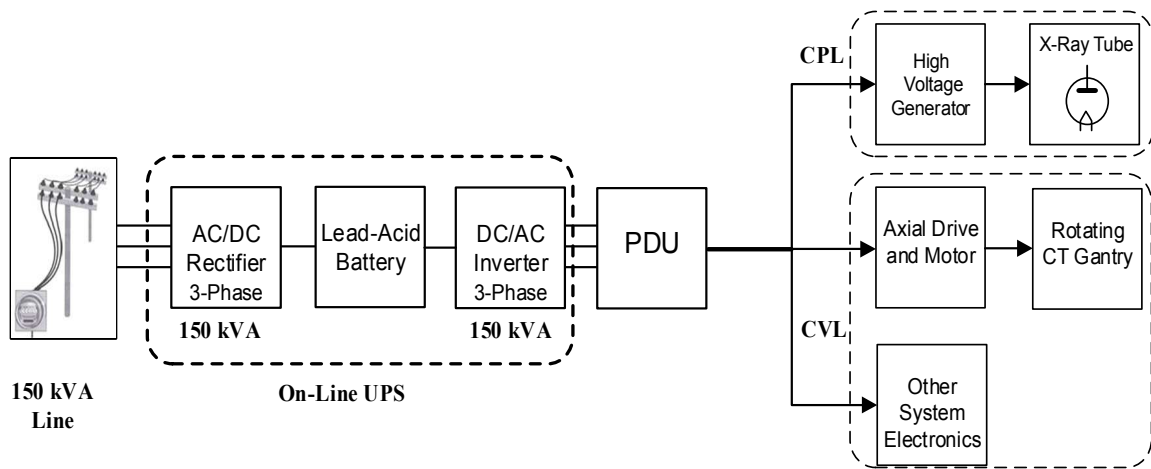


Figure 2.1: Schematic of the conventional CT scan system with on-line UPS. The load represents the CT machine.

Figure 2.1 shows configuration of a conventional CT scan machine in which an on-line UPS configuration is utilized and figure 2.2 illustrates configuration of the proposed system with the DC UPS topology. The conventional CT scan system includes a 150kVA input

line, three-phase online UPS rated at 150 kW, 60 Hz Power Distribution Unit (PDU), and load. The on-line UPS is typically large and expensive for 150 kW power rating. It mainly uses lead acid battery as energy storage. A 60 Hz transformer creates electrical isolation required for the medical device and powers the PDU and auxiliary loads. The PDU is an AC/DC PWM rectifier that creates 700 VDC for the high voltage generator.

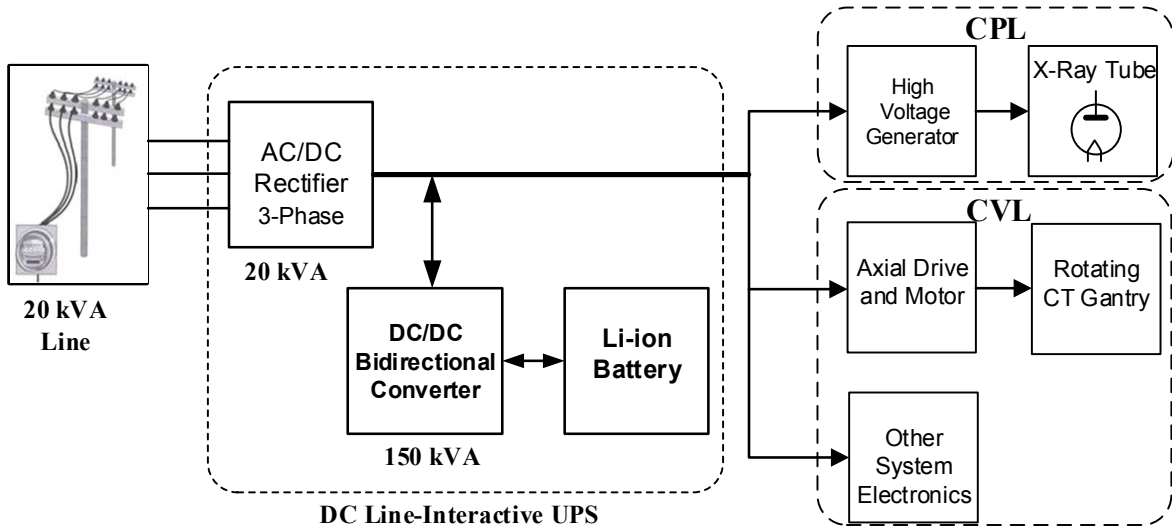


Figure 2.2: Configuration of the DC UPS system proposed for the CT machine.

The load consists of a high voltage generator, which is a constant power load (CPL), and auxiliary loads, which are considered as a constant voltage load (CVL). The high voltage generator has pulsed load profile as shown in figure 2.3. The load, CPL, is nearly 140 kW for two seconds and it is zero for another 200 seconds. The average load of the machine considering the auxiliary loads, CVL, is under 10 kW. Overall, the load comprises of a high peak power of 150 kW for a period of two seconds, when both CPL and CVL are on, and a 10 kW for 200 seconds, when only CVL is on.

Figure 2.2 illustrates the block diagram of the proposed system. The 60Hz PDU is replaced with a high frequency resonant PDU (HFPDU) which offers much smaller size and higher efficiency. The UPS configuration is changed from an on-line UPS to a line interactive DC UPS. A bi-directional DC/DC converter is utilized to charge and discharge the battery. Double conversion of electric power is removed, which increases the overall efficiency. However, improving efficiency is the least improvement made here. The system size is drastically reduced due to reduction from a three-phase double conversion to single-phase single stage DC/DC conversion. The lead-acid batteries are also replaced by safe, reliable, and more compact Li-ion batteries. In case of any input power disruption, the converter provides the required power from batteries to the 700VDC bus. Since the input and output voltages are DC, the transients are minimized. The stability concerns are largely mitigated and there is no synchronization delay or transients.

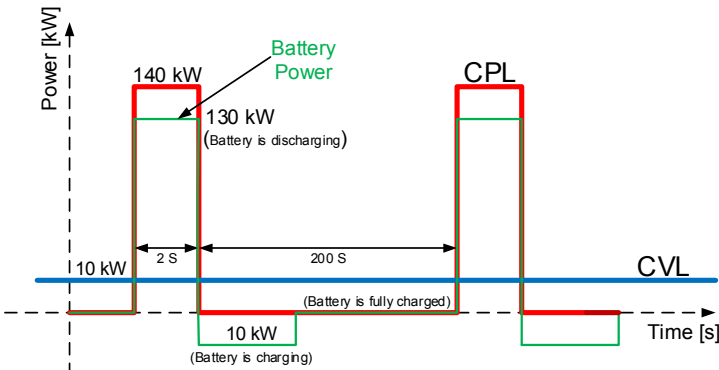


Figure 2.3: The Load Profile consists of a CPL (140 kW for 2 s and 0 kW for 200 s) and a CVL (10 kW). The BESS provides peak pulsed power for 2 s and then charges with 10 kW from grid.

Another significant improvement comes from load power smoothing (known as load leveling). As described by figure 2.3, the peak load of the machine is very high and is near 150kW (140kW for the high voltage generator, the CPL, and 10kW for the auxiliary loads,

the CVL). The proposed DC UPS will support the main line by providing the pulsed demand of the load. Roughly, when the high voltage generator needs 140kW of power for two seconds, 130kW will be provided by the DC UPS and 20kW will be provided by the main line. When the pulsed load, the CPL, is reduced to zero, the converter uses 10 kW out of 20 kW power from the main line to charge the battery back to initial state in the rest time.

The main blocks of the proposed DC UPS are, as illustrated in figure 2.4, including AC/DC rectifier, DC/DC bidirectional converter, battery energy storage system (BESS). The description of each block is provided as follow.

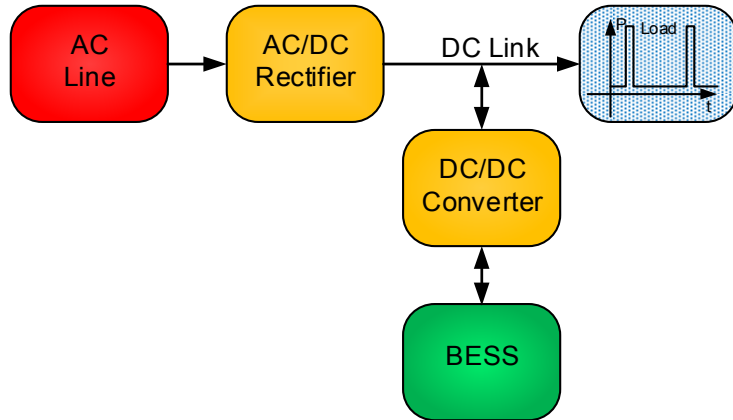


Figure 2.4: Block diagrams of the proposed DC UPS system.

2.2 AC/DC Rectifier

The main line is connected to the DC link through an AC/DC rectifier to provide a portion of the load power that is less than 20 %, from the grid. Based on the proposed DC UPS, the rectifier delivers 20 kW constant power to the DC link at unity power factor. This rectifier is almost eight time smaller than the AC/DC rectifier used in the conventional CT machine with on-line UPS configuration system which is rated for full rated power at 150 kVA.

The 20 kW power provided by this converter is used as a small portion of the 2 s peak pulsed power demand of the load and also a charging source for the battery modules during the rest periods.

2.3 DC/DC Bidirectional Converter

In the proposed system, the battery energy storage system (BESS) is connected to the DC link via a DC/DC converter. The high power DC/DC converter has a critical role in the proposed topology since the BESS is providing most the load power and this converter regulates the DC link voltage while BESS is not fully charged and is in the circuit.

The converter should have bidirectional capability to manage power flow in both directions as BESS is charged and discharged. Moreover, in the proposed topology, the DC/DC converter is a high power converter, therefore an efficient topology which is capable of handling high current with low current ripple should be considered. High current ripple affects the life span of the energy storage devices and decreases the capacity and life time of the BESS [21-24]. Several topologies for such DC/DC converters used to interface energy storage systems with their advantages and disadvantages, are discussed and reviewed in the literature [25-29]. The multi-phase interleaved technique is widely used to reduce the current/voltage ripple and increase the power capacity of the DC/DC converters. Using this technique not only reduce the current ripple, but also minimize the size and weight of the key elements in the power converters. The number of phases is designed based on the system requirements and can be defined per the minimum current ripple for a specific duty ration of the converter.

A bidirectional 2-phase interleaved DC/DC converter is proposed to connect the BESS to the DC link. The merit of interleaving technique depresses the ripple of the battery current which is induced by switching and this could minimize deterioration of the BESS.

2.4 Modes of Operation

Four operational modes have been defined for the proposed DC UPS system in order to study the dynamics of the system during different conditions of the system. These modes are defined based on the load profile, BESS status, connection and disconnection of the system from the main AC grid. These modes are ***load leveling*** mode, when the system is supplying the 2 second pulsed peak power for the load including CPL and CVL, ***standby mode***, during 200 s rest period when the system is powering CVL and charging the BESS, ***online or grid-connected*** mode, when the BESS is fully charged during 200second rest period and ***UPS or islanded*** mode is when the grid is out and BESS is providing power for the system. At each mode, the goal is to provide required power for the load and maintains the DC link voltage constant according to the different situations associated with the defined modes. Description of each mode is provided in the next sections.

2.4.1 Mode I: Load Leveling Mode

First mode, the load leveling mode or high rate discharging mode is when the load requires a 2 second peak pulsed power of 150 kW including 140 kW from high voltage generator pulsed load profile, the CPL, and 10 kW for auxiliary loads, the CVL.

The main line in this mode provides 20 kW power and the BESS supports the main line by delivering the rest of the required power, which is 130 kW to the DC link. This is the load leveling feature of the proposed DC UPS. Since the BESS is providing majority of the

power, the DC/DC power converter regulates the DC link. Therefore, the DC/DC converter operates in voltage mode, to keep the DC bus voltage constant at the rated value. The BESS provides the requested pulsed power by high rate discharging (up to 15 C). The released BESS energy in this 2 second is less than 1 % state of charge (SOC) of the BESS and the associated energy management system ensures that the BESS has at least 50 % SOC when providing this amount of power. The rectifier supplies 20 kW power by performing in current mode. Figure 2.5 illustrates power flow during the load leveling mode.

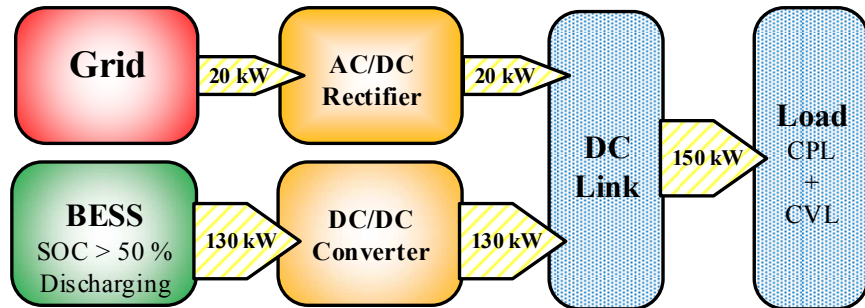


Figure 2.5: The power flow of the proposed DC UPS during load leveling mode.

The amount of energy released by discharging the BESS during this mode, E_I , earned as:

$$E_I = 130 \text{ kW} \times 2 \text{ s} / 3600 = 72.2 \text{ Wh} \quad [2.1]$$

and if the BESS consists of 108 Li-ion cells connected in series with each cell terminal voltage of 3.2V-3.3V, then the BESS terminal voltage, V_b , can be around 350 V, then the amount of capacity, C_I in Ah, released during this mode and also change of the state of charge, ΔSOC_I , obtained as:

$$C_I = E_I / V_b = 0.206 \text{ Ah} \quad [2.2]$$

$$\Delta SOC_I = C_I / C_n = 0.69 \% \quad [2.3]$$

Where C_n is the nominal capacity of the BESS, which is 30 Ah. This means that during mode I, the load leveling mode, almost 0.7 % of the nominal capacity of the BESS is consumed to support the 2-second peak pulsed power demand for the CPL. Technically speaking, the depth of discharge (DOD) to support the 2-second pulsed CPL demand during this mode for the BESS is 0.69 %.

2.4.2 Mode II: Standby Mode

The standby mode begins after 2 second pulsed power of the load leveling mode. During this mode, the CPL is off and CVL is still on. The main line provides 20 kW power at unity power factor. The CVL is fed by half of the power provided from the grid and the other half of grid power charges the BESS to recover the energy which was released during load leveling mode. The 130 kW power discharged for 2 s can be recharged by 26 s charging at 10 kW.

The AC/DC rectifier is still working on current mode to ensures 20 kW power delivered to the DC link. The DC/DC power converter maintain the DC bus voltage by operating on voltage mode. It is assumed that in this mode the BESS is not fully charged ($SOC < 99\%$) which means that it can absorb/charge extra power. Once the battery is fully charged, next mode begins. The schematic of the system working in this mode is illustrated in figure2.6.

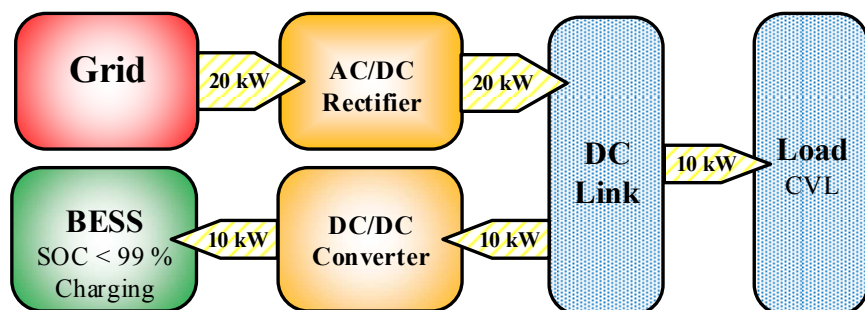


Figure 2.6: The power flow of the proposed DC UPS during standby mode.

During this mode, the energy received by the BESS during 200 s, E_{II} , with the same assumptions as mode I, is achieved like this:

$$E_{II} = 10 \text{ kW} \times 200 \text{ s} / 3600 = 555.6 \text{ Wh} \quad [2.4]$$

$$C_{II} = E_{II}/V_b = 1.59 \text{ Ah} \quad [2.5]$$

$$\Delta SOC_{II} = C_{II}/C_n = 5.29 \% \quad [2.6]$$

Which means that during this mode, the BESS can receive 1.59 Ah which is considered as 5.29 % of its nominal capacity leads to the SOC of the BESS raises up by 5.29%. It is possible that the BESS becomes fully charged by all or portion of this energy during this mode and avoids any further charge, then the next mode which deals with the fully charged BESS is started.

2.4.3 Mode III: Online Mode

During mode II, the BESS could become fully charged and avoids extra charge from the grid, then the third mode, the On-line mode starts to operate. The CVL is directly powered from the grid through the rectifier.

Consequently, the DC/DC converter is at rest mode and the AC/DC rectifier will oversee the DC link regulation. The rectifier performs in voltage mode during this mode to maintain the DC link voltage constant while providing 10 kW power for the CVL.

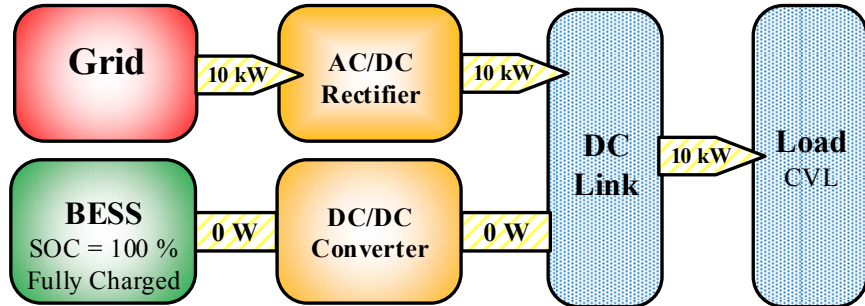


Figure 2.7: Block diagram of the DC UPS system during mode III, the BESS is fully charged and does not have any power exchange with the DC link.

The DC/DC converter will take over the control of the DC link voltage, once request for extra power is issued, in other words, once the CPL turns on or grid disconnects, the DC/DC converter manages the system to maintain the DC link voltage while providing peak pulsed power for the CPL. During online mode, the DC/DC converter does not have any power exchange with the DC link. Figure 2.7 illustrates the operation of the system during mode III.

2.4.4 Mode IV: Islanded Mode

Finally, the last mode, islanded mode, is when the system is disconnected from the main AC source due to power destructions, like power outage or any grid disturbances. Then the BESS provides entire load profile for a limited time according to its available capacity and system policy, till the main power returns. The DC/DC converter provides the required power from the BESS to the load and simultaneously regulates the DC link voltage. To avoid any damage to the BESS life time by deep discharging the BESS, it is required to consider a minimum SOC or a maximum DOD for the BESS to operate safely during this mode. Figure 2.8 shows the DC UPS system during the islanded mode.

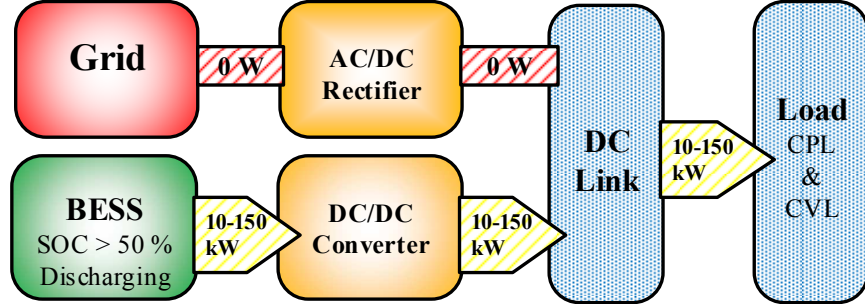


Figure 2.8: Block diagram of the DC UPS system during islanded mode; the DC/DC converter provides entire load power from the BESS.

The amount of energy that the BESS can potentially provide during the islanded mode, assuming the BESS is fully charged and will be completely discharged or 100 % DOD is allowed, can be achieved as E_{BESS} :

$$E_{BESS} = 30 \text{ Ah} \times 350 \text{ V} = 10.5 \text{ kWh} \quad [2.7]$$

Considering E_{cycle} is the energy required for a full load cycle by including 150 kW power for 2 s (CPL+ CVL) and 10 kW (CVL) power for 200 s, then E_{cycle} is obtained as:

$$E_{cycle} = (150 \text{ kW} \times 2 \text{ s} + 10 \text{ kW} \times 200 \text{ s})/3600 = 638.9 \text{ Wh} \quad [2.8]$$

$$\text{Number of load Cycles} = E_{BESS}/E_{cycle} = 16.4 \text{ cycles} \quad [2.9]$$

2.5 The Load Profile

The load consists of a high voltage generator, a 140 kW constant power load (CPL), and the auxiliary loads, 10 kW constant voltage load (CVL). The CPL only shows up in the mode I and IV while the CVL exists all the time. The CVL has a 10 kW constant power demand. The whole load profile is illustrated in figure 2.9 in which the solid black line represents the total load profile, CPL plus CVL, with a peak of 150 kW and a low power of 10 kW for the auxiliary loads when the high voltage generator is at rest period. The

green line also represents the power supplied by BESS and the negative part of the green line represents the charging period for the BESS during mode II, while in mode III there is not any energy exchange with the BESS since it's fully charged (SOC > 99%). The blue line, in the figure 2.9, represents the power from grid which is 20 kW and during mode III it is reduced to 10 kW and during mode IV, the islanded mode, it reduces to zero. This profile could frequently repeat during a normal operation day of the medical machine.

The high voltage generator pulsed load in mode I, has negative incremental impedance characteristic of the constant power loads (CPLs) in which although the instantaneous value of the impedance is positive but the incremental impedance is negative [30-32]. This characteristic mainly challenges the stability of the system when the DC/DC converter provides the most of the required power to the pulsed power demand.

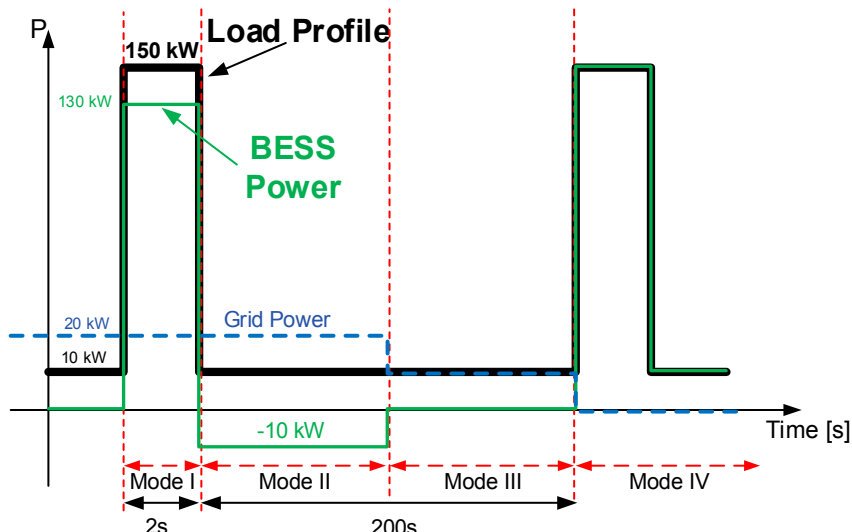


Figure 2.9: The load and the BESS power profiles during different modes of the DC UPS.

2.6 Battery Energy Storage System (BESS)

The BESS provides the load leveling feature, also known as peak shaving or power smoothing, for the grid input power by supplying the peak pulsed power demand. In

addition, the BESS can serve as an urgent power supply or UPS system in case of any AC power outage for a limited time. The BESS consists of the Li-ion battery modules and the battery management system.

A comprehensive study on different type of batteries were conducted to find the appropriate type which meets the DC UPS system requirements including high power and energy density, safe and reliable design. The Li-ion LFP and NCA cell types were down selected, due to their superiority in energy and power density, safety and their long life cycle. It should be mentioned that the new design Li-ion cells have the capability of high pulsed discharging up to 15C for less than 5 seconds. This capability well-matched with the requirements of the peak pulsed power demand for two seconds. Each LFP cell rated at 3.3 V nominal voltage and 30 Ah (at 0.2C) nominal capacity. The cell is capable of pulsed discharging with high rate current up to 450 A for less than 5 seconds.

Two Li-ion LFP based battery modules consist of 108 cells connected in series (each module contains 54 cells) were designed and built for the DC UPS system. The modules are connected in series and supply 350 V terminal voltage and 10.5 kWh energy. The modules can deliver a peak power of 150 kW for 2 second to the DC link. A battery management system (BMS) has designed and installed to monitor the cells/modules safety operation. Next chapter explains more in details about the BESS.

CHAPTER III: Energy Storage Systems and Battery Chemistry Selection

3.1 Introduction

There is a shift in the decades-old paradigm of energy generation, distribution, and consumption. Several technical and non-technical factors are driving this change including concerns on impacts of fossil-based fuels, advancement of alternative energy technologies, increasing penetrations of distributed generations, and demand for higher energy efficiency and reliability [33]. Energy Storage Systems (ESSs) are acting as enablers to support this paradigm shift. They have been employed in a wide range of electrical systems from consumer's electronics to automotive industry and to utility level transmissions and generations. The higher energy density and smaller size of newer ESS technologies have significantly improved the mobile and portable consumer electronic devices. In the automotive industry, advanced ESSs have enabled efficient Hybrid Electric Vehicles (HEV) and Electric Vehicles (EV). Advancements in energy storage and power electronics technologies have also transformed industrial energy conversion systems such as Uninterruptible Power Supplies (UPS) and systems with pulse loads or sources.

In the electrical power systems, the emerging paradigm includes new elements such as deregulations, Distributed Generations (DG), energy storage, DC systems, and power electronics-based systems at different power scales. With increasing concerns over energy reliability and security, energy cost, and environmental concerns over fossil-based sources, alternative energy systems have also experienced a large growth in the recent years. Majority of growth has been happening in renewable energy systems, especially in solar Photovoltaic (PV) and wind energy. When the penetration of these sources increases in the

grid, they are required to participate in the grid support functions. The intermittent nature of these sources needs support from energy storage systems to make them dispatchable and more predictable in the grid operation.

Support for renewable energy systems can be realized at several time lengths from short-term (less than 5 seconds) to long-term (several hours). Short-term support is needed during solar PV clouding, wind power gusting, and power ramp rate limitation. The appropriate energy storage for this application does not need to have high energy capability but must have a large power capability. Long-term support can include power shifting and spinning reserve function. The daytime solar PV power can be moved to early evening peak demand hours and energy storage can supplement when forecasted renewable energy does not occur. For these applications, the ESS must have appropriate energy and power capabilities.

Electrical utility systems can also take advantages of ESSs at distribution, transmission and generation levels. ESSs can help stabilize the electric power system by providing voltage and frequency support, load leveling and peak power shaving, spinning reserve, and other ancillary services. They also count as extra energy capacity for the generation and transmission systems to defer the upgrade cost. Time shifting of the energy delivery is another major benefit of integrating ESSs into grid.

For various applications, different types of ESSs with respective strengths and weaknesses have been developed. Electrical energy can be converted to several other types of energy and then can be stored. The energy can be released by converting back to the electrical form when needed. There are several types of energy storage technologies, including

electrochemical, mechanical and electrical/magnetic fields. Figure 3.1 shows the classification of electrical energy storage systems and examples for each category. Electrochemical energy storages are batteries in which electrical energy is stored as electrochemical reactions and then released by changing back to electrical energy.

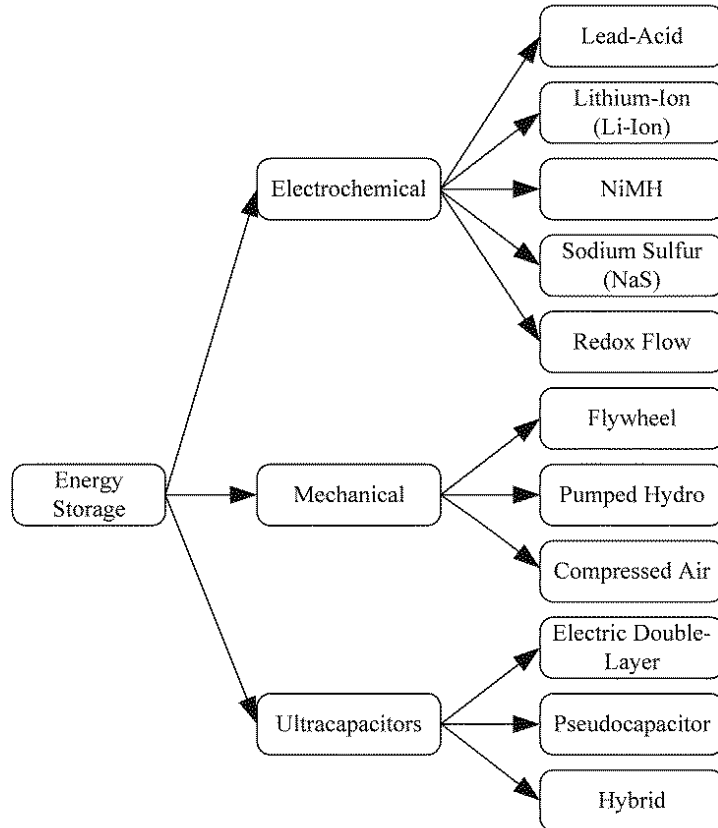


Figure 3.1: Different types of energy storage systems.

Lead-acid (LAB), Lithium-ion (Li-ion), Nickel-Metal Hydride (NiMH), Sodium Sulfur (NaS) and redox flow batteries are the most common electrochemical energy storage systems. Electrical energy is also changed to kinetic energy and saved in mechanical energy storage systems such as flywheel, compressed air and pumped hydro. In capacitors, electrical energy is saved in the electrical field established between the capacitor plates.

Mechanical energy storage technologies have primarily been adapted for large-sized storage systems while batteries and capacitors cover a wide range of applications from consumer electronics to industrial and utility level applications. Table 3.1 reports an estimation of total electrical energy storage capacity which is currently installed worldwide, according to the Electric Power Research Institute (EPRI) [33].

Table 3.1: Worldwide installed electrical energy storage capacity [33]

Energy Storage Technology	Installed Capacity [MW]
Pumped Hydro	127000
Compressed Air Energy Storage (CAES)	440
Sodium-Sulfur Battery (NaS)	316
Lead-Acid Battery	35
Nickel-Cadmium Battery	27
Flywheels	25
Lithium-Ion Battery	20
Redox-Flow Battery	3

Currently, the majority of bulk storage capacity worldwide is in the forms of pumped hydro and compressed air while the rest of storage technologies account for less than one percent of the total capacity. However, due to the geographical limitations, distance from the demand and initial capital cost, other storage technologies, which are accessible everywhere, are gaining market share.

Table 3.2: Characteristics of common energy storage systems.

Characteristic/ Energy Storage Type	Specific Power [W/kg]	Specific Energy [Wh/kg]	Cycle Life [cycles]	Self- Discharge at 25°C [%] per month	Efficiency [%]
Ultracapacitor	2000-14000	1.5-15	10^5 - 10^6	Very low	> 90
Lead-acid Battery	100-200	20-40	200-2500	Medium	70-80
Li-ion Battery	300-1500	100-300	2000-5000	Low	80-90
NiMH Battery	220-1000	60-120	500-2000	High	50-80
NaS Battery	150-230	150-240	2000-4500	Very low	75-90
ZnBr Flow Battery	300-600	30-60	2000-3000	Very low	70-80
Flywheel	1000-5000	10-50	10^5 - 10^7	Very high	80-90
Pumped hydro	N/A	0.3-30	> 20 years	Very low	65-80
CAES	N/A	10-50	> 20 years	High	50-70

Batteries are receiving significant attention for industrial and grid applications, due to their portable characteristics, and are the most promising energy storage type of future. Various characteristics of the energy storage technologies, which have been extracted from [33-36] are summarized in figure 3.2 and Table 3.2

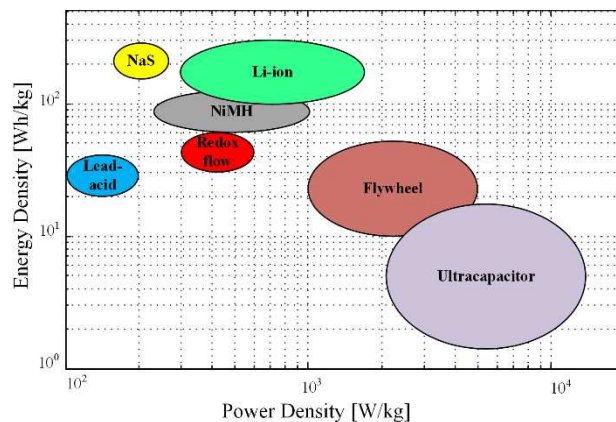


Figure 3.2: Ragone plot for energy and power density for ultracapacitors (UCap), flywheel energy storage (FES), and batteries of the: nickel-metal hydride (NiMH), zinc-bromine (Zn-Br); lead-acid (LAB), lithium-ion (Li-ion); sodium sulfur (NaS) types.

This chapter briefly covers energy storage topic and explains the Li-ion batteries and several commercially existing chemistries. The goal is to determine a battery chemistry and type, which ensures safe and reliable operation. In addition, battery must provide high power density. The initial rating for the battery pack (108 series connected cells) is 12.5 kWh and 125 kW. The battery should be able to deliver the specific power profile and provides long life and proper performance.

Based on the literature review, two Li-ion battery chemistries, Lithium Nickel Cobalt Aluminum oxide (also known as NCA) and Lithium Iron Phosphate (referred as LFP), have been met the requirement criteria and selected down to conduct the performance tests.

3.2 Battery Energy Storage System (BESS): Types, Characteristics and Modeling

3.2.1 Lead Acid

The oldest rechargeable battery technology, which was invented some 150 years ago, is based on the use of lead-acid. The modern version of the technology is able to deliver relatively large power for relatively low cost, making such batteries strong candidates for applications in which a surge power support with low depth of discharge is required, including backup power supply like UPS, emergency power and power quality management.

The short life cycle and very low energy density are two main disadvantages [37]. Deep cycling and high discharging rate have a serious impact on the life span of the battery. The latest developments, including advanced materials, resulted in lead-acid batteries in better performance and longer life cycle, and include low-maintenance versions, such as, GEL-

cells and Absorbed Glass-Mat (AGM) collectively known as Valve-Regulated Lead-Acid (VRLA) batteries [38].

3.2.2 Lithium-Ion

One of the most popular types of batteries commercially available is based on Li-ion and provides comparatively very good performance, with high power density and satisfactory energy density. A long life cycle without memory effect, together with high columbic efficiency and low self-discharge characteristics, makes this type of battery the preferred energy storage choice for a wide variety of applications, spanning from costumer electronic devices and mobile products, all the way to the latest generation of plug in hybrid EV, and systems for frequency regulation at the utility level [39].

The electrode material greatly influences the battery specifications in terms of power and energy density, voltage characteristics, life time, and safety. A typical cathode, i.e. the positive active electrode, is made of a lithium metal oxide, and common materials such as cobalt (LiCoO_2 or LCO) and manganese (LiMn_2O_4 or LMO). Combined chemistries including nickel cobalt aluminum (NCA), nickel manganese cobalt (NMC), and iron phosphate (LFP) are also employed for the cathode. Graphite and lithium titanate ($\text{Li}_4\text{Ti}_5\text{O}_{12}$ or LTO) are the typical choices for the anode, i.e. the negative active electrode.

A comparison of the battery chemistries, clearly illustrating the advantage of different battery types, is presented in Table 3.3.

Table 3.3: Characteristic comparison between batteries of Li-ion family chemistry, lead-acid and ultracapacitor. The highest figure of merit, which is associated with best performance, is equal to 6.

Energy Storage Type	Power Density	Energy Density	Safety	Cycle Life	Cost
LFP	4	4	4	4	4
LTO	4	4	4	4	2
NCA	5	6	2	4	3
NMC	4	6	3	3	4
LCO	3	3	2	2	4
LMO	4	5	3	2	4
Lead-acid	3	2	3	2	6
Ultracapacitor	6	1	3	6	2

3.2.3 Sodium Sulfur (NaS)

Sodium sulfur (NaS) rechargeable batteries are mostly developed for large scale applications, as they operate at a high operating temperature of 300 °C - 350 °C. Such batteries are made with inexpensive materials and they are known as high power and energy storage devices with high columbic efficiency up to 90%, good thermal behavior, and they are long life cycle made. The primary applications are large scale power and energy support, such as load leveling, renewable energy integration, and UPS systems. The battery contains hazardous materials like sodium, which can burn spontaneously in contact with air and moisture, or sodium polysulfide that is highly corrosive [40].

3.2.4 Other Types of Batteries and Energy Storage Systems

Some of the other common energy storage technologies include Nickel–Metal Hydride (NiMH) batteries, which can be recharged, have higher energy density and shorter cycle life compared to Nickel Cadmium (NiCd) chemistries, but still suffers from strict

maintenance requirements due to the memory effect. The high rate of self-discharging is the main disadvantage of NiMH batteries [41].

Flow batteries, also known under the Redox (reduction-oxidation) name, employ for storage chemical compounds, dissolved in the liquid electrolyte and separated by a membrane. Such batteries have been developed using zinc bromine (ZnBr), sodium bromine (NaBr), vanadium bromine (VBr), or polysulfide bromine (PSB). A unique advantage of flow batteries is that their energy capacity is completely separated from their power, and therefore the design can be scaled with more flexibility [42]. Redox batteries can be matched very well for the integration of renewable energy to the grid and for frequency regulation [43-44].

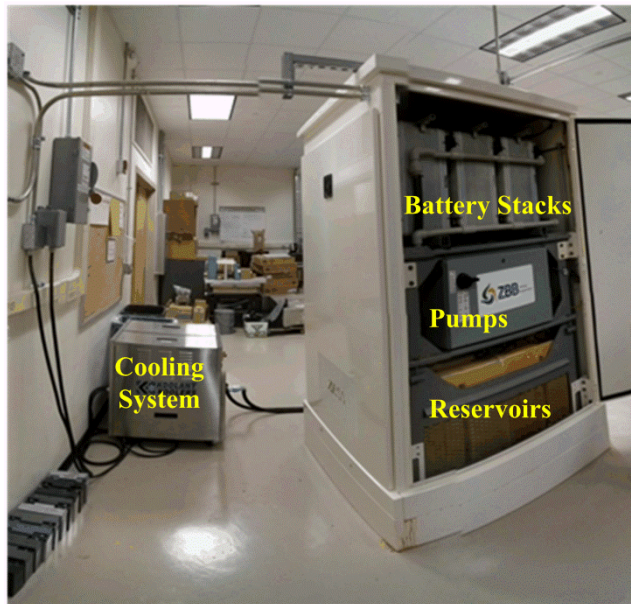


Figure 3.3: Zinc-Bromide (ZnBr) flow battery used in the University of Wisconsin-Milwaukee (UWM) Lab for experimentally demonstrating the mitigation of power variability from renewable energy sources. The battery is rated at 50 kW, 675 Ah and when fully charged.

A Zinc-Bromine (ZnBr) flow battery system, shown in figure 3.3, is used in the Power Electronics Laboratory at University of Wisconsin – Milwaukee (UWM) for demonstrating techniques of mitigating wind power fluctuations [44].

Energy can also be stored using electromechanical systems employing high-speed high-inertia flywheels. The absorption and the release of electrical energy will result in an increase or decrease of the flywheel speed, respectively. A main advantage is represented by the rapid response time, recommending the technology especially for applications such as transportation, backup power, UPS, and power quality improvement [45].

Other forms of energy storage suitable for large-scale grid applications employ pumped hydro and compressed air. In the first case, water is pumped uphill in a natural or man-made reservoir, for example during off-peak hours, and released downhill to turn a turbine and produce electricity when needed, for example during peak hours. In the second case, the air is typically stored underground and then used as needed to generate electricity from a generator coupled to a turbine. High capital investment and installation costs, coupled with geological availability, environmental concerns and restrictions, represent challenges for these types of storage, and may generate opportunities for developments for electrical batteries.

3.2.5 Battery Energy Storage Modeling and Test Setups

In order to design, analyze, and optimize the energy storage systems, suitable battery models, which can address the main characteristics and the behavior for the application

specifics, are a vital requirement. The battery model should be able to satisfactorily predict the dynamics of the system with a reasonable low computational complexity. Reduced order models that neglect phenomena of less significance may provide a suitable tradeoff between accuracy and simplicity.

Battery models may be classified in three major groups: physical or electrochemical, mathematical, and electrical, respectively. A physical model is based on the electrochemical reactions and thermodynamic phenomena that take place inside the battery cell. Such models involve high order differential equations, they are complex and time consuming, but provide, in principle, the basis for the most accurate results [46-47]. To reduce complexity, reduced-order simplified electrochemical models have been proposed [48-50].

Mathematical battery models, without any electrical properties, are limited to the prediction of system level performance indices, such as energy efficiency, run-time, and capacity. In this type of models, the result accuracy is highly dependent on the experimental data employed for model identification, the models are typically applicable only to a reduced range of devices and ratings, and they do not include terminal voltage and current characteristic, which are essential for circuit analysis and system simulation [51-52].

The electrical models for batteries employ lumped equivalent circuit parameters with sources and passive elements, i.e. resistances and capacitance. Such models are the most familiar to electrical engineers and can be successfully employed for system simulation.

A comprehensive model that combines the transient capability of a Thevenin-based model, the AC features of an impedance-based model, and the information specific to a runtime-based model, has been proposed and validated for lead-acid, NiMH and Li-ion batteries [53-56]. The model, which is schematically represented in figure 3.4, includes two equivalent circuits: figure 3.4(a) for battery lifetime, capacity, state of charge and runtime of the battery, and figure 3.4(b) for the voltage-current characteristics of the battery.

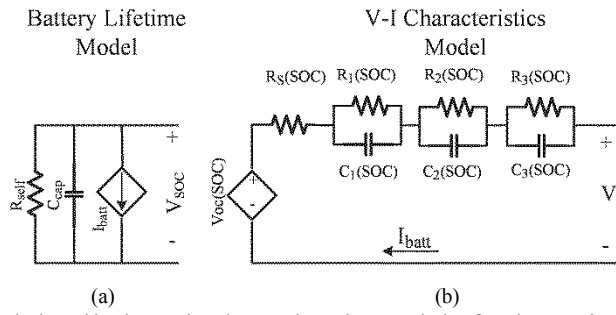


Figure 3.4: Combined detailed equivalent circuit models for batteries,
 (a) battery lifetime model and (b) V-I characteristics model [53].

Battery lifetime, has been modeled through three elements, a resistance, R_{self} , quantifying the self-discharge energy loss during storage operation, a current-dependent source for charging and discharging, I_{bat} , and a capacitance, C_{cap} , which provides the state of charge for the battery as a scaled voltage drop, V_{soc} , with a per unit value between 0 to 1. The capacitance, C_{cap} , accounts for the entire charge stored in the battery and can be calculated as:

$$C_{cap} = 3600 \cdot C_n \cdot f_1(T) \cdot f_2(n) \cdot f_3(i) \quad [3.1]$$

where C_n is the nominal battery capacity in Ah and $f_1(T)$, $f_2(n)$ and $f_3(i)$ are correction factors dependent of temperature, number of cycles and current, respectively.

The battery voltage-current characteristics are modeled through the equivalent circuit depicted in figure 3.4(b). In this case, all equivalent circuit elements are dependent of the State of Charge (SOC). Voltage-current non-linearity is incorporated through a dependent voltage source, V_{oc} , and a resistor, R_s , is responsible for immediate voltage change in step response. Several RC parallel networks, i.e. R_i and C_i , are connected in series to provide multiple time-transient constants. Typically, three such time-constant RC network are considered satisfactory for most practical purposes. The parameters identified in figure 3.4(b) are a function of SOC, as shown in the following equations, and they are also affected by other operational characteristics, such as temperature.

The state of charge, SOC, and the terminal voltage, V_t , are calculated as:

$$SOC(t) = SOC_0 - \frac{1}{C_{cap}} \int_0^t i(t) \cdot d(t) \quad [3.2]$$

$$V_t = V_{oc}(SOC) - (V_{Rs} + V_{C1} + V_{C2} + V_{C3}) \quad [3.3]$$

where V_{C1} , V_{C2} and V_{C3} are the voltages across capacitors and V_{Rs} is the voltage drop across the internal resistor (R_s). An open-circuit voltage, V_{oc} , versus SOC characteristic is exemplified in figure 3.5.

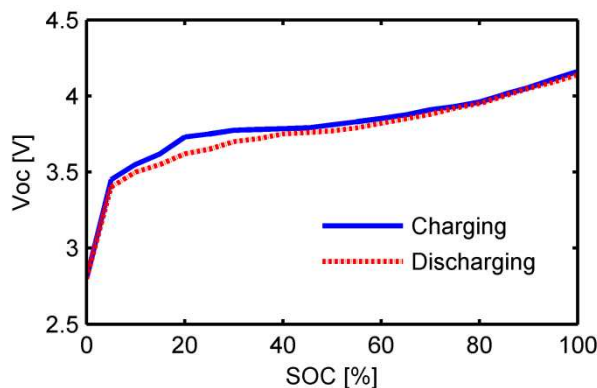


Figure 3.5: Open-circuit voltage (V_{oc}) versus state of charge (SOC) for

an example Lithium-ion battery of 2.6 Ah.

3.2.5.1 Test Procedure and Model Extraction

To extract all the parameters introduced by proposed model a test bed system and procedure were conducted. The system includes a DC digitally programmable load, a DC source, current sensor, NI CompactRIO and LabVIEW software, figure 3.6 (left). The DC load and source were hooked up to the CompactRIO serial port to communicate with LabVIEW interface. A breaker contactor is used to disconnect the DC source in discharging periods. Two channels of a CompactRIO analogue IO (input/output) differential module digitize and carry the measured current and voltage signal at each sampling instance to the LabVIEW interface, figure 3.6 (right). A model was developed in LabVIEW environment for collecting data and performing charge and discharge cycles and commanding appropriately to the load and source.

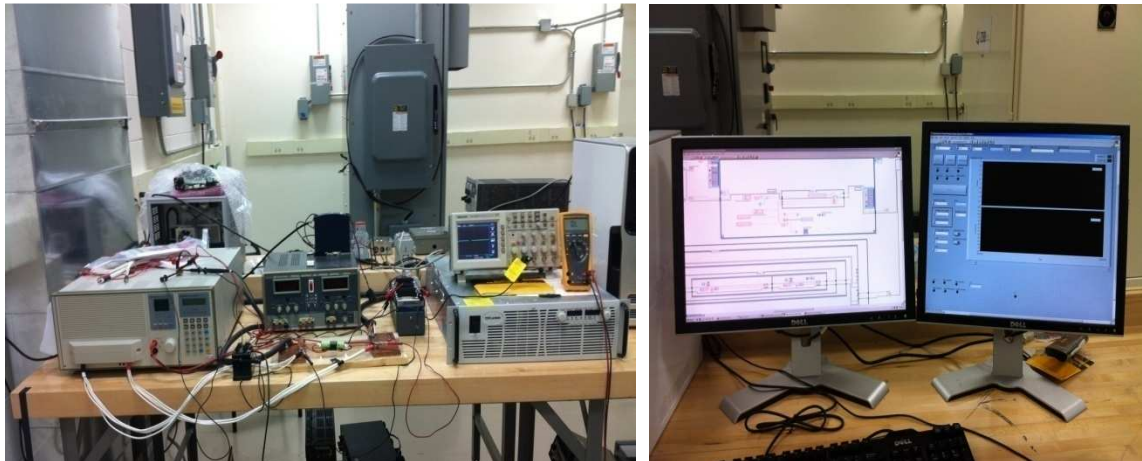


Figure 3.6: Test bed system of the battery (left) and LabVIEW interface model (right)

A new 2.6 Ah cylindrical lithium-ion battery cell grabbed from laptop battery pack, was used for this experiment. Several pulse current discharging cycles with different current rates from were performed to earn enough data for identifying model parameters. During

the test, cell temperature was recorded as well. However, according to the low current rate tests, the cell temperature was almost constant as ambient standard temperature at 25 C. Details on model extraction methods and procedures could be found in [53-57]. Figure 3.7 depicts a typical pulse discharging voltage and current curves saved by LabVIEW model.

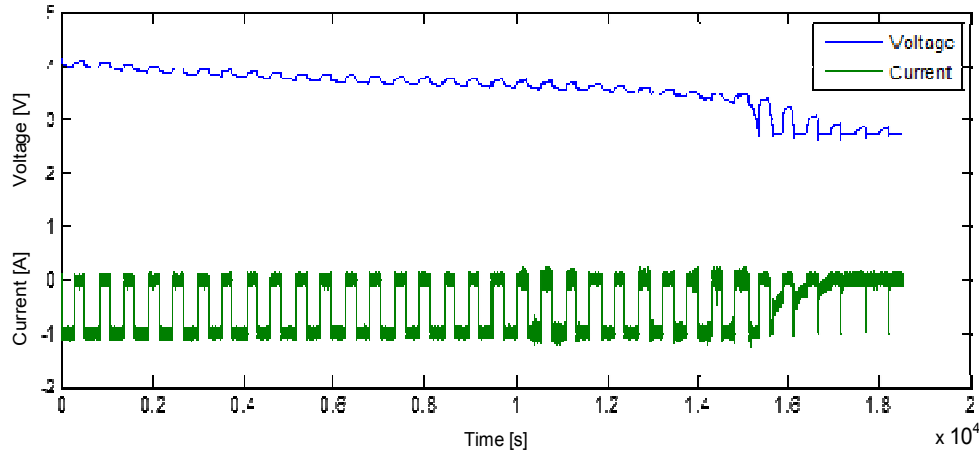


Figure 3.7: Pulse discharging voltage and current with 1 A (sampling frequency is 100 Hz)

Parameters shown in the combined battery model are analyzed and found via designed algorithms implemented in MATLAB. The voltage and current data are used to find the open-circuit voltage, series resistance and three RC transient circuit elements, which are non-linear functions of state of charge (SOC). For each model element, several curve fitting algorithms were used to find the best curve fitted on the data extracted from the V-I curves. Figures 3.8 through 3.11 show the results of the model extraction.

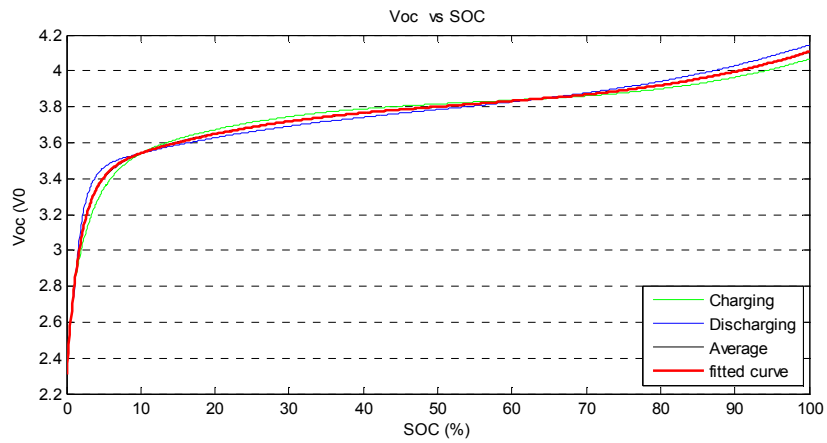


Figure 3.8: Open-circuit voltage (Voc) as a function of state of charge (SOC)

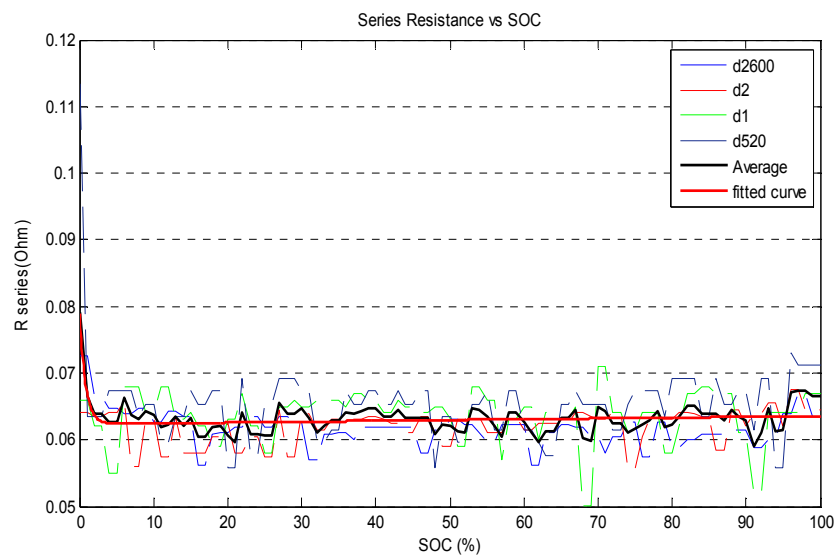


Figure 3.9: Series resistance as a function of soc for various discharging rate (for 0.52, 1, 2, 2.6 A discharging current).

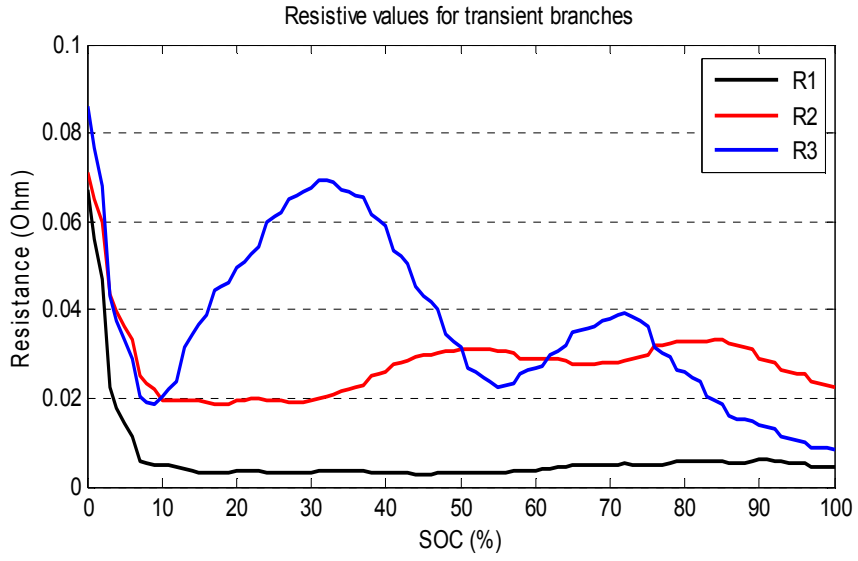


Figure 3.10: Transient resistances as functions of SOC

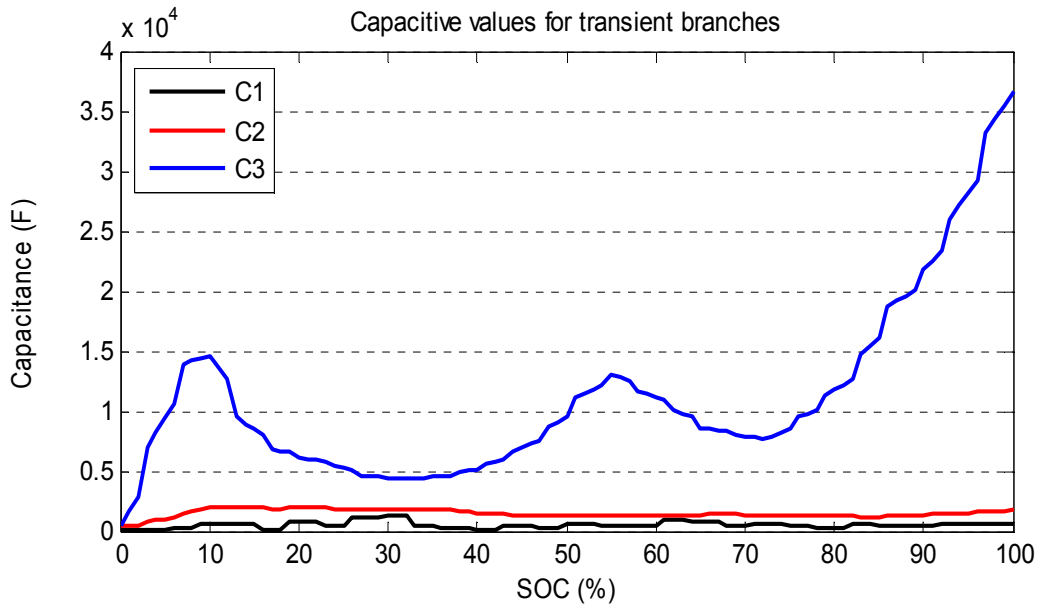


Figure 3.11: Transient capacitances as functions of SOC

Rate factor and temperature factor were determined based on the method offered in [57].

Tables 3.4 through 3.6 include the measured correction values for various temperatures, charging and discharging currents. Since all the battery tests were conducted under the

standard lab temperature, for the temperature correction factor, the data grabbed from the battery datasheet.

Table 3.4: Correction rate factors for various temperatures

Current [A]	-10	0	25	40
f_2	0.5	0.8	1	0.8

Table 3.5: Correction rate factors for various discharging currents

Current [A]	0.52	1	2	2.6
f_3	1	0.9826	0.9585	0.9234

Table 3.6: Correction rate factors for various charging currents

Current [A]	0.52	1	2	2.6
f_3	1	0.95	0.8252	0.7546

Figure 3.12 shows the battery model implemented in the MATLAB-Simulink environment.

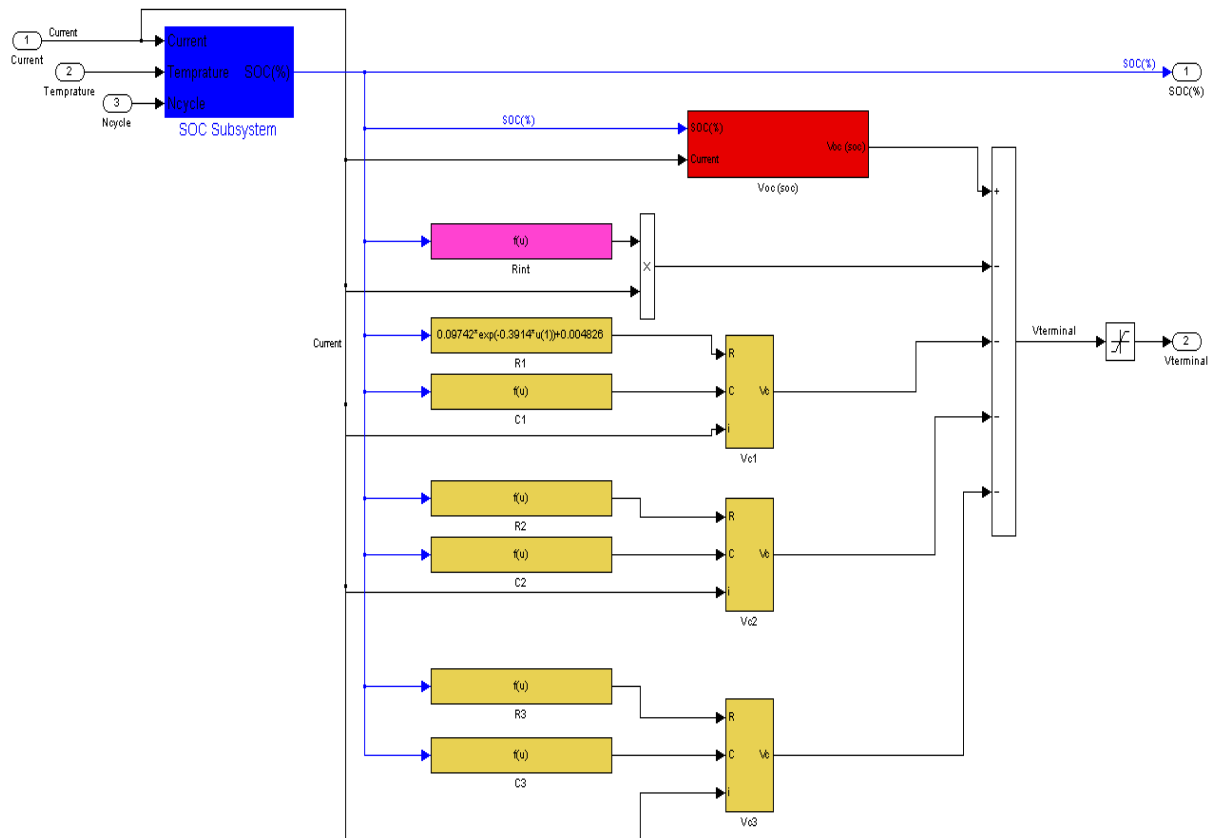


Figure 3.12: Block diagram of the battery model

3.2.5.2 Battery Electrical Model Verification

In order to verify the accuracy of the extracted results, several tests were carried out to compare the simulation results with experimental ones. The same pulse current in various rates were injected to the battery and Simulink model and terminal voltage of the battery in the simulation and experimental were compared. The Simulink model results were comparable to the experimental results from the battery and verify the accuracy of the model. Figure 3.13 illustrates the simulation terminal voltage of the battery model and experimental data.

The round off error of the MATLAB calculation was the main source of the error while the curve fitting was carried out and causes most portion of the output error. The other source of error was the resolution and accuracy of the measurement instruments. These two were the main source of error in the results.

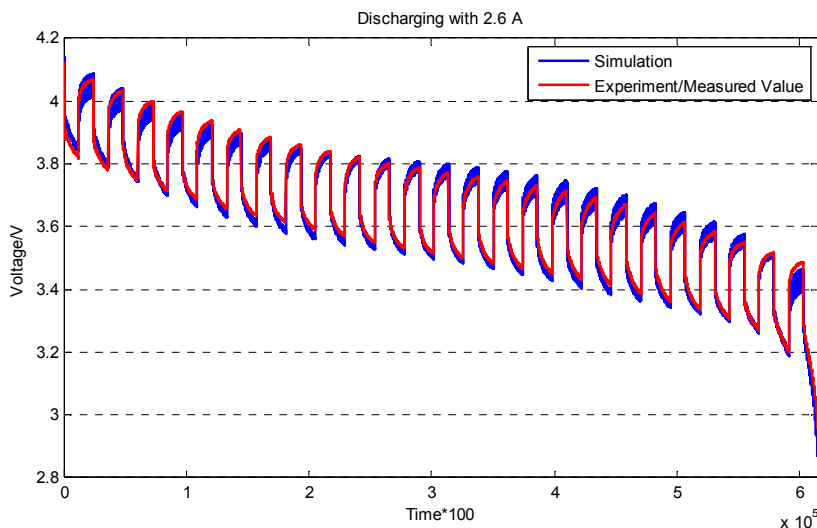


Figure 3.13: Terminal voltage of the battery Simulink model and experimental data

3.3 Ultracapacitors Energy Storage: Types, Characteristics and Modeling

3.3.1 Ultracapacitor Types and Characteristics

Ultracapacitors, which are also referred to as super-capacitors, provide energy storage and they can fast charge/discharge and delivering high power for a very short period of time, in the order of fraction of seconds. The significant improvements in capacity and energy density over conventional capacitors, while maintaining the same high power density values, are possible using a much larger surface area for the electrodes and thinner dielectrics. In comparison with other energy storage devices, ultracapacitors have a very high power density while their energy density is substantially lower than that of electric batteries. Ultracapacitors are especially suitable for applications that require high-rate and short deep cycles, such as backup power supplies, Hybrid Electric Vehicles (HEV), automotive start-stop applications, DC link voltage support in converter and power quality correction in utility applications.

Based on their electrode design, ultracapacitors may be classified into three main groups: Electrical Double-Layer Capacitors (EDLCs), pseudocapacitors, and hybrid capacitors (see figure 3.14). The double layer capacitors rely on the electrostatic field between two plates, while pseudocapacitors employ electrochemical reactions to store the electric charge. The hybrid capacitors combine the two phenomena and include the popular Li-ion ultracapacitors [58-60].

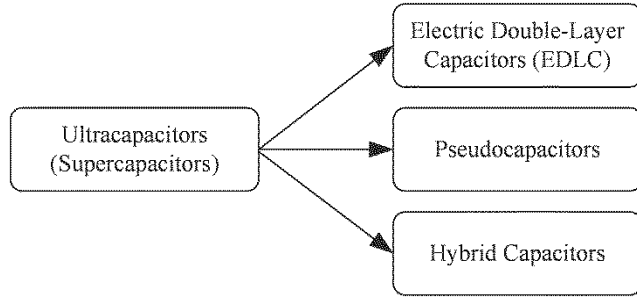


Figure 3.14: Classification of ultracapacitors based on the electrode design.



Figure 3.15: Examples of Li-ion ultracapacitors of 2200F, 2300F and 3300F.

Ultracapacitors are superior to batteries both in terms of life cycling, with more than 105 cycles being possible, as well as energy efficiency. Deep cycling does not have a significant influence on ultracapacitors' life span, while this is definitely not the case for the lead-acid or Li-ion batteries. Examples of Li-ion ultracapacitors of 2,200 F, 2,300 F and 3,300F Li-ion ultracapacitors are shown in figure 3.15. In order to reach higher voltages, currents, or capacities, ultracapacitors are connected in series or parallel in banks as the one shown in figure 3.16, which have been used in the University of Wisconsin-Milwaukee (UWM) lab for demonstrating grid integration methods for intermittent renewable energy generation [61-62].

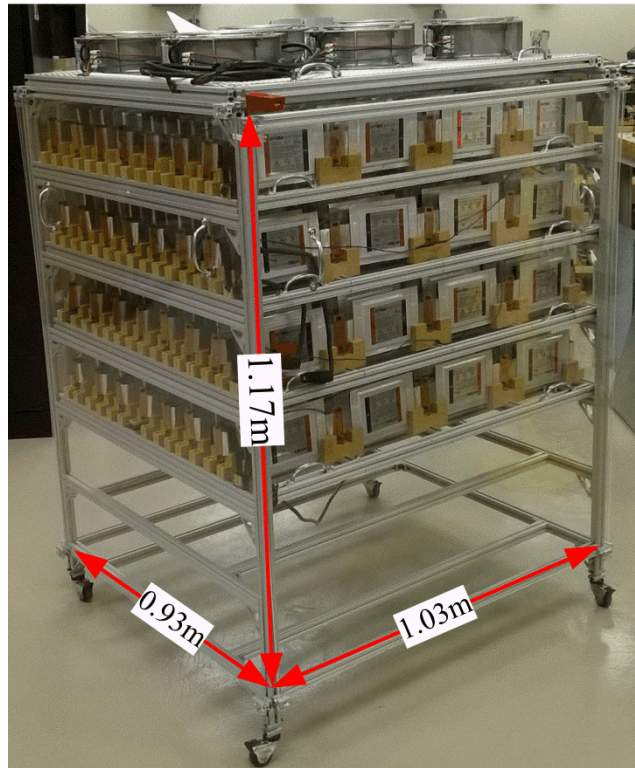


Figure 3.16: Ultracapacitor bank in the UWM Lab. The approximate overall dimensions are $1.03 \times 0.93 \times 1.17$ m. Rated at 720V and 0.5Ah.

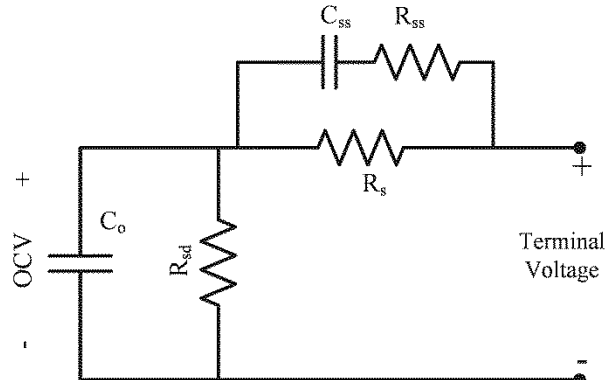


Figure 3.17: Electric equivalent circuit model for an ultracapacitor [61].

3.3.2 Ultracapacitor Modeling

Models for ultracapacitors may be categorized into three main groups of the physical/electrochemical, equivalent circuit, and behavioral neural network type, respectively. The physical models rely on the electrochemical reactions and corresponding

high order differential equations, and therefore they are the most phenomenological relevant and, in principle also, the most accurate [63-64].

The equivalent circuit models for ultracapacitors typically employ several passive circuit elements, such as resistors and capacitors [65-68]. A simplified equivalent circuit model for Li-ion ultracapacitors, based on the concept proposed in [61], is shown in Figure 3.17, where the self-discharging characteristic of ultracapacitor is modeled by R_{sd} , the cell and the junction resistance are totally quantized by series resistance R_s and the RC elements, R_{ss} and C_{ss} , model the transient response of ultracapacitor. The Parameter identification requires multiple AC and DC tests. The equivalent incremental internal capacitance is calculated as:

$$C_0(OCV_i) = \frac{\Delta Q_i}{\Delta OCV_i} = \frac{\sum_i I_i(t)\Delta t}{\Delta OCV_i} \quad [3.4]$$

where OCV is the open circuit voltage, I is the current and Q is the columbic charge for the data point i . It should be noted that a columbic counting technique has been employed to estimate the state of charge, which varies approximately linearly with OCV.

An 1100 F li-ion ultracapacitor was charged during 16 cycles which each cycle consists of 10 seconds charging and then rest (disconnected from the source) for 20 seconds. Figure 3.18 verifies the accuracy of the equivalent circuit model of figure 13.9 by comparing the terminal voltage of the ultracapacitor and the simulation model.

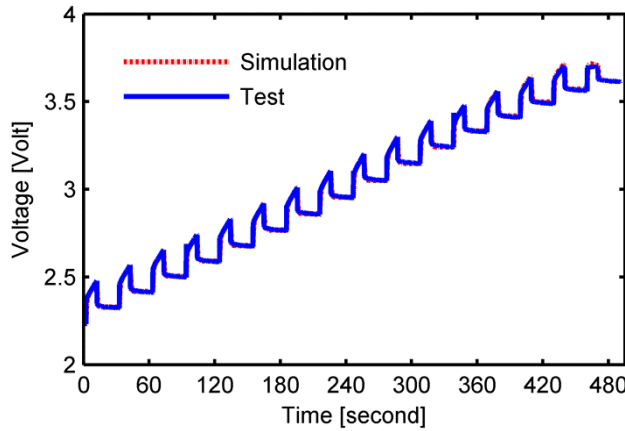


Figure 3.18: Experimental data and simulation results for the Li-ion Ultracapacitor, 10 A pulsed charging DC test at 25°C [61].

Some models that combine equivalent circuits and electrochemistry fundamentals have also been proposed [63-64]. Yet in another approach, a training data represented by the voltage, current, and temperature values measured during charging and discharging experiments have been used to train a neural network [69].

3.4 Energy Storage Management Systems (ESMSs)

3.4.1 Main Concepts

An Energy Storage Management System (ESMS) is typically employed in order to ensure optimal and safe operation of devices, such as batteries and ultracapacitors. A typical ESMS configuration includes: an effective cell balancing mechanism; cooling and ventilation; data acquisition and controls; communications and interfaces between subsystems and with the power system; protections; for example, to overvoltage and short circuit, condition monitoring for SOC and SOH, temperature etc.

The management systems for both batteries and ultracapacitors share the same basic principles, but batteries require additional care as their life time and safe performance are

highly sensitive to parameters like high temperatures, Depth of Discharge (DOD), and current rate. Consequently, the focus in this section is on Battery Management Systems (BMS) and includes topics related to the State of Charge (SOC), State Of Health (SOH), and State Of Life (SOL).

In terms of functionality, BMSs may be divided into three categories: centralized, modular or master-slave, and distributed. In a centralized BMS, parameters, such as voltage, current, and temperature are measured for individual cells and sent to the main BMS board. This topology is compact, cost efficient, and well suited for trouble shooting. In a modular BMS, slave cards collect the data from each cell and send it to a master card, which coordinates the management of the entire system (figure 3.19). This topology enables a modular expansion for larger size packs. In a distributed BMS, as shown in figure 3.20, each cell has its own individual electronic board and a main controller, which is responsible for communications and necessary computations [70].

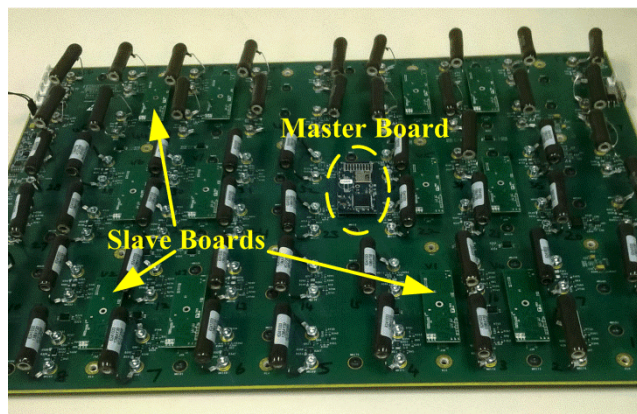


Figure 3.19: A modular battery management system (BMS) topology: several slave boards collect cells data and send it to the master board.

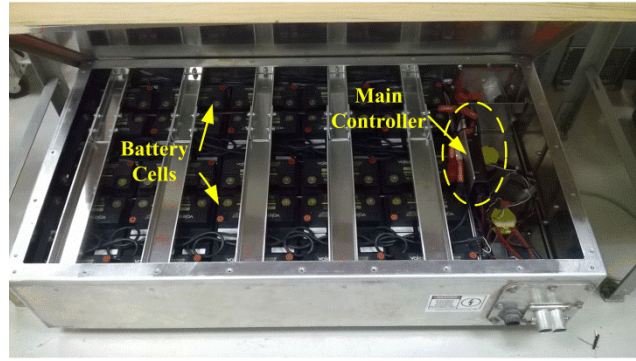


Figure 3.20: A distributed Battery Management System (BMS): each cell sends the data to the main controller.

Xing et al. [71] have proposed a generic BMS structure in which various sensors are installed in the battery pack, gather real-time data for system safety and battery state calculation [71]. The data is employed for cell balancing and thermal management, protection, and for state determination, which in turn is used for the electrical control, as shown in figure 3.21.

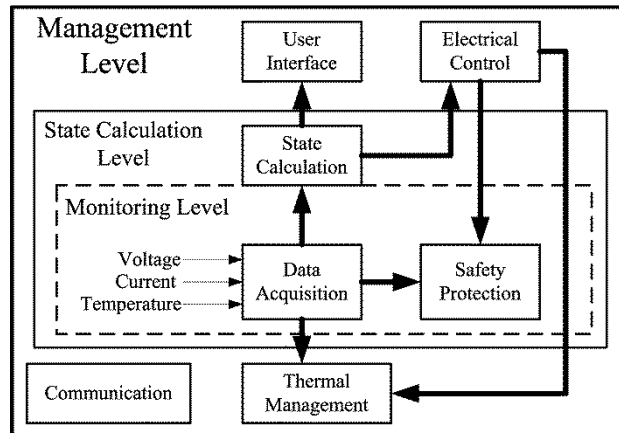


Figure 3.21: Block diagram of a typical BMS [71].

3.4.2 State of Charge

The SOC is an indicator of the amount of remaining energy or charge available in a battery as a fraction of the nominal value, i.e. rated value of capacity. Since the SOC is not

measurable directly, it needs to be evaluated based on other parameters that significantly affect the state of charge like battery current, temperature, and number of lifetime cycles. It should be noted that the maximum capacity of a battery gradually and non-linearly degrades over time, making it very challenging to extract and estimate the exact value of the SOC. Extensive research has been conducted in recent years in this respect.

The most common approach for estimating SOC is coulomb counting, in which the capacity of the battery is calculated by integrating the battery current over time. This method is well suited for Li-ion batteries, which have high columbic efficiency [39]. The accuracy of this method is highly dependent of the initial value of the SOC and the nominal capacity of the battery, which is decreasing as a battery ages. To reduce the possible initial SOC error, and also to compensate for the possible accumulated error due to integration, the SOC estimation based on the Open-Circuit Voltage (OCV) versus SOC table, a table in which each OCV value is associated with a SOC value, has been proposed [72]. Although the on-line (real-time) measurement of OCV has its own challenges, computationally intelligent methods, such as neural and fuzzy algorithms, have been developed in this respect to estimate SOC [73-74]. Because these methods are very sensitive to the model error and disturbance, the estimated results may fluctuate widely. Furthermore, the OCV versus SOC or DOD curves for some battery chemistries are almost flat for most of the operating range, due to their cathode chemistry (figure 3.22). Some types, such as LFP, also have a very long voltage relaxation time, limiting the practical application of this technique.

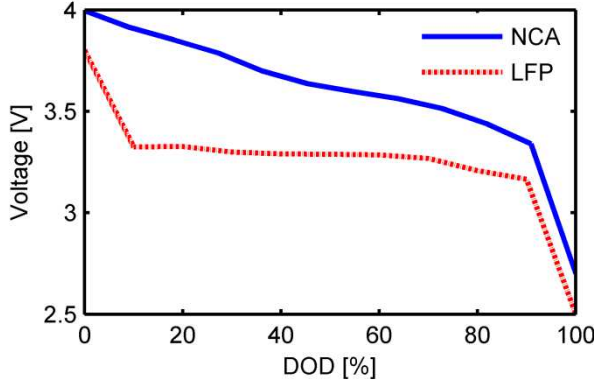


Figure 3.22: Open Circuit Voltage (OCV) versus Depth of Discharge (DOD) for NCA and LFP types of Li-ion batteries.

Extended Kalman filter (EKF) is widely used for estimating SOC. The EKF approach is highly sensitive to the accuracy of the battery model and parameter values, and, therefore, special care should be taken to avoid significant error and divergence [75-76]. To reduce the sensitivity to the model parameters, an adaptive EKF was proposed in [77]. Several other methods, including robust H_∞ and sliding mode observers, and support vector machine techniques have been also employed to estimate the SOC of batteries [78-80].

3.4.3 State of Health (SOH)

The state of health or SOH has several definitions, such as: the maximum charge that can be released after the battery has been fully charged [81], or the battery's capacity of storing energy and preserving charge for long periods [82-83], or the remaining battery capacity for the current cycle as compared to the original battery capacity [84]. The SOH can also be defined as a set of indicators or diagnostic flags, which reflect the health status and physical condition of the battery, such as loss of rated capacity [85].

The value of SOH is beneficial for applications like HEV and EV, where it is used as an indication of specified power or to estimate the driving range. Similar to the SOC problem, several techniques have been developed for SOH estimation including: Extended Kalman Filter [85], adaptive observer [79], and probabilistic neural networks [81]. Measuring the internal equivalent dc resistance of a cell, which increases with capacity degradation, is another characterization tool for SOH [84].

3.4.4 State of Life (SOL)

The state of life (SOL) is defined as the Remaining Useful Life (RUL) of a battery or as the time when battery should be replaced [71]. This indicator is considered from the design stage to plan the maintenance and replacement schedules, prevent failures during operation and increase the reliability and availability of an ESS. Several methods have been published for RUL estimation [86-88].

3.4.5 Cell Balancing Systems

To achieve higher voltage and current, a battery pack consists of several cells, which are connected in series and parallel layouts, respectively. The cells in a string could have different SOC levels due to several internal and external sources of unbalancing, which may result in different capacity fading rates between cells. Internal imbalances include different self-discharging resistance and impedance and external causes may include thermal variation across the string [89-90]. During charging or discharging, imbalances in between cells may lead to extreme voltages and hence severe overcharging and over-discharging that could seriously damage cells, reduce useful life time, and even cause fires.

and explosions. Therefore, an effective battery cell balancing system, which maintains the SOC of the cells to the same level, is an important feature of any BMS.

Cell balancing systems are either passive or active. According to the typical passive balancing methods, the extra energy of an imbalanced cell is released by increasing the cell body temperature, a technique that is useful especially for small battery packs with low voltage [91]. This technique is relatively straightforward and inexpensive to implement, but its applicability is mostly limited to cells that do not damage severely due to overcharging [92].

The active balancing technique utilizes an active circuit to distribute as evenly as possible the energy among the cells [89]. Active balancing techniques are employed in several different ways including shunting, and shuttling and energy converting method. From the energy flow point of view, the active balancing methods comprise dissipative and non-dissipative methods [93]. The extra energy in the dissipative methods is wasted as heat across a resistor, while in non-dissipative techniques, the excess energy is distributed among the string cells, leading to a higher system efficiency.

3.5 Battery Chemistry Selection

In order to choose the best battery chemistry a comprehensive literature review has been performed to investigate the characteristics of different Li-ion batteries. Moreover, several tests have also been conducted to extract cell information like internal resistance, ability of high rate discharging, cycle life and temperature effect on the cell's performance.

Based on the literatures review and battery datasheets provided online, candidates which meet the criteria, have been selected for the battery tests. The criteria which come from the project requirement include safety, energy and power densities, cycle life, performance and cost. Since the battery associated with a medical imaging machine and will be used in the medical centers, the battery should be among the safest chemistry available. The risk of having any kind of fire or explosion regarding to the chemical reaction in side of the battery or in case of any abuses must be as low as possible. In terms of power density, the candidate should be able to provide a specific load profile. The load profile has a peak power rating for a short period (couple of seconds) and battery needs to be discharged with high rate (around 10C for 2 second time periods) to support the load which also referred as load shedding mode. See figure 3.23.

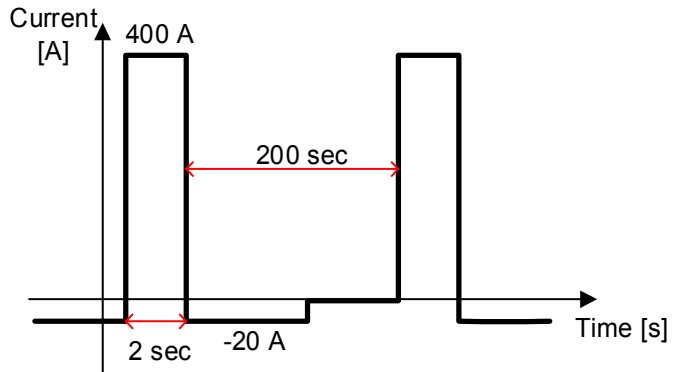


Figure 3.23: The required load profile. The candidate battery should can provide a peak power rating as high as 400 A discharging for 2 second periods.

Besides the power demand, the ability of battery to provide a long term support as an Uninterruptable Power Supply (UPS), in case of any power outage or break, needs the battery to have a high energy density as well. This is another reason why Li-ion batteries have been selected over Li-ion ultra-capacitors which could even offer a higher power density but just for a couple of second time scale.

The load profile which is basically a medical imaging machine will be repeated several times during a day and will work for years. Then the candidate battery faces the specific discharging rate for many times during its useful cycle life period, which means it has to have a excellent cycle life to be able to deliver the required power as many cycles as possible over a specific time period. It is worth to mention that each battery has a cycle life and a calendar (or float) life. The cycle life represents the number of discharging cycles with different depth of discharge (DOD) rate before it retirements and calendar life shows how many days/years which battery will last and normally a battery is retired when its rated capacity drops below a determined threshold. The threshold depends on the application in which battery will be used.

The performance of the battery on different discharging rates and operating temperatures also matters. The candidate should present a perfect performance on the lab tests which will be discussed later.

According to the limited budget, cost of the battery is another criterion. The least expensive batteries which satisfy the required criteria would be preferred.

Based on the table 3.3 two Li-ion battery chemistries have been chosen to do the final performance tests. The finalized battery chemistry candidates are LFP and NCA. Lithium Iron Phosphate presents an excellent safety aspect as well as cycle life, performance and cost, while the NCA chemistry represents a superior power and energy density besides its excellent life span and performance. Three batteries, two LFP cell type from CALB and SAFT and one NCA chemistry based cell from Johnson Control In. A 40 Ah LFP cell from CALB, which is the least expensive one cost wise, lower than half of the cost of two others,

capable of discharging with high rate for couple of seconds, have been selected as one of the candidates to perform the battery performance test. Another 30 Ah LFP based cell from SAFT, which has been claimed to have a higher power density and life span than CALB with higher cost. The third candidate is a 42 Ah NCA type cell from JCI. The performance tests on the selected batteries are presented in the chapter 6.

CHAPTER IV: System Modeling

4.1 Introduction

In this chapter model of the DC UPS system is introduced. The state space average modeling technique is utilized for modeling the entire system. In order to analysis the system dynamics and characteristics under different situations, transfer functions are derived from the state-space average modeling of the system. The goal of this chapter is to provide required tools for the analysis of the system which is the topic of the next chapter.

The average modeling technique is used to model two converters in the system, the AC/DC and DC/DC. The model of each converter is presented separately and then the model of entire system is discussed.

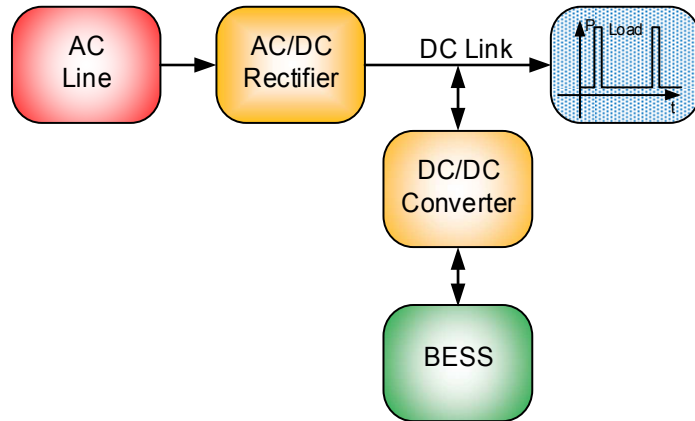


Figure 4.1: Block diagram of the DC UPS system, including AC/DC and DC/DC converters

4.2 AC/DC Converter Modeling

Figure 4.2 shows the schematic diagram of the DC Line-Interactive UPS system including the AC/DC and the DC/DC converters and battery energy storage system (BESS). This section describes the mathematic model of the rectifier. The AC main input line, here

known as grid is connected to the DC link through an AC/DC rectifier. The rectifier is a three-phase two-level voltage-source converter.

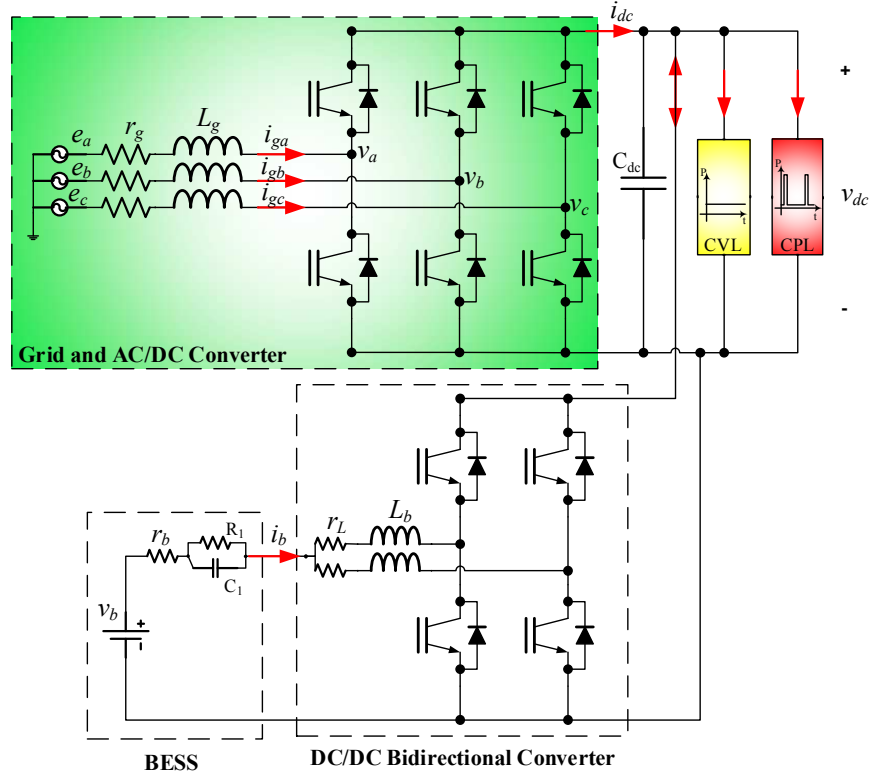


Figure 4.2: Schematic diagram of the DC UPS system.

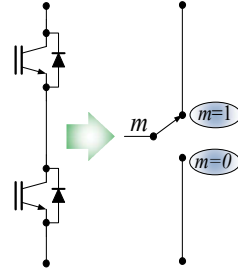
The AC source voltages are e_a , e_b and e_c . The grid currents are i_{ga} , i_{gb} and i_{gc} . L_g and r_g are the grid side impedance modeled as an inductance series with resistance, respectively. The DC side voltage and current of the rectifier are characterized by v_{dc} and i_{dc} , respectively. The DC side capacitor is C_{dc} . By considering the converter input voltages as v_a , v_b and v_c , then by using KVL law in the left side of the rectifier, these equations are achieved.

$$\begin{cases} e_a = r_g i_{ga} + L_g \frac{d}{dt} i_{ga} + v_a \\ e_b = r_g i_{gb} + L_g \frac{d}{dt} i_{gb} + v_b \\ e_c = r_g i_{gc} + L_g \frac{d}{dt} i_{gc} + v_c \end{cases} \quad [4.1]$$

Then the mathematic model of the rectifier in the abc reference frame is

$$\begin{cases} \frac{d}{dt} i_{ga} = \frac{1}{L_g} (-r_g i_{ga} + e_a - v_a) \\ \frac{d}{dt} i_{gb} = \frac{1}{L_g} (-r_g i_{gb} + e_b - v_b) \\ \frac{d}{dt} i_{gc} = \frac{1}{L_g} (-r_g i_{gc} + e_c - v_c) \end{cases} \quad [4.2]$$

State vector model of the three-phase rectifier is adopted by means of using a switching space vector. The switching function $m_i(t)$ is defined as



$$m_i(t) = \begin{cases} 1 & \text{when the upper switch is closed} \\ 0 & \text{when the lower switch is closed} \end{cases} \quad i = a, b, c \quad [4.3]$$

thus, the switching space vector is

$$\bar{m}(t) = \frac{2}{3} [m_a(t) + \alpha m_b(t) + \alpha^2 m_c(t)] \quad [4.4]$$

where $\alpha = e^{j2\pi/3}$. Then by substituting the converter input voltages, the grid input voltages and the rectifier input currents, the associated space vectors are achieved as $\bar{v}(t)$, $\bar{e}(t)$ and $\bar{i}(t)$ respectively.

$$\begin{cases} \bar{v}(t) = \frac{2}{3} [v_a(t) + \alpha v_b(t) + \alpha^2 v_c(t)] \\ \bar{e}(t) = \frac{2}{3} [e_a(t) + \alpha e_b(t) + \alpha^2 e_c(t)] \\ \bar{i}(t) = \frac{2}{3} [i_a(t) + \alpha i_b(t) + \alpha^2 i_c(t)] \end{cases} \quad [4.5]$$

By using the space vectors, the input voltage of the rectifier is achieved as

$$\bar{v}(t) = \bar{m}(t)v_{dc}(t) \quad [4.6]$$

Then the mathematic model of the AC/DC rectifier in space vector form is obtained

$$\frac{d}{dt}\bar{v}_g(t) = \frac{1}{L_g}[-r_g\bar{v}_g(t) + \bar{e}(t) - \bar{v}(t)] \quad [4.7]$$

The model (4.7) can also be presented in the stationary and rotating frames.

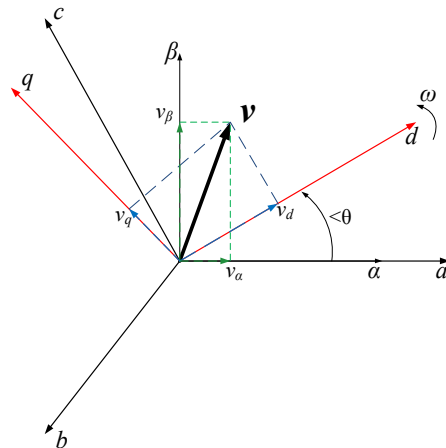


Figure 4.3: Representation of space vector of rectifier voltage in stationary $\alpha\beta$ frame and dq rotating frame.

Figure 4.3 illustrates the presentation of the rectifier input voltage in stationary $\alpha\beta$ frame and dq rotating or synchronous frame. By using the Clarke and Park transformations, the projection of the rectifier voltage space vector on the $\alpha\beta$ stationary frame and synchronous frame are obtained.

The $\alpha\beta$ components of the switching space vector is achieved by using Park transformation

$$\begin{bmatrix} m_\alpha \\ m_\beta \end{bmatrix} = \frac{2}{3} \begin{bmatrix} 1 & -1/2 & -1/2 \\ 0 & -\sqrt{3}/2 & \sqrt{3}/2 \end{bmatrix} \begin{bmatrix} m_a \\ m_b \\ m_c \end{bmatrix} \quad [4.8]$$

and the Clark transformation is used to find the synchronous frame components.

$$\begin{bmatrix} m_p \\ m_q \end{bmatrix} = \frac{2}{3} \begin{bmatrix} \cos\theta & \cos(\theta - 2\pi/3) & \cos(\theta + 2\pi/3) \\ \sin(\theta) & \sin(\theta - 2\pi/3) & \sin(\theta + 2\pi/3) \end{bmatrix} \begin{bmatrix} m_a \\ m_b \\ m_c \end{bmatrix} \quad [4.9]$$

where θ is the phase angle between α -axis and d -axis. The dq frame rotates with the grid frequency or same angular speed, $\omega = 2\pi f$, as the grid voltage space vector. The transformation matrices in (4.8) and (4.9) can be used to find the direct and quadrature components of the grid voltages, the rectifier input currents and the rectifier input voltages.

The mathematical model of the rectifier in the $\alpha\beta$ stationary frame is

$$\begin{cases} \frac{d}{dt} i_\alpha(t) = \frac{1}{L_g} [-r_g i_\alpha(t) + e_\alpha(t) - m_\alpha(t)v_{dc}(t)] \\ \frac{d}{dt} i_\beta(t) = \frac{1}{L_g} [-r_g i_\beta(t) + e_\beta(t) - m_\beta(t)v_{dc}(t)] \end{cases} \quad [4.10]$$

and in the dq synchronous reference frame, at the angular speed ω , the model represents as

$$\begin{cases} \frac{d}{dt} i_d(t) = \frac{1}{L_g} [-r_g i_d(t) + \omega L_g i_q(t) + e_d(t) - m_d(t)v_{dc}(t)] \\ \frac{d}{dt} i_q(t) = \frac{1}{L_g} [-r_g i_q(t) - \omega L_g i_d(t) + e_q(t) - m_q(t)v_{dc}(t)] \end{cases} \quad [4.11]$$

where the rectifier input voltage can be rewritten as

$$\begin{cases} v_d(t) = m_d(t)v_{dc}(t) \\ v_q(t) = m_q(t)v_{dc}(t) \end{cases} \quad [4.12]$$

In the dq rotating frame, the direct and quadrature differential equations for the rectifier current are dependent because of the two terms with the angular speed or the cross-coupling terms $\omega L_g i_q(t)$ and $\omega L_g i_d(t)$.

It is worth to mention that, by considering d-axis aligned on the grid voltage vector, \bar{e} , the quadratic component of the grid voltage vector or the projection of the grid voltage vector on the q-axis of the synchronous rotating frame will be zero, $e_q = 0$, while the direct component, the projection of the grid voltage vector on the d-axis of the synchronous rotating frame is equal to the grid voltage, $e_d = \bar{e}$.

4.3 DC/DC Bidirectional Converter Modeling

Since the terminal voltage of the BESS is almost half of the DC link voltage, it is required to use a DC/DC converter and to be able to handle power flow between DC link and BESS, the converter should be bidirectional. Furthermore, it is important to keep the current ripple as low as possible as the high current ripples decrease the BESS life time. Interleave techniques are widely used in the energy storage power electronics interfacing to address the concerns, reducing current ripples and simultaneously increasing the power capacity of the converter. Using interleaved technique allows to achieve a same current ripple by a smaller inductor in terms of size and weigh [23, 25-29].

The number of legs can be appropriately chosen based on the requirement minimum current ripples and the converter duty ratio. Two or four legs show a minimum input current ripples when the duty ratio is close to 0.5 [23,24].

A two-phase interleaved bidirectional DC/DC converter is used to connect the BESS to the DC link which is highlighted in the figure 4.4. Each phase/leg has 180 degree phase difference.

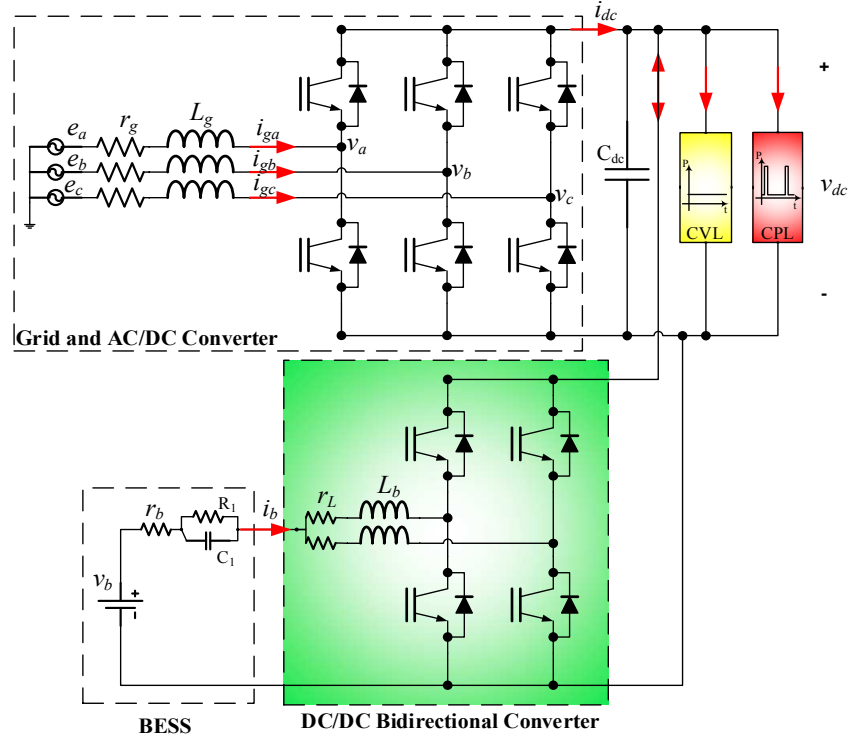


Figure 4.4: A two-phase interleaved bidirectional DC/DC converter is used to connect the BESS to the DC link.

For modeling purpose, the DC/DC converter is simplified to one-leg with equivalent inductance and resistance. Figure 4.5 illustrates the equivalent circuit where the r_{eq} and L_{eq} are defined as

$$\begin{cases} r_{eq} = r_b + \frac{r_L}{2} \\ L_{eq} = \frac{L_b}{2} \end{cases} \quad [4.13]$$

and the i_{dc} in the figure 4.5, models the grid and AC/DC converter, as the AC/DC converter is controlled in current mode to deliver a constant power at unity power factor to the DC link.

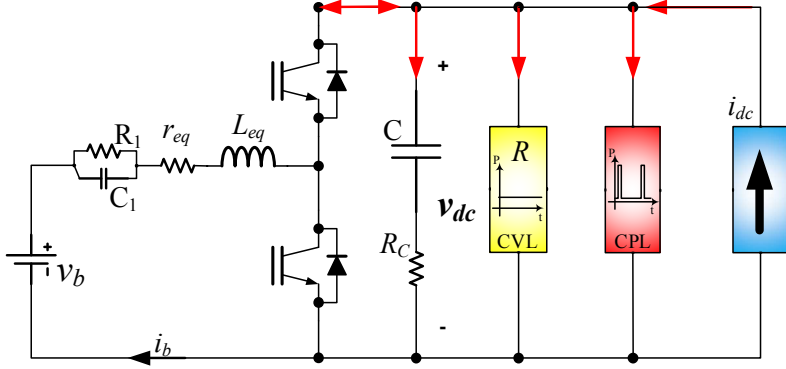


Figure 4.5 Simplified model of the DC/DC converter, i_{dc} represents the power from the grid.

To find the differential equation describing the DC/DC converter, two switching intervals over a switching period, T are considered.

$$\begin{cases} v_b(t) = v_{c1}(t) + r_{eq}i_b(t) + L_{eq}\frac{d}{dt}i_b(t) + v_{dc}(t) & 0 \leq t < dT \\ v_b(t) = v_{c1}(t) + r_{eq}i_b(t) + L_{eq}\frac{d}{dt}i_b(t) & dT \leq t < T \end{cases} \quad [4.14]$$

where d and T are the duty ratio and switching period of the DC/DC converter, respectively and v_{c1} is the voltage across the RC network or the capacitor C_1 . The first switching period ($0 \leq t < DT$) is when the upper switch is closed and lower switch is opened. During this period, the BESS is charging and current flows through the upper switch and lower diode. The second switching period ($DT \leq t < T$) is when the BESS is providing power to the DC link by discharging its stored energy. During this period the lower switch and upper diode conduct. By averaging the two equations in (4.14) over the switching period of T , the equivalent average model of the converter is achieved as

$$L_{eq}\frac{d}{dt}i_b(t) = -r_{eq}i_b(t) - v_{c1}(t) - d\dot{v}_{dc}(t) + v_b(t) \quad [4.15]$$

The differential equation in (4.15) represents the averaged switch model of the DC/DC converter.

4.4 Battery Energy Storage System Modeling

The comprehensive electrical model for the Li-ion battery is described in the previous chapter. Figure 4.4 shows the model used for the BESS in which the open circuit voltage is represented by a DC voltage source, v_b , a series resistance r_b models the internal resistance of the battery and a RC network to characterize the transient behavior of the BESS. All the parameters of the BESS are considered constant and temperature-independent during the modeling period.

By applying a KCL in the RC network, this equation can be achieved.

$$i_b(t) = \frac{v_{c1}(t)}{R_1} + C_1 \frac{d}{dt} v_{c1}(t) \quad [4.16]$$

Then by rearranging the equation based on the voltage across the capacitor C_1 ,

$$C_1 \frac{d}{dt} v_{c1}(t) = i_b(t) - \frac{v_{c1}(t)}{R_1} \quad [4.17]$$

This equation models the transient response of the BESS.

4.5 CPL Modeling

Basically, loads in power electronic systems can be categorized into two groups, constant voltage loads or CVLs and constant power loads or CPLs. Constant voltage loads which include conventional loads have *positive incremental impedance* characteristics and require regulated voltage across them. The auxiliary loads in this project are considered as

a CVL which just need the regulated voltage across them. Constant power loads, on the other hands, sink constant power from their input buses and have *negative incremental impedance* characteristics which can cause instability issues for the feeding power converter. This effect is also known as negative impedance instability. Figure 4.6 illustrates the V-I characteristics of a CPL and the negative incremental impedance associated with the CPL [94-98].

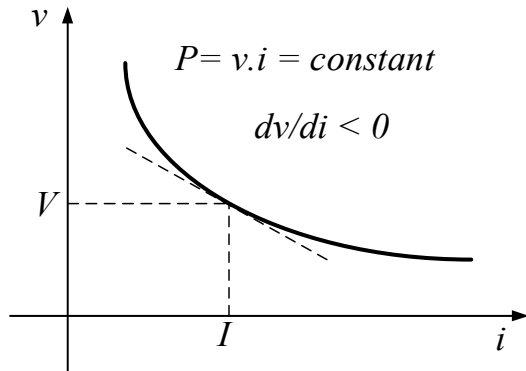


Figure 4.6 V-I characteristic of a CPL and the negative incremental impedance characteristic of the CPL.

In the constant power loads, the negative incremental impedance means that although the instantaneous value of the impedance is positive, the incremental impedance is negative. On the other words, since the load power is assumed to be constant and knowing that power is the multiplication of voltage and current ($P = vi = \text{constant}$), although the instantaneous values of voltage and current are positive, but the rate of changing for voltage over current is negative ($\frac{dv}{di} = -\frac{P}{v^2} < 0$) or in better words, by increasing/decreasing voltage, current decreases/increases [94-95].

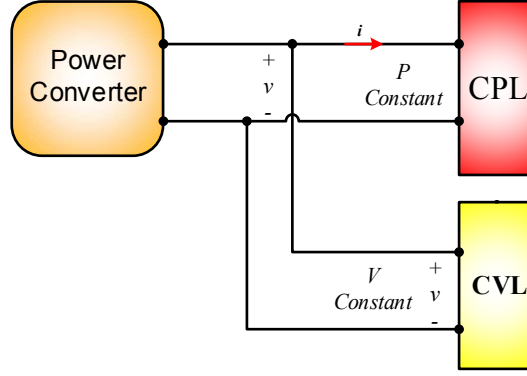


Figure 4.7 Illustration of a power converter feeding a constant power load, CPL, and a constant voltage load, CVL.

Figure 4.7 illustrates a power converter loaded with CVL and CPL. If the power of the CPL is P and v , i and r are the bus voltage, current of the CPL and the equivalent resistance of the CPL, respectively, then

$$P = V_o I_o = \frac{V_o^2}{R_o} = R_o I_o^2 \quad [4.18]$$

where V_o , I_o and R_o are the bus voltage, CPL current and equivalent resistance of the CPL at operating points. By means of small signal analysis around operating points while considering small disturbances on the voltage, current and equivalent resistance of the CPL,

$$\begin{cases} i = I_o + \tilde{i} \\ v = V_o + \tilde{v} \\ r = R_o + \tilde{r} \end{cases} \quad [4.19]$$

the equivalent resistance of the CPL can be expressed as

$$r = \frac{P}{i^2} = \frac{P}{(I_o + \tilde{i})^2} = \frac{P}{I_o^2 + \tilde{i}^2 + 2I_o\tilde{i}} \quad [4.20]$$

where the second-order signal perturbations have been assumed to be zero.

$$r \cong \frac{P}{I_o^2 + 2I_o \tilde{I}} = \frac{P/I_o^2}{1 + 2\tilde{I}/I_o} \quad [4.21]$$

By using Tylor series expansion, while ignoring higher order terms, the equivalent resistance of the CPL is obtained as

$$r \cong \frac{P/I_o^2}{1 + 2\tilde{I}/I_o} \cong \frac{P}{I_o^2} \left(1 - 2\tilde{I}/I_o\right) = R_o(1 - 2\tilde{I}/I_o) \quad [4.22]$$

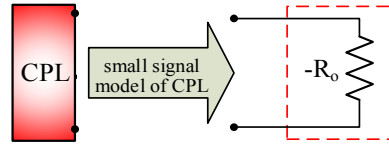
Now by applying achieved equivalent resistance relation in the bus voltage,

$$v = V_o + \tilde{v} = r \cdot i = R_o(1 - 2\tilde{I}/I_o)(I_o + \tilde{I}) \quad [4.23]$$

ignoring the higher order terms of the signal perturbations in the 4.23, the bus voltage is obtained as

$$v = V_o + \tilde{v} = r \cdot i = R_o I_o - R_o \tilde{I} \quad [4.24]$$

which means that the term “ $-R_o$ ” represents the small signal model of the equivalent resistance of the CPL, where $R_o = \frac{V_o^2}{P}$.



4.6 DC UPS System Modeling

In this section the state space averaged switch modeling of the entire DC UPS system is discussed. Previous sections discussed how to model each part of the system separately

while in this section all described sections of the system are considered together in a DC UPS system.

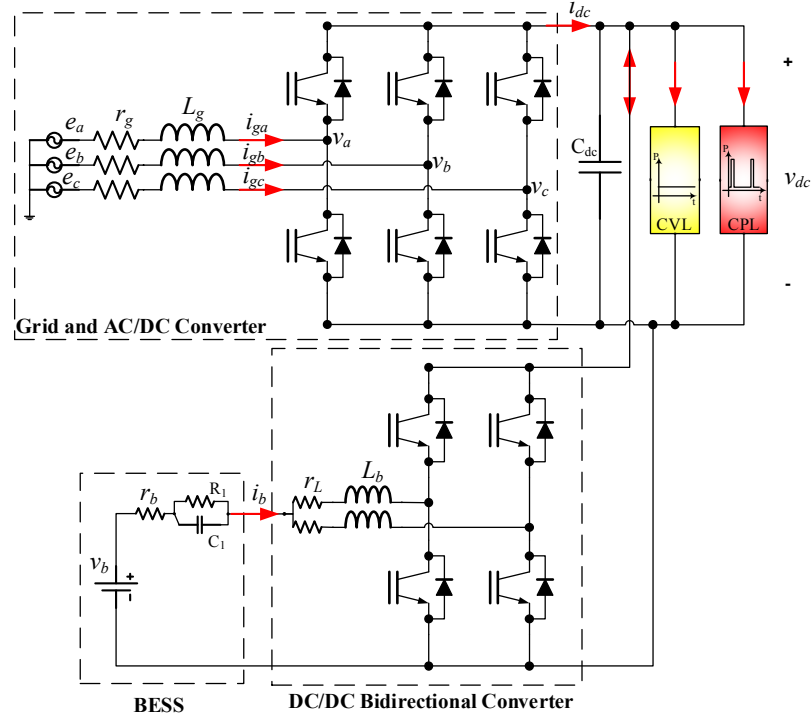


Figure 4.8: Schematic of the DC UPS.

The DC UPS system consists of four main sections which should be described by differential equations. The AC/DC section including grid and rectifier was discussed in the section 4.2, and can be expressed by two grid currents in the dq synchronous rotating frame, i_d and i_q . The associated equations in (4.11) can model the dynamics of the AC/DC subsystem. The DC/DC section is explained with equation (4.15) based on the battery discharging current i_b , discussed in the section 4.3. Equation 4.17 can capture battery behavior based on the voltage across the RC branch v_{C1} . Finally, to model the DC link behavior, an equation based on the voltage of the DC link capacitance v_{dc} as the output voltage, is necessary. Thus, the entire DC UPS system demonstrates based on the five independent states. Therefore, the state vector is obtained as:

$$x(t) = [i_d(t), i_q(t), v_{dc}(t), i_b(t), v_{c1}(t)]^T \quad [4.25]$$

By rewriting the equations 4.11, 4.15 and 4.17 and adding one more equation describing the DC link dynamics, the differential equations describing the entire system is achieved as:

$$\begin{cases} \frac{d}{dt} i_d(t) = \frac{1}{L_g} [-r_g i_d(t) + \omega L_g i_q(t) + e_d(t) - m_d(t)v_{dc}(t)] \\ \frac{d}{dt} i_q(t) = \frac{1}{L_g} [-r_g i_q(t) - \omega L_g i_d(t) + e_q(t) - m_q(t)v_{dc}(t)] \\ \frac{d}{dt} v_{dc}(t) = \frac{1}{C_{dc}} [i_{dc}(t) + d(t).i_b(t) - \left(\frac{v_{dc}(t)}{R} + \frac{P}{v_{dc}(t)} \right)] \\ \frac{d}{dt} i_b(t) = \frac{1}{L_{eq}} [-r_{eq} i_b(t) - v_{c1}(t) - d(t).v_{dc}(t) + v_b(t)] \\ \frac{d}{dt} v_{c1}(t) = \frac{1}{C_1} [i_b(t) - \frac{v_{c1}(t)}{R_1}] \end{cases} \quad [4.26]$$

where the CVL is modeled as a resistive load R and the CPL is modeled by a constant power P, then $\frac{v_{dc}}{R}$ and $\frac{P}{v_{dc}}$ are their related currents, respectively. The i_{dc} is the current from AC/DC flows in the DC link and can be obtained as follow.

Considering a lossless AC/DC rectifier, the input AC power, P_{ac} , into the rectifier should be equal to the output DC power P_{dc} and by using power calculation in the dq frame, it is achieved that:

$$P_{ac}(t) = P_{dc}(t) \quad [4.27]$$

$$\frac{3}{2} (i_d(t)v_d(t) + i_q(t)v_q(t)) = i_{dc}(t)v_{dc}(t) \quad [4.28]$$

By substituting (4.12) in the right hand side of 4.28,

$$\frac{3}{2} (i_d(t)m_d(t)v_{dc}(t) + i_q(t)m_q(t)v_{dc}(t)) = i_{dc}(t)v_{dc}(t) \quad [4.29]$$

And by canceling out the v_{dc} from both sides of (4.29), the i_{dc} is achievable as (4.30)

$$\frac{3}{2}(i_d(t)m_d(t) + i_q(t)m_q(t)) = i_{dc}(t) \quad [4.30]$$

Then i_{dc} is a representative for the grid currents into the DC link.

The set of equations 4.26 represents the entire dynamics of the DC UPS system. The equations are nonlinear and for further analysis it is required to linearize the system around an operating point. The equations mathematically model the several components in the system by using the average modeling technique. Since the DC UPS system operates in four different modes, the system model at each mode is presented as follow.

4.6.1 Mode I: Load Leveling Mode

In this mode, BESS supports the grid-tied rectifier by providing the peak pulsed power demanded by CPL for a short period while the rectifier operates on current mode to provide constant power to the DC link. Since the rectifier works on current mode control and keeps the amount of power delivered to the DC link, constant, regardless of the load power demand, also knowing the fact that the DC/DC converter regulates the DC link, then for sake of simplicity and also reducing the number of states, the grid and AC/DC rectifier can be modeled by a constant current source of i_{dc} . By this technique, the first two equations in 4.26 are removed at this mode. The resulted system is illustrated in figure 4.9. The system presented in the figure 4.9 is explained in section 4.3.

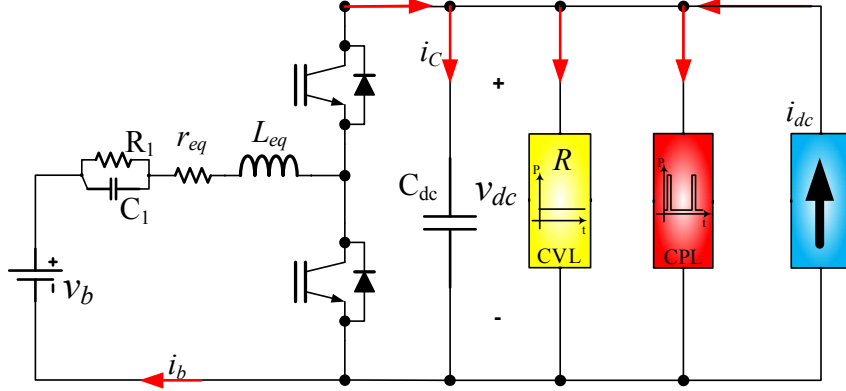


Figure 4.9: The simplified model of the DC UPS system in mode I. i_{dc} represents the current from the grid and rectifier.

Then the set of equations in 4.26 becomes a new set of three equations with three states as equations 4.31.

$$\begin{cases} \frac{d}{dt} v_{dc}(t) = \frac{1}{C_{dc}} \left[i_{dc}(t) + d(t) \cdot i_b(t) - \left(\frac{v_{dc}(t)}{R} + \frac{P}{v_{dc}(t)} \right) \right] \\ \frac{d}{dt} i_b(t) = \frac{1}{L_{eq}} [-r_{eq} i_b(t) - v_{c1}(t) - d(t) \cdot v_{dc}(t) + v_b(t)] \\ \frac{d}{dt} v_{c1}(t) = \frac{1}{C_1} [i_b(t) - \frac{v_{c1}(t)}{R_1}] \end{cases} \quad [4.31]$$

The set of equations 4.31 represents the system in mode I.

4.6.2 Mode II: Standby Mode

During mode II still the grid provides same constant power through AC/DC rectifier, which operates on current mode, to feed the CVL and charge the BESS. The DC/DC converter regulates the DC link voltage. Again, in this mode the grid and the rectifier can be represented by an independent constant current supply to the DC link. Figure 4.10 illustrates the equivalent electrical circuit for the DC UPS system in this mode.

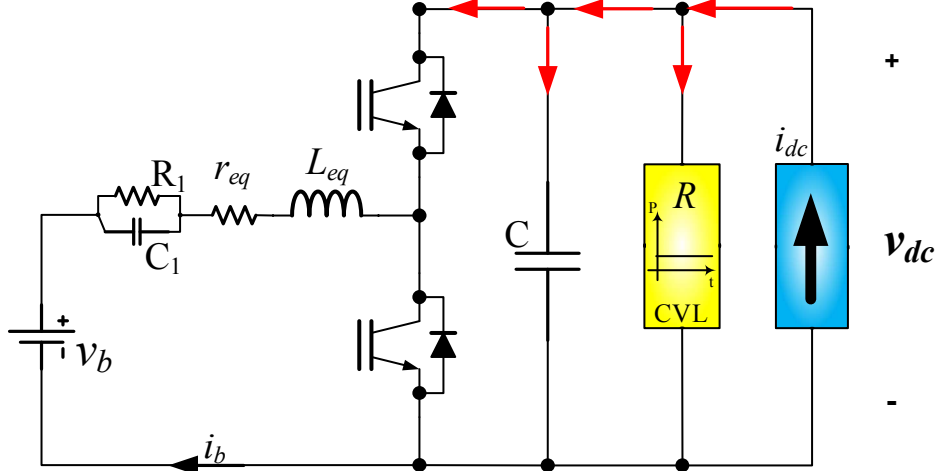


Figure 4.10: Electrical equivalent circuit of the DC UPS system in mode II.

The load is a CVL and modeled by a resistor with the specific power. The mathematic model in this mode achieved as 4.32.

$$\begin{cases} \frac{d}{dt}v_{dc}(t) = \frac{1}{C_{dc}}[i_{dc}(t) + d(t).i_b(t) - \frac{v_{dc}(t)}{R}] \\ \frac{d}{dt}i_b(t) = \frac{1}{L_{eq}}[-r_{eq}i_b(t) - v_{c1}(t) - d(t).v_{dc}(t) + v_b(t)] \\ \frac{d}{dt}v_{c1}(t) = \frac{1}{C_1}[i_b(t) - \frac{v_{c1}(t)}{R_1}] \end{cases} \quad [4.32]$$

where the CVL is represented by $\frac{v_{dc}(t)}{R}$.

The grid constant power is used to feed the CVL and charging the BESS. Since the BESS discharged during mode I, then it can the charging power. However, during the charging period, the BESS could be fully charged and does not accept any further power from grid. This is the moment that DC USP operating in the next mode which is Online mode.

4.6.3 Mode III: Online Mode

During mode II, the BESS is charging with grid constant power. It is possible that the BESS becomes fully charged, then third mode, which is online mode happens. During this mode,

the power flow between BESS and the DC link is zero and the rectifier is in charge of the DC link regulation. The grid power is reduced to the CVL and the AC/DC rectifier works on voltage mode. Figure 4.11 shows the schematic of the DC UPS during this mode.

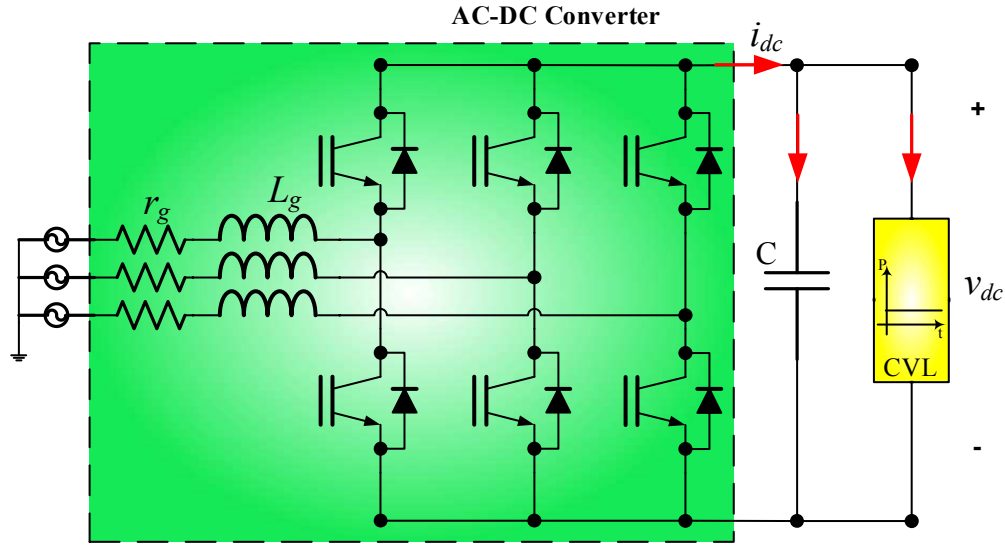


Figure 4.11: Schematic of the DC UPS during mode III, the Online mode.

By using average modeling approach, the mathematic model of the system operating on mode III is obtained as 4.33.

$$\begin{cases} \frac{d}{dt} i_d(t) = \frac{1}{L_g} [-r_g i_d(t) + \omega L_g i_q(t) + e_d(t) - m_d(t)v_{dc}(t)] \\ \frac{d}{dt} i_q(t) = \frac{1}{L_g} [-r_g i_q(t) - \omega L_g i_d(t) + e_q(t) - m_q(t)v_{dc}(t)] \\ \frac{d}{dt} v_{dc}(t) = \frac{1}{c_{dc}} [i_{dc}(t) - \frac{v_{dc}(t)}{R}] \end{cases} \quad [4.33]$$

During this mode, the DC UPS system are only providing power for the CVL and the AC/DC rectifier are rated almost twice the CVL power. Technically, the DC UPS system during this mode, operates as a three-phase rectifier providing power for a CVL. The

rectifier operates on voltage mode and keeps the Dc link voltage constant. However, the system is waiting for a high power demand from the CPL to switch to the first mode.

4.6.4 Mode IV: Islanded/UPS Mode

The DC UPS can operate on his BESS without power from grid for specific amount of time. Using Li-ion batteries gives the UPS capability to works on islanded mode when the power from the grid is disconnected due to any power disturbance. Since the DC/DC power converter is rated at the full power of the CVL plus CPL, during this mode, the DC UPS can provide required power for supporting the CPL and CVL for several cycles based upon its initial State of Charge (SOC). Figure 4.12 depicts the system model during this mode.

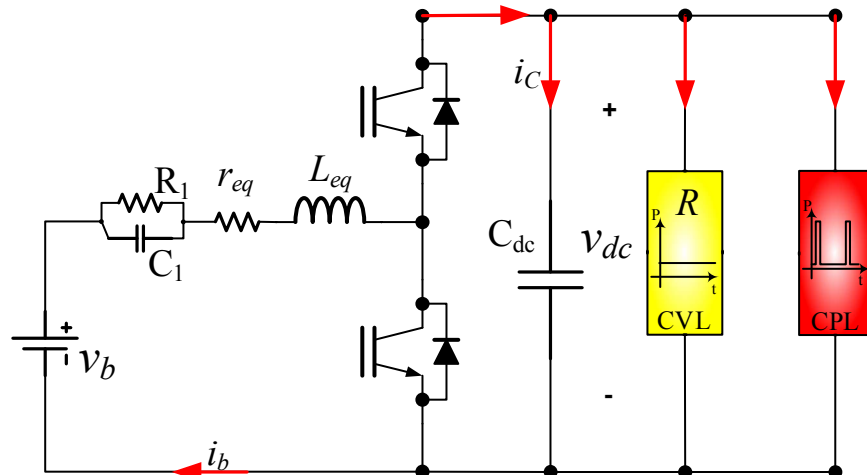


Figure 4.12: Schematic of the DC UPS model during islanded mode.

During this mode, the DC/DC converter becomes a boost converter to boost up the BESS terminal voltage to the DC link voltage level. The mathematic model of the system during mode IV is presented in 4.34

$$\begin{cases} \frac{d}{dt} v_{dc}(t) = \frac{1}{C_{dc}} \left[d(t) \cdot i_b(t) - \left(\frac{v_{dc}(t)}{R} + \frac{P}{v_{dc}(t)} \right) \right] \\ \frac{d}{dt} i_b(t) = \frac{1}{L_{eq}} \left[-r_{eq} i_b(t) - v_{c1}(t) - d(t) \cdot v_{dc}(t) + v_b(t) \right] \\ \frac{d}{dt} v_{c1}(t) = \frac{1}{C_1} \left[i_b(t) - \frac{v_{c1}(t)}{R_1} \right] \end{cases} \quad [4.34]$$

Chapter V: System Analysis and Control

5.1 Introduction

Different parts of the DC UPS have been introduced in chapter 4. The state space average modeling technique was used to extract the describing differential equations of the system in all operational modes. In this chapter, first small signal analysis of the system during operational modes is presented, then control schemes based on the small signal stability analysis are designed and discussed.

Since the differential equations presented in the chapter 4 are nonlinear, these equations linearized around an operating point and then small signal analysis around the point is performed. By extracting transfer functions out of small signal analysis, the performance and stability of the system is achieved. Based on these transfer functions, the control algorithms are designed and simulated.

The goal of this chapter is to find the stability region of the system during operational modes and design appropriate controller to ensure reliable and stable output results.

5.2 Stability Analysis of the System During Mode I

State space averaging model of the system during this mode is presented at chapter 4 where the set of equations 4.31 mathematically characterized dynamic model of the system during load leveling mode.

$$\begin{cases} \frac{d}{dt} v_{dc}(t) = \frac{1}{C_{dc}} \left[i_{dc}(t) + d(t) \cdot i_b(t) - \left(\frac{v_{dc}(t)}{R} + \frac{P}{v_{dc}(t)} \right) \right] \\ \frac{d}{dt} i_b(t) = \frac{1}{L_{eq}} [-r_{eq} i_b(t) - v_{c1}(t) - d(t) \cdot v_{dc}(t) + v_b(t)] \\ \frac{d}{dt} v_{c1}(t) = \frac{1}{C_1} [i_b(t) - \frac{v_{c1}(t)}{R_1}] \end{cases} \quad [4.31]$$

These are nonlinear equations and need to be linearized. Considering small perturbations in the state variables due to small disturbances in the duty ratio and input signals.

$$\begin{cases} v_{dc} = V_{dc} + \tilde{v}_{dc} \\ i_b = I_b + \tilde{i}_b \\ v_{c1} = V_{c1} + \tilde{v}_{c1} \\ v_b = V_b + \tilde{v}_b \\ d = D + \tilde{d} \\ i_{dc} = I_{dc} + \tilde{i}_{dc} \\ i_L = \frac{P}{v_{dc}} = I_L + \tilde{i}_L = \frac{P}{V_{dc}} - \frac{P}{V_{dc}^2} \tilde{v}_{dc} \end{cases} \quad [5.1]$$

Where the variables in capital letters are operating points or average values of corresponding variables. The last equation in 5.1 represents the current in the CPL branch.

By replacing 5.1 into 4.31, the model of the system achieved as

$$\begin{cases} \frac{d}{dt} (V_{dc} + \tilde{v}_{dc}) = \frac{1}{C_{dc}} \left[(I_{dc} + \tilde{i}_{dc}) + (D + \tilde{d}) \cdot (I_b + \tilde{i}_b) - \left(\frac{V_{dc} + \tilde{v}_{dc}}{R} + \frac{P}{V_{dc}} - \frac{P}{V_{dc}^2} \tilde{v}_{dc} \right) \right] \\ \frac{d}{dt} (I_b + \tilde{i}_b) = \frac{1}{L_{eq}} [-r_{eq} (I_b + \tilde{i}_b) - (V_{c1} + \tilde{v}_{c1}) - (D + \tilde{d}) \cdot (V_{dc} + \tilde{v}_{dc}) + (V_b + \tilde{v}_b)] \\ \frac{d}{dt} (V_{c1} + \tilde{v}_{c1}) = \frac{1}{C_1} [(I_b + \tilde{i}_b) - \frac{V_{c1} + \tilde{v}_{c1}}{R_1}] \end{cases}$$

[5.2]

The dynamic model of the system at steady state condition becomes

$$\begin{cases} I_{dc} + D \cdot I_b - \left(\frac{V_{dc}}{R} + \frac{P}{V_{dc}} \right) = 0 \\ -r_{eq} \cdot I_b - V_{c1} - D \cdot V_{dc} + V_b = 0 \\ I_b - \frac{V_{c1}}{R_1} = 0 \end{cases} \quad [5.3]$$

Substituting 5.3 into 5.2, the nonlinear equations of the system model becomes

$$\begin{cases} \frac{d}{dt} \tilde{v}_{dc} = \frac{1}{C_{dc}} \left[\tilde{i}_{dc} + D \cdot \tilde{i}_b + I_b \cdot \tilde{d} - \left(\frac{1}{R} - \frac{P}{V_{dc}^2} \right) \tilde{v}_{dc} \right] \\ \frac{d}{dt} \tilde{i}_b = \frac{1}{L_{eq}} \left[-r_{eq} \cdot \tilde{i}_b - \tilde{v}_{c1} - V_{dc} \cdot \tilde{d} - D \cdot \tilde{v}_{dc} + \tilde{v}_b \right] \\ \frac{d}{dt} \tilde{v}_{c1} = \frac{1}{C_1} \left[\tilde{i}_b - \frac{1}{R_1} \tilde{v}_{c1} \right] \end{cases} \quad [5.4]$$

Applying Laplace Transform to transfer the equations from time domain to S domain, the equations 5.4 in S domain become

$$\begin{cases} S \tilde{v}_{dc} = \frac{1}{C_{dc}} \left[\tilde{i}_{dc} + D \cdot \tilde{i}_b + I_b \cdot \tilde{d} - \left(\frac{1}{R} - \frac{P}{V_{dc}^2} \right) \tilde{v}_{dc} \right] \\ S \tilde{i}_b = \frac{1}{L_{eq}} \left[-r_{eq} \cdot \tilde{i}_b - \tilde{v}_{c1} - V_{dc} \cdot \tilde{d} - D \cdot \tilde{v}_{dc} + \tilde{v}_b \right] \\ S \tilde{v}_{c1} = \frac{1}{C_1} \left[\tilde{i}_b - \frac{1}{R_1} \tilde{v}_{c1} \right] \end{cases}$$

And by sorting and rearranging, the new set of equations can be written as

$$\begin{cases} C_{dc} \left(S + \frac{1}{C_{dc}} \left(\frac{1}{R} - \frac{P}{V_{dc}^2} \right) \right) \tilde{v}_{dc} = \tilde{i}_{dc} + D \cdot \tilde{i}_b + I_b \cdot \tilde{d} \\ L_{eq} \left(S + \frac{r_{eq}}{L_{eq}} \right) \tilde{i}_b = -\tilde{v}_{c1} - V_{dc} \cdot \tilde{d} - D \cdot \tilde{v}_{dc} + \tilde{v}_b \\ C_1 \left(S + \frac{1}{R_1 \cdot C_1} \right) \tilde{v}_{c1} = \tilde{i}_b \end{cases} \quad [5.5]$$

To make the equations easy to read and write, these constant variables are considered

$$\begin{cases} \omega_P = \frac{1}{C_{dc}} \left(\frac{1}{R} - \frac{P}{V_{dc}^2} \right) \\ \omega_L = \frac{r_{eq}}{L_{eq}} \\ \omega_B = \frac{1}{R_1 \cdot C_1} \end{cases} \quad [5.6]$$

Then by replacing new variables into 5.5, the set of equations become

$$\begin{cases} C_{dc}(S + \omega_P)\tilde{v}_{dc} = \tilde{i}_{dc} + D \cdot \tilde{i}_b + I_b \cdot \tilde{d} \\ L_{eq}(S + \omega_L)\tilde{i}_b = -\tilde{v}_{c1} - V_{dc} \cdot \tilde{d} - D \cdot \tilde{v}_{dc} + \tilde{v}_b \\ C_1(S + \omega_B)\tilde{v}_{c1} = \tilde{i}_b \end{cases} \quad [5.7]$$

The set of equations in 5.7 characterizes the dynamic model of the DC UPS during mode I in the S domain. Different transfer functions can be achieved from 5.7. To analysis dynamics of DC link voltage and battery current, two set of equations are driven and sorted based on DC link voltage and battery current. The DC link voltage set of equations is

$$\begin{cases} (a_3S^3 + a_2S^2 + a_1S^1 + a_0)\tilde{v}_{dc} = \\ \quad DC_1(S + \omega_B)\tilde{v}_b \\ + [L_{eq}C_1S^2 + L_{eq}C_1(\omega_B + \omega_L)S^1 + L_{eq}C_1\omega_B\omega_L + 1]\tilde{i}_{dc} \\ \quad + (b_2S^2 + b_1S^1 + b_0)\tilde{d} \end{cases} \quad [5.8]$$

and equations based on battery current are

$$\begin{cases} (a_3S^3 + a_2S^2 + a_1S^1 + a_0)\tilde{i}_b = \\ \quad [C_1C_{dc}S^2 + C_1C_{dc}(\omega_B + \omega_P)S^1 + C_{dc}C_1\omega_B\omega_P]\tilde{v}_b \\ \quad - [f_2S^2 + f_1S^1 + f_0]\tilde{d} \\ \quad - DC_1(S + \omega_B)\tilde{i}_{dc} \end{cases} \quad [5.9]$$

where the coefficients are defined as

$$\begin{cases} a_3 = L_{eq}C_1C_{dc} \\ a_2 = L_{eq}C_{dc}C_1(\omega_B + \omega_L + \omega_P) \\ a_1 = L_{eq}C_{dc}C_1(\omega_B\omega_L + \omega_L\omega_P + \omega_B\omega_P) + C_{dc} + D^2C_1 \\ a_0 = L_{eq}C_{dc}C_1\omega_B\omega_L\omega_P + C_{dc}\omega_P + D^2C_1\omega_B \end{cases} \quad [5.10]$$

and

$$\begin{cases} b_2 = I_bL_{eq}C_1 \\ b_1 = I_bL_{eq}C_1(\omega_B + \omega_L) - DV_{dc}C_1 \\ b_0 = I_bL_{eq}C_1\omega_B\omega_L + I_b - DV_{dc}C_1\omega_B \end{cases} \quad [5.11]$$

and

$$\begin{cases} f_2 = V_{dc}C_{dc}C_1 \\ f_1 = V_{dc}C_{dc}C_1(\omega_B + \omega_P) + I_bDC_1 \\ f_0 = V_{dc}C_{dc}C_1\omega_B\omega_P + I_bDC_1\omega_B \end{cases} \quad [5.12]$$

Equations 5.8 and 5.9 present the DC link voltage and battery current dynamics based on battery voltage, grid current and duty ratio of the DC-DC converter. Then transfer functions of DC link voltage versus each of variables will be achieved by ignoring the effect of other two variables.

Here, the goal is to find the dynamics of the DC link voltage based on the disturbances from duty ratio of the DC/DC converter, battery voltage and grid current, see figure 5.1, or to find the transfer functions, $G_{vd}(s)$, $G_{vv}(s)$ and $G_{vi}(s)$, in the following equation.

$$\tilde{v}_{dc}(s) = G_{vd}(s).\tilde{d}(s) + G_{vv}(s).\tilde{v}_b(s) + G_{vi}(s).\tilde{i}_{dc}(s)$$

The set of equations in 5.8 and 5.9 give adequate information to extract different transfer functions. Based on the 5.8 and 5.9, transfer functions of DC link voltage versus duty ratio, battery voltage and grid current can be achieved as below.

$$G_{vd}(s) = \frac{\tilde{v}_{dc}}{\tilde{d}} \Big|_{\substack{\tilde{v}_b=0 \\ \tilde{i}_{dc}=0}} = \frac{b_2 s^2 + b_1 s^1 + b_0}{a_3 s^3 + a_2 s^2 + a_1 s^1 + a_0} \quad [5.13]$$

$$G_{vv}(s) = \frac{\tilde{v}_{dc}}{\tilde{v}_b} \Big|_{\substack{\tilde{d}=0 \\ \tilde{i}_{dc}=0}} = \frac{DC_1(s+\omega_B)}{a_3 s^3 + a_2 s^2 + a_1 s^1 + a_0} \quad [5.14]$$

$$G_{vi}(s) = \frac{\tilde{v}_{dc}}{\tilde{i}_{dc}} \Big|_{\substack{\tilde{d}=0 \\ \tilde{v}_b=0}} = \frac{Leq C_1 s^2 + Leq C_1 (\omega_B + \omega_L) s^1 + Leq C_1 \omega_B \omega_L + 1}{a_3 s^3 + a_2 s^2 + a_1 s^1 + a_0} \quad [5.15]$$

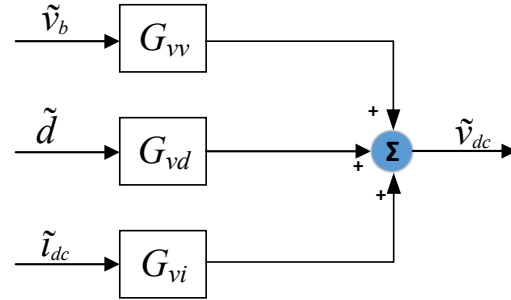


Figure 5.1: The DC link voltage affected by battery voltage, duty ratio of the DC/DC converter and grid current.

The transfer functions of the battery current versus duty ratio, battery voltage and grid current can be achieved as below.

$$G_{id}(s) = \frac{\tilde{i}_b}{\tilde{d}} \Big|_{\substack{\tilde{v}_b=0 \\ \tilde{i}_{dc}=0}} = \frac{-[f_2 s^2 + f_1 s^1 + f_0]}{a_3 s^3 + a_2 s^2 + a_1 s^1 + a_0} \quad [5.16]$$

$$G_{iv}(s) = \frac{\tilde{i}_b}{\tilde{v}_b} \Big|_{\substack{\tilde{d}=0 \\ \tilde{i}_{dc}=0}} = \frac{C_1 C_{dc} s^2 + C_1 C_{dc} (\omega_B + \omega_P) s^1 + C_{dc} C_1 \omega_B \omega_P}{a_3 s^3 + a_2 s^2 + a_1 s^1 + a_0} \quad [5.17]$$

$$G_{ii}(s) = \frac{\tilde{i}_b}{\tilde{i}_{dc}} \Big|_{\substack{\tilde{d}=0 \\ \tilde{v}_b=0}} = \frac{-DC_1(s+\omega_B)}{a_3 s^3 + a_2 s^2 + a_1 s^1 + a_0} \quad [5.18]$$

By having the transfer function, it is possible to find the stability region of the system during this mode of operation. The stability analysis can be performed by applying Routh-

Hurwitz stability criterion which gives the necessary and sufficient condition for the stability of a LTI system.

To find the stability region, it's required to find the characteristic equation, $\Delta(s)$, of the system which is the denominator of the transfer function, and then to establish the Routh table to determine if the system is stable. Based on the Routh-Hurwitz stability criterion, system is stable if and only if, all the coefficients at the first column of the table is positive.

First, the characteristic equation:

$$\Delta(s) = a_3S^3 + a_2S^2 + a_1S^1 + a_0$$

Then the Routh table:

S^3	a_3	a_1	0
S^2	a_2	a_0	0
S^1	\det_{31}	\det_{32}	0
S^0	\det_{41}	\det_{42}	0

From 5.10,

$$a_3 = L_{eq}C_1C_{dc} > 0$$

$$a_2 = L_{eq}C_{dc}C_1(\omega_B + \omega_L + \omega_P) > 0 \rightarrow \omega_B + \omega_L + \omega_P > 0$$

From 5.6,

$$\begin{aligned} \frac{1}{R_1.C_1} + \frac{r_{eq}}{L_{eq}} + \frac{1}{C_{dc}}\left(\frac{1}{R} - \frac{P}{V_{dc}^2}\right) > 0 &\rightarrow \frac{1}{C_{dc}}\left(\frac{1}{R} - \frac{P}{V_{dc}^2}\right) > -\frac{1}{R_1.C_1} - \frac{r_{eq}}{L_{eq}} \\ P < \frac{V_{dc}^2}{R} + C_{dc}V_{dc}^2\left(\frac{1}{R_1.C_1} + \frac{r_{eq}}{L_{eq}}\right) \end{aligned} \quad [5.19]$$

$$\det_{31} = -\frac{\begin{vmatrix} a_3 & a_1 \\ a_2 & a_0 \end{vmatrix}}{a_2} = \frac{a_1a_2 - a_0a_3}{a_2} > 0 \rightarrow a_1a_2 - a_0a_3 > 0$$

$$(\omega_B + \omega_L)\omega_P^2 + \left(\omega_B^2 + 2\omega_B\omega_L + \omega_L^2 + \frac{D^2}{L_{eq}C_{dc}} \right) \omega_P + \left(\omega_B^2\omega_L + \omega_L^2\omega_B + \frac{\omega_B}{L_{eq}C_1} + \frac{\omega_L}{L_{eq}C_1} + \frac{\omega_L D^2}{L_{eq}C_1} \right) > 0 \quad [5.20]$$

And

$$\omega_B^2 + 2\omega_B\omega_L + \omega_L^2 + \frac{D^2}{L_{eq}C_{dc}} > 0 \quad \text{always positive}$$

$$\omega_B^2\omega_L + \omega_L^2\omega_B + \frac{\omega_B}{L_{eq}C_1} + \frac{\omega_L}{L_{eq}C_1} + \frac{\omega_L D^2}{L_{eq}C_1} > 0 \quad \text{always positive}$$

Equation 5.20 is a second order polynomial based on ω_P in which all the coefficients are positive, then the statement in 5.20 is always positive and true.

$$\det_{32} = -\frac{\begin{vmatrix} a_3 & 0 \\ a_2 & 0 \end{vmatrix}}{a_2} = 0$$

$$\det_{41} = -\frac{\begin{vmatrix} a_2 & a_0 \\ \det_{31} & \det_{32} \end{vmatrix}}{\det_{31}} = a_0 > 0 \rightarrow (L_{eq}C_{dc}C_1\omega_B\omega_L + C_{dc})\omega_P + D^2C_1\omega_B > 0$$

$$P < \frac{V_{dc}^2}{R} + \frac{D^2V_{dc}^2}{R_1+r_{eq}} \quad [5.21]$$

Considering non-equivalent equations in 5.19 and 5.21,

$$P_{max} = \min \left\{ \frac{V_{dc}^2}{R} + C_{dc}V_{dc}^2 \left(\frac{1}{R_1C_1} + \frac{r_{eq}}{L_{eq}} \right), \frac{V_{dc}^2}{R} + \frac{D^2V_{dc}^2}{R_1+r_{eq}} \right\} \quad [5.22]$$

This is the necessary and sufficient stability condition for the open loop system, when the equation in 5.22 is satisfied. This equation basically states that the open loop system is

stable if the power of the constant power load, represented by P , stays under than power of the constant voltage load, represented by the term $\frac{v_{dc}^2}{R}$, plus extra terms due to the battery and DC/DC converter.

On the other side, if the power of the constant power load, P , is greater than the power of constant voltage load, $P_{CVL} = \frac{v_{dc}^2}{R}$ and the extra term, the system is unstable and a robust controller is required to be designed to keep the system stable.

Figures 5.2 to 5.5 illustrate the stability region of the open loop system against variation of DC link voltage (v_{dc}), constant voltage load (R), equivalent series resistance of the DC/DC converter inductances plus the battery internal resistance (r_{eq}), and the duty ratio (D), respectively.

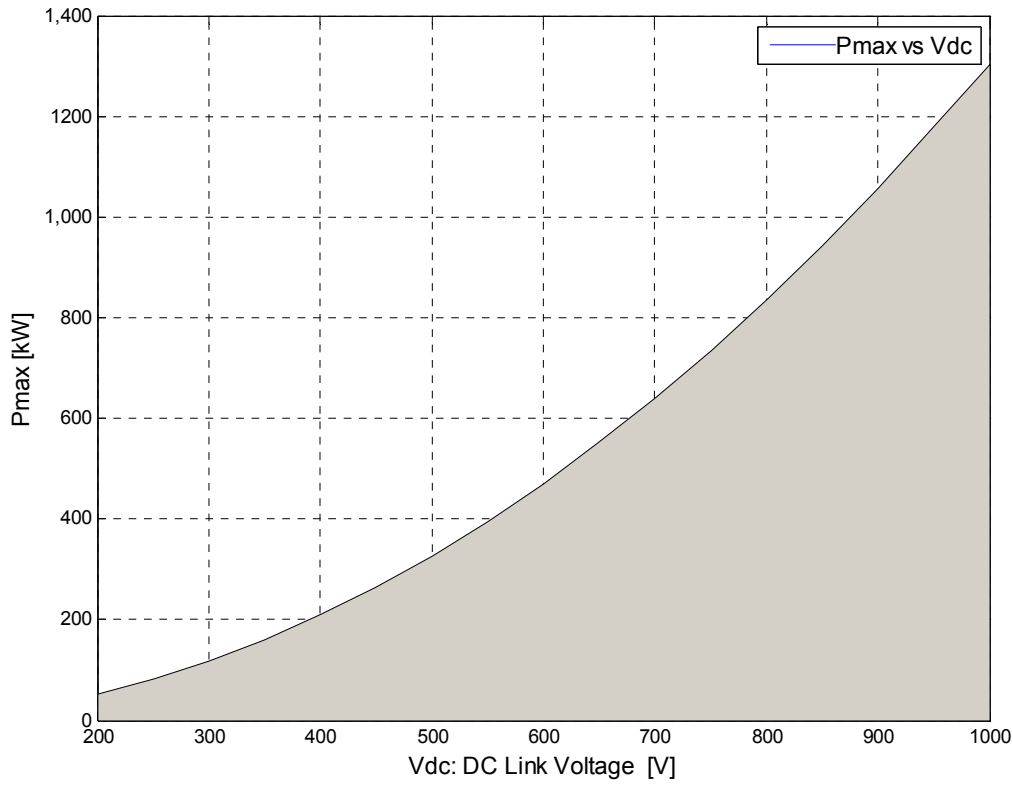


Figure 5.2: Stability region of the open loop system while DC link voltage (v_{dc}) varies.

Figure 5.2 shows the stability region of the open loop system with variation of the DC link voltage. Based on the equation 5.22, there is an exponential relation between the P_{max} and the DC link voltage, v_{dc} . Increasing the link voltage expands the stability region.

Figure 5.3 shows the stability zone for the open loop system while the constant voltage load, represented by R , varies from 20 Ohm to 200 Ohm which is equal to a variation of the power from 2.4 kW to 25 kW. By increasing the R , the CVL power ($P_{CVL} = \frac{v_{dc}^2}{R}$) is decreased and consequently the stability region becomes smaller.

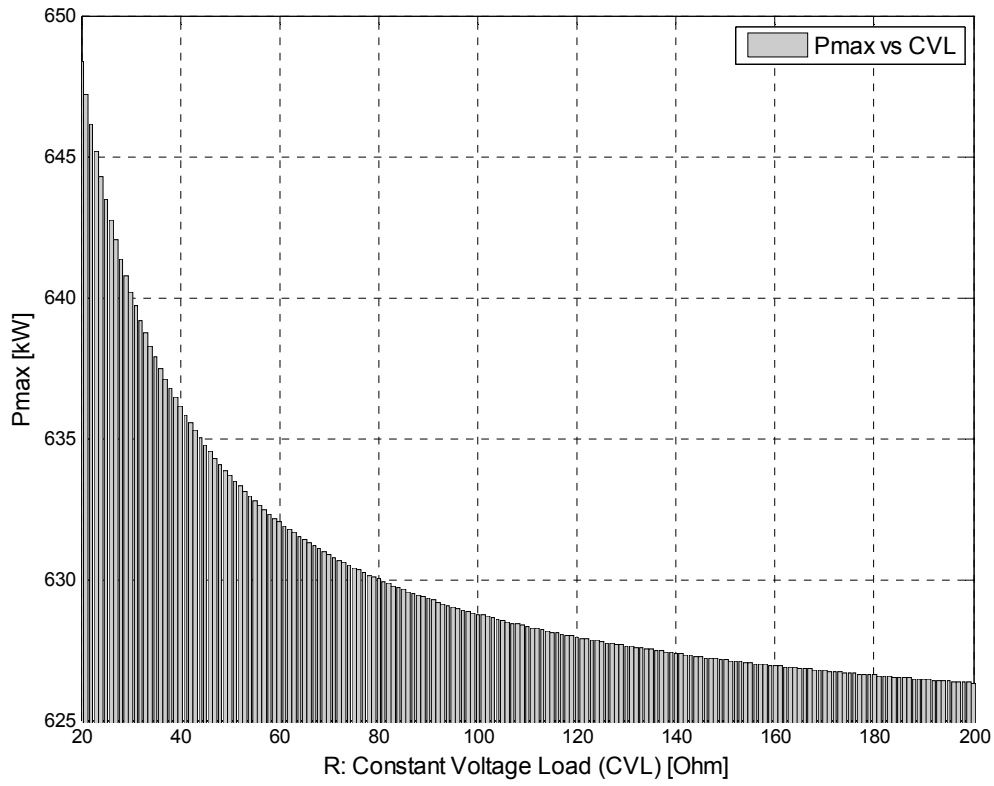


Figure 5.3: Stability region of the open loop system while constant voltage load (CVL) varies.

Stability region of the open loop system is also affected by ESR of the inductances and internal resistance of the battery pack, totally represented by r_{eq} . Figure 5.4 depicts the stability region by variation of the r_{eq} . The curve has two sections, a linear part due to the

$\frac{r_{eq}}{L_{eq}}$ term, and a nonlinear part due to the $\frac{1}{R_1+r_{eq}}$ term.

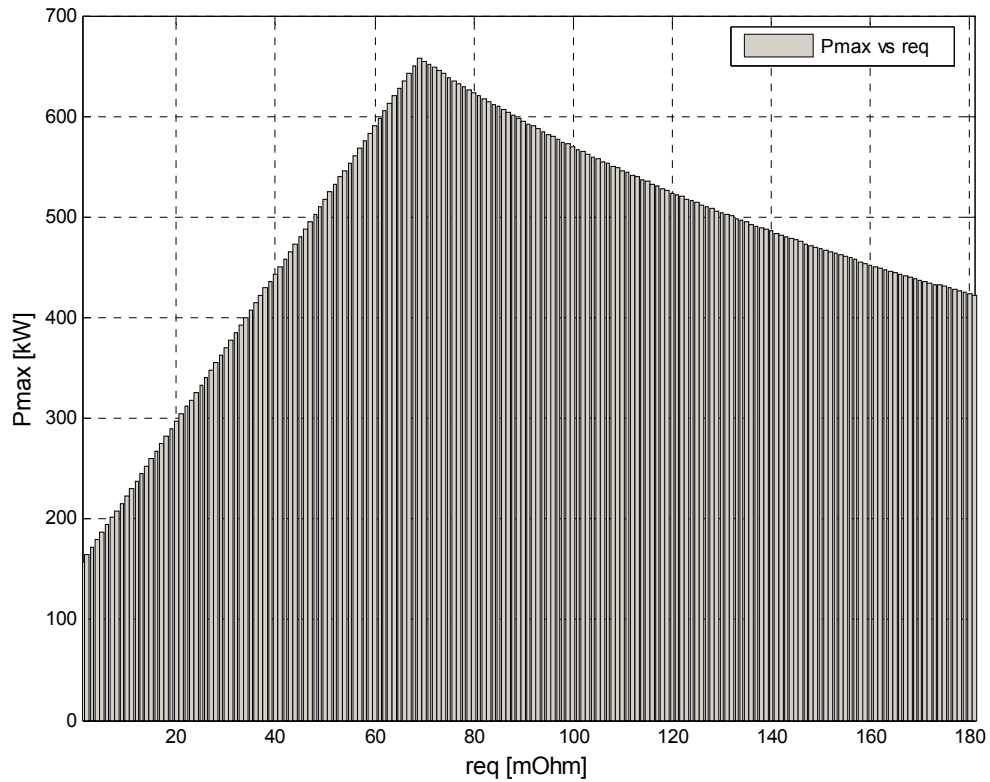


Figure 5.4: Stability region of the open loop system while equivalent resistant (r_{eq}) varies.

Variation of the DC/DC converter duty ratio on the stability region is presented in figure 5.5. By increasing the duty ratio, the stability region is expanded up to 55%, and saturated afterwards, means that by increasing the duty ratio more than 55%, the Pmax stays the same since the first term in the equation 5.22 becomes the minimum of the statement and it does not affect by the duty ratio.

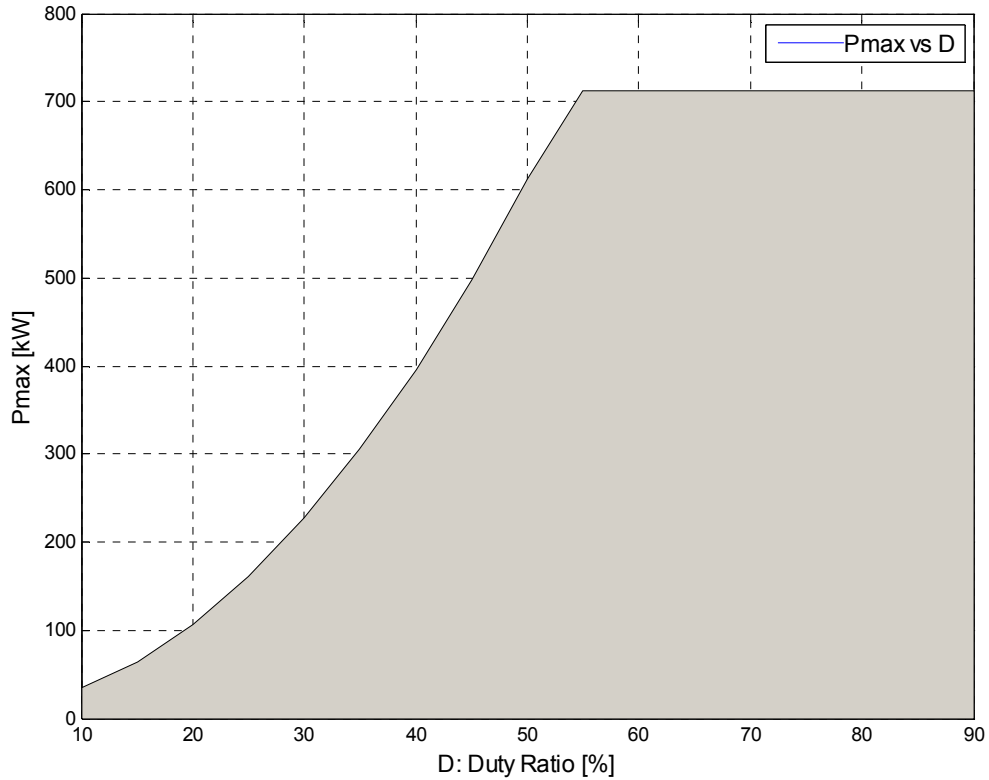


Figure 5.5: Stability region of the open loop system while duty ratio of the DC/DC converter (D) varies.

5.3 Stability Analysis of the System During Mode II

State space averaging model of the system during this mode is presented at chapter 4 where the set of equations 4.32 mathematically characterized dynamic model of the system during standby mode.

$$\begin{cases} \frac{d}{dt} v_{dc}(t) = \frac{1}{c_{dc}} \left[i_{dc}(t) + d(t) \cdot i_b(t) - \frac{v_{dc}(t)}{R} \right] \\ \frac{d}{dt} i_b(t) = \frac{1}{L_{eq}} [-r_{eq} i_b(t) - v_{c1}(t) - d(t) \cdot v_{dc}(t) + v_b(t)] \\ \frac{d}{dt} v_{c1}(t) = \frac{1}{c_1} [i_b(t) - \frac{v_{c1}(t)}{R_1}] \end{cases} \quad [4.32]$$

The 4.32 ignores the ESR of the C_{dc} , so by considering the R_c , the set of equations representing the system during mode II becomes

$$\begin{cases} \frac{d}{dt}v_c(t) = \frac{1}{C_{dc}} \left[\frac{R}{R+R_c} i_{dc}(t) + d(t) \frac{R}{R+R_c} i_b(t) - \frac{1}{R+R_c} v_c(t) \right] \\ \frac{d}{dt}i_b(t) = \frac{1}{L_{eq}} \left[(-r_{eq} - d(t)R_c \frac{R}{R+R_c}) i_b(t) - v_{c1}(t) - d(t) \frac{R}{R+R_c} v_c(t) + v_b(t) - d(t)R_c \frac{R}{R+R_c} i_{dc}(t) \right] \\ \frac{d}{dt}v_{c1}(t) = \frac{1}{C_1} \left[i_b(t) - \frac{v_{c1}(t)}{R_1} \right] \\ v_{dc}(t) = v_c(t) + R_c i_c(t) = v_c(t) + R_c C_{dc} \frac{d}{dt} v_c(t) \end{cases}$$

[5.23]

Where $v_c(t)$ is voltage across the DC link capacitor, C_{dc} and $v_{dc}(t)$ is the DC link voltage.

In 5.23 since $R \gg R_c$ then $\frac{R}{R+R_c} \approx \frac{R}{R} = 1$ then 5.23 becomes

$$\begin{cases} \frac{d}{dt}v_c(t) = \frac{1}{C_{dc}} \left[i_{dc}(t) + d(t)i_b(t) - \frac{1}{R+R_c} v_c(t) \right] \\ \frac{d}{dt}i_b(t) = \frac{1}{L_{eq}} \left[(-r_{eq} - d(t)R_c)i_b(t) - v_{c1}(t) - d(t)v_c(t) + v_b(t) - d(t)R_c i_{dc}(t) \right] \\ \frac{d}{dt}v_{c1}(t) = \frac{1}{C_1} \left[i_b(t) - \frac{v_{c1}(t)}{R_1} \right] \\ v_{dc}(t) = v_c(t) + R_c C_{dc} \frac{d}{dt} v_c(t) \end{cases}$$

[5.24]

Equations in 5.24 characterized the dynamic model of the system during mode II of operation. Like the previous section, these are nonlinear equations and need to be linearized. Considering small perturbations in the state variables due to small disturbances in the duty ratio and input signals.

$$\begin{cases} v_{dc} = V_{dc} + \tilde{v}_{dc} \\ i_b = I_b + \tilde{i}_b \\ v_{c1} = V_{c1} + \tilde{v}_{c1} \\ v_b = V_b + \tilde{v}_b \\ d = D + \tilde{d} \\ i_{dc} = I_{dc} + \tilde{i}_{dc} \\ v_c = V_c + \tilde{v}_c \end{cases} \quad [5.25]$$

Where the variables in capital letters are operating points or average values of corresponding variables. By replacing 5.25 into 5.24, the small signal model of the system achieved as

$$\begin{cases} \frac{d}{dt}(V_c + \tilde{v}_c) = \frac{1}{C_{dc}} [(I_{dc} + \tilde{i}_{dc}) + (D + \tilde{d})(I_b + \tilde{i}_b) - \frac{V_c + \tilde{v}_c}{R + R_c}] \\ \frac{d}{dt}(I_b + \tilde{i}_b) = \frac{1}{L_{eq}} [(-r_{eq} - (D + \tilde{d}(t))R_c)(I_b + \tilde{i}_b) - (V_{c1} + \tilde{v}_{c1}) - (D + \tilde{d})(V_c + \tilde{v}_c) + (V_b + \tilde{v}_b) - (D + \tilde{d}(t))R_c(I_{dc} + \tilde{i}_{dc})] \\ \frac{d}{dt}(V_{c1} + \tilde{v}_{c1}) = \frac{1}{C_1} [(I_b + \tilde{i}_b) - \frac{V_{c1} + \tilde{v}_{c1}}{R_1}] \end{cases} \quad [5.26]$$

The dynamic model of the system at steady state condition during this mode is obtained as

$$\begin{cases} I_{dc} + D \cdot I_b - \frac{V_c}{R + R_c} = 0 \\ (-r_{eq} - DR_c)I_b - V_{c1} - D \cdot V_c + V_b - DR_c I_{dc} = 0 \\ I_b - \frac{V_{c1}}{R_1} = 0 \end{cases} \quad [5.27]$$

Substituting 5.27 into 5.26, the nonlinear equations of the system model becomes

$$\begin{cases} \frac{d}{dt} \tilde{v}_c = \frac{1}{C_{dc}} \left[\tilde{i}_{dc} + D\tilde{i}_b + I_b \tilde{d} - \frac{\tilde{v}_c}{R+R_c} \right] \\ \frac{d}{dt} \tilde{i}_b = \frac{1}{L_{eq}} \left[(-r_{eq} - DR_c) \tilde{i}_b - (R_c I_b + V_c + R_c I_{dc}) \tilde{d} - \tilde{v}_{c1} - D\tilde{v}_c + \tilde{v}_b - DR_c \tilde{i}_{dc} \right] \\ \frac{d}{dt} \tilde{v}_{c1} = \frac{1}{C_1} \left[\tilde{i}_b - \frac{1}{R_1} \tilde{v}_{c1} \right] \end{cases}$$

[5.28]

Applying Laplace Transform to transfer the equations from time domain to S domain, equations 5.28 in S domain become

$$\begin{cases} S\tilde{v}_c = \frac{1}{C_{dc}} \left[\tilde{i}_{dc} + D \cdot \tilde{i}_b + I_b \cdot \tilde{d} - \frac{\tilde{v}_c}{R + R_c} \right] \\ S\tilde{i}_b = \frac{1}{L_{eq}} \left[(-r_{eq} - DR_c) \tilde{i}_b - (R_c I_b + V_c + R_c I_{dc}) \tilde{d} - \tilde{v}_{c1} - D\tilde{v}_c + \tilde{v}_b - DR_c \tilde{i}_{dc} \right] \\ S\tilde{v}_{c1} = \frac{1}{C_1} \left[\tilde{i}_b - \frac{1}{R_1} \tilde{v}_{c1} \right] \end{cases}$$

And by sorting and rearranging, the new set of equations can be written as

$$\begin{cases} C_{dc} \left(S + \frac{1}{C_{dc}} \frac{1}{R+R_c} \right) \tilde{v}_c = \tilde{i}_{dc} + D\tilde{i}_b + I_b \tilde{d} \\ L_{eq} \left(S + \frac{r_{eq}}{L_{eq}} + \frac{DR_c}{L_{eq}} \right) \tilde{i}_b = -(R_c I_b + V_c + R_c I_{dc}) \tilde{d} - \tilde{v}_{c1} - D\tilde{v}_c + \tilde{v}_b - DR_c \tilde{i}_{dc} \\ C_1 \left(S + \frac{1}{R_1 \cdot C_1} \right) \tilde{v}_{c1} = \tilde{i}_b \end{cases}$$

[5.29]

In order to make the equations easy to read and write, these constant variables are considered

$$\begin{cases} \omega_{P2} = \frac{1}{C_{dc}} \frac{1}{R+R_c} \\ \omega_{L2} = \frac{r_{eq}}{L_{eq}} + \frac{DR_c}{L_{eq}} \\ \omega_B = \frac{1}{R_1 \cdot C_1} \end{cases} \quad [5.30)$$

Then by replacing new variables into 5.29, the set of equations become

$$\begin{cases} C_{dc}(S + \omega_{P2})\tilde{v}_c = \tilde{i}_{dc} + D\tilde{i}_b + I_b\tilde{d} \\ L_{eq}(S + \omega_{L2})\tilde{i}_b = -(R_c I_b + V_c + R_c I_{dc})\tilde{d} - \tilde{v}_{c1} - D\tilde{v}_c + \tilde{v}_b - DR_c \tilde{i}_{dc} \\ C_1(S + \omega_B)\tilde{v}_{c1} = \tilde{i}_b \end{cases} \quad [5.31]$$

The set of equations in 5.31 characterizes the dynamic model of the DC UPS during mode II in the S domain. Different transfer functions can be achieved from 5.31. In order to analysis dynamics of DC link voltage and battery current, two set of equations are driven and sorted based on DC link voltage and battery current. The DC link voltage set of equations is

$$\begin{cases} (a_{32}S^3 + a_{22}S^2 + a_{12}S^1 + a_{02})\tilde{v}_c = \\ \quad DC_1(S + \omega_B)\tilde{v}_b \\ + [L_{eq}C_1S^2 + (L_{eq}C_1(\omega_B + \omega_{L2}) - D^2R_cC_1)S^1 + L_{eq}C_1\omega_B\omega_{L2} + 1 - D^2R_cC_1\omega_B] \tilde{i}_{dc} \\ + [(b_{22}S^2 + b_{12}S^1 + b_{02})\tilde{d}] \end{cases} \quad [5.32]$$

(5.32) and equations based on battery current are

$$\begin{cases} (a_{32}S^3 + a_{22}S^2 + a_{12}S^1 + a_{02})\tilde{i}_b = \\ \quad [C_1C_{dc}S^2 + C_1C_{dc}(\omega_B + \omega_{P2})S^1 + C_{dc}C_1\omega_B\omega_{P2}] \tilde{v}_b \\ - [f_2S^2 + f_1S^1 + f_0]\tilde{d} \\ - [DR_cC_{dc}C_1S^2 + (DR_cC_{dc}C_1(\omega_B + \omega_{P2}) + DC_1)S + DR_cC_{dc}C_1\omega_B\omega_{P2} + DC_1\omega_B] \tilde{i}_{dc} \end{cases} \quad [5.33]$$

(5.33) where the coefficients are defined as

$$\begin{cases} a_{32} = L_{eq} C_1 C_{dc} \\ a_{22} = L_{eq} C_{dc} C_1 (\omega_B + \omega_{L2} + \omega_{P2}) \\ a_{12} = L_{eq} C_{dc} C_1 (\omega_B \omega_{L2} + \omega_{L2} \omega_{P2} + \omega_B \omega_{P2}) + C_{dc} + D^2 C_1 \\ a_{02} = L_{eq} C_{dc} C_1 \omega_B \omega_{L2} \omega_{P2} + C_{dc} \omega_{P2} + D^2 C_1 \omega_B \end{cases} \quad [5.34]$$

and

$$\begin{cases} b_{22} = I_b L_{eq} C_1 \\ b_{12} = I_b L_{eq} C_1 (\omega_B + \omega_{L2}) - k D C_1 \\ b_{02} = I_b L_{eq} C_1 \omega_B \omega_{L2} + I_b - k D C_1 \omega_B \\ k = R_c I_b + V_c + R_c I_{dc} \end{cases} \quad [5.35]$$

and

$$\begin{cases} f_2 = k C_{dc} C_1 \\ f_1 = k C_{dc} C_1 (\omega_B + \omega_{P2}) + I_b D C_1 \\ f_0 = k C_{dc} C_1 \omega_B \omega_{P2} + I_b D C_1 \omega_B \end{cases} \quad [5.36]$$

Equations 5.32 and 5.33 present the DC link voltage and battery current dynamics based on battery voltage, grid current and duty ratio of the DC-DC converter. Then transfer functions of DC link voltage versus each of variables will be achieved by ignoring the effect of other two variables.

The set of equations in 5.32 and 5.33 give adequate information to extract different transfer functions. Based on the 5.32 and 5.33, transfer functions of DC link voltage versus duty ratio, battery voltage and grid current can be achieved as below.

$$G_{vd}(s) = \frac{\tilde{v}_c}{\tilde{d}} \Big| \begin{matrix} \tilde{v}_b=0 \\ \tilde{I}_{dc}=0 \end{matrix} = \frac{b_{22}s^2 + b_{12}s^1 + b_{02}}{a_{32}s^3 + a_{22}s^2 + a_{12}s^1 + a_{02}} \quad [5.37]$$

$$G_{vv}(s) = \frac{\tilde{v}_c}{\tilde{v}_b} \Big| \begin{matrix} \tilde{d}=0 \\ \tilde{I}_{dc}=0 \end{matrix} = \frac{D C_1 (s + \omega_B)}{a_{32}s^3 + a_{22}s^2 + a_{12}s^1 + a_{02}} \quad [5.38]$$

$$G_{vi}(s) = \frac{\tilde{v}_c}{\tilde{i}_{dc}} \Big|_{\tilde{d}=0} = \frac{DR_c C_{dc} C_1 S^2 + (DR_c C_{dc} C_1 (\omega_B + \omega_{P2}) + DC_1)S + DR_c C_{dc} C_1 \omega_B \omega_{P2} + DC_1 \omega_B}{a_{32} S^3 + a_{22} S^2 + a_{12} S^1 + a_{02}}$$

[5.39]

The transfer functions of the battery current versus duty ratio, battery voltage and grid current can be achieved as below.

$$G_{id}(s) = \frac{\tilde{i}_b}{\tilde{d}} \Big|_{\tilde{v}_b=0} = -\frac{f_2 S^2 + f_1 S^1 + f_0}{a_{32} S^3 + a_{22} S^2 + a_{12} S^1 + a_{02}}$$

[5.40]

$$G_{iv}(s) = \frac{\tilde{i}_b}{\tilde{v}_b} \Big|_{\tilde{i}_{dc}=0} = \frac{C_1 C_{dc} S^2 + C_1 C_{dc} (\omega_B + \omega_{P2}) S^1 + C_{dc} C_1 \omega_B \omega_{P2}}{a_{32} S^3 + a_{22} S^2 + a_{12} S^1 + a_{02}}$$

[5.41]

$$G_{ii}(s) = \frac{\tilde{i}_b}{\tilde{i}_{dc}} \Big|_{\tilde{d}=0} = -\frac{DR_c C_{dc} C_1 S^2 + (DR_c C_{dc} C_1 (\omega_B + \omega_{P2}) + DC_1)S + DR_c C_{dc} C_1 \omega_B \omega_{P2} + DC_1 \omega_B}{a_{32} S^3 + a_{22} S^2 + a_{12} S^1 + a_{02}}$$

[5.42]

In order to find the DC link voltage transfer functions, from the last equation in 5.29

$$v_{dc}(t) = v_c(t) + R_c C_{dc} \frac{d}{dt} v_c(t)$$

[5.43]

By applying small perturbation in the equation and using Laplace transform

$$\tilde{v}_{dc} + V_{dc} = \tilde{v}_c + V_c + R_c C_{dc} S (\tilde{v}_c + V_c)$$

[5.44]

Considering the steady state condition, in which

$$V_{dc} = V_c$$

[5.45]

Then by replacing 5.45 in 5.44

$$\widetilde{v_{dc}} = R_c C_{dc} \left(S + \frac{1}{R_c C_{dc}} \right) \widetilde{v_c} = R_c C_{dc} (S + \omega_c) \widetilde{v_c} \quad [5.46]$$

Where $\omega_c = \frac{1}{R_c C_{dc}}$. By replacing 5.32 with 5.46, the DC link voltage equation based on the states obtained as:

$$\begin{cases} (a_3 S^3 + a_2 S^2 + a_1 S^1 + a_0) \widetilde{v_{dc}} = \\ \quad D R_c C_{dc} C_1 (S^2 + (\omega_c + \omega_B) S + \omega_c \omega_B) \widetilde{v_b} \\ \quad + \left[L_{eq} R_c C_{dc} C_1 S^3 + R_c C_{dc} (L_{eq} C_1 \omega_c + L_{eq} C_1 (\omega_B + \omega_{L2}) - D^2 R_c C_1) S^2 + R_c C_{dc} (L_{eq} C_1 \omega_B \omega_{L2} + \right. \\ \quad \left. 1 - D^2 R_c C_1 \omega_B + \omega_c (L_{eq} C_1 (\omega_B + \omega_{L2}) - D^2 R_c C_1) S + R_c C_{dc} \omega_c (L_{eq} C_1 \omega_B \omega_{L2} + 1 - D^2 R_c C_1 \omega_B) \right] \widetilde{i_{dc}} \\ \quad + [b_{33} S^3 + b_{23} S^2 + b_{13} S^1 + b_{03}] \tilde{d} \end{cases} \quad [5.47]$$

where

$$\begin{cases} b_{33} = R_c C_{dc} b_{22} \\ b_{23} = R_c C_{dc} (b_{12} + b_{22} \omega_c) \\ b_{13} = R_c C_{dc} (b_{02} + b_{12} \omega_c) \\ b_{03} = R_c C_{dc} b_{02} \omega_c \end{cases} \quad [5.48]$$

Equations 5.47 are used to extract transfer functions of the DC link voltage versus duty ratio, battery terminal voltage and grid current.

By having the transfer function, it is possible to find the stability region of the system during this mode of operation. The stability analysis can be performed by applying Routh-Hurwitz stability criterion which gives the necessary and sufficient condition for the stability of a LTI system.

In order to find the stability region, it's required to find the characteristic equation, $\Delta(s)$, of the system which is the denominator of the transfer function, and then to establish the Routh table to determine if the system is stable. Based on the Routh-Hurwitz stability

criterion, system are stable if and only if, all the coefficients at the first column of the table is positive.

First, the characteristic equation:

$$\Delta(s) = a_{32}s^3 + a_{22}s^2 + a_{12}s^1 + a_{02}$$

Then the Routh table

S^3	a_{32}	a_{12}	0
S^2	a_{22}	a_{02}	0
S^1	\det_{31}	\det_{32}	0
S^0	\det_{41}	\det_{42}	0

From 5.34,

$$\begin{aligned}
 a_{32} &= L_{eq}C_1C_{dc} > 0 \\
 a_{22} &= L_{eq}C_{dc}C_1(\omega_B + \omega_{L2} + \omega_{P2}) > 0 \rightarrow \omega_B + \omega_{L2} + \omega_{P2} > 0 \\
 \rightarrow \frac{1}{R_1C_1} + \frac{r_{eq}}{L_{eq}} + \frac{DR_c}{L_{eq}} + \frac{1}{C_{dc}(R_c+R)} &> 0 \text{ Always true!} \\
 a_{12} &= L_{eq}C_{dc}C_1(\omega_B\omega_{L2} + \omega_{L2}\omega_{P2} + \omega_B\omega_{P2}) + C_{dc} + D^2C_1 > 0 \text{ Always true!} \\
 \det_{31} &= -\frac{\begin{vmatrix} a_{32} & a_{12} \\ a_{22} & a_{02} \end{vmatrix}}{a_{22}} = \frac{a_{12}a_{22} - a_{02}a_{32}}{a_{22}} > 0 \rightarrow a_{12}a_{22} - a_{02}a_{32} > 0 \\
 \rightarrow (L_{eq}C_{dc}C_1(\omega_B\omega_{L2} + \omega_{L2}\omega_{P2} + \omega_B\omega_{P2}) + C_{dc} \\
 &\quad + D^2C_1)(L_{eq}C_{dc}C_1(\omega_B + \omega_{L2} + \omega_{P2})) \\
 &\quad - (L_{eq}C_{dc}C_1\omega_B\omega_{L2}\omega_{P2} + C_{dc}\omega_{P2} + D^2C_1\omega_B)(L_{eq}C_1C_{dc}) > 0 \\
 (\omega_B + \omega_{L2})\omega_{P2}^2 + \left(2\omega_B\omega_{L2} + \frac{D^2}{L_{eq}C_{dc}} + \omega_B^2 + \omega_{L2}^2\right)\omega_{P2} + \left(\omega_B^2\omega_{L2} + \frac{\omega_B}{L_{eq}C_{dc}} + \omega_{L2}^2\omega_B + \frac{\omega_{L2}}{L_{eq}C_{dc}} + \frac{\omega_{L2}D^2}{L_{eq}C_{dc}}\right) &> 0 \quad \text{Always true!} \tag{5.49}
 \end{aligned}$$

Equation 5.49 is a second order polynomial based on ω_{P2} in which all the coefficients are positive, then the statement in 5.49 is always positive and true.

$$\det_{32} = -\frac{\begin{vmatrix} a_{32} & 0 \\ a_{22} & 0 \end{vmatrix}}{a_{22}} = 0$$

$$det_{41} = - \frac{\begin{vmatrix} a_2 & a_0 \\ det_{31} & det_{32} \end{vmatrix}}{det_{31}} = a_0 > 0 \rightarrow L_{eq} C_{dc} C_1 \omega_B \omega_{L2} \omega_{P2} + C_{dc} \omega_{P2} + D^2 C_1 \omega_B > 0$$

[5.50]

Then since all the coefficients in the characteristics equation are positive, the system during this mode is stable.

5.4 Stability Analysis of the System During Mode III

Mode III is extension of modes II. During mode II when the BESS is fully charged the system becomes a regular grid tied AC/DC rectifier providing power for the light CVL load. The rectifier operates on voltage mode to regulate the DC link voltage and provides required active power for the CVL.

From 5.24,

$$\left\{ \begin{array}{l} \frac{d}{dt} v_c(t) = \frac{1}{C_{dc}} \left[i_{dc}(t) + d(t)i_b(t) - \frac{1}{R+R_c} v_c(t) \right] \\ \frac{d}{dt} i_b(t) = \frac{1}{L_{eq}} [(-r_{eq} - d(t)R_c)i_b(t) - v_{c1}(t) - d(t)v_c(t) + v_b(t) - d(t)R_c i_{dc}(t)] \\ \frac{d}{dt} v_{c1}(t) = \frac{1}{C_1} \left[i_b(t) - \frac{v_{c1}(t)}{R_1} \right] \\ v_{dc}(t) = v_c(t) + R_c C_{dc} \frac{d}{dt} v_c(t) \end{array} \right.$$

[5.24]

Since during this mode, the BESS is fully charged, there will be no current flow between battery and DC link so the converter switches are open and the equations in 5.24 are adjusted accordingly.

$$\begin{cases} \frac{d}{dt}v_c(t) = \frac{1}{C_{dc}} \left[i_{dc}(t) - \frac{1}{R+R_c} v_c(t) \right] \\ \frac{d}{dt}i_b(t) = \frac{1}{L_{eq}} [-v_{c1}(t) + v_b(t)] \\ \frac{d}{dt}v_{c1}(t) = \frac{1}{C_1} \left[-\frac{v_{c1}(t)}{R_1} \right] \\ v_{dc}(t) = v_c(t) + R_c C_{dc} \frac{d}{dt} v_c(t) \end{cases} \quad [5.51]$$

According to equation 4.30 from chapter 4, and the fact that the grid voltage vector is aligned with d axis and performing unity power factor,

$$i_{dc}(t) = \frac{3}{2} m_d i_d(t) \quad [5.52]$$

Substituting 5.52 in 5.51, the system model becomes

$$\begin{cases} \frac{d}{dt}v_c(t) = \frac{1}{C_{dc}} \left[\frac{3}{2} m_d i_d(t) - \frac{1}{R+R_c} v_c(t) \right] \\ v_{dc}(t) = v_c(t) + R_c C_{dc} \frac{d}{dt} v_c(t) \end{cases} \quad [5.53]$$

Then by applying small signal stability analysis on 5.53, the small signal model is achieved as

$$\frac{d}{dt}(V_c + \tilde{v}_c) = \frac{1}{C_{dc}} \left[\frac{3}{2} (M_d + \tilde{m}_d)(I_d + \tilde{i}_d) - \frac{V_c + \tilde{v}_c}{R+R_c} \right] \quad [5.54]$$

By ignoring second order items, the small signal model becomes

$$\frac{d}{dt}\tilde{v}_c = \frac{1}{C_{dc}} \left[\frac{3}{2} (M_d \tilde{i}_d + I_d \tilde{m}_d) - \frac{\tilde{v}_c}{R+R_c} \right] \quad [5.55]$$

Applying Laplace transformation, 5.55 becomes

$$C_{dc}(S + \omega_{P2})\tilde{v}_c = \frac{3}{2} M_d \tilde{i}_d + \frac{3}{2} I_d \tilde{m}_d \quad [5.56]$$

And from 5.46,

$$\widetilde{v_{dc}} = R_c C_{dc} \left(S + \frac{1}{R_c C_{dc}} \right) \widetilde{v_c} = R_c C_{dc} (S + \omega_c) \widetilde{v_c} \quad [5.57]$$

Replacing 5.57 into 5.56, the small signal model of the system during mode III becomes

$$(S + \omega_{P2}) \widetilde{v_{dc}} = \frac{3}{2} M_d R_C (S + \omega_c) \widetilde{i_d} + \frac{3}{2} I_d R_C (S + \omega_c) \widetilde{m_d} \quad [5.58]$$

Equation 5.58 describes the small signal dynamic model of the system during this mode which explains that transients in the DC link voltage causes due to disturbances from the modulation factor of AC/DC converter and the direct component of the grid current. All the poles and zeros of the equation 5.58 are placed at left hand side of the S plane, meaning the system is stable during this mode.

5.5 Stability Analysis of the System During Mode IV

When the grid is disconnected, the system operates on mode IV, the UPS mode. This mode can be considered as an extension of mode I without grid power when BESS provides entire pulsed peak power for the CPL load and the DC/DC converter regulates the DC link voltage. The grid current does not have any effect on the stability of the system in this mode, as it is shown in equation 5.22, below is the steps to drive the transfer function of the DC link voltage versus DC/DC converter's duty ratio and battery voltage.

From 4.31, and removing grid current, the system model described as

$$\begin{cases} \frac{d}{dt} v_{dc}(t) = \frac{1}{C_{dc}} \left[d(t) \cdot i_b(t) - \left(\frac{v_{dc}(t)}{R} + \frac{P}{v_{dc}(t)} \right) \right] \\ \frac{d}{dt} i_b(t) = \frac{1}{L_{eq}} [-r_{eq} i_b(t) - v_{c1}(t) - d(t) \cdot v_{dc}(t) + v_b(t)] \\ \frac{d}{dt} v_{c1}(t) = \frac{1}{C_1} [i_b(t) - \frac{v_{c1}(t)}{R_1}] \end{cases} \quad [5.59]$$

By performing small signal analysis,

$$\begin{cases} \frac{d}{dt} \tilde{v}_{dc} = \frac{1}{C_{dc}} \left[D \cdot \tilde{i}_b + I_b \cdot \tilde{d} - \left(\frac{1}{R} - \frac{P}{V_{dc}^2} \right) \tilde{v}_{dc} \right] \\ \frac{d}{dt} \tilde{i}_b = \frac{1}{L_{eq}} [-r_{eq} \tilde{i}_b - \tilde{v}_{c1} - V_{dc} \cdot \tilde{d} - D \cdot \tilde{v}_{dc} + \tilde{v}_b] \\ \frac{d}{dt} \tilde{v}_{c1} = \frac{1}{C_1} [\tilde{i}_b - \frac{1}{R_1} \tilde{v}_{c1}] \end{cases} \quad [5.60]$$

Applying Laplace transformer,

$$\begin{cases} C_{dc}(S + \omega_P) \tilde{v}_{dc} = D \cdot \tilde{i}_b + I_b \cdot \tilde{d} \\ L_{eq}(S + \omega_L) \tilde{i}_b = -\tilde{v}_{c1} - V_{dc} \cdot \tilde{d} - D \cdot \tilde{v}_{dc} + \tilde{v}_b \\ C_1(S + \omega_B) \tilde{v}_{c1} = \tilde{i}_b \end{cases} \quad [5.61]$$

Finally, the small signal model of the system during this mode is achieved as

$$(a_3 S^3 + a_2 S^2 + a_1 S^1 + a_0) \tilde{v}_{dc} = D C_1 (S + \omega_B) \tilde{v}_b + (b_2 S^2 + b_1 S^1 + b_0) \tilde{d} \quad [5.62]$$

The stability region of the system during this mode is the same as mode I, since the grid current does not have any contribution in the stability condition. Then the stability zone for system during this mode is equal to 5.22 equation.

$$P_{max} = \min \left\{ \frac{V_{dc}^2}{R} + C_{dc} V_{dc}^2 \left(\frac{1}{R_1 \cdot C_1} + \frac{r_{eq}}{L_{eq}} \right), \frac{V_{dc}^2}{R} + \frac{D^2 V_{dc}^2}{R_1 + r_{eq}} \right\}$$

5.6 Control Strategy

In the previous sections in this chapter, open loop transfer functions of the system are extracted and the characteristic equations of the system during each mode are achieved. It has been presented that the system is stable during mode II and III, however transfer functions and characteristic equations have been shown that the system is not stable or has limited stability during mode I and IV. This means that the system needs a reliable controller to stabilize its operation during modes two and four. In general, the controller should be designed in such a way that the system operates stable in all four modes. Moreover, the controller should be robust enough so the system not only operates at operating point, but also works stable in all other operating points. In addition, the controller should provide a continuous and stable performance for the system against disturbances and noises.

General speaking, controllers can be sorted into two major groups, linear and nonlinear. Linear controllers such as PI, PID, lead, lag, etc. are easy to design and provide robust and reliable performance, however tuning the controller parameters could be a challenge. This type of controllers does not need transfer function of the system. Since most of practical systems are nonlinear, in order to use linear controllers, first the system is linearized around an operating points and then linear controllers are used to meet the performance requirements of the system. Since such systems are linearized around a specific operating point, the linear controllers usually provide limited stability around the operating point and are not able to offer a global stable performance for the system. Thus, it is necessary to check the stability of the system in some other points rather than the operating point to ensure the reliability and robustness of the controller.

Nonlinear controllers can deal with nonlinear systems without linearization. However, this type of controller requires an exact transfer function of the system and most of them are sensitive to the model imperfections and components mismatches. Usually to simplify the model of complicated nonlinear system, it is required to ignore some parts and it could cause instability issue for the system performance.

The goal for the controller is to maintain stability and consistent performance of the system during all operational modes in the face of disturbance and modeling imperfection and keep the DC Bus voltage regulated at rated value during mode transitions.

Finding a robust controller that can provide a reliable, stable and continuous performance is a major task in designing a controller. In this section a linear controller will be presented. The controller satisfies the stability conditions and regulate the output voltage.

5.6.1 AC/DC Rectifier Control Scheme

5.6.1.1 Direct Power Control of AC/DC Rectifier

The DC UPS system is connected to the grid through an AC/DC rectifier. The rectifier manages the power flow from grid to the DC link. It is a unidirectional path for the power and current from grid to the DC link. The rectifier controller ensures a continuous and constant power delivered to the link regardless of the link voltage.

The goal for the grid tied AC/DC rectifier is to deliver constant power to the DC link. In order to satisfy the control goal, the rectifier operates on current mode and is controlled by the Direct Power Control (DPC) method [99].

In the direct power control scheme, the direct and quadrature components of the grid currents (i_d and i_q), are used to control active and reactive power independently.

According to the fact that the grid voltage vector (e), is aligned with the d axis in the rotating frame, then the projection of the grid voltage on the q axis will be zero ($v_{qg} = 0$).

Furthermore, the rectifier operates on the unity power factor, which means that the ideal value for the quadrature component of the grid current is zero.

$$\begin{cases} P = \frac{3}{2}(i_d v_{dg} + i_q v_{qg}) = \frac{3}{2} i_d v_{dg} \xrightarrow{v_{dg} \text{ is constant}} i_d^* = \frac{P^*}{\frac{3}{2} v_{dg}} \\ Q = \frac{3}{2}(i_d v_{qg} - i_q v_{dg}) = -\frac{3}{2} i_q v_{dg} \xrightarrow{Q^*=0} i_q^* = 0 \end{cases} \quad [5.63]$$

Block diagram of the rectifier and the control scheme is illustrated in the figure 5.6. In this figure, grid angle, θ , is extracted by PLL block and used by transformation blocks to change grid voltages and currents from abc stationary frame to the dq synchronous rotary frame and vice versa.

The measured currents in dq frame are compared to the set values and a linear PI controller compensates the error. The output subtracts from summation of grid voltage and cross sectional term to set an ideal value for input voltage of the rectifier.

$$\begin{cases} v_d^* = v_{dg} - (k_p + \frac{k_i}{s})(i_d^* - i_d) + \omega L_g i_q(t) \\ v_q^* = v_{qg} - \left(k_p + \frac{k_i}{s}\right)(i_q^* - i_q) - \omega L_g i_q(t) \end{cases} \quad [5.64]$$

The ideal values, then are fed to the PWM generation block to be compared with the reference waveforms. The output of this block is the gate drive pulses for the rectifier.

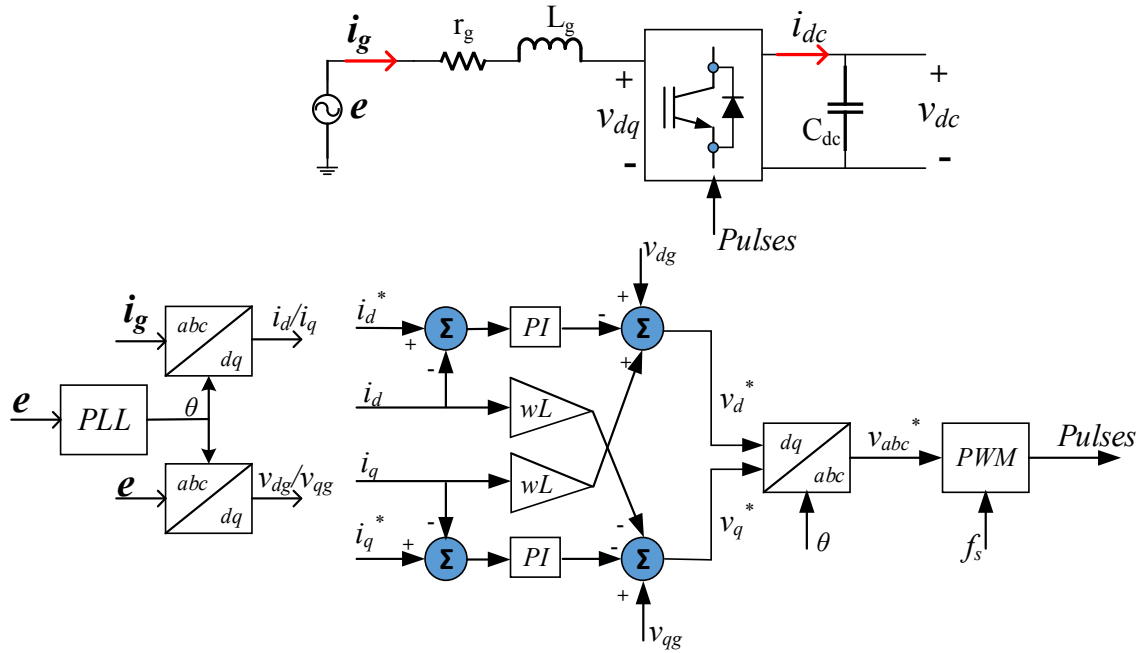


Figure 5.6: Block diagram of the grid tied AC/DC rectifier and controller scheme. Direct Power Control method is used to control the rectifier.

5.6.1.2 Simulation Results

A simulation model is conducted in the MATLAB/Simulink software to illustrate the DPC scheme and performance of the system during some disturbances from load. Figure 5.7 shows the simulation model which is used for this part. The model includes a three-phase power supply connected to an AC/DC rectifier block which controlled by Direct Power Control (DPC) technique. The model also includes a DC/DC converter which connects a battery energy storage to the DC link. The DC/DC converter's controller regulates the link voltage and the DPC control the AC/DC rectifier in such a way to deliver constant power to the link against disturbances come from load.

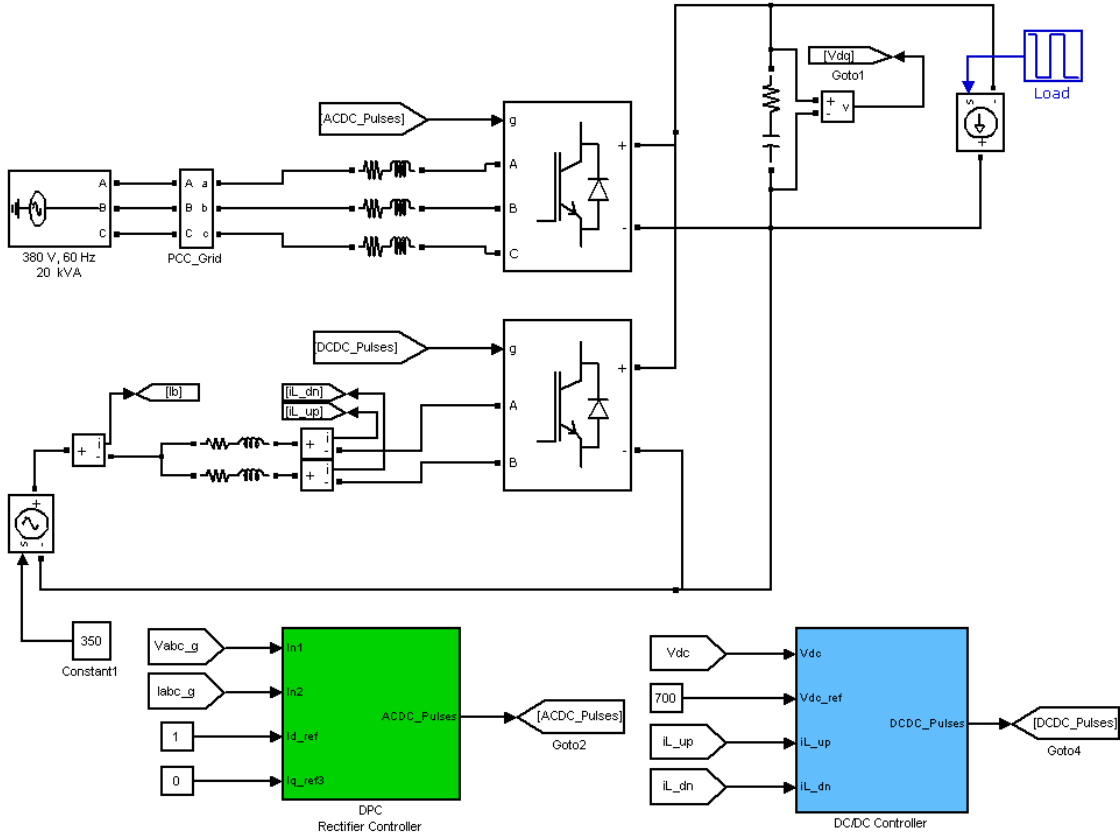


Figure 5.7: DC UPS system used to illustrate the Direct Power Control (DPC) scheme performance while load varies.

Specification of the DC UPS system is presented in the table 5.1.

Table 5.1: DC UPS specifications for the model implemented in the Simulink.

Output Voltage	$P_{Load\ Max}$	L	C	f_{sw}	Grid Power	Battery Voltage
700 V	140 kW	0.2 mH	3 mF	20 kHz	20 kW	350 V

The result is presented in figure 5.8 where the load varies from 0 to 140 kW and the DC link voltage is regulated by the DC/DC converter. The power from grid is 20 kW constant although the load requirement power is changing. The extra required power demand is provided by the battery energy storage system. The power from the grid is constant and continuous at unity power factor (the reactive power from grid is kept zero).

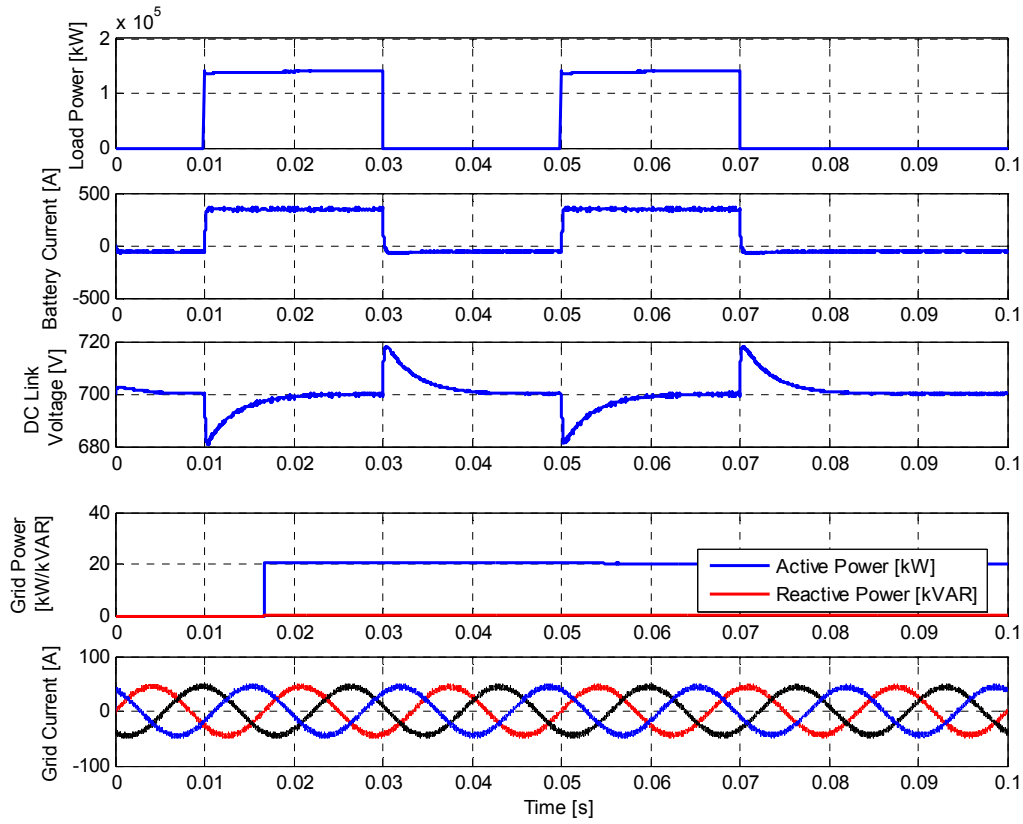


Figure 5.8: The of the DC UPS simulation. The AC/DC rectifier is controlled by direct power control (DPC) method to deliver constant power while the load varies.

5.6.2 DC/DC Power Converter Controller

Since the rectifier is controlled independently and delivers constant power at the DC link, then the grid current has a minority effect on the DC link voltage stability. Moreover, since Li-ion batteries have a very slow rate of voltage change over time while working on operating range (usually between 20% to 90% of SOC), the voltage across the battery terminals do not change suddenly, thus it is reasonable to assume that the battery voltage is constant when dealing with the transients in DC link voltage. These assumptions lead us to the figure 5.9, where a controller closes the loop based on the output voltage and controls the DC link voltage and battery current by changing the duty ratio of the DC/DC converter.

Figure 5.9 shows block diagram of the DC UPS system. A Dual-Loop Control (DLC) scheme has been chosen to stabilize the system performance. The controller consists of two main loops, an inner current loop and an outer voltage loop. The controller can monitor battery current while regulates the DC link voltage. G_{vd} (from equation 5.13), G_{vv} (from equation 5.14), G_{vi} (from equation 5.15) are the transfer functions of DC link voltage versus duty ratio of the DC/DC converter, battery voltage and grid current respectively. G_{id} (from equation 5.16) is the transfer function of battery current versus duty ratio of the converter. G_{ci} and G_{vi} are the compensations which need to be designed appropriately. This figure shows the disturbances from grid current and battery voltage.

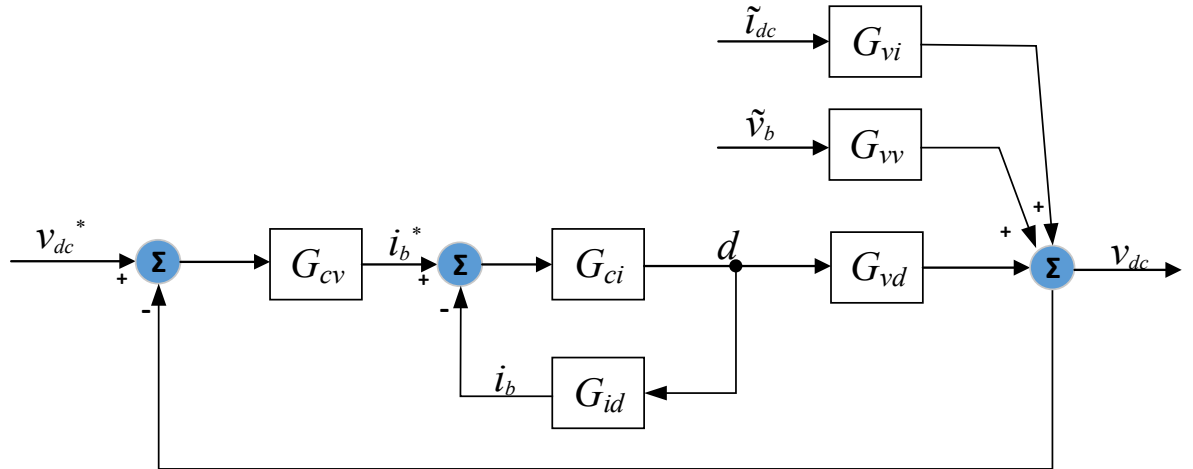


Figure 5.9: Block diagram of the DC UPS system.

The proposed controller has two loops and two compensators, then it required to design the compensators to meet the goals. The goal for the system is to maintain stable and provide a constant and continuous performance in face of disturbances from grid, load and battery. The proposed control scheme consists of two sections, the inner current loop design and the outer voltage loop.

There are several ways to design the compensators, such as desired pole/zero placement, step response or frequency response. In this section, the compensators are designed and tuned based on the frequency response characteristics such as desired phase margin and crossover frequency (w_{wc}). It is desired for the system to have a cross over frequency 5-10 times lower than switching frequency and a phase margin of greater than 40 degree to have enough marginal stability.

Based on the figure 5.9, the open loop transfer function of the inner current loop is achieved as

$$\begin{cases} H_i(s) = G_{ci}(s)G_{id}(s) \\ T_i(s) = \frac{i_b}{i_b^*} = \frac{G_{ci}(s)G_{id}(s)}{1+G_{ci}(s)G_{id}(s)} \end{cases} \quad [5.63]$$

Where the H_i and T_i are the current open loop and closed loop transfer functions, respectively. For the voltage loop transfer functions are as follow:

$$\begin{cases} H_v(s) = \frac{G_{cv}(s)G_{ci}(s)G_{vd}(s)}{1+H_i(s)} \\ T_v(s) = \frac{v_{dc}}{v_{dc}^*} = \frac{G_{cv}(s)G_{ci}(s)G_{vd}(s)}{1+G_{ci}(s)G_{id}(s)+G_{cv}(s)G_{ci}(s)G_{vd}(s)} \end{cases} \quad [5.64]$$

Where the H_v and T_v are the voltage open loop and closed loop transfer functions, respectively. The compensators are PI controller with transfer function in frequency domain such as

$$G_c(jw) = k_p + \frac{k_i}{jw} \quad [5.65]$$

The goal for the system is to have a phase margin not less than 40 degree and a crossover frequency 5 to 10 times below the converter switching frequency for the inner current loop

and to avoid interaction between the inner and outer loop, lower bandwidth is considered for the outer voltage loop to give the system enough stability margin in order to operate in a wide range of operating points. The proportional and integral controller gains k_p and k_i are selected accordingly.

5.6.2.1 Inner Current Loop

Figure 5.10 shows the bode plot of the current open loop gain, the inner loop gain. The figure shows that the open loop system does not have the desired cross over frequency and shows a negative gain margin.

The current controller G_{ci} is designed in such a way to have a cross over frequency 10 times below the switching frequency, which is assumed to be 20 kHz, and a gain margin above 50 degrees. The current compensator is a PI controller with one pole and one zero. The controller gains can be designed based on the desired frequency response characteristics, i.e. phase margin and cross over frequency. The controller transfer function in frequency domain is obtained as:

$$G_{ci}(jw) = k_p + \frac{k_i}{jw}$$

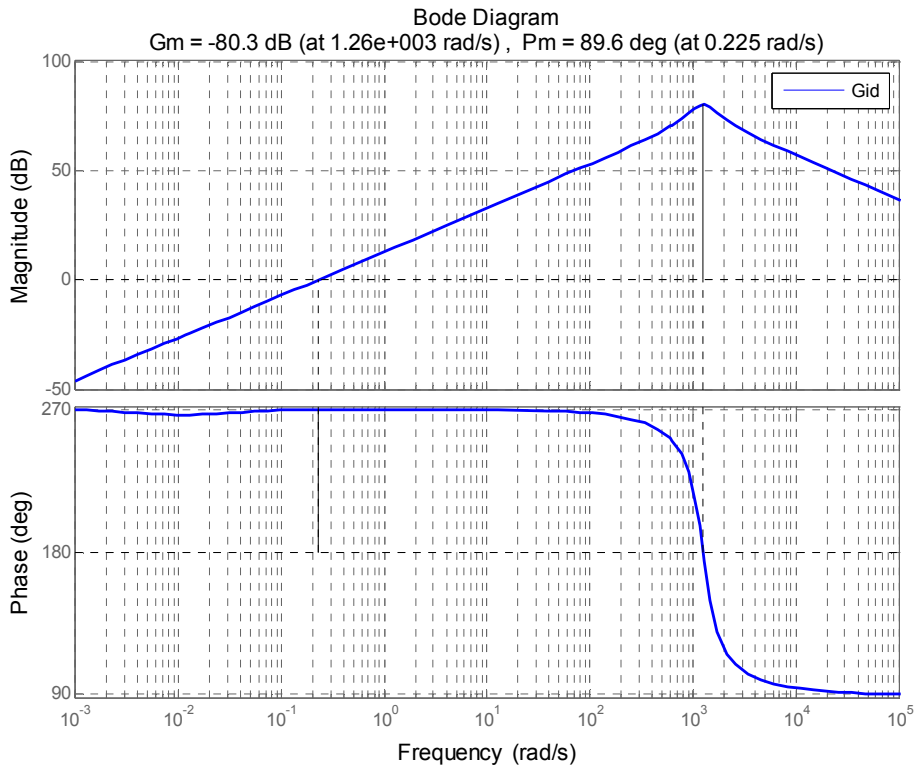


Figure 5.10: Bode diagram of the current open loop gain

Where k_p and k_i are the proportional and integral gains of the compensator. The proportional gain determines the dynamic response of the system and the integral gain adjusts the phase shift between the output and reference. These gains are adjusted based on the open loop bode plots and desired characteristics or based on the equation presented in [29], in which

$$k_p = \frac{\cos \theta}{|G_p(j\omega_{wc})|}$$

$$k_i = \frac{-\omega_{wc} \sin \theta}{|G_p(j\omega_{wc})|}$$

and

$$\theta = 180 + \varphi_d - \angle G_p(j\omega_{wc})$$

Where k_i and k_p are controller proportional and integral gains, ω_{wc} is the desired cross over frequency, φ_d is the required phase margin and G_p is the open loop transfer function, e.g. G_{id} or G_{vd} . Considering a cross over frequency around 2 kHz and a phase margin of 60 degree, figure 5.11 shows the PI controller bode diagrams and the resulted current open loop gain, H_i . This figure illustrates the effect of PI compensator on the current vs duty ratio plant model, G_{id} , and bode diagrams show that the open loop gain has desired frequency response characteristics. The current open loop gain has a cross over frequency of 2 kHz and a phase margin of 60 degrees.

According to the figure 5.11, the gain margin of the H_i is 60 degrees with a cross over frequency at $1.26e4$ rad/s (~ 2 kHz). Since the phase of the open loop gain never cross the -180 degrees, and is always above the -180 degree line, then there is no phase cross over frequency and hence the gain margin is infinite.

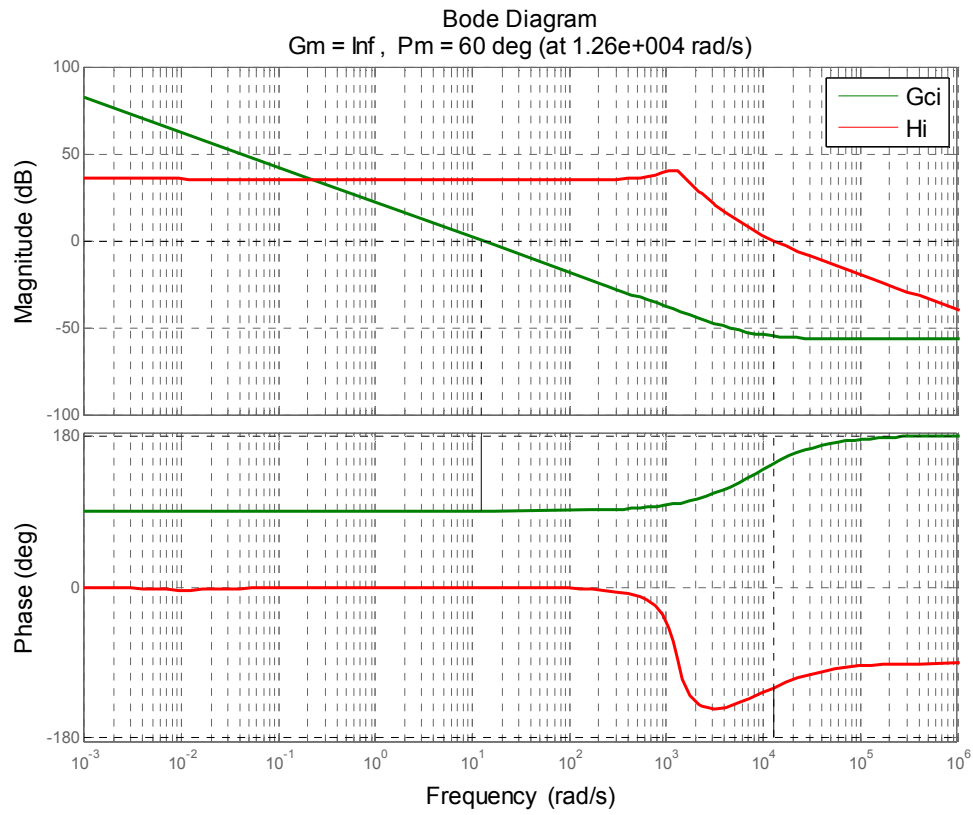


Figure 5.11: Bode diagrams of the PI controller, G_{ci} and the current open loop gain, H_i

5.6.2.2 Outer Voltage Loop

According to the figure 5.9 In order to design the outer voltage controller, first it needs to calculate the middle section, T_i , illustrated in the figure 5.12.

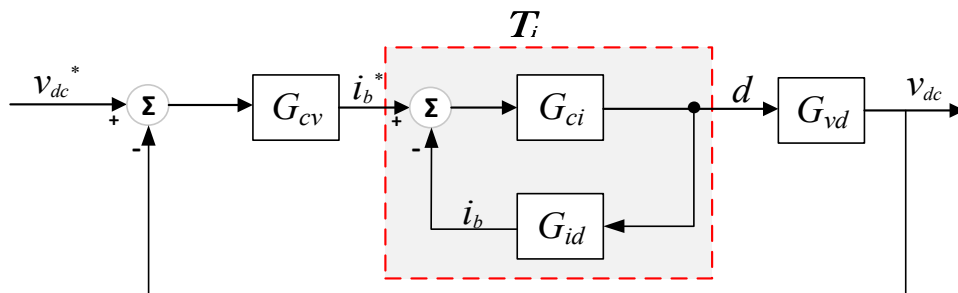


Figure 5.12: The gray area illustrates the current inner loop, T_i

$T_i(s)$ is achieved as:

$$T_i = \frac{d}{i_b^*} = \frac{G_{ci}}{1 + G_{ci}G_{id}}$$

Now the open loop gain of the voltage becomes

$$H_v = G_{cv}T_iG_{vd} = \frac{G_{cv}G_{ci}G_{vd}}{1 + G_{ci}G_{id}}$$

And the voltage closed loop system becomes

$$T_v = \frac{v_{dc}}{v_{dc}^*} = \frac{G_{cv}(s)G_{ci}(s)G_{vd}(s)}{1 + G_{ci}(s)G_{id}(s) + G_{cv}(s)G_{ci}(s)G_{vd}(s)}$$

Figure 5.13 shows the bode diagrams of the voltage open loop plant, G_{vd} . The bode diagrams illustrate that the system has a negative gain and an undesired cross over frequency. The system desired to have a cross over frequency far away from the current loop frequency to avoid any possible interference between two loops, considering the 2 kHz cross over frequency of the inner loop, then the voltage cross over frequency is designed to be around 50 Hz. Also, the voltage loop designed to have 70 degree phase margin at the cross over frequency.

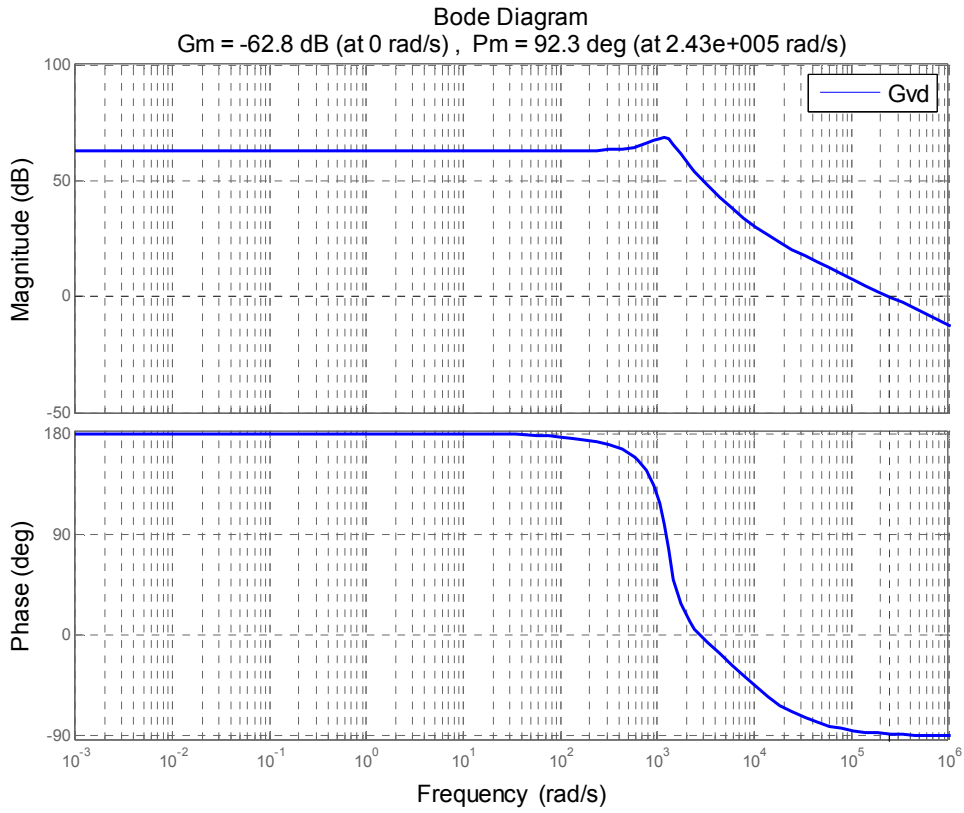


Figure 5.13: Bode diagrams of the voltage open loop plant, G_{vd} .

Transfer function for the voltage compensator is as same as current one, a PI controller with one pole and zero. The controller's gains also designed based on the equation presented in the current section which are matched with the desired frequency response of the system.

$$G_{cv}(jw) = k_p + \frac{k_i}{jw}$$

Figure 5.14 shows the bode diagrams of the designed controller, G_{cv} and the voltage open loop gain, H_v . The bode diagrams show that the open loop gain of voltage has a phase margin of 70 at the cross over frequency of 50 Hz (314 rad/s).

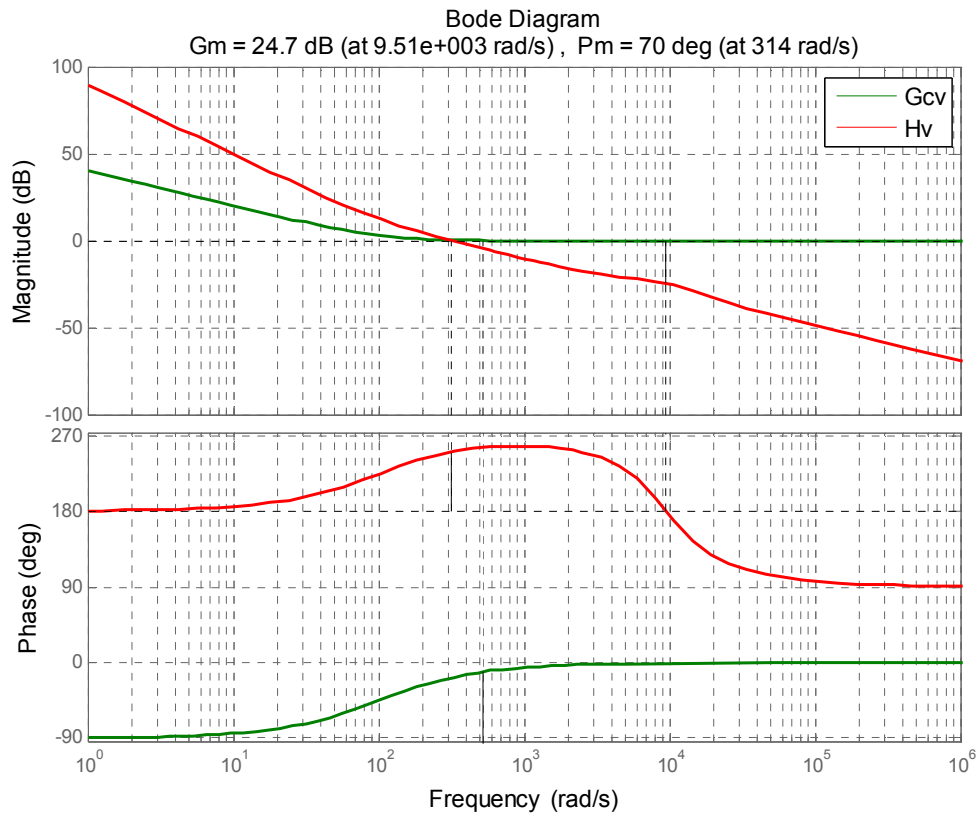


Figure 5.14: Bode diagrams of the voltage compensator, G_{cv} , and the open loop gain, H_v

By closing the loop on output voltage, the system closed loop transfer function, T_v is achieved. Figure 5.15 illustrates the bode diagrams of the closed loop system. The closed loop system has a bandwidth of 400 rad/s.

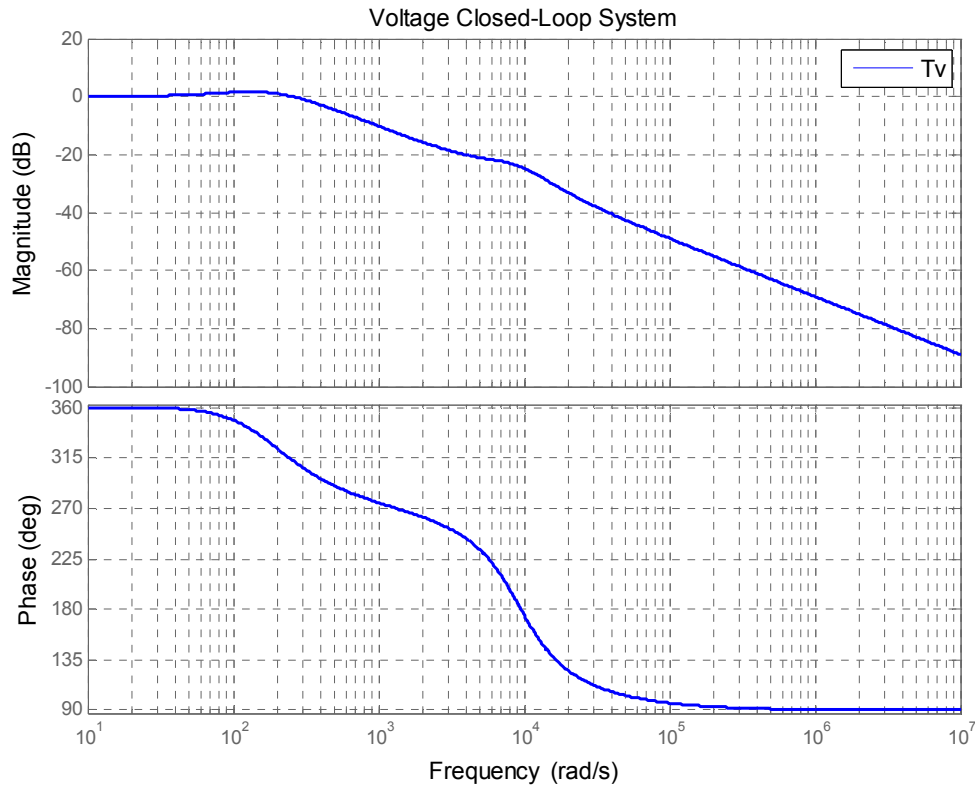


Figure 5.15: The bode diagrams of the closed loop system

The root locus diagram of the closed loop system is illustrated in the figure 5.16. The diagram shows the stability region of the system. As it is illustrated in the figure, system has a limited stability due to a closed loop zero located at the right hand side plane. All the poles are terminated either in a zero or infinite, thus having a zero at right hand side of the S-plane can lead to instability and can limit the stability region of the system. To maintain the system stable with a continuous performance, the controller gains should be designed in such a way to keep the system stable.

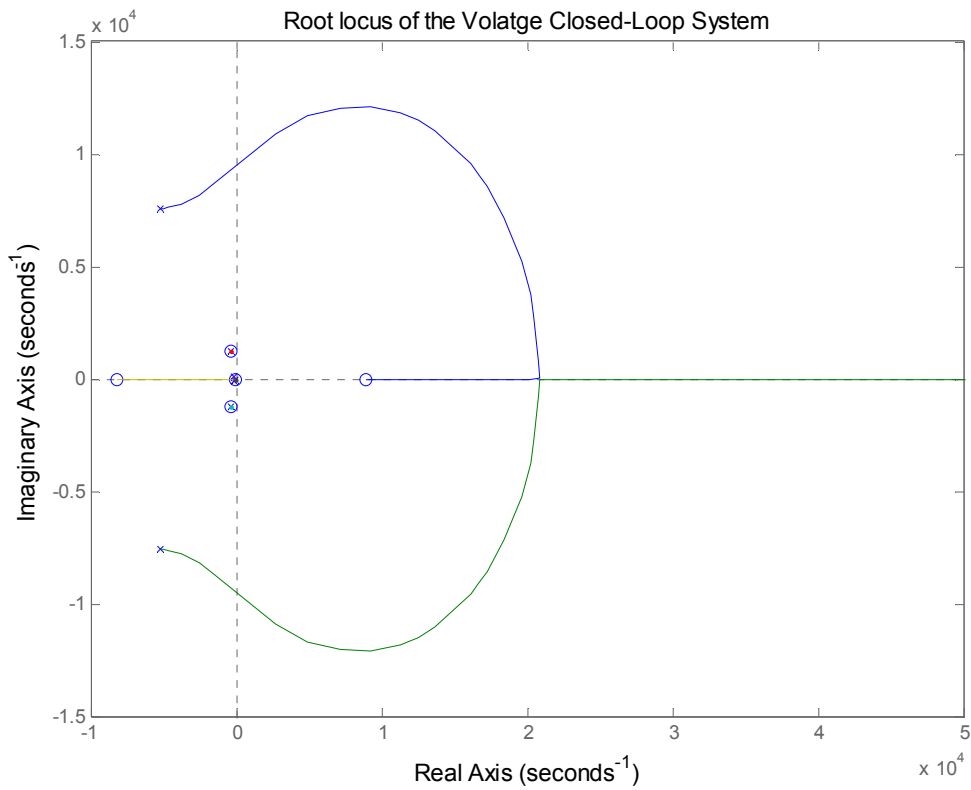


Figure 5.16: The root locus diagram of the closed loop system

By using the Routh-Hurwitz stability criterion, the stability region of the controller can be achieved. The stable zone for inner current loop controller gains are to stay less than zero. The stability region for the outer voltage gains are

$$\begin{cases} k_p < 17 \\ k_i < 8200 \end{cases}$$

By increasing the proportional gain, the complex poles are moving on the root locus from left toward right hand side of the plane, which means by increasing the proportional gain, the complex poles are closing to the imaginary axis and system faces instability. By increasing the integral gain, the pole close to the origin is moving away from the origin

toward left hand side of the plane. Figure 5.17 illustrates the variation on the poles by changing the proportional gain from 1 to 16 and integral gain from 1 to 8000.

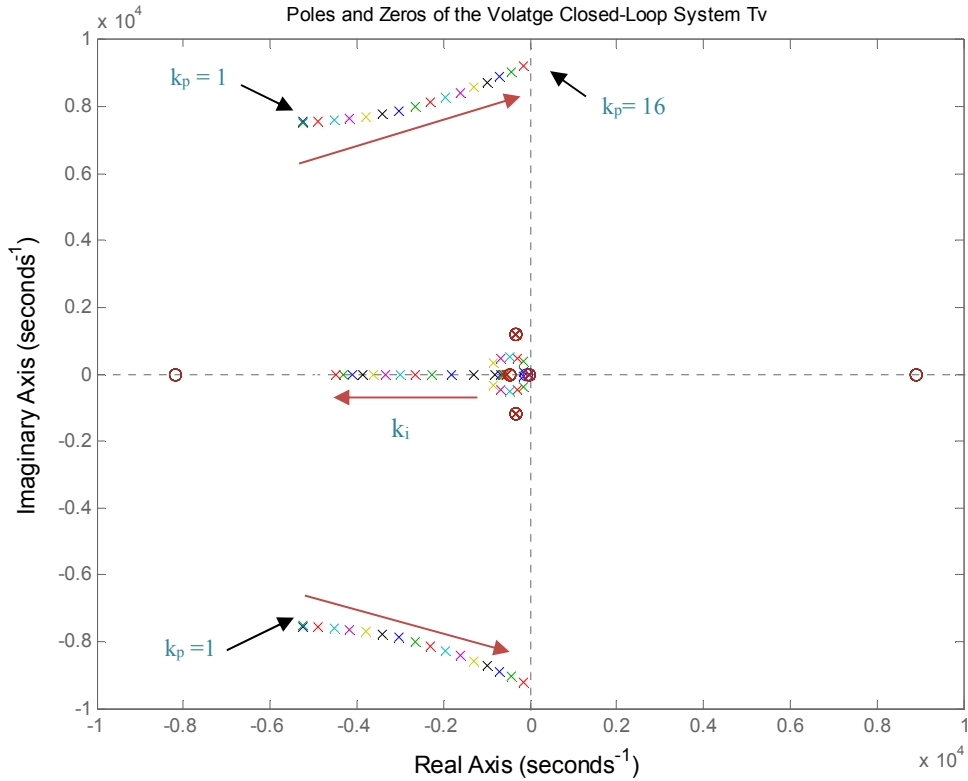


Figure 5.17: By increasing the k_p and k_i , the proportional and integral gains, the complex poles move toward right hand side and the pole close to origin move away from origin toward left hand side.

Figure 5.18 shows that by keeping $k_p = 1$ and increasing k_i more than 17000, the system faces instability as the pole close to origin moves to the right hand side of the plane, see figure 5.18.

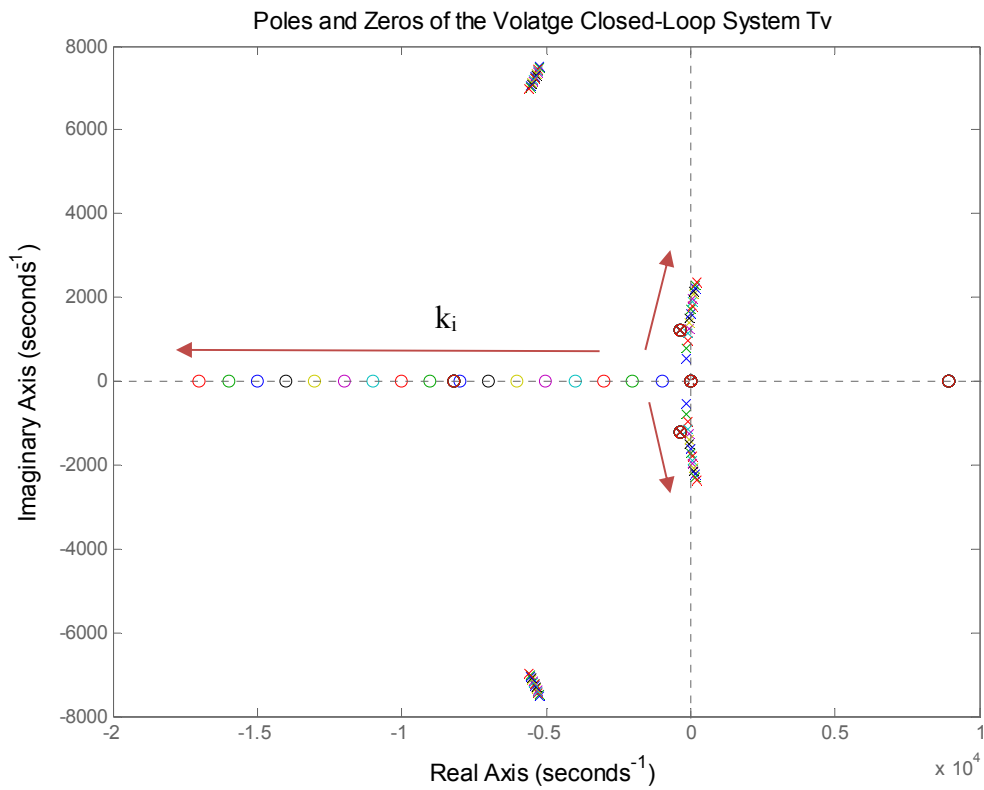


Figure 5.18: $k_p = 1$, and increasing k_i up to 17000, further than its stability zone.

The step response of the closed loop system is presented in the figure 5.19. The step response of the system has a 4.3 ms rise time and settling time of 29 ms.

BY increasing the k_p from 1 to 13 and k_i from 400 to 5200, the step response becomes faster with more overshoot, see figure 5.20.

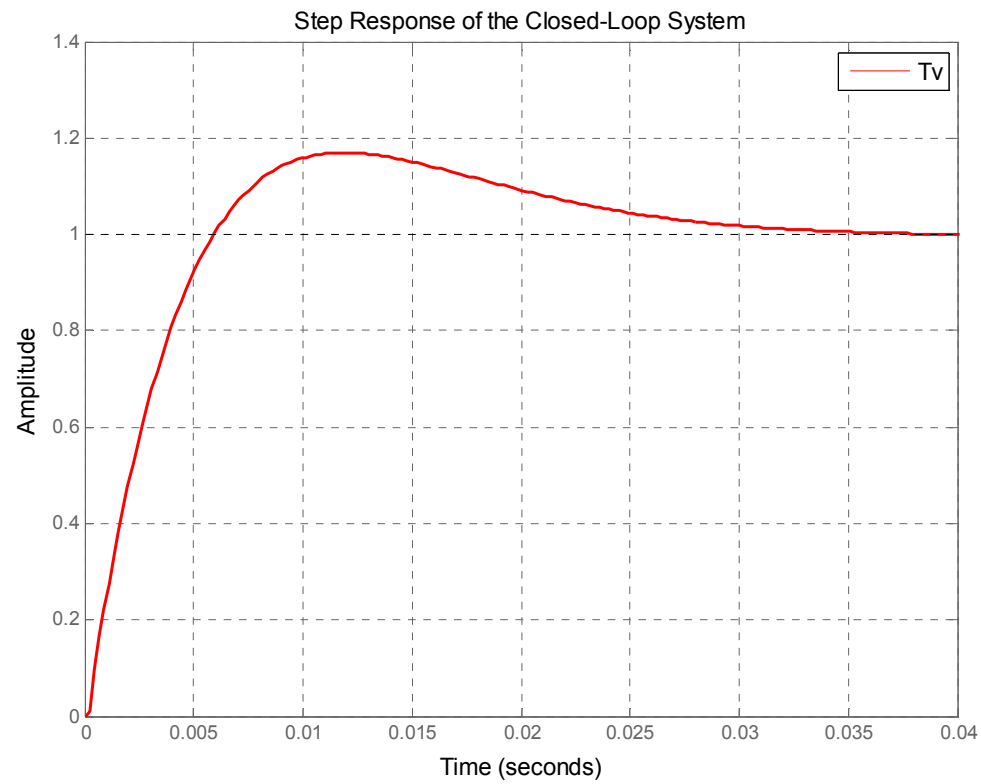


Figure 5.19 Step response of the closed loop system.

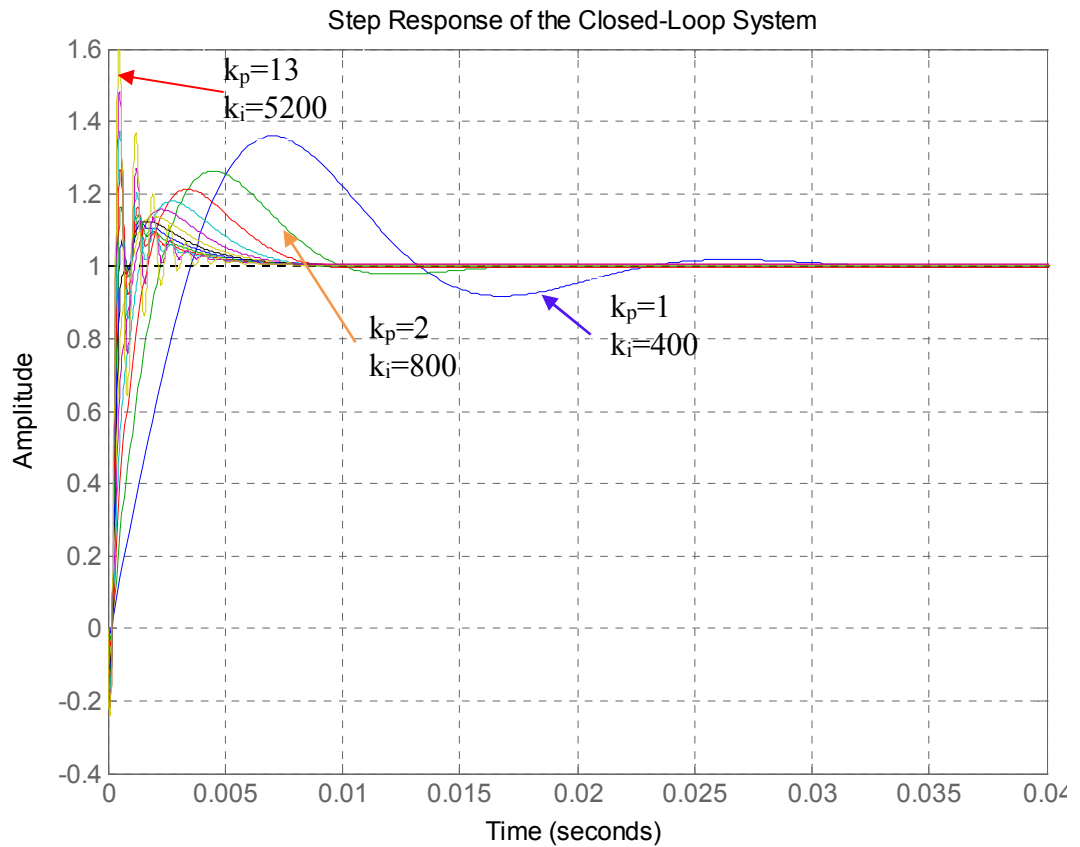


Figure 5.20: By increasing k_p from 1 to 13, and k_i from 1 to 6000, the step response becomes faster with more oscillation.

5.6.2.3 Robustness of the DLC Controller

It is common that a component measured value is different from the value in the system model and sometimes this component mismatch could lead to instability issue. Then robustness against disturbances such as model imperfection, component mismatch or inaccuracy is one of main criteria for the controller to meet. The chosen controller should be able to stabilize system against disturbances and provide the system with constant performance. Capacitors are a good candidate for this regard as their capacity reduces over time. To investigate robustness of the controller against component mismatch, a variation

in the DC link capacitance is considered. It is assumed that the capacitor varies between 0.5 to 2 times of its rated or nominal value. Figure 5.21 illustrates this simulation. When the DC link capacitor changes from 0.5 to 2 times of its nominal value, the complex poles closed to the origin moved toward the imaginary axis, but the system still stable and all the poles are at the left hand side. The figure shows that by increasing the capacitance value, the poles moves toward the imaginary axis.

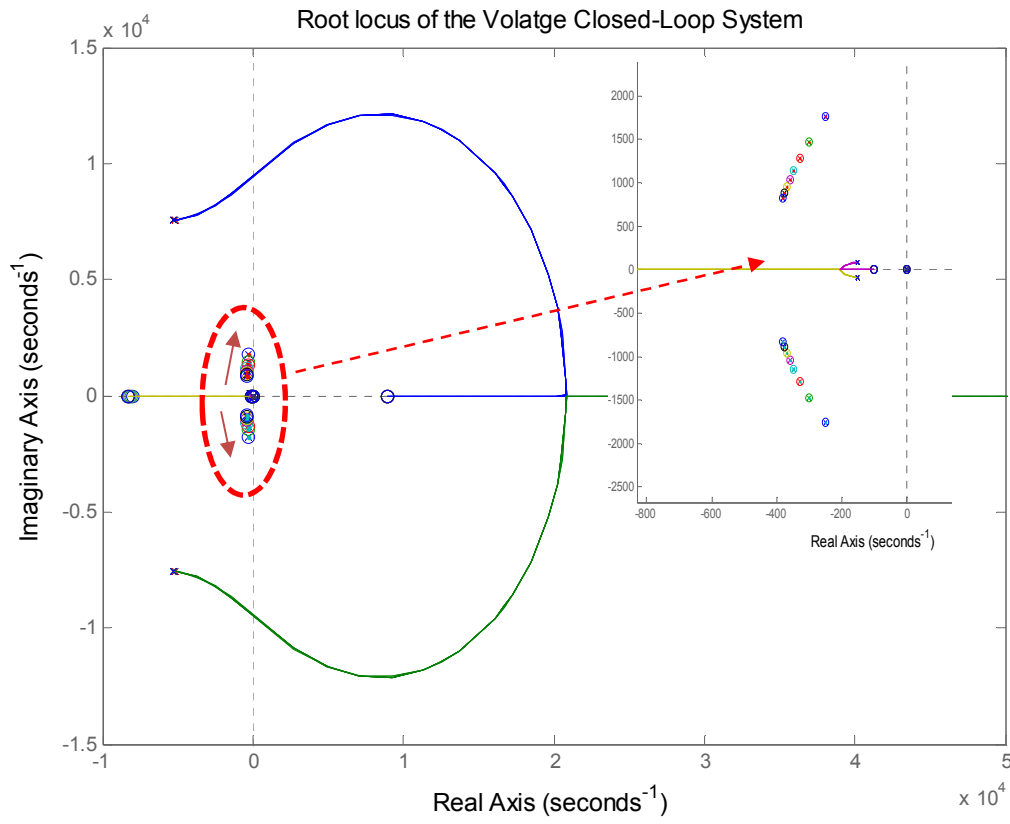


Figure 5.21: By increasing the DC link capacitance, the poles move toward imaginary axis.

5.6.2.4 Simulation results of the proposed controller

A simulation model was performed in the MATLAB/Simulink environment to model the DC UPS system. The system specifications are as listed in the table 5.1 and figure 5.22 shows the simulation model.

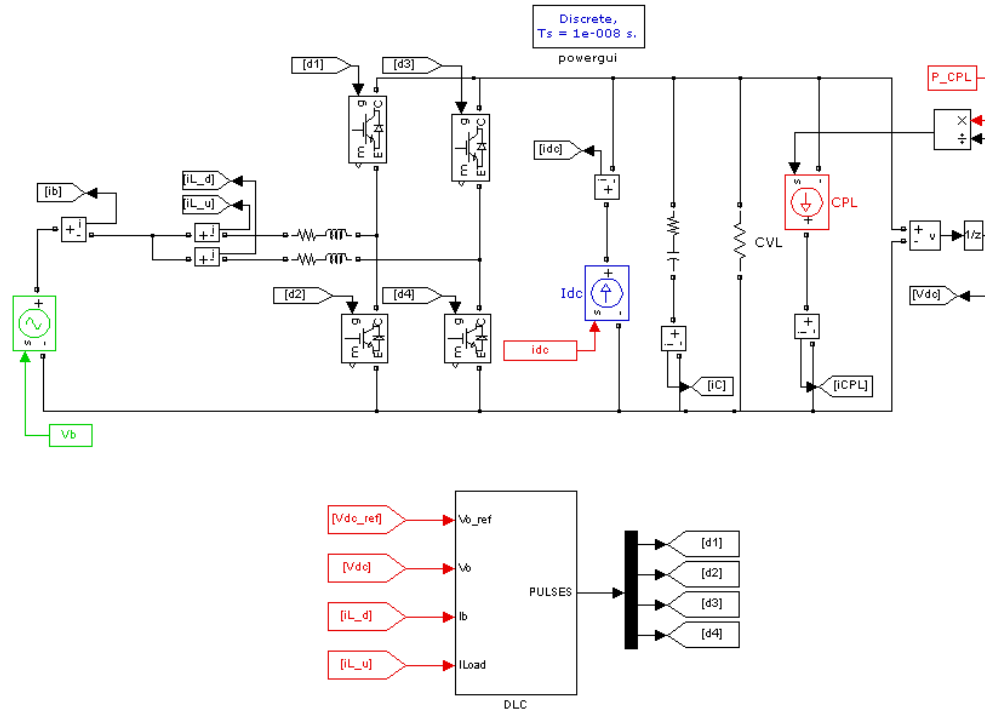


Figure 5.22: Simulation model of the DC UPS and the Dual-Loop Controller (DLC)

Figure 15.23 shows the performance of the system working under rated operating values, 700 VDC output voltage and 140 kW as the CPL value. The CVL is a 10 kW constant resistive load and the input power from the grid is 20 kW which is modeled as a current source.

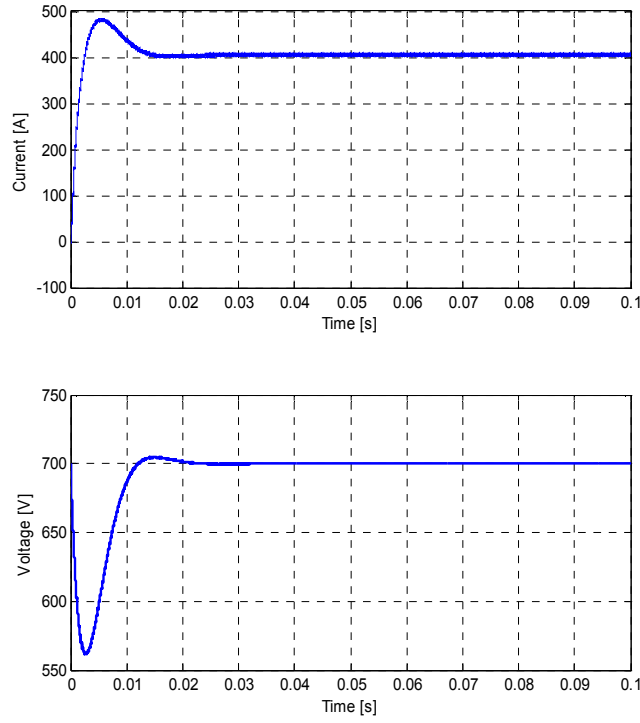


Figure 5.23: Performance of the system while working on the rated value, battery current and DC link voltage.

Figure 5.24 illustrates the robustness of the DLC controller against disturbances from the CPL load. Increasing the CPL from 0 kW to 140 kW in several steps to capture the transients on the DC link and battery current. As shown in figure 5.24, the battery current is negative when the CPL is zero, which means that battery is charging with extra energy from the grid power. next step starts from $t=0.05$ s where the CPL is 10 kW and all the grid power is used by CVL and CPL, thus battery has zero power exchange with the system. Then CPL has three more steps up at 50 kW, 100 kW and finally at 140 kW. Battery current increases as the CPL increases. The DLC controller regulates the DC link voltage so by increasing the CPL, since the power from the grid is constant, the controller manages the DC/DC converter to inject more current to the link. The battery operates at high discharging

mode and respond to the request by increasing the discharge rate as needed. By injecting more power to the link suddenly, the current will increase and consequently the voltage dropped as the power is constant. Then there will be some voltage sags in the DC link dynamics during changing the CPL load. This fact illustrates in the figure 15.24, as the CPL increases, the battery current increases and the voltage drops.

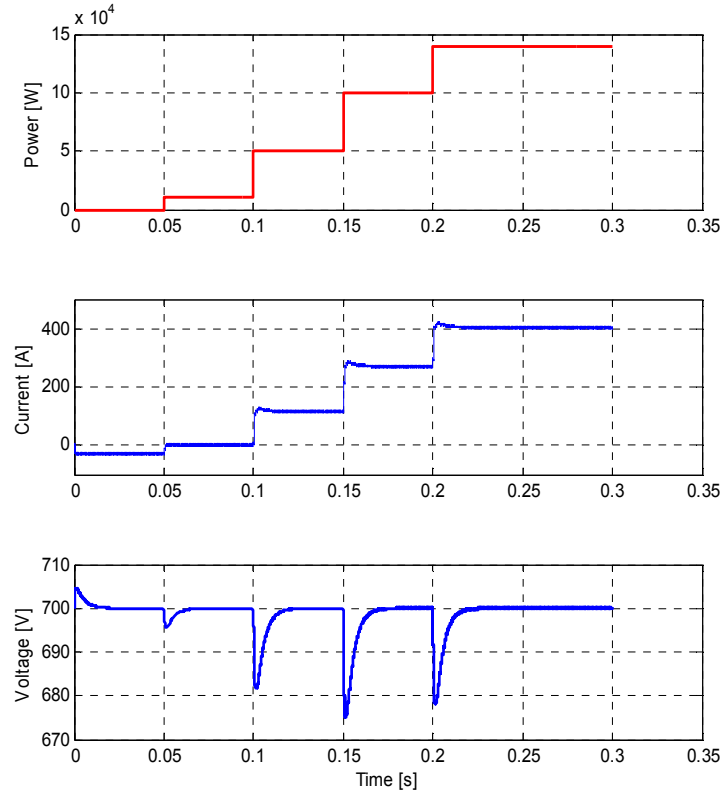


Figure 5.24: Performance of the DLC against the CPL variation. The CPL step changes are 0, 10, 50, 100 and 140 kW.

In order to validate the performance of the system during different four operating modes, a load profile is designed to simulate different modes of the DC UPS system and test the performance of the proposed DLC under different situations, as shown in figure 5.25. The load pattern is started at mode II, $0 < t < 0.01$ s, in which the grid power is 20 kW and CPL

power is zero, then battery is charged with 10 kW and thus battery current is negative. At $t=0.01$ s, system moved to mode I, the load leveling mode, where power from the grid stays the same, while the CPL power is jumped to 140 kW peak. Since the incoming power from the grid is constant, the BESS provides the rest of high peak power demand and battery current is changed from negative charging mode to a high positive discharging mode to take care of the power demand. The DC link voltage is dropped around 70 V ($\sim 10\%$ voltage drop) due to the transition and recovered smoothly to the reference value. At $t = 0.03$ s, the CPL power becomes zero, then the DC UPS system goes to mode II, the standby mode, again. The battery current is negative, charging state, during this mode. At $t = 0.04$ s, the battery is fully charged and the power exchange between battery and the DC link is zero. The grid power is reduced to half since CVL is the only active load during this mode. At $t = 0.05$ s, the grid power is zero. This is the UPS mode which represents the power outage moment when the grid is not available. Then the BESS is responsible for providing entire required power. The BESS is responding to the pulsed peak power demand from CPL load by high rate discharging the saved energy. At $t = 0.07$ s, the grid power is available again and the CPL power becomes zero. These different situations are designed to mimic the four operating modes of the DC UPS system and validate the performance of the designed sliding mode controller during different transitions caused by different operating modes of the system. During all situations and transitions, the proposed DLC controller has been provided system stability and consistent performance for the DC UPS.

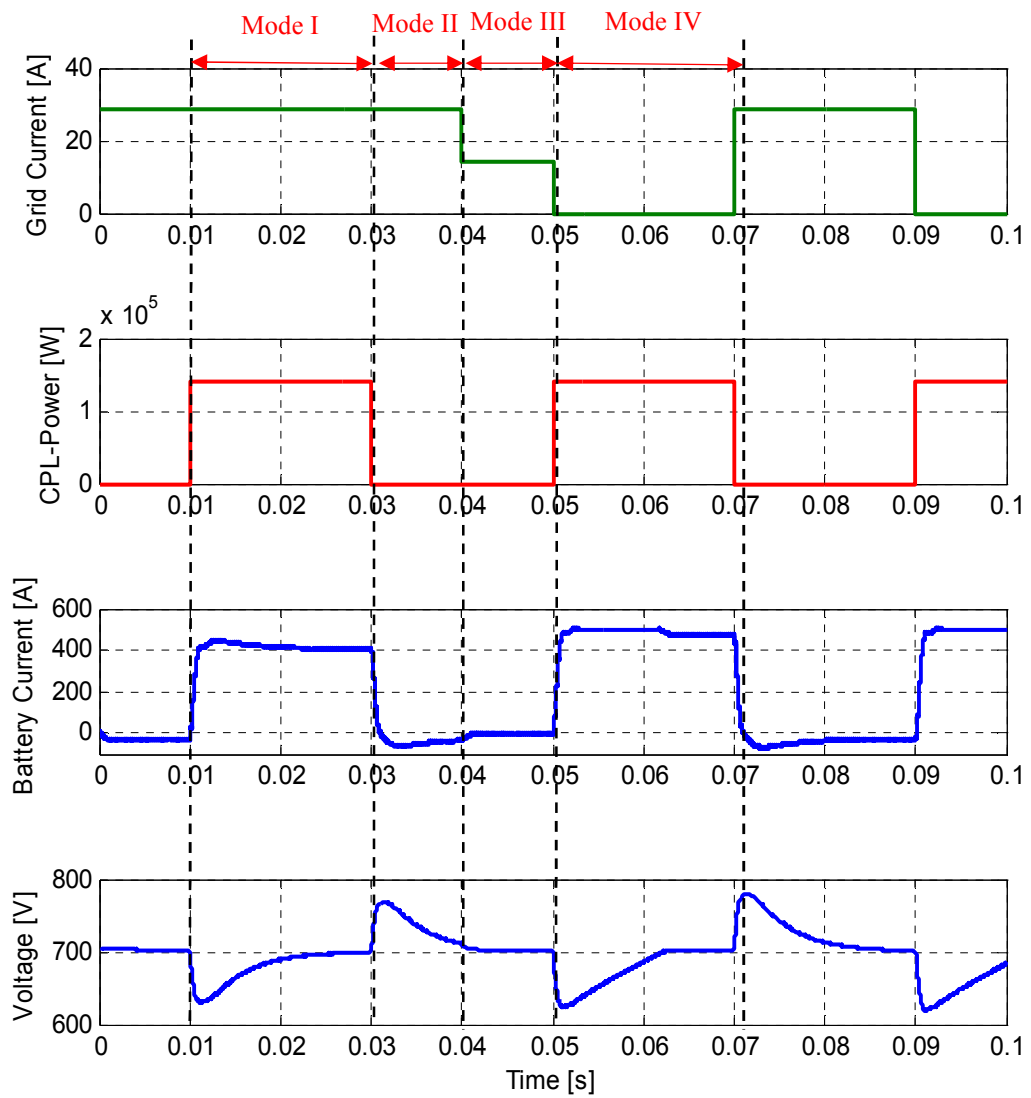


Figure 5.25: Performance of the proposed DLC controller during different operating modes.

5.6.3 Constant Frequency Sliding Mode Control (CFSMC)

5.6.3.1 Introduction

The dual-loop controller with linear compensators, presented in the previous section, has a limited stability region and the voltage regulation at DC link does not satisfy the desired rate of $\pm 5\%$ regulation.

To satisfy the desired control goals such as tighter regulation, better performance during transitions and also expand the stability region, a nonlinear robust controller is proposed.

Robust controllers are well-known for their stability and robustness and usually preferred when dealing with a nonlinear system with imprecise model. The imprecision may come from the actual uncertainty from the plant or from a purposeful choice of the simplified representation of the model's dynamics which is the one in this case [100-101].

Sliding Mode Controller which is a robust controller approach, has been proposed to meet the desired control goals by providing stability and consistent performance in the face of modeling imperfections. The proposed controller can tolerate the model and parameter inaccuracies while tracking the goal. The control law, which is the main challenge for designing the controller, consists of two main parts, an equivalent control law and a switching law. The former part tracks the desired reference path to achieve steady state while the latter part deals with the switching uncertainties. This type of controller has been successfully applied to other fields such as electric motor control, robotics and power systems [102-106].

The proposed sliding mode controller has a variable switching frequency which is unfavorable for power converter control applications. Hence, here a *constant frequency sliding mode controller* (CFSMC) is presented which makes it interesting for power electronics applications in which PWM based power converters utilized and constant switching frequency is a major requirement. Literature have been shown that by imposing the sliding mode, the closed-loop control system gains advantages of robustness and low sensitivity to parameter variations [107-115].

5.6.3.2 Basics of Sliding Mode Control

Considering a general form of a single input system in state space format as

$$x^{(n)} = AX + Bu \quad [5.6]$$

Where the scalar x is the output of interest (e.g. DC link voltage), the scalar u is the control input which is generated by a switching control law, $X = [x, \dot{x}, \dots, x^{(n-1)}]^T$ is the state vector and A and B are parameter matrices of the system [101]. In case of a DC/DC converter, $n=1$ and the equation becomes

$$\dot{x} = Ax + Bu \quad [5.67]$$

Considering reference or desired output value as x_d , then the state tracking error is defined as

$$\tilde{x} = x - x_d \quad [5.68]$$

The control problem is to get the state x to track the desired value in the presence of model imprecision on the system parameter matrices, A and B , then controller has a commonly designed switching function as

$$u = \frac{1}{2}[1 + sign(s)] = \begin{cases} 1 & \text{when } S > 0 \\ 0 & \text{when } S < 0 \end{cases} \quad [5.69]$$

Where S is the instantaneous state variable's trajectory, a function of the state tracking error or sliding surface. The nth-order S function is generally defined as

$$S(x; t) = \left(\frac{d}{dx} + \lambda \right)^{n-1} \tilde{x} \quad [5.70]$$

Here λ is a strictly positive constant [102-103]. Designing a switching control law to drive the plant state to the switching surface and maintain it on the surface upon interception is a major task. In order to ensure the desired sliding mode dynamics are attained and maintained, several methods are proposed in the literature [103-108]. Lyapunov approach is commonly used to ensure the existence of sliding mode operation. This method is usually used to determine the stability properties of an equilibrium point without solving the state equation [101-104].

Considering V as a positive definitive candidate for the Lyapunov function,

$$V(S) = \frac{1}{2} S^2 \quad [5.71]$$

Then to ensure the controller stability and convergence of the state trajectory to the desired sliding surface, the switching control law should ensure that gradient of the Lyapunov function with respect to time, is always negative.

$$\dot{V} = S\dot{S} < 0 \quad \text{for } s \neq 0 \quad [5.72]$$

It also known as the reachability condition. The switching control should satisfy this condition to guarantee the state trajectory at locations near the sliding surface will be always directed toward the sliding surface.

The dynamics of the state of interest in the sliding mode can be driven by solving the equation of

$$\dot{S} = 0 \quad [5.73]$$

This equation presents the dynamics of the system while in the sliding mode and the obtained expression by solving the equation is called the equivalent control law, $0 < u_{eq} < 1$, which is the continuous control law that would maintains the $\dot{S} = 0$, if the plant dynamics are exactly known [101-104].

The equivalent control law is a varying frequency signal which can be used as the duty ratio of a converter, however this way the sliding mode control will have a variable switching frequency. The proposed control law consists of two parts, an equivalent control law, u_{eq} , a continuous function to maintain the desired dynamics or track the desired output, and a switching control law, u_{sw} which is a switching function used to manage disturbances, model imprecision and parameter mismatches. Then the control law is used as the control signal for PWM generator block with a constant switching frequency [101-104].

$$u = u_{eq} + u_{sw} \quad [5.74]$$

5.6.3.3 Constant Frequency Sliding Mode Control for DC UPS System

The SMC design is started by driving the state space equations of the DC/DC converter as shown in the figure 5.26.

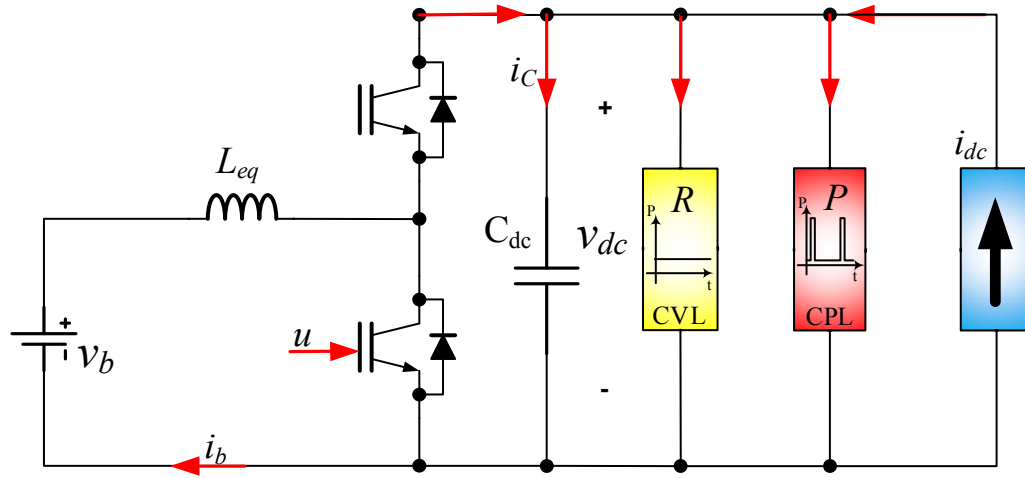


Figure 5.26: Schematic of the DC UPS system used for performing Sliding Mode Control (SMC)

The state space of the converter can be achieved as

$$\begin{cases} i_c = C_{dc} \frac{d}{dt} v_{dc}(t) = \bar{u}(t) \cdot i_b(t) + i_{dc}(t) - \left(\frac{v_{dc}(t)}{R} + \frac{P}{v_{dc}(t)} \right) \\ v_L = L_{eq} \frac{d}{dt} i_b(t) = v_b(t) - \bar{u}(t) \cdot v_{dc}(t) \end{cases}$$

The DC link voltage is the state of desired, then the tracking error defined as

$$e_v = V_{ref} - v_{dc} \quad [5.75]$$

Where V_{ref} is the reference output voltage and e_v is the tracking error. The sliding surface is defined based on the general form at 5.70 and considering the integral control, or defining

the variable of interest as integral of tracking error, which in this case a third order Sliding surface relative to the $\int_0^t \tilde{x} dt$ defines as [101]

$$S(x; t) = \left(\frac{d}{dx} + \lambda \right)^{n-1} \tilde{x}$$

$$S(x; t) = \left(\frac{d}{dx} + \lambda \right)^2 \int_0^t \tilde{x} dt = \dot{\tilde{x}} + 2\lambda \tilde{x} + \lambda^2 \int_0^t \tilde{x} dt \quad [5.76]$$

By replacing e_v as the tracking error, the 5.76 becomes

$$S = a_1 e_v + a_2 \dot{e}_v + a_3 \int e_v dt \quad [5.77]$$

Where $a_i > 0$, $i=1, 2$ and 3 , are positive coefficients [109-112]. In order to find the equivalent control law, as it mentioned earlier at 5.73, it needs to find the first derivative of the sliding surface, which is

$$\dot{S} = a_1 \dot{e}_v + a_2 \ddot{e}_v + a_3 e_v \quad [5.78]$$

And the first and second time derivatives of the tracking error are achieved as

$$\dot{e}_v = -\frac{i_c}{C_{dc}} = -\frac{1}{C_{dc}} \left(\bar{u} \cdot i_b + i_{dc} - \left(\frac{v_{dc}}{R} + \frac{P}{v_{dc}} \right) \right)$$

$$\dot{e}_v = -\frac{1}{C_{dc}} \left(\bar{u} \int_0^t \frac{v_b - v_{dc}}{L_{eq}} dt + i_{dc} - \left(\frac{v_{dc}}{R} + \frac{P}{v_{dc}} \right) \right) \quad [5.79]$$

$$\ddot{e}_v = -\frac{1}{C_{dc}} \left(\frac{1}{L_{dc}} (v_b - v_{dc}) \bar{u} + S i_{dc} - \left(\frac{1}{R} - \frac{P}{v_{dc}^2} \right) \frac{i_c}{C_{dc}} \right)$$

$$\ddot{e}_v = \frac{1}{c_{dc}L_{dc}}(v_{dc} - v_b)\bar{u} - \frac{Si_{dc}}{c_{dc}} + \frac{1}{c_{dc}^2}\left(\frac{1}{R} - \frac{P}{v_{dc}^2}\right)i_c \quad [5.80]$$

Substituting 5.79 and 5.80 into 5.78, the first time derivative of the sliding surface yields as

$$\begin{aligned} \dot{S} &= a_1\left(-\frac{i_c}{c_{dc}}\right) + a_2\left(\frac{1}{c_{dc}L_{dc}}(v_{dc} - v_b)\bar{u} - \frac{Si_{dc}}{c_{dc}} + \frac{1}{c_{dc}^2}\left(\frac{1}{R} - \frac{P}{v_{dc}^2}\right)i_c\right) + a_3e_v \\ \dot{S} &= \left(-\frac{a_1}{c_{dc}} + \frac{a_2}{c_{dc}^2}\left(\frac{1}{R} - \frac{P}{v_{dc}^2}\right)\right)i_c + \frac{a_2}{L_{eq}C_{dc}}(v_{dc} - v_b)\bar{u} - \frac{a_2}{c_{dc}}Si_{dc} + a_3e_v \end{aligned} \quad [5.81]$$

Now, by solving the equation $\dot{S} = 0$, the equivalent control law which is the necessary condition to maintain the dynamics of the system in the sliding surface, will be achieved.

$$\dot{S} = 0 \rightarrow$$

$$\bar{u}_{eq} = \frac{1}{v_{dc}-v_b} \frac{L_{dc}C_{dc}}{a_2} \left(\left(\frac{a_1}{c_{dc}} - \frac{a_2}{c_{dc}^2} \left(\frac{1}{R} - \frac{P}{v_{dc}^2} \right) \right) i_c + \frac{a_2}{c_{dc}} Si_{dc} - a_3 e_v \right) \quad [5.82]$$

$$\bar{u}_{eq} = \frac{1}{v_{dc}-v_b} \left(\left(\frac{a_1}{a_2} - \frac{1}{c_{dc}} \left(\frac{1}{R} - \frac{P}{v_{dc}^2} \right) \right) L_{eq} i_c + L_{eq} Si_{dc} - \frac{a_3}{a_2} L_{eq} C_{dc} e_v \right)$$

$$u_{eq} = 1 - \bar{u}_{eq} = \frac{1}{v_{dc}-v_b} \left((v_{dc} - v_b) - k_1 i_c + k_2 e_v - L_{eq} Si_{dc} \right) \quad [5.83]$$

Where the coefficients define as

$$\begin{cases} k_1 = \left(\frac{a_1}{a_2} - \frac{1}{c_{dc}} \left(\frac{1}{R} - \frac{P}{v_{dc}^2} \right) \right) L_{eq} \\ k_2 = \frac{a_3}{a_2} L_{eq} C_{dc} \end{cases}$$

This is the continuous control function which is bounded between 0 and 1. Since this signal is bounded, then can be directly used as a switching signal to drive a converter switches. However, it has a variable duration which is not favorable for constant frequency switching functions and designing circuit components under a variable switching frequency would not be easy and optimum. In order to solve this problem, according to [104], if the switching frequency of the converter becomes very high, then the averaged dynamics of a sliding mode controlled system is equivalent to the averaged dynamics of a PWM controlled system, which means that the equivalent control law, u_{eq} will be equal to the duty ratio, d of the PWM [108-111, 113]. Thus, the control law of the sliding mode can be used as the duty ratio of a PWM generator of a converter with constant switching frequency [110-114].

According to the 5.74, the sliding mode control law consists of two parts, an equivalent control law, continuous function to maintain the controller stability and tracking the reference output value, and a switching control law to handle disturbances, which is defined as

$$u_{sw} = k \cdot sign(s) \quad [5.84]$$

Therefore, the control law achieved as

$$\begin{aligned} u &= u_{eq} + u_{sw} = u_{eq} + k \cdot sign(s) \\ u &= \frac{1}{v_{dc} - v_b} \left((v_{dc} - v_b) - k_1 i_c + k_2 e_v - L_{eq} S i_{dc} \right) + k \cdot sign(s) \end{aligned} \quad [5.85]$$

The equation presented in 5.85 is the control law for the sliding mode controller used for control the DC/DC converter in the DC UPS system. The controller involved the equivalent

and switching sections. Now, by considering this control law, the existence of the sliding mode or convergence of the state trajectory to the desired sliding surface should be verified.

To verify the existence of the sliding mode controller with the designed control law, condition in 5.72 should be always satisfied.

$$\dot{V} = S\dot{S} < 0$$

Replacing 5.83 into 5.81,

$$\dot{V} = S\dot{S} < 0 \rightarrow$$

$$\begin{aligned} \dot{V} = S \left[\left(-\frac{a_1}{C_{dc}} + \frac{a_2}{C_{dc}^2} \left(\frac{1}{R} - \frac{P}{V_{dc}^2} \right) \right) i_c + \frac{a_2}{L_{eq} C_{dc}} (v_{dc} - v_b) \bar{u} - \frac{a_2}{C_{dc}} S i_{dc} + a_3 e_v \right] = \\ S \left[\left(-\frac{a_1}{C_{dc}} + \frac{a_2}{C_{dc}^2} \left(\frac{1}{R} - \frac{P}{V_{dc}^2} \right) \right) i_c + \frac{a_2}{L_{eq} C_{dc}} (v_{dc} - v_b) (1 - (u_{eq} + u_{sw})) - \frac{a_2}{C_{dc}} S i_{dc} \right. \\ \left. + a_3 e_v \right] = \\ = S \left(-\frac{a_2}{L_{eq} C_{dc}} (v_{dc} - v_b) \cdot k \cdot sign(s) \right) \\ = -\frac{a_2}{L_{eq} C_{dc}} (v_{dc} - v_b) \cdot k \cdot |S| < 0 \end{aligned}$$

By defining the switching function coefficient as

$$k = \frac{|e_v|}{v_{dc} - v_b} \quad [5.86]$$

Therefore,

$$\frac{|e_v| \cdot a_2}{L_{eq} C_{dc}} \cdot |S| > 0$$

$$\dot{V} = S\dot{S} = -\frac{|e_v| \cdot a_2}{L_{eq} C_{dc}} \cdot |S| < 0$$

Since a_2 is a positive coefficient, the inequality in 5.84 is always satisfied and existence of the sliding mode is guaranteed by controllers in 5.84.

The sliding mode controller is designed and the control law, the equivalent and switching sections, is presented at 5.85, the existence of the controller is verified. Thus, the control law can be applied to the PWM block with constant switching frequency as the converter's duty ratio. Therefore, the duty ratio of the converter is defined as,

$$d_{SMC} = u = \frac{1}{v_{dc} - v_b} \left((v_{dc} - v_b) - k_1 i_c + k_2 (V_{ref} - v_{dc}) - L_{eq} S i_{dc} \right) + \frac{|e_v|}{v_{dc} - v_b} \cdot sign(s)$$

[5.87]

where,

$$\begin{cases} k_1 = \left(\frac{a_1}{a_2} - \frac{1}{C_{dc}} \left(\frac{1}{R} - \frac{P}{v_{dc}^2} \right) \right) L_{eq} \\ k_2 = \frac{a_3}{a_2} L_{eq} C_{dc} \end{cases}$$

The control law in 5.87 is adaptive to the variations of the parameters appears in the equation, battery voltage, DC link voltage, grid current and load power. The input control signal or the duty ratio for the PWM block should be between 0 and 1. Thus, to ensure that

the output value of the controller does not saturate the PWM block, the sliding mode control law designed as [111-114]

$$d = \begin{cases} 1 & d_{SMC} \geq 1 \\ d_{SMC} & 0 < d_{SMC} < 1 \\ 0 & d_{SMC} \leq 1 \end{cases} \quad [5.88]$$

The control law presented in 5.88 is the desired duty ratio applied to the PWM block with constant frequency. The PWM output is the control pulses for the converter's switches. The combined sliding mode controller and the PWM block is defined as the Constant Frequency Sliding Mode Controller or **CFSMC**. Figure 5.27 illustrates the proposed controller.

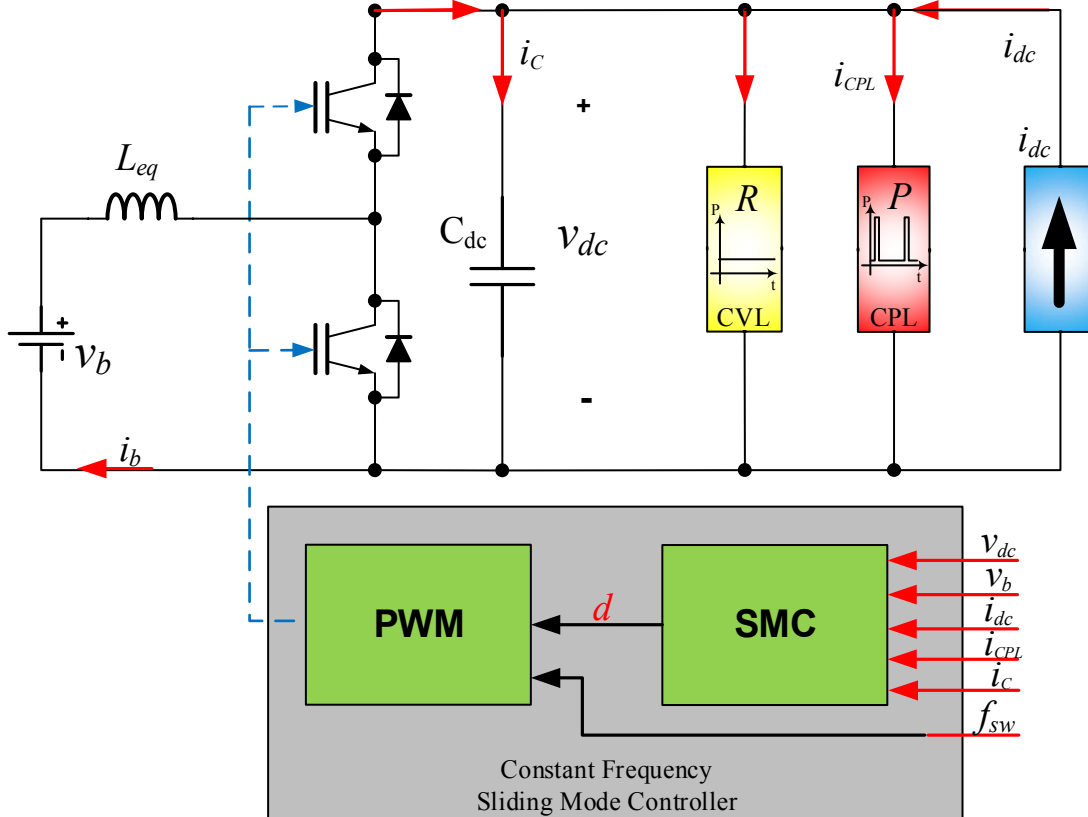


Figure 5.27: Block diagram of the proposed constant frequency sliding mode controller

5.6.3.4 Robustness of the CFSMC

The proposed controller should also be robust again parameter variations in the system. The control law presented in 5.87 has several online and offline parameters. Voltage of battery and DC link and current of the grid are online parameters which measured online, so the controller is updated with new values at each sampling period. However, the components value in the control law might not be the exact as expected and usually there are some uncertainties due to mismatch between their value in the control law and their measured value. Capacitors are more subject to these uncertainties than inductors. The uncertainties come from the capacitor can cause the control law to vary from its desired value and consequently, the equivalent controller cannot maintain the condition in 5.73, $\dot{S} = 0$ and the existence of the sliding mode is questionable. These types of uncertainties should be well managed by the switching section of the controller. In the following, the robustness of the proposed controller against the uncertainties form the DC link capacitor is provided [111].

It's assumed that during the operation of the system, the value of the DC link capacitor varies from C_{dc} to \hat{C}_{dc} . Consequently, the equivalent control law is affected. Substituting the new capacitor in the 5.83, the new equivalent control achieved as

$$\text{if } C_{dc} \rightarrow \hat{C}_{dc}$$

$$\hat{u}_{eq} = \frac{1}{v_{dc} - v_b} \left((v_{dc} - v_b) - \left(\frac{a_1}{a_2} - \frac{1}{\hat{C}_{dc}} \left(\frac{1}{R} - \frac{P}{v_{dc}^2} \right) \right) L_{eq} i_c + L_{eq} S i_{dc} - \frac{a_3}{a_2} L_{eq} \hat{C}_{dc} e_v \right)$$

[5.89]

Then the new control law becomes

$$u = u_{eq} + u_{sw} = \hat{u}_{eq} + \frac{|e_v|}{v_{dc} - v_b} sign(s) \quad [5.90]$$

Replacing this control law, 5.90 into the 5.81, the time derivative of the sliding surface becomes,

$$\begin{aligned} \dot{S} &= \left(-\frac{a_1}{C_{dc}} + \frac{a_2}{C_{dc}^2} \left(\frac{1}{R} - \frac{P}{V_{dc}^2} \right) \right) i_c + \frac{a_2}{L_{eq} C_{dc}} (v_{dc} - v_b) \left[1 - \hat{u}_{eq} - \frac{|e_v|}{v_{dc} - v_b} sign(s) \right] - \\ &\frac{a_2}{C_{dc}} S i_{dc} + a_3 e_v \\ \dot{S} &= a_3 \left(1 - \frac{\hat{C}_{dc}}{C_{dc}} \right) e_v - \frac{a_2}{L_{eq} C_{dc}} |e_v| \cdot sign(s) \end{aligned} \quad [5.91]$$

Then the existence condition in 5.72 should be satisfied.

$$\dot{V} = S \cdot \dot{S} < 0 \Rightarrow S \cdot \left(a_3 \left(1 - \frac{\hat{C}_{dc}}{C_{dc}} \right) e_v - \frac{a_2}{L_{eq} C_{dc}} |e_v| \cdot sign(s) \right) < 0 \quad [5.92]$$

Considering two cases,

If $S > 0$, then \dot{S} should be negative to meet the existence condition.

$$\begin{aligned} \text{if } S > 0 \xrightarrow{\dot{S} < 0} a_3 \left(1 - \frac{\hat{C}_{dc}}{C_{dc}} \right) e_v - \frac{a_2}{L_{eq} C_{dc}} |e_v| < 0 \Rightarrow \\ \frac{a_2}{a_3} > L_{eq} (C_{dc} - \hat{C}_{dc}) \frac{e_v}{|e_v|} \end{aligned} \quad [5.93]$$

If $S < 0$, then \dot{S} should be positive to meet the existence condition.

$$\begin{aligned}
& \text{if } S < 0 \xrightarrow{\dot{S}} a_3 \left(1 - \frac{\hat{C}_{dc}}{C_{dc}} \right) e_v + \frac{a_2}{L_{eq} C_{dc}} |e_v| > 0 \Rightarrow \\
& \frac{a_2}{a_3} < L_{eq} (\hat{C}_{dc} - C_{dc}) \frac{e_v}{|e_v|} \quad [5.94]
\end{aligned}$$

In order to meet the stability condition, 5.93 and 5.94 should happen at the same time, then

$$\frac{a_2}{a_3} > L_{eq} |C_{dc} - \hat{C}_{dc}| \quad [5.95]$$

The inequality in 5.95 is the necessary condition to ensure the existence of the sliding mode, also by selecting appropriate values for a_2 and a_3 . The inequality in 5.95 also guarantees the robustness of the proposed controller against uncertainties from DC link capacitor.

Considering these cases as possible situations for the capacitor value, the capacitor value becomes double or half,

$$\begin{cases} \hat{C}_{dc} = 2C_{dc} \rightarrow \frac{a_2}{a_3} > L_{eq} C_{dc} \\ \hat{C}_{dc} = \frac{1}{2}C_{dc} \rightarrow \frac{a_2}{a_3} > \frac{1}{2}L_{eq} C_{dc} \end{cases} \xrightarrow{\text{Max}} \frac{a_2}{a_3} > L_{eq} C_{dc} \quad [5.95]$$

The worst case scenario is when the capacitor value becomes double, then condition in 5.95 ensures the stability of the system in worst case. This inequality help to find the coefficient values range. Simply by considering a unity gain for a_2 , then

$$\text{if } a_2 = 1 \rightarrow a_3 < \frac{1}{L_{eq} C_{dc}} \quad [5.96]$$

The coefficients a_i can be also calculated by driving the differential equation of the sliding mode in 5.77,

$$S = a_1 e_v + a_2 \dot{e}_v + a_3 \int e_v dt = 0$$

By driving the first time derivative of the equation, this equation is obtained.

$$a_2 \ddot{e}_v + a_1 \dot{e}_v + a_3 e_v = 0 \quad [5.97]$$

Which is a second order linear system differential equation. The characteristic equation of the differential equation becomes

$$s^2 + \frac{a_1}{a_2} s + \frac{a_3}{a_2} = 0 \quad [5.98]$$

This is a standard second order equation in which the coefficients are defined as

$$\begin{cases} \frac{a_1}{a_2} = 2\rho\omega_n \\ \frac{a_3}{a_2} = \omega_n^2 \end{cases} \quad [5.99]$$

Where ρ is the damping ratio and ω_n is the natural frequency of the system. The natural frequency of the system defines as $\omega_n = 2\pi f_{BW}$ and f_{BW} is the bandwidth of the system which is usually 1/5 to 1/10 of the switching frequency. The damping ratio, ρ can also be between 0 and 1 ($0 \leq \rho < 1$) in order to have an underdamped system, equal one for acritically damped and greater than one for a overdamped system. These conditions should be considered with the condition in 5.95 to ensure stability and robustness of the system.

Considering 5.95 and 5.99, these results for coefficients are achieved.

$$\begin{cases} \frac{a_1}{a_2} = 2\rho\omega_n \\ \frac{a_3}{a_2} = \omega_n^2 \\ \frac{a_2}{a_3} > L_{eq}C_{dc} \end{cases} \xrightarrow{a_2=1} \begin{cases} a_1 = 2\rho\omega_n < \frac{2\rho}{\sqrt{L_{eq}C_{dc}}} \\ a_3 = \omega_n^2 < \frac{1}{L_{eq}C_{dc}} \end{cases} \quad [5.100]$$

5.6.3.5 Simulation Results of the CFSMC

In order to validate the proposed constant frequency sliding mode controller on the DC UPS, several simulations have been performed. A DC UPS model is implemented in MATLAB/Simulink. The system model is illustrated in the figure 5.28.

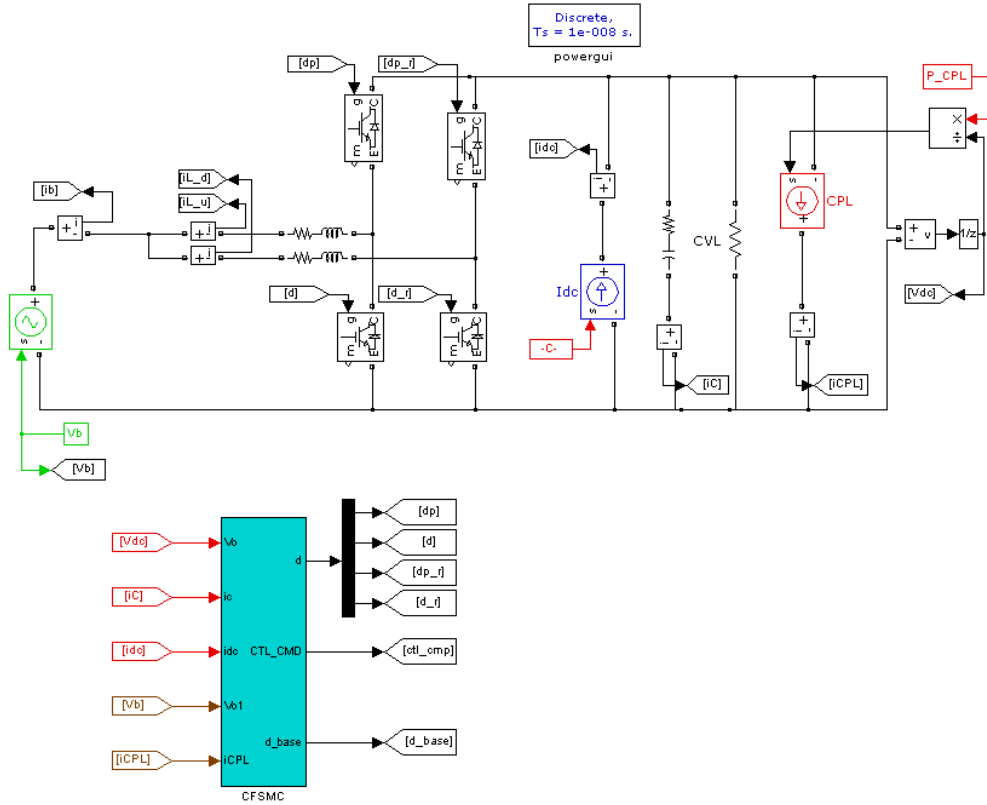


Figure 5.28: DC UPS system modeled in MATLAB/Simulink. The proposed constant frequency sliding mode controller (CFSMC) is managed the system.

Table 5.2 presents specifications of the DC UPS system modeled in Simulink. A constant frequency sliding mode controller, as explained and designed in 5.83, is also implemented in MATLAB/Simulink environment and applied to the DC UPS model.

Table 5.2: DC UPS specifications for the model implemented in the Simulink.

Output Voltage	P_{CPL}	P_{CVL}	L	C	f_{sw}	Grid Power	Battery Voltage
700 V	140 kW	10 kW	0.1 mH	1.5 mF	100 kHz	20 kW	350 V

Figure 5.29 shows the DC link voltage or output voltage at the operating point. The operating point is defined as 700 VDC reference output voltage while a constant power load is operating at 140 kW. Grid also provides 20 kW constant power and the CVL load is rated at 10 kW.

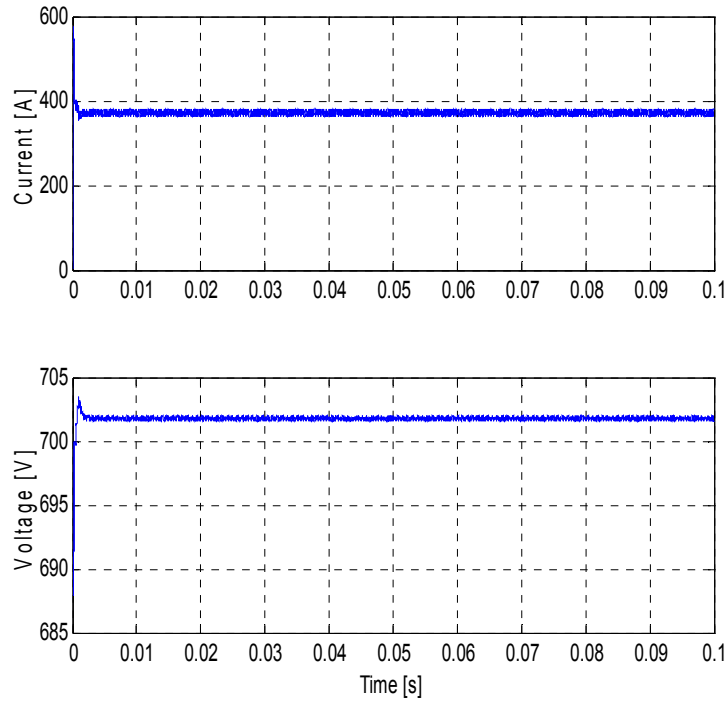


Figure 5.29: DC UPS system output results. Battery energy storage discharging current and the DC link voltage.

Figure 5.30 shows the performance of the system while the CPL load varies from 0 to 140 kW. The DC link voltage plot shows that the output voltage is kept constant against disturbances from the CPL. During this simulation, the grid power is constant at 20 kW and battery energy storage reacts to the high power demands by increasing the discharging current up to 371 A. During the first section of the simulation, the battery current is negative, which means BESS is charging, since 20 kW power is provided by the grid and 10 kW out of that is fed to the CVL and the rest is charging the battery. When the CPL jumped to 10 kW, the battery current is zero, since provided power by the grid is equal to the required power from CVL and CPL together. Then, by increasing the CPL power demand above 10 kW, BESS is discharged to provide the extra power.

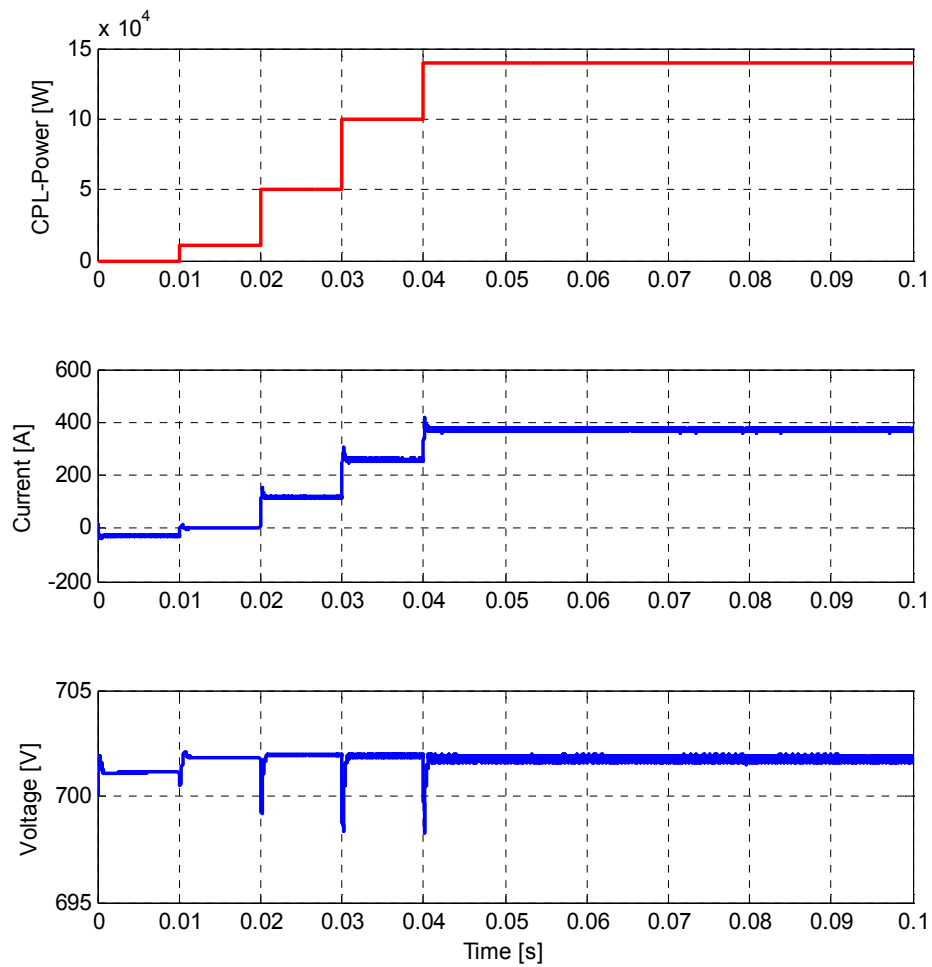


Figure 5.30: Performance of the DC UPS system with CFSMC while CPL load varies.

To validate the performance of the system during different four operating modes, a load profile is designed to simulate different modes of the DC UPS system and test the performance of the proposed CFSMC under different situations, as shown in figure 5.31. The load pattern is started at mode II, $0 < t < 0.01$ s, in which the grid power is 20 kW and CPL power is zero, then battery is charged with 10 kW and thus battery current is negative. At $t=0.01$ s, system moved to mode I, the load leveling mode, where power form the grid stays the same, while the CPL power is jumped to 140 kW peak. Since the incoming power

from the grid is constant, the BESS provides the rest of high peak power demand and battery current is changed from negative charging mode to a high positive discharging mode to take care of the power demand. The DC link voltage is dropped around 13 V (~ 2% voltage drop) due to the transition and recovered quickly to the reference value. At $t = 0.03$ s, the CPL power becomes zero, then the DC UPS system goes to mode II, the standby mode, again. The battery current is negative, charging state, during this mode. At $t = 0.04$ s, the battery is fully charged and the power exchange between battery and the DC link is zero. The grid power is reduced to half since CVL is the only active load during this mode. At $t = 0.05$ s, the grid power is zero. This is the UPS mode which represents the power outage moment when the grid is not available. Then the BESS is responsible for providing entire required power. The BESS is responding to the pulsed peak power demand from CPL load by high rate discharging the saved energy. At $t = 0.07$ s, the grid power is available again and the CPL power becomes zero. These different situations are designed to mimic the four operating modes of the DC UPS system and validate the performance of the designed sliding mode controller during different transitions caused by different operating modes of the system. During all situations and transitions, the proposed CFSMC controller has been provided system stability and consistent performance for the DC UPS.

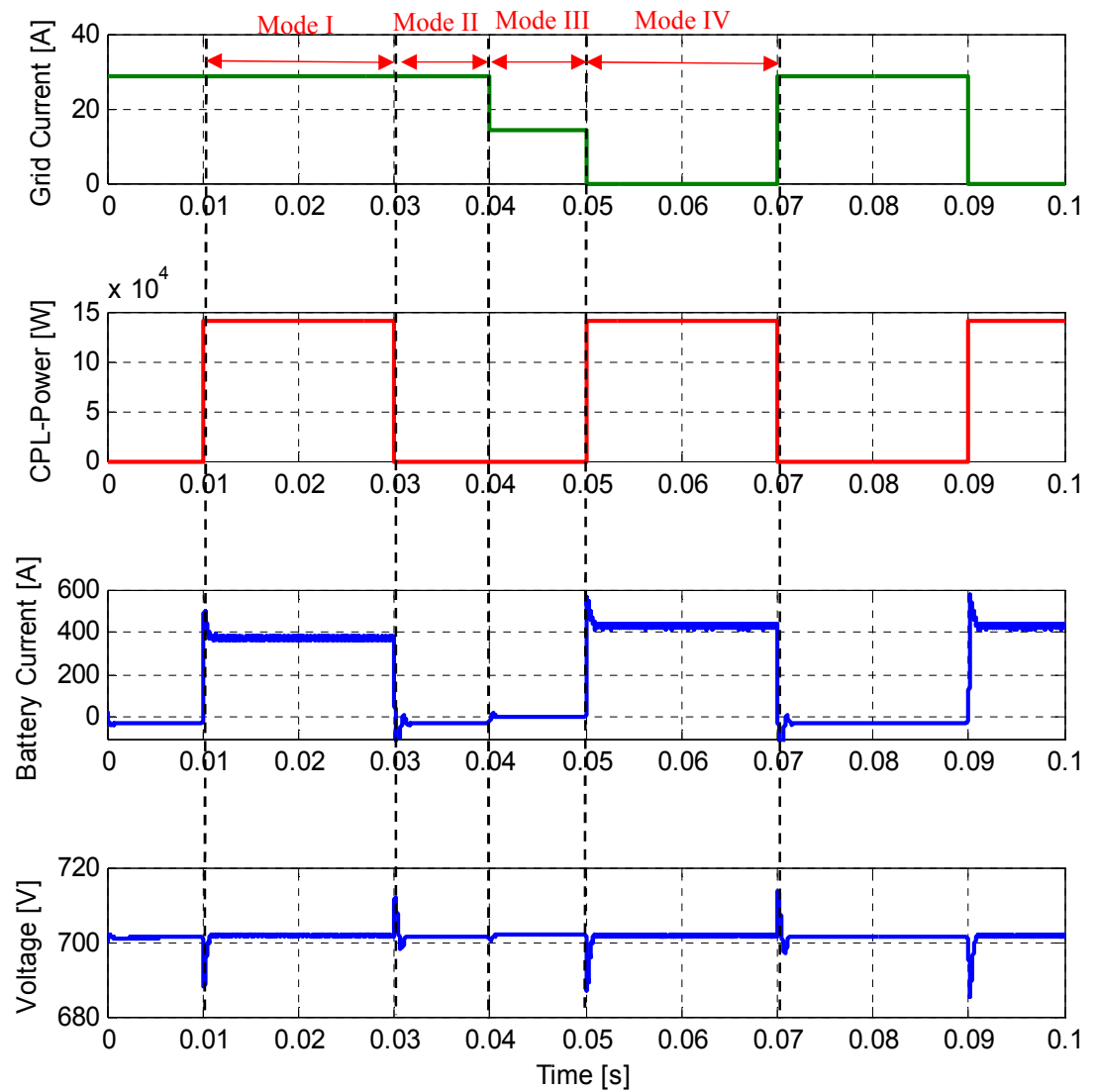


Figure 5.31: Performance of the proposed CFSMC controller during different operating modes.

CHAPTER VI: Experimental Results

6.1 Introduction

During previous chapters the DC UPS concepts has been proposed and its performance during different operational modes has been discussed and analyzed. Furthermore, control techniques have been introduced and verified with simulation models.

This chapter presents the testbed that is designed and developed to provide a setup for verifying the proposed DC UPS and control techniques. The testbed is a scaled down version of the proposed system. The experimental setups associated with the DC UPS and the results are presented in this chapter. The battery module with its performance tests and BMS are presented first and followed by the power interface sections which show the simulation and experimental results of the system.

6.2 Battery Energy Storage System (BESS)

The battery energy storage system and the system requirement which the selected battery need to satisfy are discussed in the chapter 3. Based on the material provided in the chapter 3, Li-ion battery family can meet the system requirements in terms of life cycle, power and energy density, performance and cost effectiveness. Figure 6.1 represents a comparison between several types of battery chemistries considering lithium iron phosphate as a reference case. An appropriate type is chosen based on the requirements for energy and power density, cost, cycle life, performance, and safety. Among different Li-ion batteries cathode materials exist in the market now, it has been investigated that compared with the

other chemistries, the lithium iron phosphate, LFP, and nickel cobalt aluminum, NCA, both with graphite anode electrode, have superiority in aforementioned aspects and have been chosen for several performance tests to ensure their power and performance capability.

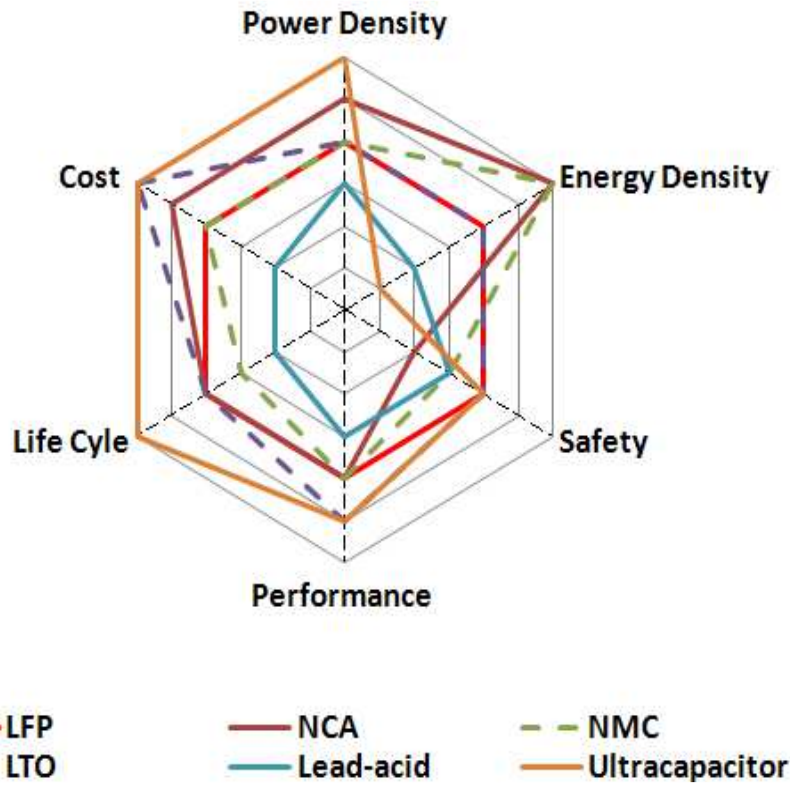


Figure 6.1: Characteristic comparison between several types of batteries.

The chosen battery cells have been subjected to the performance test as described in next section to verify their performances at low and high rate discharge. Three cells have been selected including a 42 Ah NCA type cathode Li-ion from JCI (Johnson Controls, Inc.), a 40 Ah LFP type cathode Li-ion from CALB (CALB USA Inc.) and a 30 Ah LFP type cathode from SAFT. Figure 6.2 shows the three finalist Li-ion cell types.

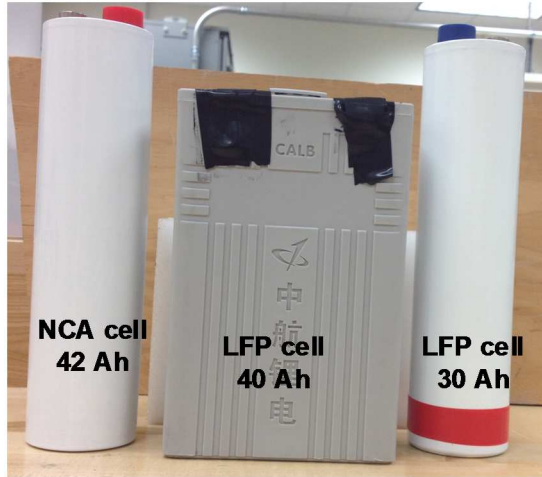


Figure 6.2: Three candidate Li-ion cells, LFP (40 Ah, CALB), NCA (42 Ah, JCI) and LFP (30 Ah, SAFT)

6.2.1 Cell Performance Tests

The performance tests include two regular and high rate tests. The regular test examines the normal operation of the cell at different rates while the high rate test investigates the performance of the cell at higher discharge rate.

All the tests have been conducted in the Energy Lab at UWM USR building, at room temperature. The regular test consists of several pulsed-discharging at different rates and the terminal voltage of the cell at each sampling frequency is recorded. The results of 1C discharging test have been reported for each battery along with measured capacity and internal resistance of the cell. The battery capacity is measured by coulomb counting method which is a common and quite accurate method for capacity measurement of the Li-ion cells due to their high coulombic efficiency accuracy. The immediate voltage drop at beginning of each discharge pulse divided by the constant discharge current represents the internal resistance of the cell at that point. Internal resistance of the battery is almost the same at difference rates.

The steady state and transient response characteristics of the cell have been analyzed and battery model parameters extracted. Open circuit voltage and internal resistance of cell as a function of state of charge would be the most important information expected as a regular performance test results. The open-circuit voltage versus state of charge is the most important part of the battery modeling and analyzing. Basically, V_{OC} is a function of several factors like state of charge, discharge rate, temperature and cycles number. However, the SOC has the most effect on the V_{OC} , and the other factors do not have a significant impact on the V_{OC} , so for the sake of simplicity, with reasonable error tolerance, the effect of other items could be ignored.

For the high rate pulsed discharging, the cell is partially discharged with 10 high current pulses with 5 seconds time duration each. A sample pulsed current and related cell terminal voltage is zoomed in and presented at each rate, 200A and 240A discharges, have been provided.

6.2.1.1 40 Ah LFP from CALB

A. The Regular Test Results

A pulsed discharging test at 1C performed in the lab and the terminal voltage and current of the cell is depicted at figure 6.3. The cell is fully discharged by several pulsed current.

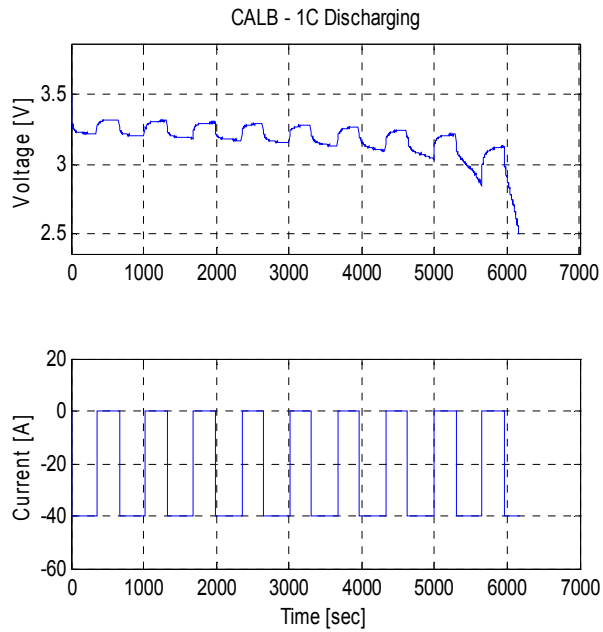


Figure 6.3: The terminal voltage (top) and current (bottom) of a 40 Ah LFP type battery from CALB at 1C discharging at room temperature.

Based on the regular test results, the open circuit voltage, V_{OC} curve of the cell is extracted.

Figure 6.4 shows the V_{OC} versus depth of discharge. It is worth to notify that the depth of discharge or DOD has a complementary meaning with the SOC, for instance a 10 % DOD is equal to 90 % SOC. The common characteristic for LFP type Li-ion batteries is to have a very flat curve in most of their SOC range, as it is well shown in the figure 6.4.

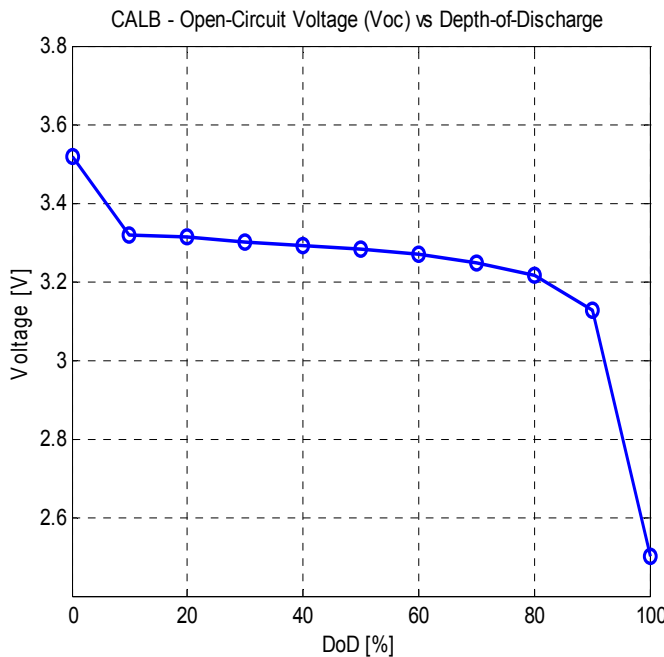


Figure 6.4: Open circuit voltage versus depth of discharge (DOD) curve extracted from 40 Ah CALB cell

B. The High Rate Pulsed Discharge Test Results

The high rate test consists of 10 high rate discharging pulses within 5 second durations.

Voltage and current curves for a sample pulse discharge at 200 A and 240 A discharge rates are depicted in figure 6.5.

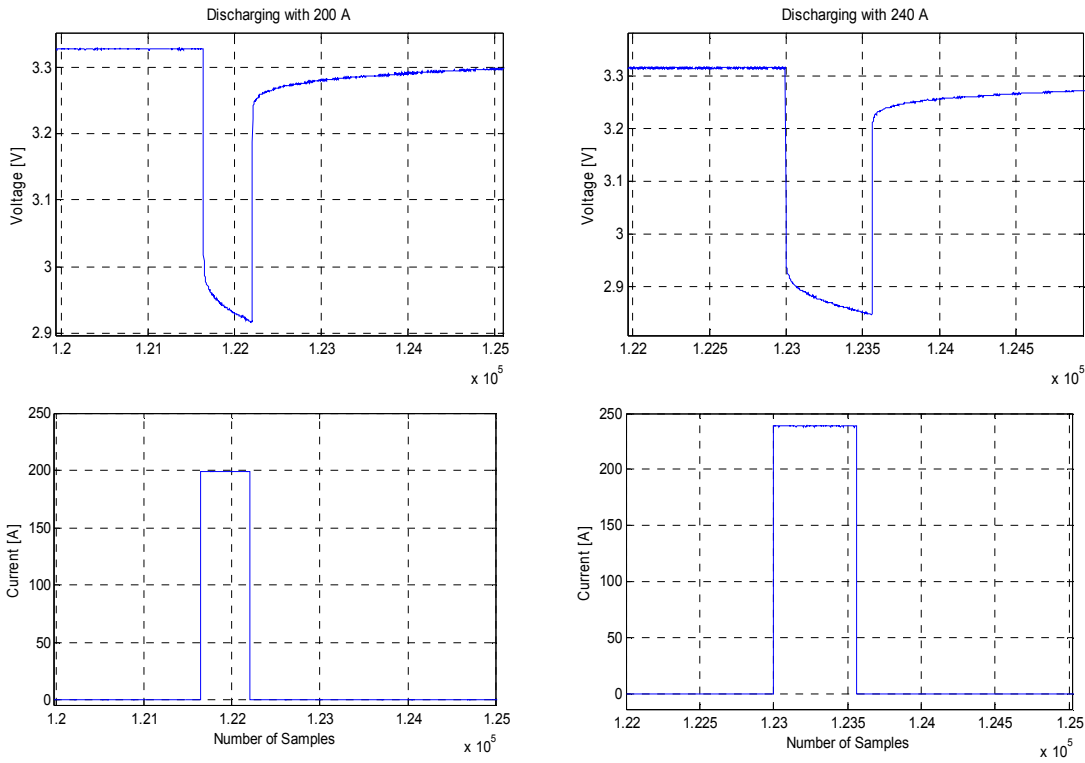


Figure 6.5: Voltages and current curves for high rate pulsed discharge test at 200 A (left side) and 240 A (right side) for the 40 Ah CALB cell.

Table 6.1 summarized the result of the test for 40 Ah LFP cell. The internal resistance of the cell is calculated based on the regular and high rate tests. The capacity is calculated just for the regular test as the high rate tests are performed for several pulses and partially discharged.

Table 6.1: The performance test result for the CALB battery cell.

Discharging Current [A]	Measured Capacity [Ah]	Internal Resistance (R_s) [mΩ]
40	38.557	1.8
200	NA	1.53
240	NA	1.51

6.2.1.2 42 Ah NCA from JCI

A. The Regular Test Results

A pulsed discharging test at 1C performed in the lab and the terminal voltage and current of the cell is depicted at figure 6.6.

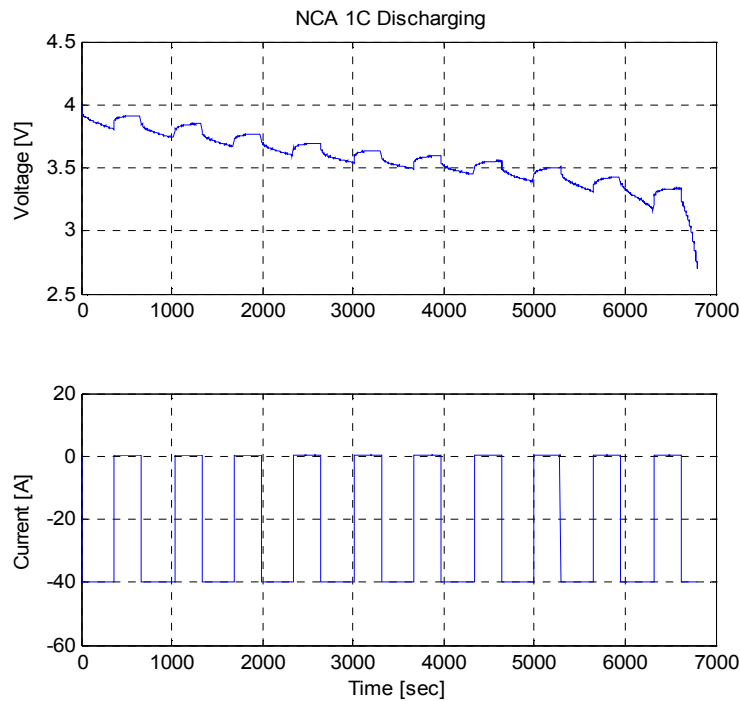


Figure 6.6: The terminal voltage (top) and current (bottom) of a 42 Ah NCA type battery from JCI at 1C discharging at room temperature.

The open circuit voltage is calculated and extracted based on the experimental data from the regular test and depicted in figure 6.7. The open circuit voltage versus DOD curve is linear with almost constant slope in most of its SOC range. This linear curve is considered a common aspect of NCA type cells compared with the flat curve of LFP cells.

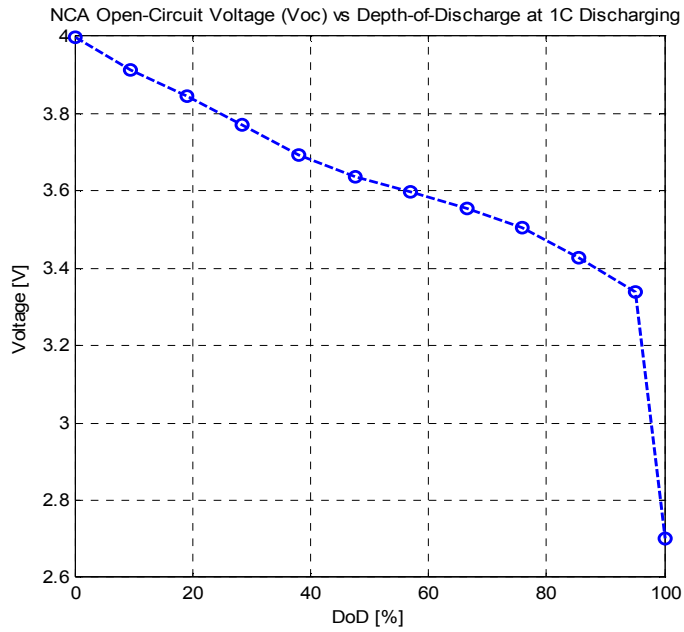
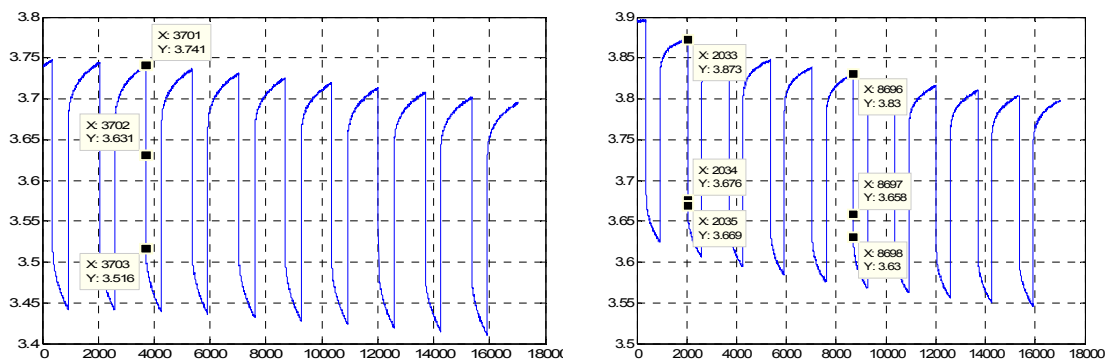


Figure 6.7: The open circuit voltage vs depth of discharge for 42 Ah NCA type Li-ion cell

B. The High Rate Test Results

The high rate test consists of 10 high rate discharging pulses within 5 second durations. Voltage and current curves for a sample pulse discharge at 200 A and 240 A discharge rates are depicted in figure 6.8.



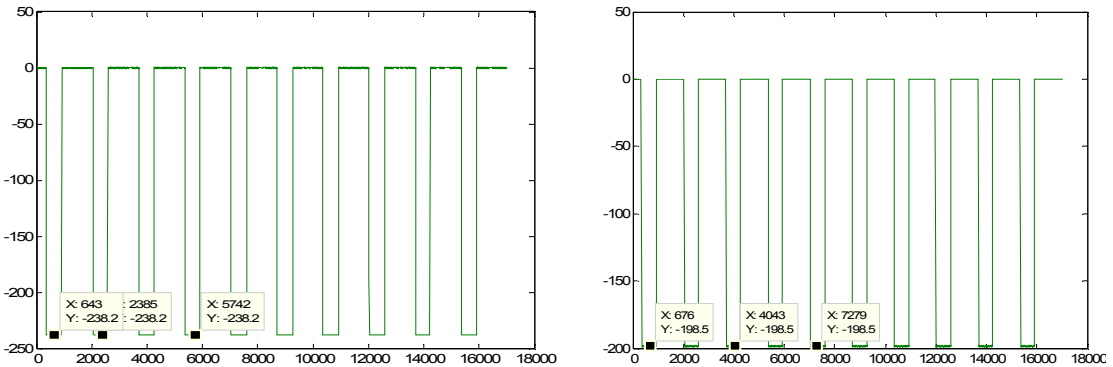


Figure 6.8: Terminal voltage and current curves for high rate test performed at 200 A and 240 A discharging.

Table 6.2 shows the performance test result for the JCI battery cell.

Table 6.2: The performance test result for the JCI battery cell.

Discharging Current [A]	Measured Capacity [Ah]	Internal Resistance (R_s) [$\text{m}\Omega$]
40	42.1142	1.1
200	-	1.027
240	-	0.945

6.2.1.3 30 Ah LFP from SAFT

A. The Regular Test Results

A pulsed discharging test at 1C performed in the lab and the terminal voltage and current of the cell is depicted at figure 6.9. The cell is fully discharged by several pulsed current.

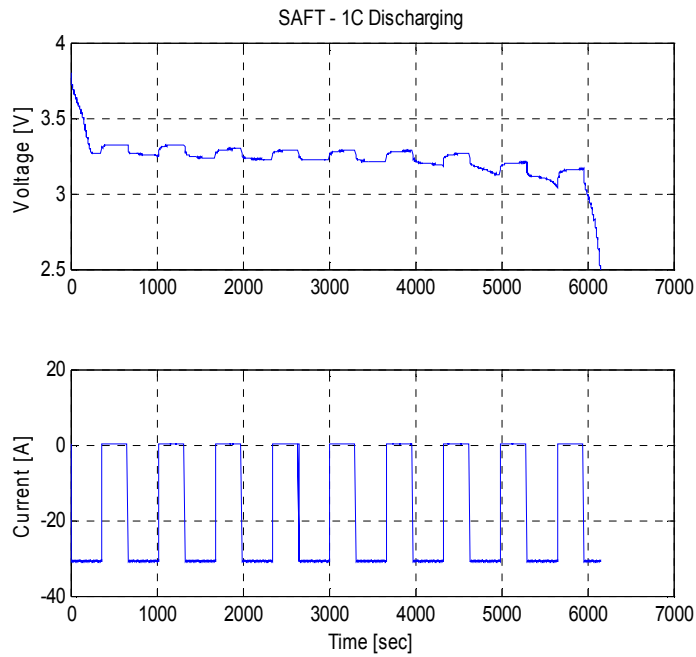


Figure 6.9: The terminal voltage (top) and current (bottom) of a 30 Ah LFP type battery from SAFT at 1C discharging (30 A) at room temperature.

Based on the regular test results, the open circuit voltage, V_{OC} curve of the cell is extracted.

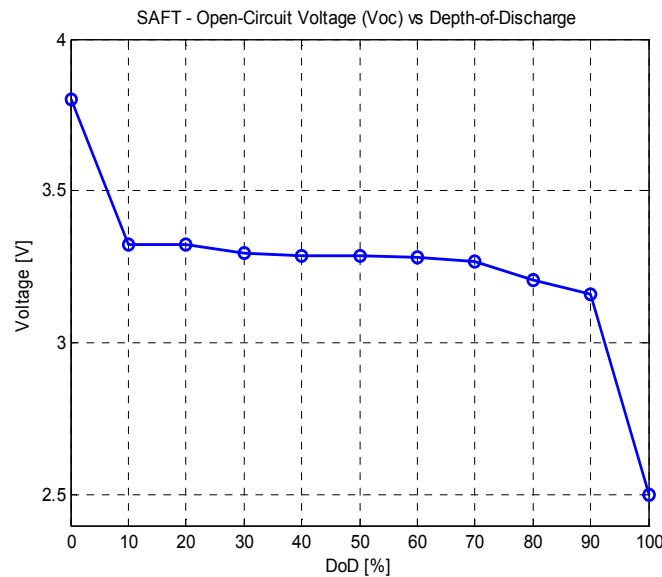


Figure 6.10: Open circuit voltage versus depth of discharge (DOD) curve extracted from 30 Ah LFP type SAFT cell.

Figure 6.10 shows the V_{OC} versus depth of discharge. As mentioned earlier, the open voltage curve is flat for the LFP type Li-ion batteries.

B. The High Rate Test Results

The high rate test consists of 5 high rate discharging pulses within 5 second durations. Voltage and current curves for a sample pulse discharge at 200 A and 240 A discharge rates are depicted in figure 6.11. Table 6.3 presents the measured capacity and internal resistance of the cell in different current rates.

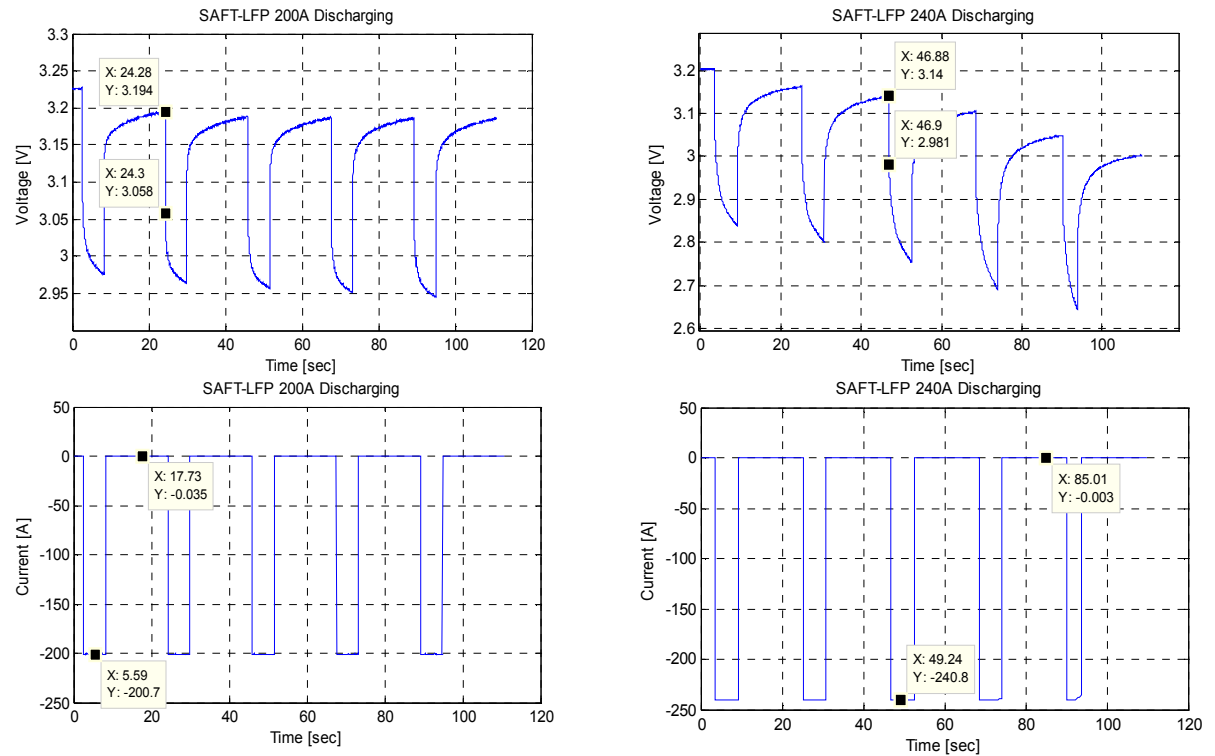


Figure 6.11: Terminal voltage and current of a LFP type SAFT cell, high rate pulsed discharging at 200 A and 240 A.

Table 6.3: The performance test result for the SAFT battery cell.

Discharging Current [A]	Measured Capacity [Ah]	Internal Resistance (R_s) [mΩ]
31	29.59	0.715
200	-	0.68
240	-	0.667

6.2.1.4 Conclusion of the Cell Performance Test

The internal resistance of the cells at high discharge rate is summarized in table 6.4. Higher the internal resistance higher would be the power loss of the battery cell due to the $R I^2$ term. Based on the table, SAFT cell shows the lowest internal resistance.

Table 6.4: Internal resistance of the three Li-ion battery cells AT HIGH RATES

Discharge Current [A]	Internal Resistance [mΩ]		
	LFP-CALB	NCA-JCI	LFP-SAFT
200	1.51	0.945	0.667
240	1.53	1.027	0.68

Table 6.5 presents calculated capacity, power and energy values of all the 3 cells. The calculated internal resistance at 240 A is used. The peak current is high pulsed discharge current capability which is obtained from the cells datasheets. Technically, that is the cell capability of providing short term (less than 10 seconds) high power. The table also provides information regarding to the pack size specifications. A battery pack consists of 108 series-connected cells. The number of cells are selected due to the terminal voltage requirement of the DC/DC converter. The pack should be able to provide a peak power of 125 kW while connected to a 700 V DC bus through the converter. The internal resistance and consequently associated power loss is necessary to maintain low. Higher energy and lower cost would also be preferred.

Table 6.5: Comparison of measured values for the three Li-ion batteries cells/packs (108 series-connected cells)

Chemistry	Rs [mΩ] (at 240 A)	Ip[A] (<10 sec)	V [V]		Capacity [Ah]	Peak Power [kW]		Energy [kWh]		PLOSS[kW]		Cost /cell \$ USD
			cell	pack		cell	Pack	cell	Pack	cell	pack	
LFP-CALB	1.51	400	3.25	351	38.6	1.3	140.4	0.126	13.5	0.24	26.1	40
LFP-SAFT	0.667	450	3.3	356	29.6	1.5	160.4	0.098	10.5	0.14	14.6	100
NCA-JCI	0.945	300	3.7	400	42.1	1.1	120	0.156	16.8	0.09	9.2	100

The NCA-JCI cell/pack shows the lowest power loss and the highest pack output voltage and energy based on the calculation while its peak power is the lowest one. The LFP-CALB meets the required peak power and current and is the least expensive pack, but the highest power loss. The LFP-SAFT has the highest power and lowest energy.

Since the Li-ion battery pack will be the most important part of the DC UPS, and the main power stress will be on the pack as it discharges with high rates, then to make a decision, it's necessary to perform a life time/cycle test to investigate reliability of each pack over a time period.

6.2.2 Li-ion Battery Pack

Depend on the battery chemistry, terminal voltage of each Li-ion cell is between 2.5V to 4.2V. According to the DC link voltage which is 700 V, several cells need to be series-connected to make an adequate voltage for the DC/DC converter. Since the converter has the lowest amount of current ripple when the duty ratio is around 0.5, then the battery pack should be able to provide around 350 V at the pack terminals. According to the regular cell performance tests in last section, the nominal voltage for LFP cell type ($V = 3.25 \text{ V}$) is lower than NCA cell type ($V = 3.6 \text{ V}$), then in order to have 350 V at terminals, 108 cells need to be connected in series.

$$\begin{cases} v_{\text{input}} = 350 \text{ V} \\ v_{\text{cell}} = 3.25 \text{ V} \end{cases} \Rightarrow \text{Cell numbers} = \frac{350}{3.25} \cong 108 \text{ series cells are required}$$

According to the standard size of the battery pack, two battery packs each contains 54 series cells were considered. Batteries are placed in the box and terminals are connected via bus bars made from copper.

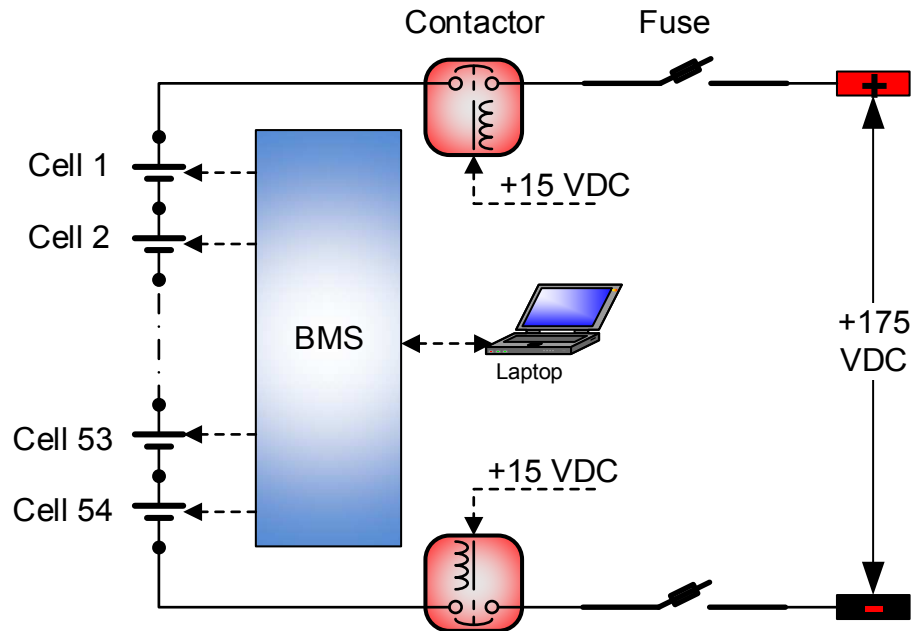


Figure 6.12: Schematic of the Li-ion battery pack.

The most positive cell battery terminal (cell 1 positive terminal) is considered the pack's positive terminal, and the most negative cell battery terminal (cell 54 negative terminal) considered pack's negative terminal. Figure 6.12 shows the schematic of the battery pack. Each pack's terminal has a contactor and fuse for safe operation.

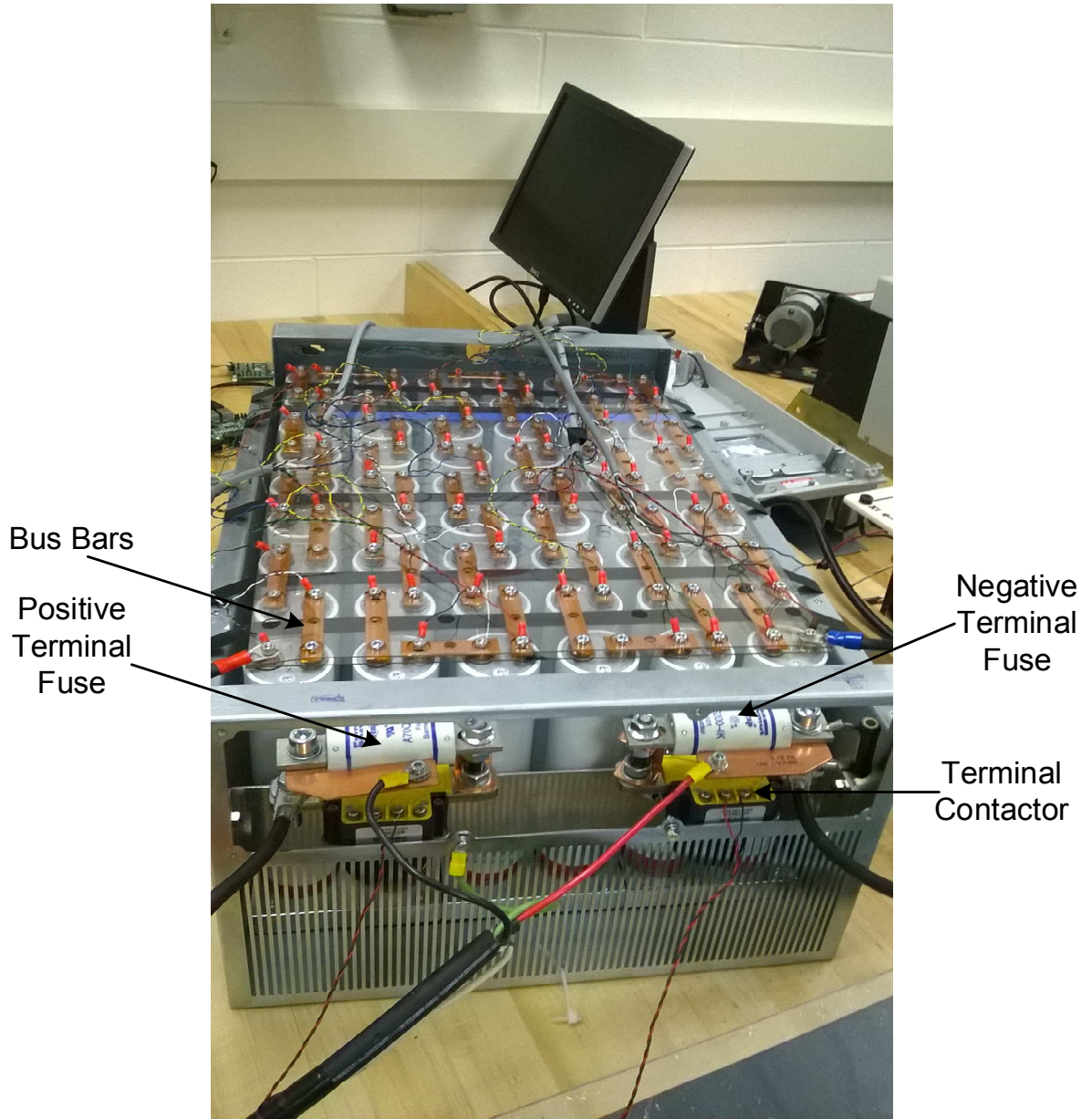


Figure 6.13: Li-ion battery pack contains 54 LFP type Li-ion cells.

The contactors are closed by applying +24 V DC to their terminals. When the contactors are closed, about 180 V would be available on the pack terminals. The first battery pack contains LFP type cells due to higher safety feature related to this type of Li-ion cells.

Figure 6.13 shows the battery pack which is developed during this project.

6.2.3 Battery Management System (BMS)

As explained in chapter 3, Li-ion batteries do not tolerate overheating and overcharging, then for a safe operation, the cells should be well monitored and protected. It is required to monitor each cell's voltage and temperature. Also, in a pack to have a long life and the best performance, cells should be balanced to have a same voltage. A cell with higher voltage in a series string forces the charging cycle to be terminated earlier otherwise the cell will be overcharged.

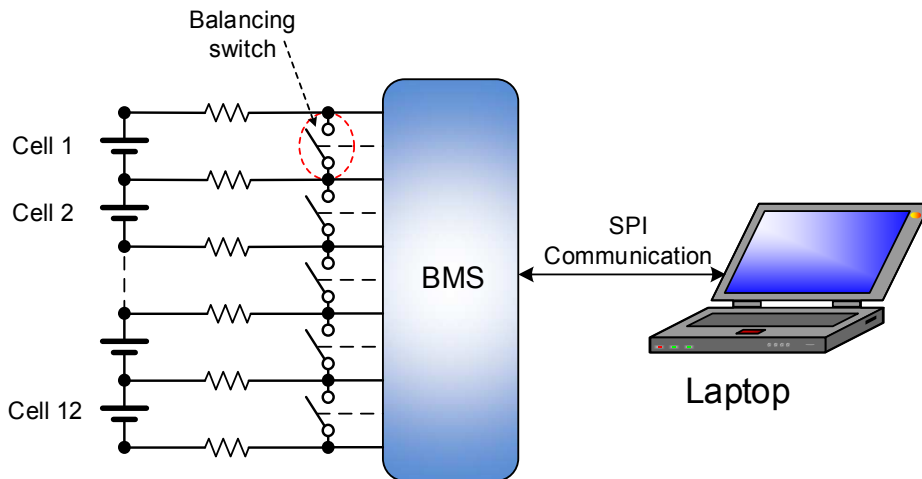


Figure 6.14: Block diagram of the battery management system (BMS) utilized for the Li-ion battery pack. The BMS can monitor up to 12 Li-ion cells.

On the other hand, a cell with lower voltage in a series string causes the discharging cycle to be shorter than expected, because the discharging cycle will be terminated once any cell hits the minimum allowed voltage. Consequently, having a balancing mechanism is a necessary requirement for a Li-ion pack not only to operate safely, but also more efficient and longer life time performance. Thus, a battery management system or BMS is an unavoidable part of any Li-ion battery pack.

Figure 6.14 shows the block diagram of the BMS system used for this project. The LTC6804 BMS board from Linear Technology Inc. is employed to monitor cells voltages and temperatures. The BMS board is a 12-cell monitor/measurement capability, which can measure up to 12 cells voltages. The board also has two analogue inputs for temperature as well.

Moreover, the BMS board also provides balancing capability which can perform passive balancing for 12 cells. The balancing circuit for each cell consists of a balancing switch and couple of resistors which provides a bay pass circuit for the cell to dissipate extra electrical energy in form of thermal energy. The board communicates to outside world through the isolated SPI (Serial Peripheral Interface) channels. This communication method is considered as series communication where each device can talk to the adjacent device and the very end/first device move the communication to the master control board.

In addition, the BMS board is stackable which means multiple boards can be connected in series configuration to monitor a higher number of cells with higher voltages. In a stack of several BMS boards, the first BMS board is connected to the PC through USB cable, so there are couple of interfacing boards which change the isolated SPI, used between boards, to regular SPI and then to USB signals.

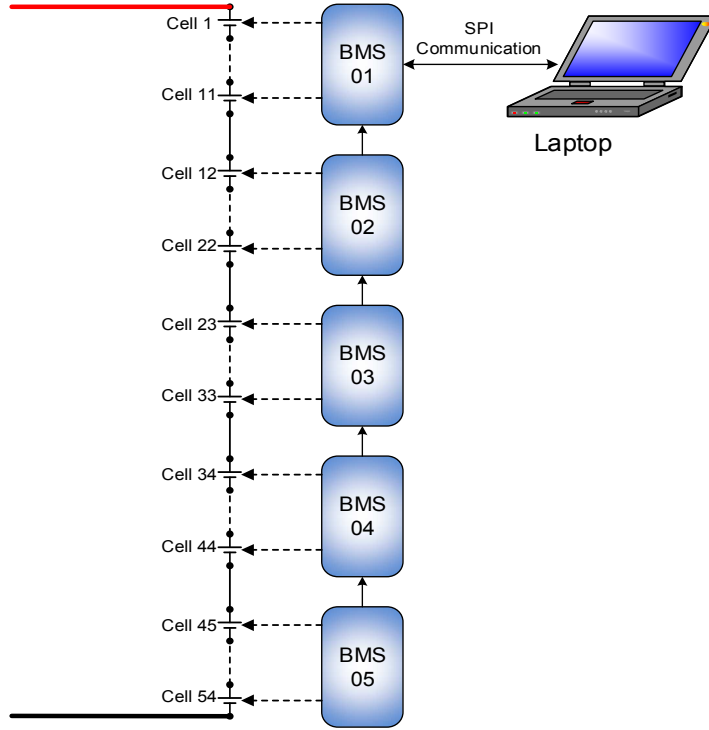


Figure 6.15: Block diagram of the 5 BMS boards monitor 54 cells in the battery pack. SPI communication is used to transfer information between the boards and laptop.

For 54 cells in the battery pack, 5 boards have been used. Figure 6.15 shows the block diagram of the 5 BMS boards monitoring 54 cells. To have even distribution of number of cells on boards, the first four boards each connects 11 cells and the last board monitors last 10 cells. Cell voltages are sensed across each cell terminals and twisted wires (to increase the signal immunity against noise/interfering signals) are used to transfer the cells voltage to the board inputs. The sensing signals transfer throughout SPI channels and end up to the PC.



Figure 6.16: 5 BMS boards monitor the Li-ion battery pack voltage and temperature.

The BMS boards collect all the cells voltages and transfer them to the laptop, which is connected to the system, to display voltages of the cells in a graphical user interface (GUI).

The software shows each cell's voltage and provide a visual way to detect if any cell's voltage is out of predetermined voltage range by dedicating a LED for each cell, so when the LED is green means the cell voltage is in the safe range, if it's yellow, then the related cell is under the minimum voltage and if the LED is red, means the cell voltage is over the maximum allowed voltage. The minimum and maximum allowed voltage can be adjusted in the GUI, see figure 6.17.

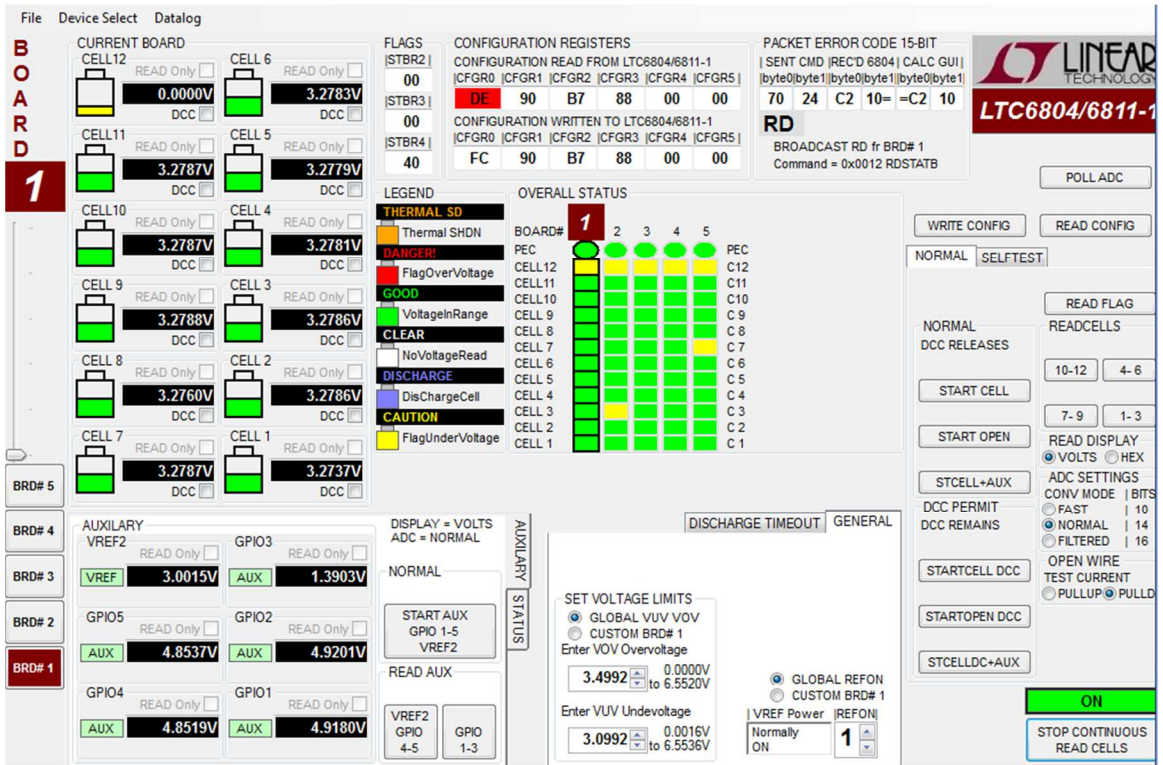


Figure 6.17: Screenshot of the BMS graphical user interface (GUI) used to read the data collected by the BMS boards.

Figure 6.18 shows the entire battery energy storage system including Li-ion battery pack with 54 LFP type cells, 5 BMS boards and the GUI. To ensure a safe operation, during the charging and discharging the pack, the GUI depicts cells voltages and it helps to detect if any cell acts weird with voltage out of range.

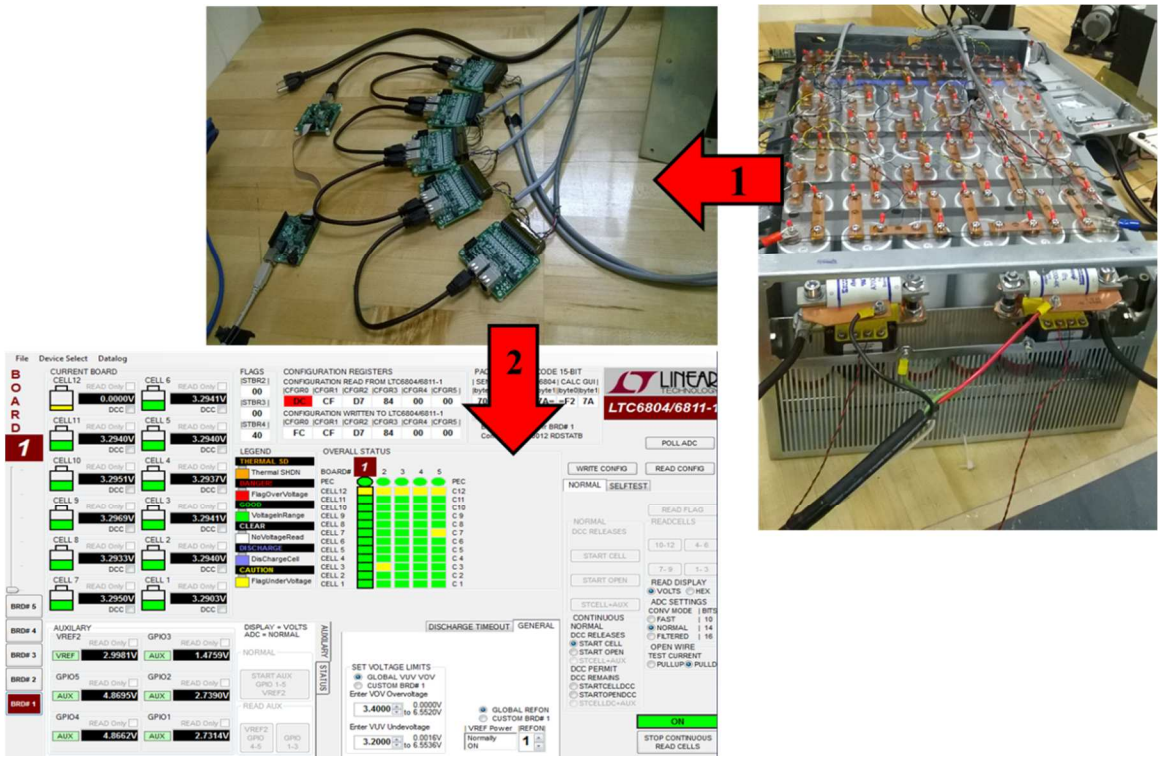


Figure 6.18: The battery energy storage system consists of Li-ion battery pack, BMS boards and the GUI.

6.3 The Power Interface

The power interface includes an AC/DC rectifier to connect the grid to the DC link and a DC/DC converter which connects the battery pack terminals to the DC link. Figure 6.19 shows block diagram of the testbed which is used in this project. The setup consists of three main sections, AC/DC grid tied rectifier, DC/AC grid tied inverter and the battery energy storage system. The DC link voltage in this system is 400 V and the inverter and rectifier are rated for up to 10 kW. The following sections explain each part.

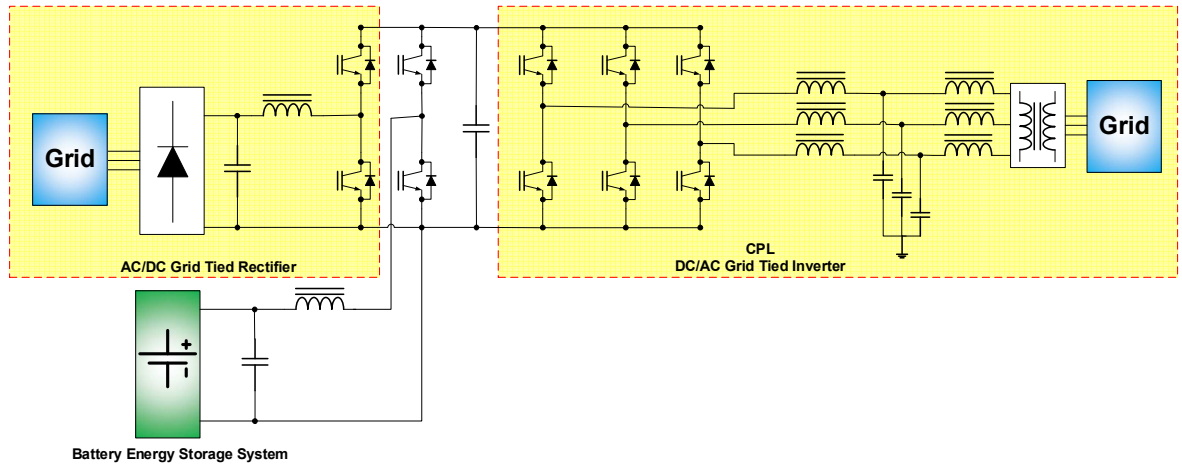


Figure 6.19: Block diagram of the DC UPS testbed

6.3.1 The Battery Energy Storage System Power Interface

The BESS power interface system consists of a DC/DC converter to connect the battery terminals to the DC link. The DC/DC converter operates as a boost converter in discharging cycle to boost the battery terminal to the DC link. The converter operates on buck mode during charging cycle. It's a two-quadrant converter which works with positive and negative currents but only positive voltage. The converter operates on voltage mode and regulates the DC link voltage. Figure 6.23 shows the FPGA-based Simulink model of the DC/DC section. The model is like the regular Simulink model but the control part is implemented via Altera DSP Builder Blockset, where the specific blocks are used to implement the control section. By using DSP Builder tool box, the required code for the FPGA control board is generated by the tool box. Once the model run and the results were satisfying, the VHDL code is generated by the tool box and can be directly download to the control board. Then, this model is the first step to run the system.

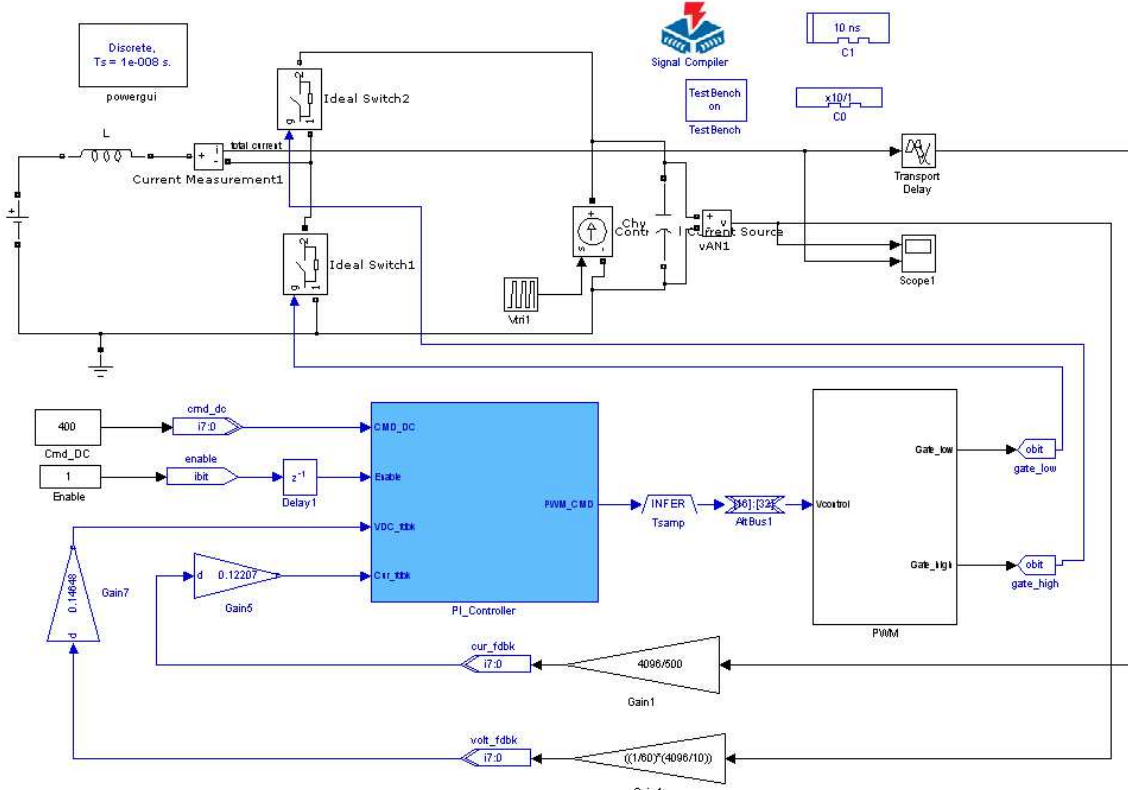


Figure 6.20: Implementation of dual-loop controller with DSP Builder Blocksets.

The PI_Controller block in the figure 6.24 is the implementation of the dual-loop control method, explained in the chapter 5, by using DSP Builder building blocks. The PWM block is also implementation of the PWM generator by using DSP Builder Blocksets. To verify the model and control technique, a variable load is attached to the model to check the performance of the converter under different modes, charging and discharging. All the measurements should be scaled down to the allowed range of ADC input channels, so the voltage and current measurement signals are multiplied to required factor to be in the safe range. Figure 6.24 shows the result of the model.

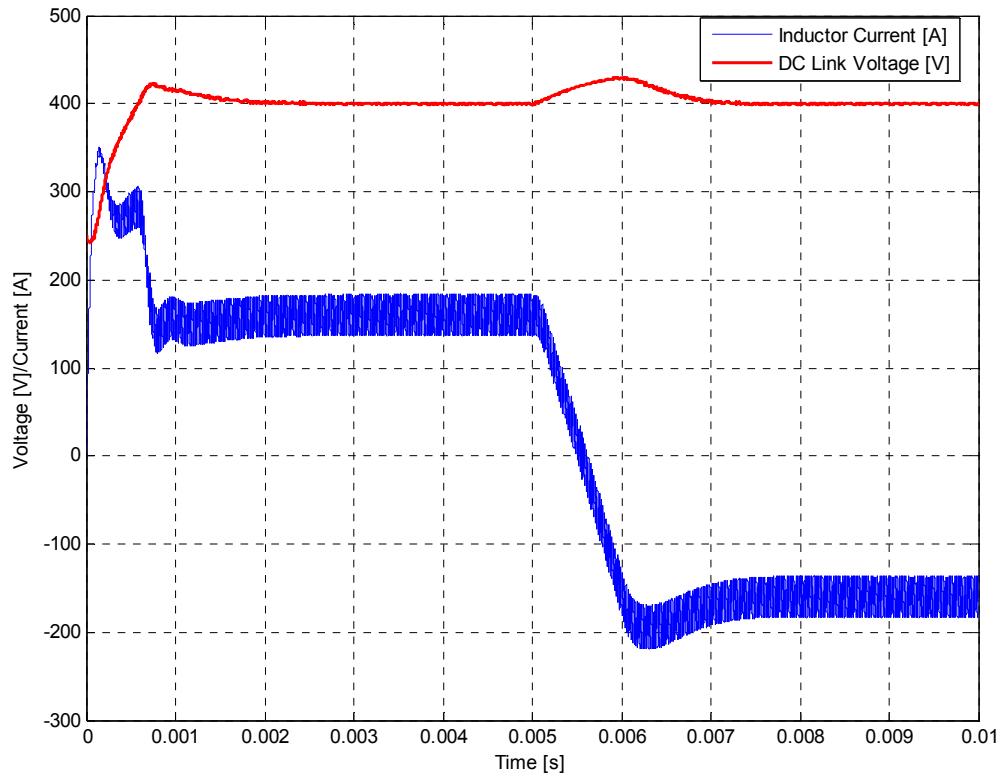


Figure 6.21: Results of the DC/DC controller implemented with DSP Builder Blocksets.

6.3.2 AC/DC Grid Tied Rectifier

The AC/DC grid tied rectifier consists of a three-phase diode bridge rectifier and a DC/DC boost converter to boost up the voltage after the diode bridge. The voltage after diode rectifier is around $\sqrt{2} \times 208 \text{ VAC} \cong 293 \text{ VDC}$ and the DC link voltage is set at 400 VDC, then a boost DC/DC converter is used to gain the diode bridge voltage up to 400 VDC. The converter operates on current mode and delivers a constant power to the link. The implementation of the rectifier is similar to the DC/DC converter, except the current mode control is used rather than voltage mode.

6.3.3 The DC/AC Grid Tied Inverter: The Constant Power Load

A three-phase grid tied inverter is utilized as the constant power load (CPL). The inverter operates on current mode and controlled by the direct power control (DPC) method as explained in chapter 5. The DPC method ensures to deliver requested power to the grid regardless to the DC link voltage. The inverter is rated for 10 kW. Figure 6.22 shows the simulation model used and the FPGA based implementation with DSP Builder Blockset and the result, phase current, depicted in figure 6.23.

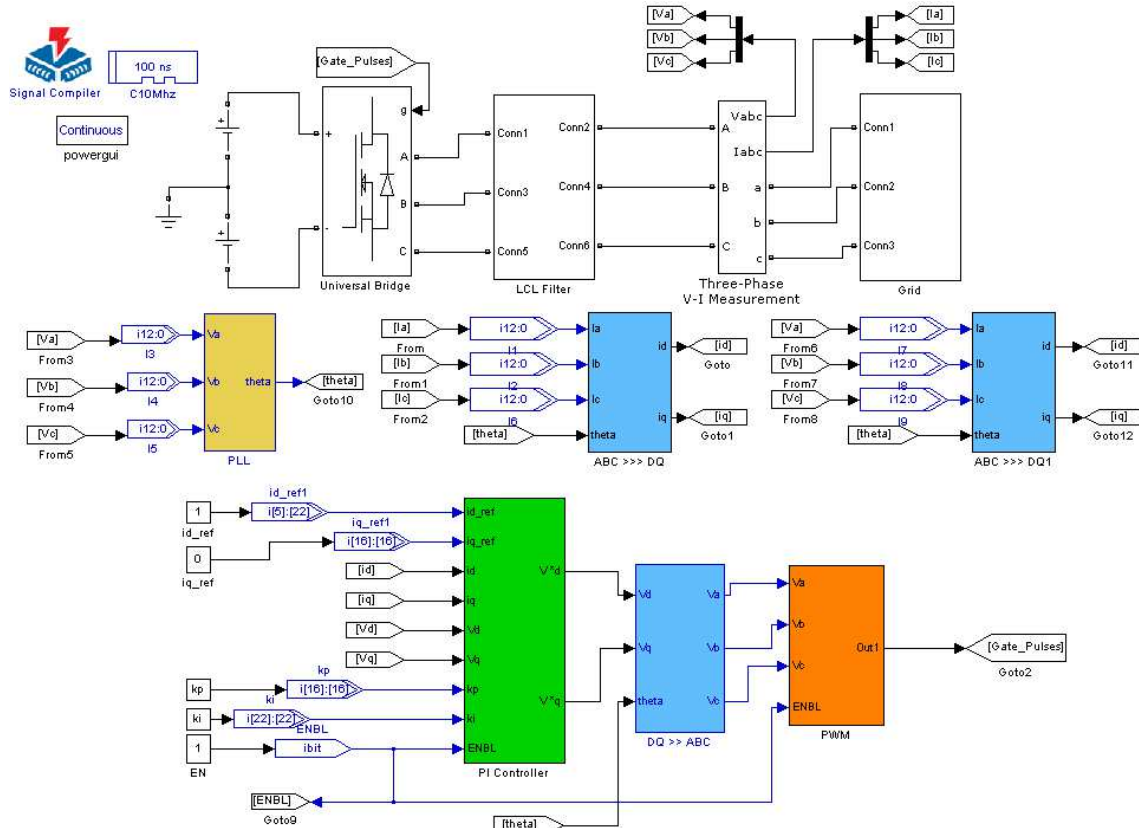


Figure 6.22: Implementation of the Inverter (CPL) controller with DSP Builder Blocksets.

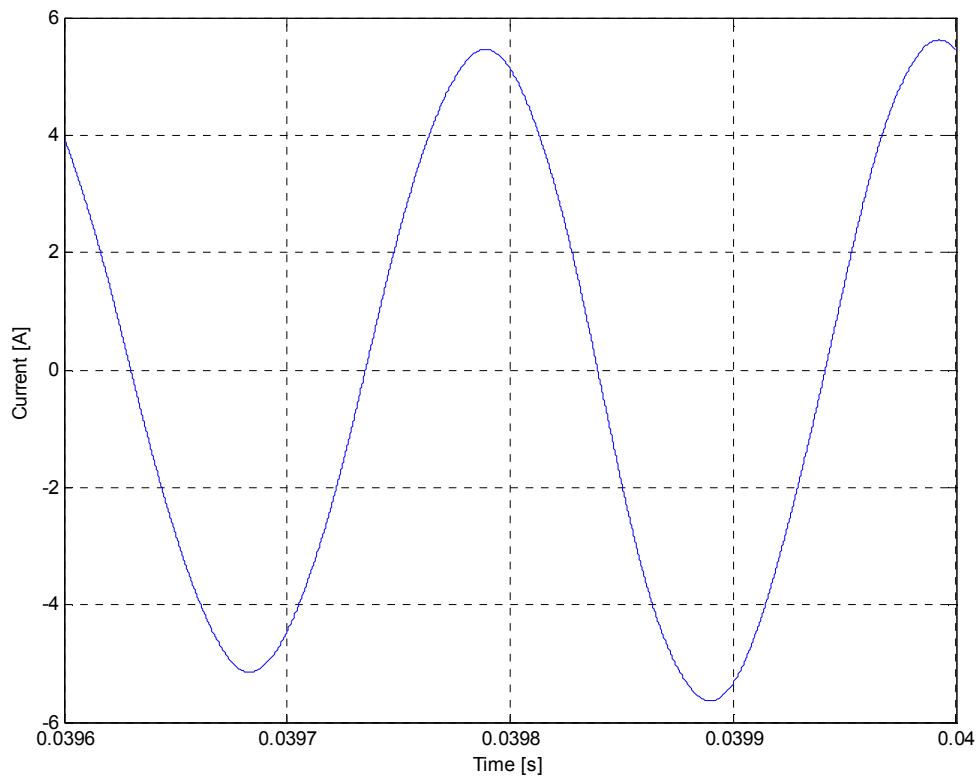


Figure 6.23: Results of the inverter model implemented with DSP Builder Blocksets.

6.4 Results for Different Modes of Operation

A DC UPS testbed as presented in figure 6.19 is developed to verify the DC UPS concept and performance during different operational modes. Figure 6.24 shows the testbed in the lab. The DC UPS testbed includes rectifier, inverter and battery power interface all in one box. The testbed is controlled with a FPGA board and different sections of the system were simulated by using DSP Builder toolbox in MATLAB and the required VHDL code in auto generated from the Simulink and downloaded to the controller board. Several modes of operation are considered and the results are presented.

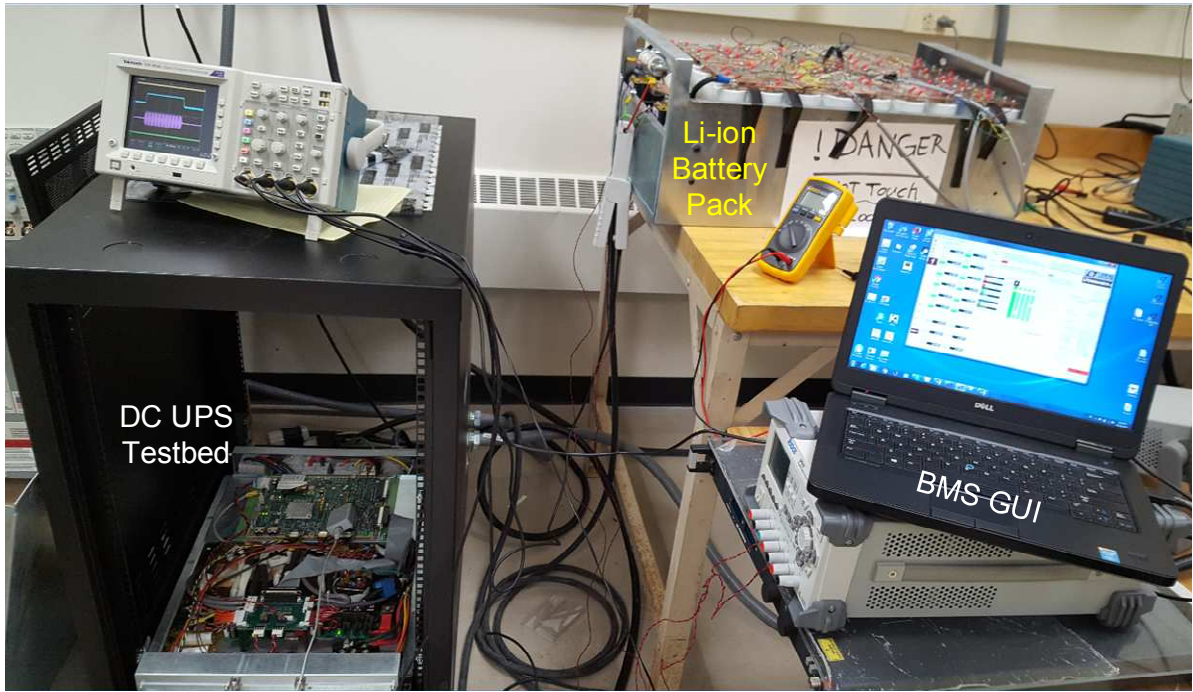


Figure 6.24: The DC UPS testbed, Li-ion battery pack and the BMS

Figures 6.25 and 6.26 illustrate the system operation in mode I. During this mode, power from the grid and BESS are supplying the CVL, the 0.3 kW resistive load, and the CPL, the 2.5 kW grid tied inverter.

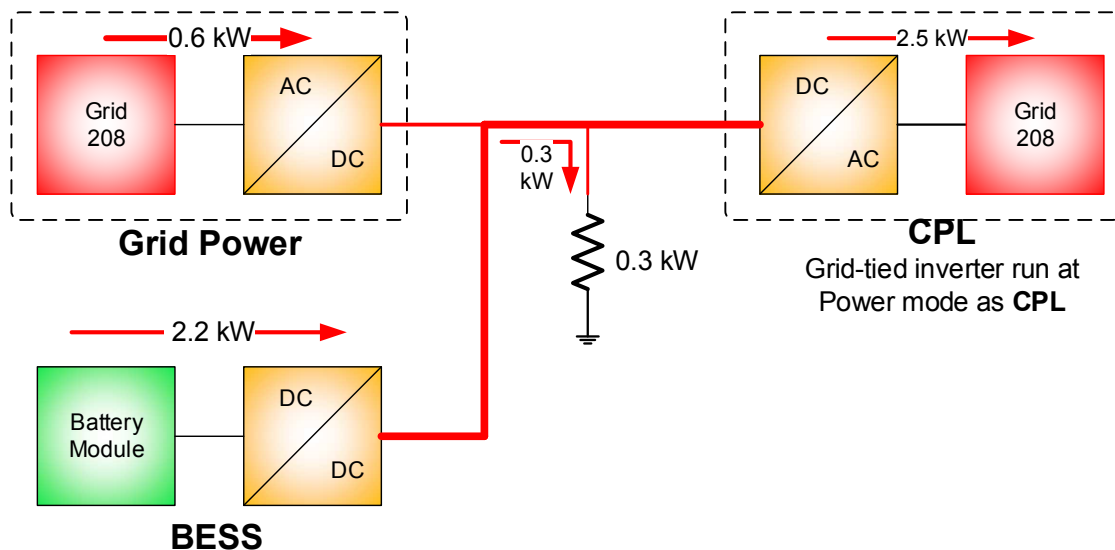


Figure 6.25: Block diagram of the DC UPS testbed in mode I

Figure 6.26 shows the power exchange between the battery, grid and loads during mode I of operation.

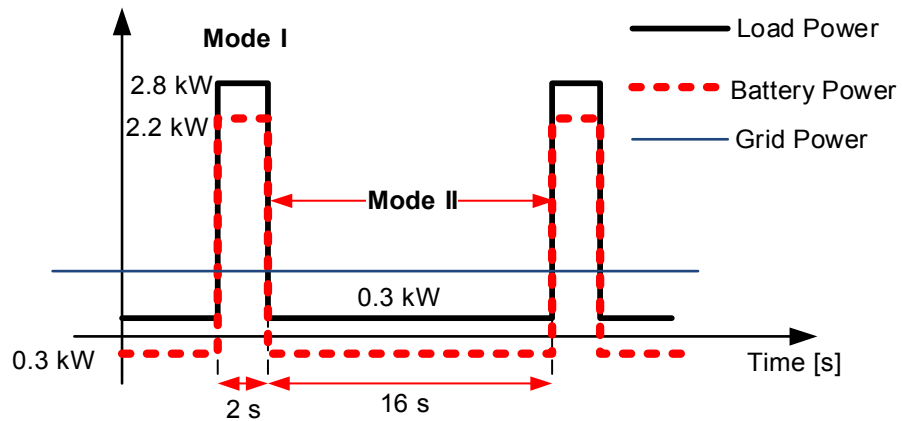


Figure 6.26: Power exchange between the battery, grid and load in the DC UPS during mode I.

Figure 6.27 presents the waveforms of the DC UPS testbed transition when the system operates between modes I and II. During the transition from mode I to II and vice versa, the Dc link voltage maintains regulated at 400 V.

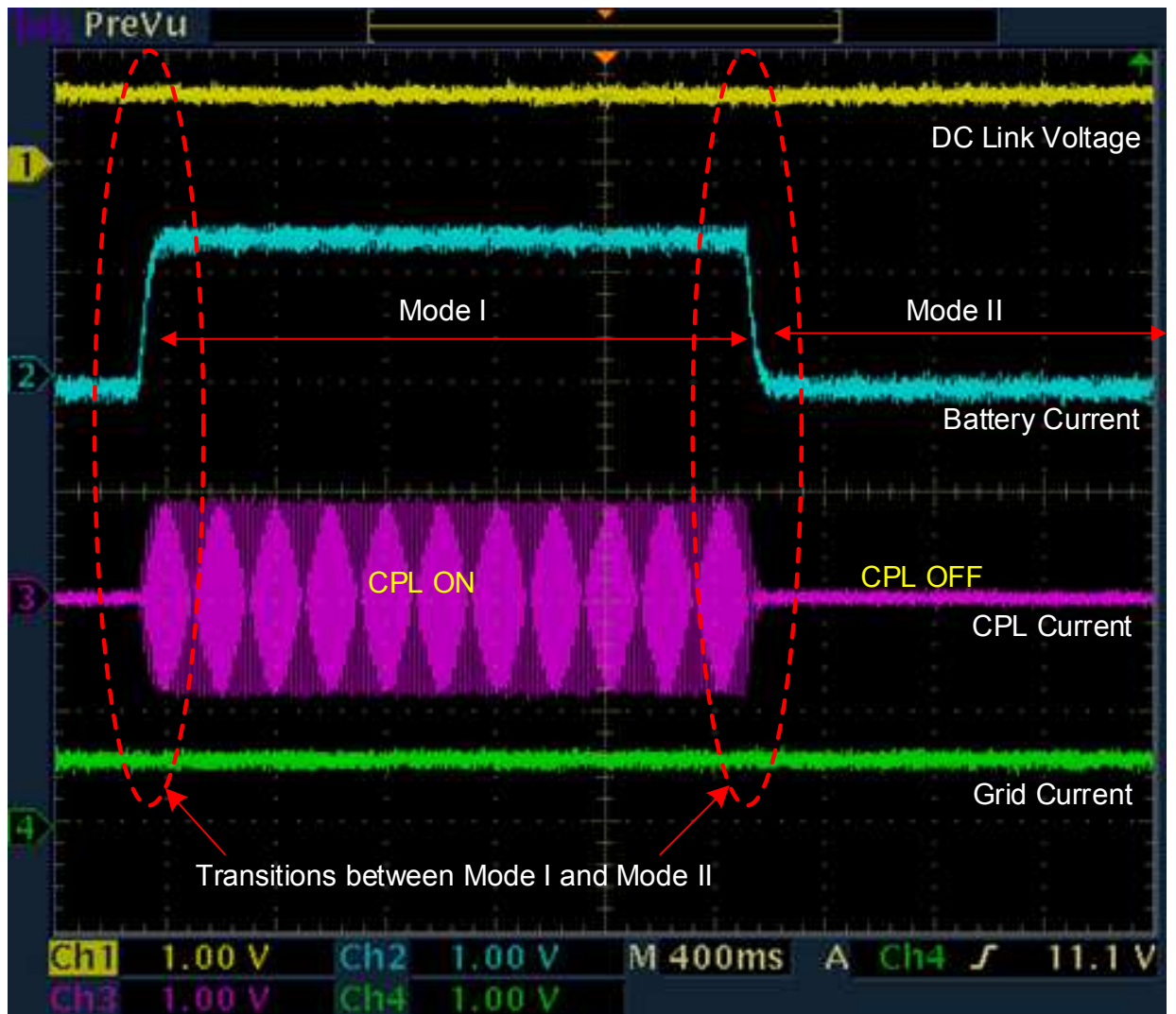


Figure 6.27: Waveforms of the DC UPS testbed operating between modes I and II.

Figure 6.27 shows the system's waveforms during mode I and mode II and the transition between these modes. The grid power stays constant as well as DC link voltage while the inverter turns on and delivers 2.5 kW to the grid.

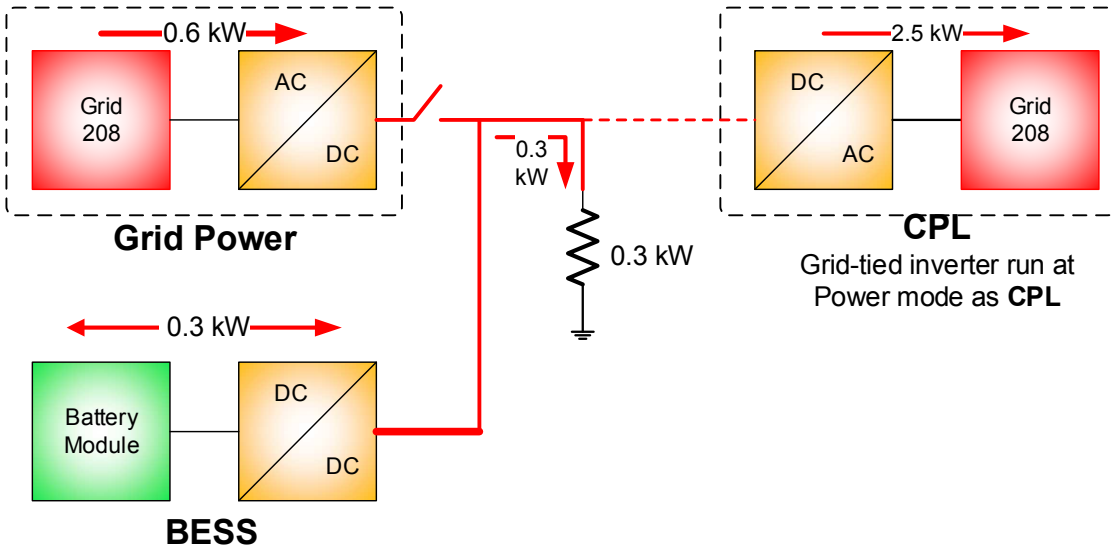


Figure 6.28: Block diagram of the DC UPS system during grid disconnection.

Figure 6.28 through 6.30 shows the system performance during mode II when the battery is charging and grid is providing constant power to support CVL power demand and also battery charging with low rate.

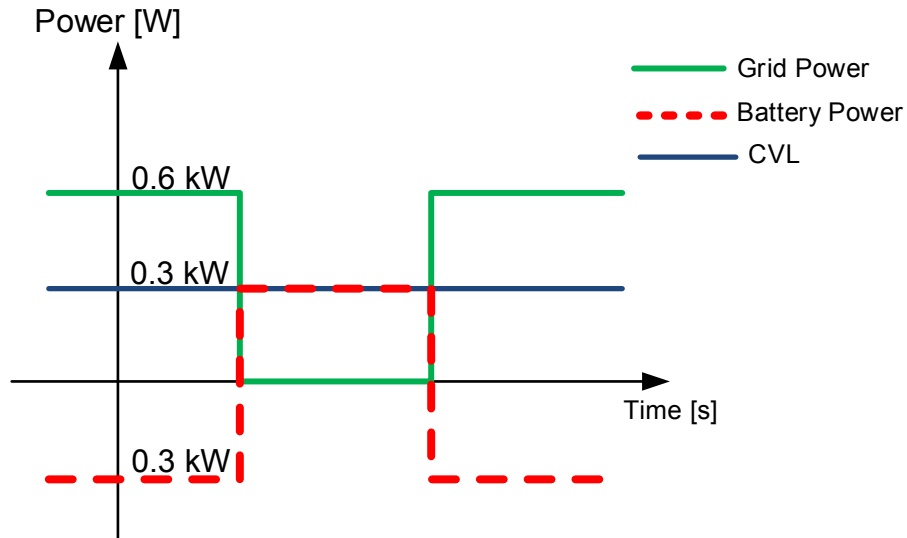


Figure 6.29: Power exchange between the DC UPS system during the grid disturbance. The battery state changes from being charge with low rate to discharge low rate to compensate the disturbance from grid.

Figure 6.28 shows the block diagram of the system during this mode. A disturbance from grid disconnects grid from the system. The controller changes the battery state from charging to discharging to provide required power for the CVL while grid is out. Figure 6.29 shows the power flow between system components during this mode while the disturbance appears.

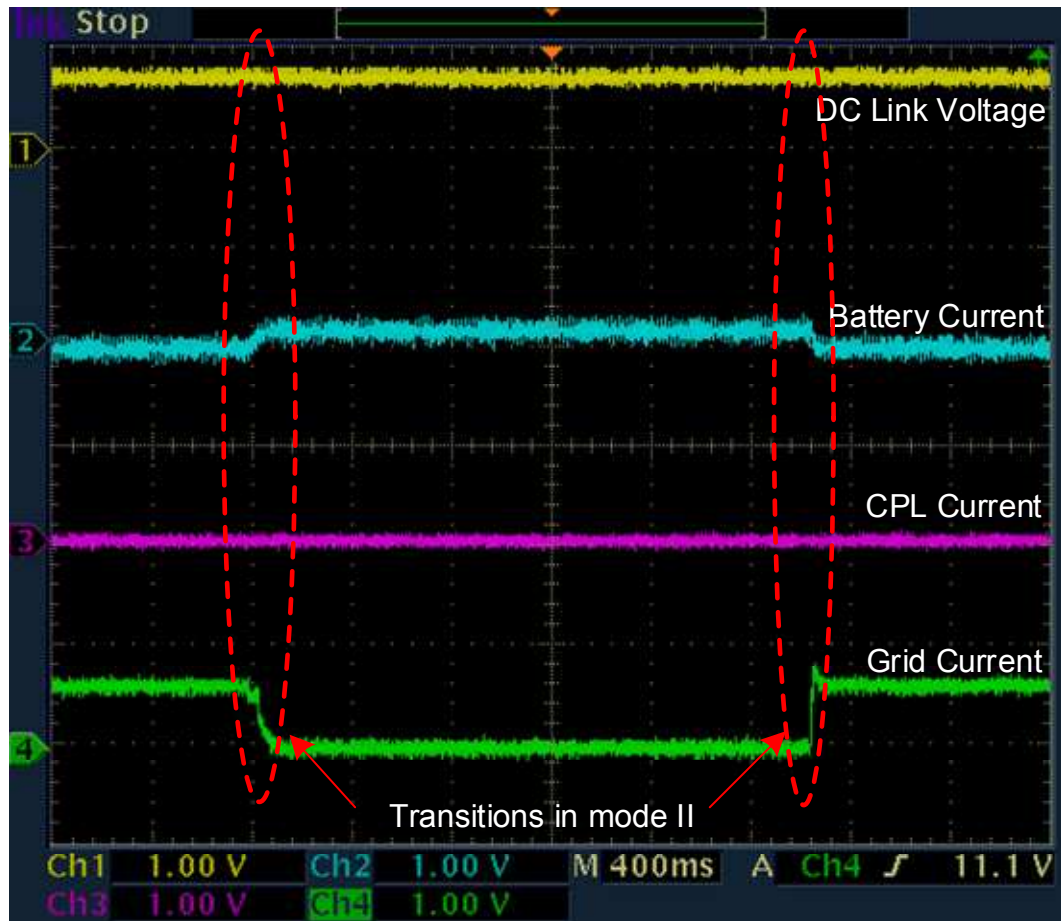


Figure 6.30: Performance of the DC UPS testbed during mode II, when grid is disconnected and connected again (grid disturbance). The battery current changes from negative value (charging) to positive value (discharging) in order to respond to the disturbance.

The system waveforms during this disturbance from grid are depicted in figure 6.30. The figure shows that while the battery current changes from negative to positive to support the power demand by CPL, the DC link voltage maintains regulated.

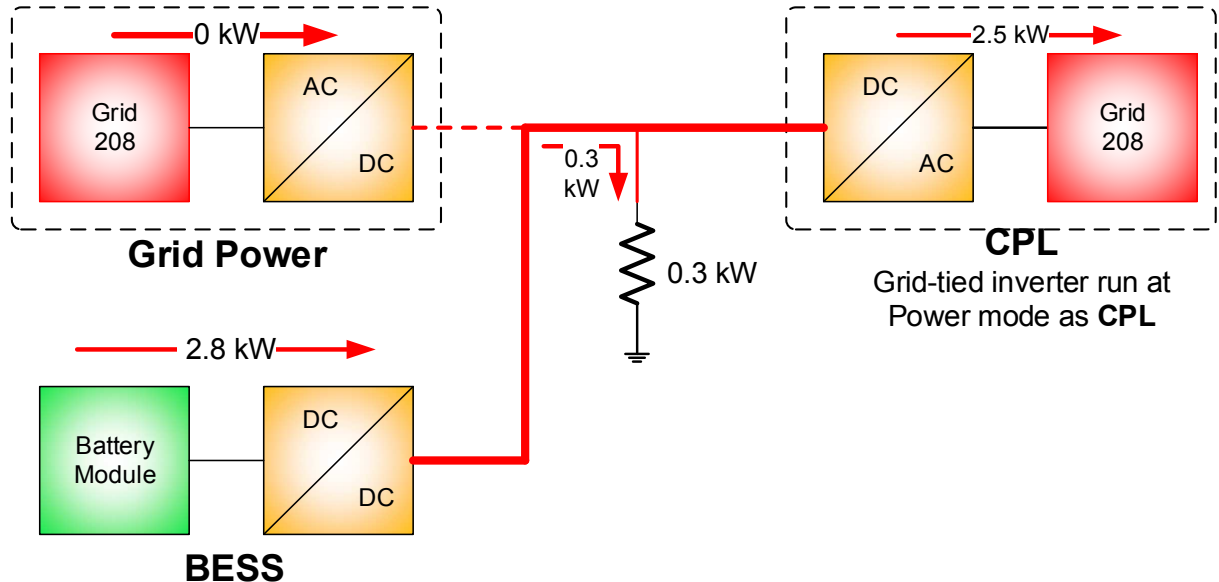


Figure 6.31: Block diagram of the DC UPS testbed and power flow during the mode IV, the UPS mode.

Figures 6.31 and 6.32 illustrate the system operation in mode IV, the UPS mode when the grid is out and battery provide the entire power. During this mode, power from the BESS is fed to the CVL, the 0.3 kW resistive load, and the CPL, the 2.5 kW grid tied inverter.

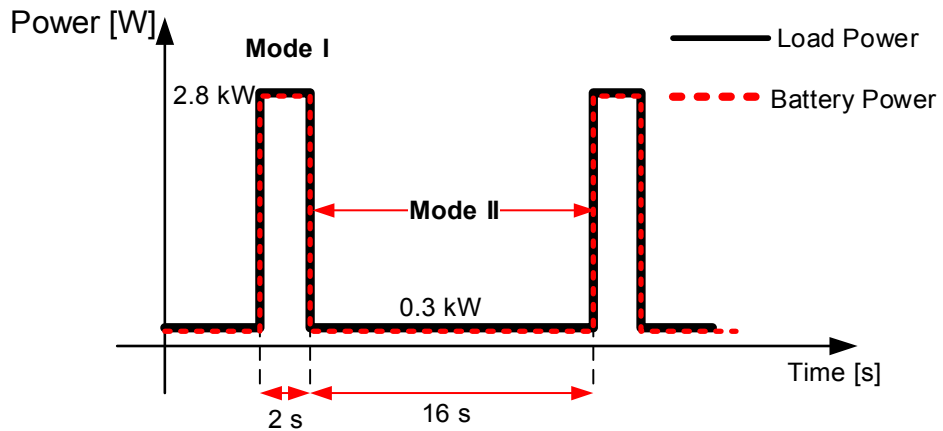


Figure 6.32: Power exchange between the battery and load in the DC UPS during mode IV, UPS mode; battery provides whole power

Figure 6.31 shows the system block diagram during this mode, UPS mode when the grid is out and as presented in figure 6.32, the power flow is from battery to the loads, CVL and CPL. Battery will be able to provide pulsed peak power as well as the average power.

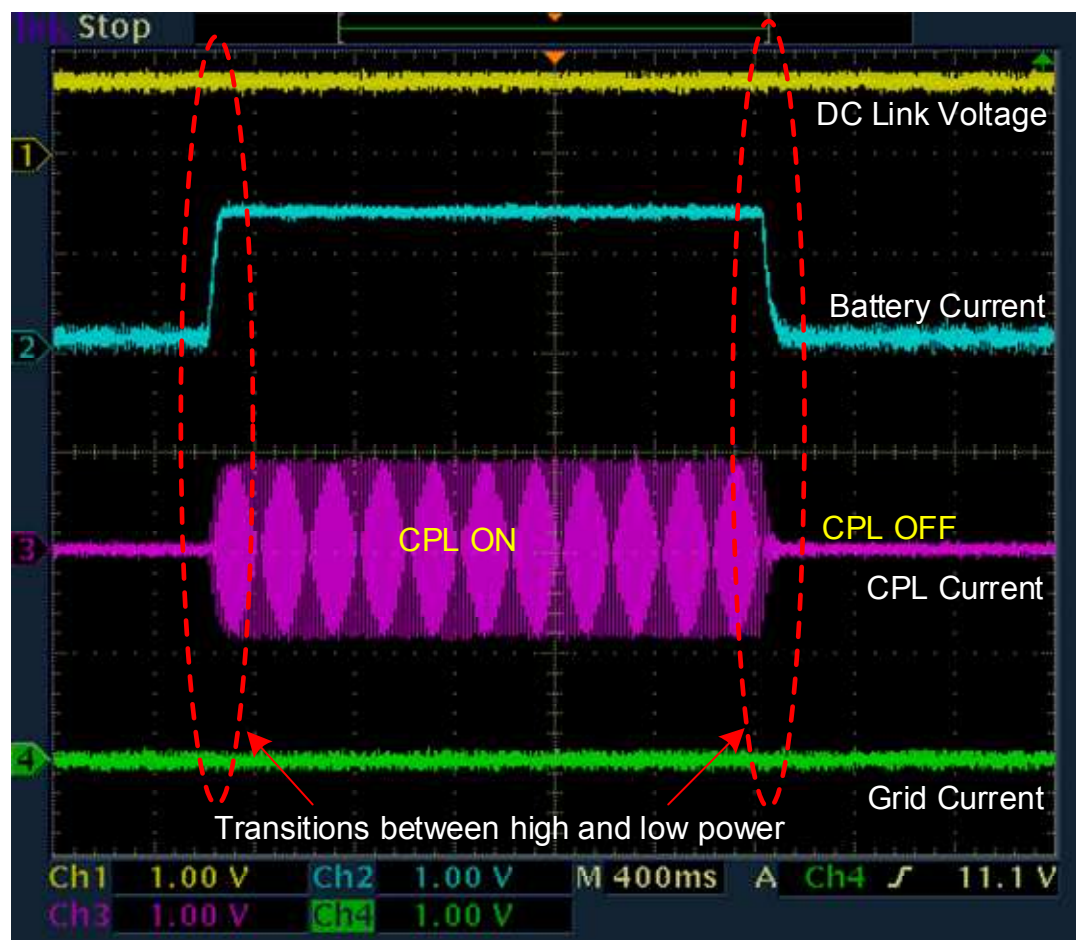


Figure 6.33: Waveforms of the DC UPS testbed operating on mode IV, the UPS mode, when the grid is out.

Chapter VII: Conclusion

A novel UPS system topology, DC line-interactive UPS, has been introduced. All the existing topologies have been reviewed and their performances along with advantageous and drawbacks associated with each configuration were briefly explained. These UPS systems are AC based where the power flow in the system has AC characteristic. The new proposed UPS system, however is based on the DC concept where the power flow in the system has DC characteristic. The new DC UPS system has several advantageous such as lower size, cost and weight due to replacing the three-phase dual converter in the on-line UPS system with a single stage single phase DC/DC converter and thus higher efficiency is expected.

The proposed system will also provide load leveling feature for the main AC/DC rectifier which has not been offered by conventional AC UPS systems. It applies load power smoothing to reduce the rating of the incoming AC line and consequently reduce the installation cost and time. Moreover, the new UPS technology improves the medical imaging system up-time, reliability, efficiency, and cost, and is applicable to several imaging modalities such as CT, MR and X-ray as well.

A comprehensive investigation on the energy storage were conducted to select down an appropriate energy storage type and chemistry. Based on the study results, couple of most promising Li-ion cell chemistries, LFP and NCA types, were chosen for further aggressive current tests.

The performance of the DC UPS has also been investigated. The mathematical models of the system while loaded with constant power load (CPL) and constant voltage load (CVL)

during all four modes of operation are obtained by means of the state space averaged modeling technique. Model of the nonlinear constant power load (CPL) is developed and used in the system models. According to the fact that the achieved system models are nonlinear, the small signal stability analysis technique has been utilized to further investigate on the stability of the system. Thus, transfer functions of outputs versus inputs were extracted and their related stability region based on the Routh-Hurwitz stability criteria were found.

The AC/DC rectifier was controlled independently due to system configuration. The rectifier operates on current mode and managed by direct power control method. The rectifier provides a constant power with unity power factor to the DC link regardless the voltage of the link, as the voltage regulates by the DC/DC converter.

The DC/DC converter regulates the DC link voltage and at the same time provides required pulsed peak power and manages the DC link voltage transients. Two different control techniques were proposed to control the DC/DC converter. A linear dual-loop control (DLC) scheme and a nonlinear robust control, a constant frequency sliding mode control (CFSMC) were investigated. The DLC offers a two controller loops to control the battery current and output voltage, including a series proportional-integral compensation controller for the current inner loop controller, and another series proportional-integral compensation controller for voltage outer loop. The performance of the controller during different conditions including system's four modes of operation were presented. The transients during mode transfers were studied. Overall, the DLC performance was convincing, however the controller has a limited stability region due to the linearization process and

negative incremental impedance characteristics of the CPL which challenge the stability of the system.

The sliding mode controller which is one of the robust controller schemes also introduced to the DC UPS system. Robust controllers are well-known for their stability and robustness and usually preferred when dealing with a nonlinear system with imprecise model. The imprecision may come from the actual uncertainty from the plant or from a purposeful choice of the simplified representation of the model's dynamics which is the one in this case.

A constant switching frequency SMC is developed based on the DC UPS system and the performance of the system were presented during different conditioned and transients during mode transfer were simulated and results were shown. The controller performances were met the control goals of the system. The voltage drop during mode transitions, was less than 2% of the rated output voltage.

Finally, the experimental results were presented. The high current discharge tests on each selected Li-ion cell were performed and results presented. A testbed was introduced to verify the DC UPS system concept. The test results were presented and verified the proposed concept.

Recommendations and Future Steps

Several recommendations based on the DC UPS system:

1. Since the emphasis of the proposed DC UPS system is on the battery pack and the fact that the electrochemical reactions of the Li-ion batteries are yet to investigate,

it is important to conduct a test to stress the batteries with several stress factors, such as depth of discharge, discharging current and temperature. These factors play a significant role in the performance of the battery pack and it is also required to conduct the test long enough to see the effect of each factor on the battery performance and on the Li-ion battery aging.

2. Develop another testbed at nominal rate of the proposed system to further investigate the transitions during mode changes.
3. Developing the CFSMC on a new testbed which has capability of switching with higher frequencies.
4. The AC/DC rectifier can be replaced with a high frequency resonant converters in which performing at higher frequency reduces the size of the system transformer and filter parameters.
5. SiC (Silicon Carbide) switches can be used rather than regular IGBT switches in order to increase the switching frequency and reducing the switching losses.

REFERENCES

- [1] A. Emadi, A. Nasiri, and S. B. Bekiarov, “Uninterruptible Power Supplies and Active Filters”, Boca Raton, FL: CRC Press, Oct. 2004.
- [2] S. B. Bekiarov and A. Emadi, “Uninterruptible power supplies: classification, operation, dynamics, and control”, in Proc. 17th Annu. IEEE Appl. Power Electron. Conf., Dallas, TX, Mar. 2002, pp. 597–604.
- [3] Ho, W.J., Lio, J.B. and Feng, W.S., “Economic UPS structure with phase-controlled battery charger and input-power-factor improvement”, IEE Proceedings of Electric Power Applications, 144 (4), 221–226, 1997
- [4] Krishnan, R. and Srinivasan, S., “Topologies for uninterruptible power supplies”, in Proceedings of the IEEE International Symposium on Industrial Electronics, Hungary, June 1993, pp. 122–127.
- [5] Martinez, S., Castro, M., Antoranz, R. and Aldana, F., “Off-line uninterruptible power supply with zero transfer time using integrated magnetics”, IEEE Transactions on Industrial Electronics, 36 (3), 629–635, 1989.
- [6] A. Nasiri, Z. Nie, S. B. Bekiarov, and A. Emadi, “An On-Line UPS System With Power Factor Correction and Electric Isolation Using BIFRED Converter”, IEEE TRANSACTIONS ON INDUSTRIAL ELECTRONICS, VOL. 55, NO. 2, FEBRUARY 2008
- [7] S. H. Bukhari, T. A. Lipo, B. Kwon, “An On-Line UPS System that Eliminates the Inrush Current Phenomenon While Feeding Multiple Load Transformers”, IEEE Transactions on Industry Applications, vol. PP, no. 99, 2016
- [8] F. Kamran, and T. Habetler, “A novel on-line UPS with universal filtering capabilities”, IEEE Transactions on Power Electronics, 13 (2), 366–371, 1998.
- [9] J. Choi, J. Kwon, J. Jung, and B. Kwon, “High-performance online UPS using three-leg-type converter”, IEEE Trans. Ind. Electron., vol. 52, no. 3, pp. 889–897, Jun. 2005.
- [10] M. Aamir, S. Mekhilef, “An Online Transformer-less Uninterruptible Power Supply (UPS) System With a Smaller Battery Bank for Low-Power Applications”, IEEE Transactions on Power Electronics, vol. 32, no. 1, 2017
- [11] G. Joos, Y. Lin, P. Ziogas, and I. Lindsay, “An online UPS with improved input-output characteristics”, in Proceedings of the 7th IEEE Applied Power Electronics Conference, Feb. 1992, pp. 598–605.
- [12] J. Wu, and H. Jou, “A new UPS scheme provides harmonic suppression and input power factor correction”, IEEE Transactions on Industrial Electronics, 42 (6), 216–226, 1995.
- [13] M. Tsai and C. Liu, “Design and implementation of a cost-effective quasi line-interactive UPS with novel topology”, IEEE Trans. Power Electron., vol. 18, no. 4, pp. 1002–1011, Jul. 2003.

- [14] H. Kim, J. Ji, J. Kim, S. Sul, and K. Kim, “Novel topology of a line interactive UPS using PQR instantaneous power theory”, in Proc. 39th IEEE Ind. Appl. Annu. Meeting, 2004, vol. 4, pp. 2232–2238.
- [15] H. Jou, J. Wu, C. Tsai, K. Wu, and M. Huang, “Novel line-interactive uninterruptible power supply”, in Proc. Inst. Elect. Eng.—Electric Power Appl., 2004, vol. 151, no. 3, pp. 359–364.
- [16] S. A. O Da Silva, P. F. Donoso-Garcia, and P. C. Cortizo, “A three phase series-parallel compensated line-interactive UPS system with sinusoidal input current and sinusoidal output voltage”, in Proc. 34th IEEE Ind. Appl. Soc. Annu. Meeting, 1999, pp. 826–832.
- [17] A. Nasiri, “Digital Control of Three-Phase Series-Parallel Uninterruptible Power Supply Systems”, IEEE TRANSACTIONS ON POWER ELECTRONICS, VOL. 22, NO. 4, JULY 2007
- [18] Rathmann, S. and Warner, H.A., “New generation UPS technology, the delta conversion principle”, in Proceedings of the 31st IEEE Industry Applications Society Annual Meeting, Oct. 1996, pp. 2389–2395.
- [19] Windhorn, A., “A hybrid static/rotary UPS system”, IEEE Transactions on Industry Applications, 28 (3), 541–545, 1992.
- [20] Hung, W.W. and McDowell, G.W.A., “Hybrid UPS for standby power systems”, Power Engineering Journal, 4 (6), 281–291, 1990.
- [21] W. Lee, B. Han, and H. Cha, “Battery Ripple Current reduction in a Three-Phase Interleaved DC-DC Converter for 5kW Battery Charger”, IEEE Energy Conversion Congress and Exposition (ECCE), Phoenix, USA, 2011.
- [22] V. S. Nguyen, V. L. Tran, W. Choi, and D. W. Kim, “Analysis of the output ripple of the DC-DC boost charger for Li-Ion Batteries”, Journal of Power Electronics, vol. 14, no. 1, pp. 135-142, 2014.
- [23] M. Kabalo, B. Blunier, D. Bouquain, and A. Miraoui, “Comparison Analysis of High Voltage Ratio Low Input Current Ripple Floating Interleaving Boost Converters for Fuel Cell Applications”, IEEE Vehicle Power and Propulsion Conference (VPPC), Sep. 2011
- [24] M. Kabalo, D. Paire, B. Blunier, D. Bouquain, “Experimental Validation of High-Voltage-Ratio Low-Input-Current-Ripple Converters for Hybrid Fuel Cell Supercapacitor Systems”, IEEE Transactions on Vehicular Technology, vol. 61, no. 8, 2012
- [25] M. Kabalo , B. Blunier , D. Bouquain, M. Simões, A. Miraoui, “Modeling and Control of 4-phase Floating Interleaving Boost Converter”, 37th Annual Conference on IEEE Industrial Electronics Society, IECON, Nov. 2011.
- [26] J. C. Hwang, L. H. Chen, S. N. Yeh, “Comprehensive analysis and design of multi-leg fuel cell boost converter”, J. Applied Energy, vol.84, Iss. 12, pp. 1274-1298, 2007.

- [27] G. Choe, J. Kim, H. Kang, and B. Lee, "An Optimal Design Methodology of an Interleaved Boost Converter for Fuel Cell Applications", Journal of Electrical Engineering & Technology, vol. 5, no. 2, pp. 319-328, 2010.
- [28] M Kabalo, D. Paire, B. Blunier, D. Bouquain, M. G. Simoes and A. Miraoui, "Experimental evaluation of four phase floating interleaved boost converter design and control for fuel cell applications", IET power Electronics, vol. 6, Iss. 2, pp. 215-226,
- [29] O. Hegazy, J. V. Mierlo, and P. Lataire, "Control and analysis of an integrated bidirectional DC/AC and DC/DC converters for plug-in hybrid electric vehicle applications", J. Power Electronics, vol. 11, no. 4, pp. 408-417, 2011.
- [30] A. Emadi, and M. Ehsani, "Negative Impedance Stabilizing Controls for PWM DC-DC Converters sing Feedback Linearization Techniques", Intersociety Energy Conversion Engineering Conference and Exhibit, (IECEC), NV, USA, Jul. 2000.
- [31] A. Emadi, "Modeling of Power Electronic Loads in AC Distribution Systems Using the Generalized State-Space Averaging Method", IEEE Transaction on Industrial Electronics, vol. 51, no. 5, pp. 992–1000, Oct. 2004.
- [32] A. Rahimi; G. Williamson; A. Emadi, "An Analytical Investigation of DC/DC Power Electronic Converters With Constant Power Loads in Vehicular Power Systems", IEEE Transactions on Vehicular Technology, vol. 58, no. 6, 2009.
- [33] D. Rastler, "Electricity Energy Storage Technology Options; a white paper primer on applications, costs and benefits", Electric Power Research Institute (EPRI), technical update, 2010.
- [34] S. Vazquez, S. M. Lukic, E. Galvan, L. G. Franquelo, and J. M. Carrasco, "Energy Storage Systems for Transport and Grid Applications", IEEE Transactions on Industrial Electronics, vol. 57, no. 12, pp.3881-3895, 2010.
- [35] A. Khaligh, and Z. Li, "Battery, Ultracapacitor, Fuel Cell, and Hybrid Energy Storage Systems for Electric, Hybrid Electric, Fuel Cell, and Plug-In Hybrid Electric Vehicles: State of the Art", IEEE Transactions on Vehicular Technology, vol. 59, no. 6, pp. 2806-2814, 2010.
- [36] A. R. Sparacino, G. F. Reed, R. J. Kerestes, B. M. Grainger, and Z. T. Smith, "Survey of battery energy storage systems and modeling techniques", IEEE Power and Energy Society General Meeting, pp. 1-8, USA, 2012.
- [37] A. Esmaili and A. Nasiri, "Energy storage for short-term and long-term wind energy support", Annual Conference on IEEE Industrial Electronics Society, IECON'2010, pp. 3281-3286, 2010.
- [38] B. McKeon, J. Furukawa and S. Fenstermacher, "Advanced Lead–Acid Batteries and the Development of Grid-Scale Energy Storage Systems", Proceedings of the IEEE, vol. 102, no. 6, pp. 951-963, 2014.
- [39] T. Horiba, "Lithium-Ion Battery Systems", Proceedings of the IEEE, Vol. 102, No. 6, pp. 939-950, 2014.

- [40] Z. Wen, "Study on Energy Storage Technology of Sodium Sulfur Battery and its Application in Power System", Proceedings of International Conference on Power System Technology, pp. 1-4, 2006.
- [41] Q. Fu, A. Hamidi, A. Nasiri, V. Bhavaraju, S. Krstic, P. Theisen, "The Role of Energy Storage in a Microgrid Concept, Examining the opportunities and promise of microgrids", IEEE Electrification Magazine, Vol. 1, No. 2, pp. 21-29, 2013.
- [42] H. Ibrahim, A. Ilincaa and J. Perronb, "Energy storage systems—Characteristics and comparisons", Renewable and Sustainable Energy Reviews, Vol. 12, No. 5, pp. 1221–1250, 2008.
- [43] D. Banham-Hall, G Taylor, C. Smith, and M. Irving, "Flow Batteries for Enhancing Wind Power Integration", IEEE Trans. Power System, Vol. 27, No. 3, pp. 1690-1697, 2012.
- [44] E. Manla, A. Nasiri, and M. Hughes, "Modeling of Zinc Energy Storage System for Integration with Renewable Energy", IEEE Industrial Electronics Conference, IECON'2009, pp. 3987-3992, 2009.
- [45] H. Liu, and J. Jiang, "Flywheel energy storage—An upswing technology for energy sustainability", Energy and Buildings, Vol. 39, No. 5, pp. 599–604, 2007
- [46] D. W. Dennis, V. S. Battaglia, and A. Belanger, "Electrochemical modeling of lithium polymer batteries", Journal of Power Sources, Vol. 110, No. 2, pp. 310-320, 2002.
- [47] J. Newan, K. E. Thomas, H. Hafezi, and D. R. Wheeler, "Modeling of lithium-ion batteries", Journal of Power Sources, Vol. 119, pp. 838-843, 2003.
- [48] K. Smith, C Rahn, and C. Wang, "Control oriented 1D electrochemical model of lithium ion battery", Energy Conversion Management, Vol. 48, No. 9, pp. 2565–2578, 2007
- [49] K. Smith, C. Rahn, and C. Wang, "Model-based electrochemical estimation and constraint management for pulse operation of lithium ion batteries", IEEE Transaction on Control Systems Technology, Vol. 18, No. 3, pp. 654-663, 2010.
- [50] K. Smith, "Electrochemical control of lithium-ion batteries", IEEE Control Systems, Vol 38, No. 2, pp. 18-25, 2010.
- [51] D. Rakhmatov, S. Vrudhula, and D. A. Wallach, "A model for battery lifetime analysis for organizing applications on a pocket computer", IEEE Transactions on VLSI Systems, Vol. 11, No. 6, pp. 1019–1030, 2003.
- [52] P. E. Pascoe and A. H. Anbukey, "VRLA battery discharge reserve time estimation", IEEE Transaction on Power Electronics, Vol. 19, No. 6, pp. 1515–1522, 2004.
- [53] M. Chen and G. A. Rincon-Mora, "Accurate electrical battery model capable of predicting runtime and I-V performance", IEEE Transactions on Energy Conversion, Vol. 21, No. 2, pp. 504-511, 2006.

- [54] R. C. Kroeze, and P.T. Krein, “Electrical battery model for use in dynamic electric vehicle simulations”, IEEE Power Electronics Specialists Conference, PESC’2008, pp. 1336-1342, 2008.
- [55] B. Schweighofer, K. M. Raab, and G. Brasseur, “Modeling of high power automotive batteries by the use of an automated test system”, IEEE Transactions on Instrumentation and Measurement, Vol. 52, No. 4, pp. 1087–1091, 2003.
- [56] S. Abu-Sharkh, and D. Doerffel, “Rapid test and non-linear model characterization of solid-state lithium-ion batteries”, Journal of Power Sources, Vol. 130, No. 1-2, pp. 266–274, 2003.
- [57] L. Gao, and S. Liu, “Dynamic Lithium-Ion Battery Model for System Simulation”, IEEE Transactions on Components and Packaging Technologies, Vol. 25, No. 3, pp. 495–505, 2002.
- [58] A. Hamidi, L. Weber, and A. Nasiri, “EV Charging Station Integrating Renewable Energy and Second-Life Battery”, International Conference on Renewable Energy Research and Applications (ICRERA), pp. 1217-1221, Spain, 2013.
- [59] L. Zubierta and R. Bonert, “Characterization of double-layer capacitor (DLCs) for power electronics application”, IEEE Transactions on Industrial Applications, Vol. 36, No. 1, pp. 199–205, 2000.
- [60] S. Sivakkumar, and A. Pandolfo, “Evaluation of lithium-ion capacitors assembled with pre-lithiated graphite anode and activated carbon cathode”, Electrochimica Acta, Vol. 65, pp. 280-287, 2012.
- [61] E. Manla, G. Mandic, and A. Nasiri, “Testing and Modeling of Lithium-Ion Ultracapacitors”, Energy Conversion Congress and Exposition (ECCE), pp. 2957-2962, USA, 2011.
- [62] G. Mandic and A. Nasiri, “Modeling and simulation of a wind turbine system with ultracapacitors for short-term power smoothing”, International Symposium on Industrial Electronics (ISIE), pp. 2431-2436, Italy, 2010.
- [63] N. Bertrand, O. Briat, J.-M. Vinassa, J. Sabatier, and H. El Brouji, “Porous electrode theory for ultracapacitor modelling and experimental validation”, IEEE Vehicle Power and Propulsion Conference (VPPC), pp. 1-6, 2008.
- [64] N. Bertrand, J. Sabatier, O. Briat, and J. M. Vinassa, “Embedded Fractional Nonlinear Supercapacitor Model and Its Parametric Estimation Method”, IEEE Transactions on Industrial Electronics, Vol. 57, No. 12, pp. 3991-4000, 2010.
- [65] L. Shi, and M. L. Crow, “Comparison of Ultracapacitor Electric Circuit Models”, IEEE PES General Meeting, pp. 1-6, 2008.
- [66] S. Buller, E. Karden, D. Kok and R.W. De Doncker, “Modeling the Dynamic Behavior of Supercapacitors Using Impedance Spectroscopy”, IEEE Transactions on Industry Applications, Vol. 38, No. 6, pp. 1622-1626, 2002.

- [67] W. Yang, J. E. Carletta, T. T. Hartley, and R. J. Veillette, “An ultracapacitor model derived using time-dependent current profiles”, Midwest Circuit and Systems, MWSCAS, pp. 726-729, 2008.
- [68] A.Grama, L. Grama, D. Petreus, and C. Rusu, “Supercapacitor Modelling Using Experimental Measurements”, International Signals, Circuits and Systems, ISSCS, pp. 1-4, 2009.
- [69] J. N. Marie-Francoise, H. Gualous, and A. Berthon, “Supercapacitor thermal and electrical behavior modeling using ANN”, IEEE Proceedings, Electric Power Applications, Vol. 153, No. 2, pp. 255-261, 2006.
- [70] D. Andrea, “Battery Management Systems for Large Lithium Ion Battery Packs”, Artech House, 1st Edition, ISBN 1608071049, UK, 2010.
- [71] Y. Xing, E. Ma, K. Tsui, and M. Pecht, “Battery Management Systems in Electric and Hybrid Vehicles”, Energies, Vol. 4, pp. 1840-1857, 2011.
- [72] K. Ng, C. Moo, Y. Chen, and Y. Hsieh, “Enhanced coulomb counting method for estimating state-of-charge and state-of-health of lithium-ion batteries”, Applied Energy, Vol. 86, No. 9, pp. 1506–1511, 2009.
- [73] J. Kozlowski, ”Electrochemical Cell Prognostics Using Online Impedance Measurements and Model-Based Data Fusion Techniques”, Proceedings of IEEE Aerospace Conference, Vol. 7, pp. 3257–3270, USA, 2003.
- [74] A. Salkind, C. Fennie, and P. Singh, “Determination of state-of-charge and state-of-health of batteries by fuzzy logic methodology”, Journal of Power Sources, Vol. 80, No. 1-2, pp. 293–300, 1999.
- [75] N. Windarko, J. Choi, and G. Chung, “SOC Estimation of LiPB Batteries Using Extended Kalman Filter Based on High Accuracy Electrical Model”, Proceedings of Power Electronics and ECCE Asia (ICPE & ECCE), pp. 2015-2022, Korea, 2011.
- [76] G. Plett, “Extended kalman filtering for battery management systems of LiPB-based HEV battery packs part 2. State and parameter estimation”, Journal of Power Sources, Vol. 134, pp. 277–292, 2004.
- [77] R. Xiong, H. He, F. Sun, and K. Zhao, “Evaluation on State of Charge Estimation of Batteries with Adaptive Extended Kalman Filter by Experiment Approach”, IEEE Transactions on Vehicular Technology, Vol. 62, No. 1, pp. 108-117, 2013.
- [78] J. Yan, G. Xu, Y. Xu, and B. Xie, “Battery State-of-Charge Estimation Based on H_∞ Filter for Hybrid Electric Vehicle”, Proceedings of International Conference on Control, Automation, Robotics and Vision (ICARCV 2008), pp. 464-469, Vietnam, 2008.
- [79] M. Gholizadeh and F. Salmasi, “Estimation of State of Charge, Unknown Nonlinearities, and State of Health of a Lithium-Ion Battery Based on a Comprehensive Unobservable Model”, IEEE Transactions on Industrial Electronics, Vol. 61, No. 3, pp. 1335-1344, 2014.

- [80] T. Hansen, and C. Wang, “Support vector based battery state of charge estimator”, Journal of Power Sources, Vol. 141, No. 2, pp. 351–358, 2004.
- [81] H. Lin, T. Liang, and S. Chen, “Estimation of Battery State of Health Using Probabilistic Neural Network”, IEEE Transactions on Industrial Informatics, Vol. 9, No. 2, pp. 679-685, 2013.
- [82] N. Watrin, B. Blunier, and A. Miraoui, “Review of adaptive systems for lithium batteries state-of-charge and state-of-health estimation”, Proceeding of IEEE Transactions on Electrification Conference, pp. 1–6, 2012.
- [83] M. Shahriari and M. Farrokhi, “Online state-of-health estimation of VRLA batteries using state of charge”, IEEE Transactions on Industrial Electronics, Vol. 60, No. 1, pp. 191–202, 2013.
- [84] Matthew T. Lawder, Bharatkumar Suthar, Paul W. C. Northrop, Sumitava De, C. Michael Hoff, Olivia Leitermann, Mariesa L. Crow, Shriram Santhanagopalan, and Venkat R. Subramanian, “Battery Energy Storage System (BESS) and Battery Management System (BMS) for Grid-Scale Applications”, Proceedings of IEEE, Vol. 102, No. 6, pp. 1014-1030, 2014.
- [85] B. S. Bhangu, P. Bentley, D. A. Stone, and C. M. Bingham, “Nonlinear Observers for Predicting State-of-Charge and State-of-Health of Lead-Acid Batteries for Hybrid-Electric Vehicles”, IEEE Transactions on Vehicular Technology, Vol. 54, No. 3, pp. 783-794, 2005.
- [86] A. Widodo, M. Shim, W. Caesarendra, and B. Yang, “Intelligent prognostics for battery health monitoring based on sample entropy”, Expert System Applications, Vol. 38, No. 9, pp. 11763–11769, 2011.
- [87] B. Saha, K. Goebel, S. Poll, and J. Christophersen, “Prognostics methods for battery health monitoring using a bayesian framework”, IEEE Transactions on Instrument and Measurement, Vol. 58, No. 2, pp. 291–296, 2009.
- [88] D. Stroe, M. Swierczy’nski, A. Stan, R. Teodorescu, and S. Andreasen, “Accelerated Lifetime Testing Methodology for Lifetime Estimation of Lithium-Ion Batteries Used in Augmented Wind Power Plants”, IEEE Transactions on Industry Applications, Vol. 50, No. 6, pp. 4006-4017, 2014.
- [89] J. Cao, N. Schofield, and A. Emadi, “Battery Balancing Methods: A Comprehensive Review”, IEEE Vehicle Power and Propulsion Conference (VPPC), pp. 1-6, China, 2008.
- [90] W. Bentley, “Cell balancing considerations for lithium-ion battery systems”, Proceeding of Annual Battery Conference on Applications and Advances, pp. 223-226, USA, 1997.
- [91] N. H. Kutkut, H. L. N. Wiegman, D. M. Divan and D. W. Novotny, “Charge equalization for an electric vehicle battery system”, IEEE Transaction on Aerospace and Electronics Systems, Vol. 34, No. 1, pp. 235-246, 1998.

- [92] S. Moore and P. Schneider, “A review of cell equalization methods for lithium ion and lithium polymer battery systems”, Proceeding of Society of Automotive Engineers, SAE, pp. 1-5, USA, 2001.
- [93] M. Uno, and K. Tanaka, “Influence of high-frequency charge–discharge cycling induced by cell voltage equalizers on the life performance of lithium-ion cells”, IEEE Transaction on Vehicular Technologies, Vol. 60, No. 4, pp. 1505–1515, 2011.
- [94] A. Emadi, B. Fahimi, and M. Ehsani, “On the concept of negative impedance instability in the more electric aircraft power systems with constant power loads”, presented at the 34th Intersoc. Energy Convers. Eng. Conf., Vancouver, BC, Canada, Aug. 2, 1999, 1999-01-2545.
- [95] A. Emadi, A. Khaligh, C. H. Rivetta, and G. A. Williamson, “Constant power loads and negative impedance instability in automotive systems: Definition, modeling, stability, and control of power electronic converters and motor drives”, IEEE Trans. Veh. Technol., vol. 55, no. 4, pp.1112–1125, Jul. 2006.
- [96] S. Yang, A. Bryant, P. Mawby, D. Xiang, L. Ran, and P. Tavner, “An industry-based survey of reliability in power electronic converters”, IEEE Trans. Ind. Appl., vol. 47, no. 3, pp. 1441–1451, May/Jun. 2011.
- [97] P. Magne, D. Marx, B. Nahid-Mobarakeh, and S. Pierfederici, “Large signal stabilization of a DC-Link supplying a constant power load using a virtual capacitor: Impact on the domain of attraction”, IEEE Trans. Ind. Appl., vol. 48, no. 3, pp. 878–887, May/Jun. 2012.
- [98] S. R. Huddy and J. D. Skufca, “Amplitude death solutions for stabilization of DC microgrids with instantaneous constant-power loads”, IEEE Trans. Power Electron., vol. 28, no. 1, pp. 247–253, Jan. 2013.
- [99] R. Teodorescu, M. Liserre and P. Rodríguez, “Grid converters for photovoltaic and wind power systems”, John Wiley & Sons, Ltd. ISBN: 978-0-470-05751-3, 2011
- [100] H. Khalil, “Nonlinear systems”, 3rd Edition, Pearson, USA, 2001.
- [101] J. E. Slotine and W. Li, “Applied nonlinear control”, 1st Edition, Prentice Hall, USA, 1991.
- [102] G. Spiazzi and P. Mattavelli, “Sliding-mode control of switched-mode power supplies”, The Power Electronics Handbook, Ch. 8, CRC Press, 2002.
- [103] V. Utkin, J. Guldner, and J. Shi, “Sliding mode control in electromechanical systems”, 1st Edition, Taylor & Francis, USA, 1999.
- [104] H. Sira-Ramirez, “A geometric approach to pulse-width modulated control in nonlinear dynamical systems”, IEEE Transactions on Automation Control, vol. 34, no. 2, pp. 184–187, 1989.
- [105] H. Sira-Ramirez and M. Rios-Bolivar, “Sliding mode control of DC to-DC power converters via extended linearization”, IEEE Transactions on Circuits and Systems I: Fundamental Theory and Applications, vol. 41, no. 10, pp. 652 – 661, 1994.

- [106] H. Sira-Ramirez, “On the generalized PI sliding-mode control of dc-to-dc power converters: A tutorial”, *International Journal Control*, vol. 76, no. 9-10, pp. 1018–1033, 2003.
- [107] H. Sira-Ramirez and M. Ilic, “A geometric approach to the feedback control of switch mode DC-to-DC power supplies”, *IEEE Transactions on Circuits Systems*, vol. 35, no. 10, pp. 1291–1298, Oct. 1988.
- [108] A. Sabanovic, “Sliding modes in power electronics and motion control systems”, *29th Annual Conference of the IEEE Industrial Electronics Society (IECON '03)*, vol. 1, pp.997 – 1002, Nov. 2003.
- [109] S. Tan, Y.M. Lai, M.K. Cheung and C.K.M. Tse, “On the practical design of a sliding mode voltage controlled buck converter”, *IEEE Transactions on Power Electronics*, vol. 20, no. 2, pp. 425-437, 2005.
- [110] S. Tan, Y. Lai, and C. Tse, “A unified approach to the design of PWM-based sliding-mode voltage controllers for basic DC-DC converters in continuous conduction mode”, *IEEE Transactions on Circuits and Systems—I: Regular Papers*, vol. 53, no. 8, 2006.
- [111] Y. Zhao, W. Qiao and D. Ha, “A Sliding-Mode Duty-Ratio Controller for DC/DC Buck Converters With Constant Power Loads”, *IEEE Transactions on Industry Applications*, vol. 50, no. 2, 2014.
- [112] Y. He and F. L. Luo, “Design and analysis of adaptive sliding-mode-like controller for DC-DC converters”, *IEE Proceedings - Electric Power Applications*, vol. 153, no. 3, pp. 401–410, May 2006.
- [113] J. Mahdavi, M. R. Nasiri, A. Agah, and A. Emadi, “Application of neural networks and state-space averaging to a DC/DC PWM converter in sliding-mode operation”, *IEEE/ASME Transactions on Mechatronics*, vol. 10, no. 1, pp. 60–67, Feb. 2005
- [114] S. C. Tan, Y. M. Lai, C. K. Tse, and M. K. H. Cheung, “A fixed frequency pulse-width-modulation-based quasi-sliding-mode controller for buck converters”, *IEEE Transactions on Power Electronics*, vol. 20, no. 6, pp. 1379–1392, Nov. 2005.
- [115] P. Mattavelli, L. Rossetto, and G. Spiazzi, “Small-signal analysis of dc–dc converters with sliding-mode control”, *IEEE Transactions on Power Electronics*, vol. 12, no. 1, pp. 96–102, Jan. 1997.

CURRICULUM VITAE

SEYED AHMAD HAMIDI

Email: hamidis@uwm.edu

I. Education

Jan. 2011 – Dec. 2016 **University of Wisconsin-Milwaukee, Milwaukee, WI, USA**

Major: Power Electronics

Minor: Biomedical Engineering-Bioelectric

Thesis title: DC Line-Interactive UPS with Load Leveling for Constant Power and Pulse Loads

GPA: 3.967/4

Sep. 2006 – May 2009 **K. N. Toosi University of Technology, Tehran, Iran.**

M.SC in Electrical Engineering

Major: Biomedical Engineering

Thesis title: Design and Implementation of a Digital Phase-Sensitive Demodulation Based on DSP

Sep. 2001 – June 2005 **Shiraz University, Shiraz, Iran**

B.SC in Electrical Engineering

Major: Control & Power Electronics

II. Academic Experience

A. Research Assistant:

Jan. 2011- May 2016 **Center for Sustainable Electrical Energy Systems (SEES), University of Wisconsin-Milwaukee, Milwaukee, WI, USA**

- Graduate Research Assistant (RA)
- Projects included power electronics and renewable systems

B. Teaching Assistant:

March 2013-Dec. 2013 **University of Wisconsin-Milwaukee, Milwaukee, WI, USA**

- Electric Machine and Drives (graduate/undergraduate)
- Controls for Renewable Energy Systems (graduate/undergraduate)

Sep. 2008-May 2009

K. N. Toosi University of Technology, Tehran, Iran

- Electrical Circuits 1 (undergraduate)

C. Instructor:

May 2009-Feb. 2010

Azad University, Tehran Branch, Tehran, Iran

- Electrical Circuits 1 and Lab (undergraduate)
- Digital Circuits and Lab (undergraduate)
- Microcontroller and Lab (undergraduate)

III. Publication

A. Book Chapter

1. S. A. Hamidi, D. Ionel and A. Nasiri, “Chapter 13: Modeling and Management of Batteries and Ultracapacitors for Renewable Energy Support in Electric Power Systems,” of “Renewable Energy: Devices and Systems with MATLAB”, D. Ionel and F. Blaabjerg (Eds.) , to be published by Taylor and Francis, 2016.
2. A. Nasiri and S. A. Hamidi, “Chapter 24: Uninterruptible Power Supplies”, of “Power Electronics Handbook”, M. H Rashid (Ed.), 4th Edition, to be published by Elsevier.

B. Journal and Conference Papers

1. S. A. Hamidi, A. Nasiri, “Design and Implementation of a DC Line-Interactive Uninterruptible Power Supply (UPS) with Load Leveling for Pulse Loads”, to be submitted on *IEEE Transaction on Industrial Electronics*, 2017.
2. S. A. Hamidi, Dan M Ionel, and Adel Nasiri, “Modeling and Management of Batteries and Ultracapacitors for Renewable Energy Support in Electric Power Systems - An Overview”, *Journal of Electric Power Components and Systems*, vol. 43, no. 12, pp. 1434-1452, 2015.
3. S. A. Hamidi, J. Katcha, and A. Nasiri, “DC Line-Interactive Uninterruptible Power Supply (UPS) with Load Leveling for Medical Devices”, *IEEE Energy Conversion Congress and Exposition (ECCE)*, Montreal, Canada, Sep. 2015.
4. S. A. Hamidi, E. Manla, and A. Nasiri, “Li-Ion Batteries and Li-Ion Capacitors: Characteristics, Modeling and their Grid Applications”, *IEEE Energy Conversion Congress and Exposition (ECCE)*, Montreal, Canada, Sep. 2015.
5. S. A. Hamidi and A. Nasiri, “Stability Analysis of a DC-DC Converter for Battery Energy Storage System Feeding CPL”, *IEEE International Telecommunications Energy Conference (IEEE Intelec 2015)*, Osaka, Japan, Oct. 2015.
6. S. A. Hamidi, A. Nasiri and T. Zhao, “Rectifier Efficiency Analysis for DC Distributed Data Centers”, *International Conference on Renewable Energy Research and Applications (ICRERA)*, Milwaukee, WI, Oct 19-22, 2014.
7. Q. Fu, S. A. Hamidi, A. Nasiri, V. Bhavaraju, B. Krstic, and P. Theisen, "The Role of Energy Storage in a Microgrid Concept", *IEEE Electrification Magazine*, vol. 1, no. 2, pp. 21-29, Dec 2013.
8. S. A. Hamidi, L. Weber and A. Nasiri, “EV Charging Station Integrating Renewable Energy and Second–Life Battery ”, *International Conference on Renewable Energy Research and Applications (ICRERA)*, Spain, 2013.
9. S. A. Hamidi, R. Jafari, A. Moosavina, and M. Soleimani, ” Design and implementation of a DSP-based digital phase sensitive demodulation for an EIT system”, *Journal of Physics*, 224 (1), 012147, 2010.

IV. Honors and Awards

<i>May 2016</i>	<i>Academic Excellence Award</i>
	University of Wisconsin-Milwaukee, Milwaukee, USA
<i>Jan. 2014</i>	<i>UWM Chancellor's Graduate Student Award</i>
	University of Wisconsin-Milwaukee, Milwaukee, USA
<i>Sep. 2013</i>	<i>UWM Chancellor's Graduate Student Award</i>
	University of Wisconsin-Milwaukee, Milwaukee, USA
<i>Jan. 2009</i>	<i>Finance Award for Excellence in Conducting M.Sc. Thesis</i>
	Research Institute of Petroleum Industry, Tehran, Iran

V. Professional Services, Peer Reviewer

1. Reviewer, *IEEE Energy Conversion Congress and Exposition (ECCE)*, (2013-present).
2. Reviewer, *IEEE Transactions on Sustainable Energy* (2013-present)
3. Reviewer, *IEEE Transactions on Industrial Electronics* (2016-present)
4. Reviewer, *IEEE Transactions on Industry Applications* (2016-present)
5. Reviewer, *IEEE Transactions on Smart Grid* (2016-present)
6. Reviewer, *Journal of Electric Power Components and Systems* (2013-present)

I. Work Experience

<i>April 2016- present</i>	Milwaukee Electric Tool, Brookfield, WI, USA Senior Design Engineer
<i>Jan. 2011- May 2016</i>	University of Wisconsin-Milwaukee, Milwaukee, WI, USA Graduate Research Assistance (RA)
<i>Jan. 2014 – Sep. 2014</i>	GE HealthCare (GEHC), Waukesha, WI, USA Electrical Engineer Intern, CT Hardware
<i>May 2013 – Aug. 2013</i>	Regal Beloit Company, Wausau, WI, USA <i>Software Development</i> Engineer Intern
<i>Nov. 2007 – Feb. 2008</i>	Chamran Hospital, Tehran, Iran Biomedical Engineer Intern
<i>June 2005 – Sep. 2005</i>	Shiraz Petrochemical Complex, Shiraz, Iran Electrical Engineer Intern

VI. Patents

<i>May 2015</i>	Adel Nasiri, Seyed Ahmad Hamidi, “DC Line-Interactive UPS with Load for DC Loads”, <i>pending</i>
<i>May 2015</i>	Adel Nasiri, Seyed Ahmad Hamidi, “Battery Management System for Li-ion Battery Module”, <i>pending</i>

VII. Project Experiences

1. 3-Level T-Type Grid-Tied Inverter (*Sep. 2015 –Dec. 2015*)

- Developing simulation model for a 150 kW 3-Level T-type DC/AC inverter
- Investigating switching and conduction losses while using SiC diodes.

2. Developing a Model of a Net Zero Energy Campus in a Micro-Grid Environment

- Studied the feasibility of rooftop wind, solar, and fuel cell at MSOE (Milwaukee School of Engineering) campus.
- Quantified power generation for the three sources based on available space, type of technology and initial cost.
- Studied the need and quantified the size for energy storage.
- Developed models for wind and solar in SAM (System Advisor Model from NREL) (funded by M-WERC, Milwaukee, WI, USA).

3. Johnson Controls Hybrid Battery Cycle Life Testing (*Mar. 2015- Oct. 2016*)

- Developing a battery test bed to perform testing on combined Li-ion/lead-acid batteries for life cycle, performance, and aging evaluation.
- Developed a fully automated LabVIEW program to perform charging/discharging cycles and log voltage, current and temperature data (funded by Johnson Controls, Glendale, WI, USA).

4. DC Line-Interactive UPS with Load Leveling for Medical Imaging Machines (*Sep. 2014 – Sep. 2016*)

- Accomplished a comprehensive study on different Li-ion battery chemistries.
- Developed a Li-ion battery test bed (for NCA and LFP types) for investigating life time/cycle of the batteries.
- Developed a battery management system (BMS) and board for NCA and LFP battery packs.
- Designed, analyzed, simulated and implemented a 20 kW 2-phase dc-dc interleaved converter for battery charging/discharging.
- Developed several advanced non-linear control approaches and implemented via DSP Builder for FPGA-based control board (funded by GEHC, Waukesha, WI, USA).

5. Converter Assessment for Data Center DC Power Distribution (*Sep. 2013 – Dec. 2013*)

- Analyzed different types of AC/DC rectifiers with associated loss calculations, considering real Silicon and SiC switch data.
- Developed simulation models in PSIM and Ansoft/Simplorer software to analyze performance and efficiency (funded by Eaton GRT, WI, USA).

6. Multi-Objective Optimization Algorithm Based on Differential Evolution (DE) (May 2013 – Aug. 2013)

- Implemented an optimization package based on DE for designing PM machines.
- Developed a Matlab-based co-simulation between Matlab/Maxwell/RMxprt software in order to conduct the optimization in multi-domain platform (Regal Beloit Company, Wausau, WI, USA).

7. Integration of Second-Life Batteries into an EV Charging Station with Renewable Energy Sources (Sep. 2012 – May 2013)

- Developed an accurate and comprehensive electrical model for Li-ion batteries.
- Designed and simulated a DC-based EV charging station with renewable energy sources integrated with second-life Li-ion batteries, retired from automotive (funded by Johnson Controls, Glendale, WI, USA).

8. Three-Phase DSP-based Monitoring System (Sep. 2011 – Aug. 2012)

- Designed and simulated a three-phase monitoring system to calculate and monitor line specifications, i.e. voltage, current, phase angle, active and reactive power.
- Developed a signal conditioning board to prepare captured data for the DSP board.
- Implemented the system on the TI F28335 DSP board via Simulink/Embedded Coder (funded by Eaton Innovation Center, Milwaukee, WI, USA).

9. DSP-Based Digital Phase-Sensitive Demodulation for an EIT System (Sep. 2008 – Sep. 2009)

- Designed and implemented a digital phase sensitive demodulation for Electrical Impedance Tomography (EIT) - an imaging technique.
- Developed based on TMS320C6713 Floating-Point Digital Signal Processor and Code Composer Studio software.

10. Study and simulation of several control techniques for renewable energy systems.

11. Modeling and simulating drive controls and switching strategies.

VIII. Special Skills

DSP programming: Code composer studio C2000 & C6000 DSP families, Embedded Coder

FPGA programming: DSP-Builder

Modeling & Analysis: Matlab, Simulink, SimPowerSystems, Control System Toolbox, Ansys-Simplorer, Ansys-Maxwell & RMxprt, dSPACE (CLP1104), LabVIEW, PSIM.